CWP-400
January 2002

Modeling and Inversion of Converted-Wave Reflection Coefficients in Anisotropic Media: A Tool for Quantitative AVO Analysis

Petr Jílek

— Doctoral Thesis —
Geophysics

Defended December 3, 2001

Committee Chair:	Dr. Thomas M. Boyd
Advisor:	Dr. Ilya D. Tsvankin
Co-advisor:	Dr. Vladimir Y. Grechka
Committee members:	Dr. John A. Desanto
	Dr. Alexander A. Kaufman
	Dr. Ken Larner

Center for Wave Phenomena
Colorado School of Mines
Golden, Colorado 80401
(1) 303 273-3557

Abstract

Although amplitude variation with offset analysis (AVO) has a potential to recover important reservoir characteristics, quantitative AVO inversion is known to be often unstable. To improve the stability, prestack P-wave amplitudes can be supplemented by amplitudes of converted PS-waves. The thesis objective is to build a theoretical foundation for joint AVO inversion of PP- and PS-waves in anisotropic media.

The quantity to be analyzed in AVO is the reflection coefficient at the target horizon. Linearized approximations for the reflection coefficients are frequently used as they provide a simple analytic insight. The approximations for PP-wave reflection coefficients are well known, but further development was necessary for converted-wave reflection coefficients in anisotropic media. I derive approximations for PS-wave reflection coefficients at a planar weak-contrast interface separating two weakly anisotropic halfspaces using first-order perturbation theory. The general expressions are further simplified and analyzed for the interface separating any two of the following media: isotropic, transversely isotropic with a vertical symmetry axis (VTI), transversely isotropic with a horizontal symmetry axis (HTI), and orthorhombic. Numerical tests reveal good agreement between the exact and approximate coefficients for most models believed to be typical for the subsurface.

I then use the linearized approximations for the joint linear inversion of the PP- and PS-wave reflection coefficients, establishing theoretical limitations of the inversion and investigating the influence of errors. Given good-quality, good-coverage data, together with *a priori* estimates of the P- to S-wave velocity ratio and one of the velocity or density contrasts across the interface, it is possible to recover the remaining contrasts along with the δ-type anisotropy parameter for VTI symmetry, and also the γ-type (shear-wave splitting) parameter for HTI symmetry. The inversion for orthorhombic models is more problematic and requires additional information. Relative to nonlinear inversion, the linear inversion is fast and provides important initial information about the medium parameters.

More sophisticated nonlinear inversion of the PP- and PS-wave reflection coefficients can be used to obtain more accurate estimates of the medium parameters. The nonlinear inversion algorithm, which I have developed and tested on several examples, strongly benefits from the analytic insight provided by the linear inversion. The accuracy of inverted results is generally better, and the resolution is higher than that of the linear inversion. Although still important, less *a priori* information is often necessary to stabilize the nonlinear inversion, compared to the linear inversion. The nonlinear inversion, however, is time consuming and must be properly guided.

The developed tools are designed to be used in conjunction with other techniques to perform quantitative AVO analysis. I discuss some practical aspects of such an analysis in the last chapter of the thesis.

The most beautiful experience we can have is the mysterious. It is the fundamental emotion which stands at the cradle of true art and true science. Whoever does not know it and can no longer wonder, no longer marvel, is as good as dead, and his eyes are dimmed.

(Albert Einstein, 1931)

Table of Contents

Acknowledgments

Without the professional advice and moral support of my teachers, my friends, and my family, I would not be able to succeed in pursuing my doctoral degree. Therefore, I wish to open this thesis by expressing my gratitude and sincere appreciation to those who helped me on this difficult but exciting journey. Without such acknowledgments, this thesis cannot be considered complete.

First of all, many thanks belong to my committee members: my advisor Ilya Tsvankin, co-advisor Vladimir Grechka, Ken Larner, Tom Boyd, Alexander Kaufman, John DeSanto, and Norm Bleistein. My committee members provided me with a solid guidance throughout all my PhD study. They gave me valuable advice and shared their insights with me. They always exposed the problem to be solved from many different perspectives that opened my eyes many times. Importantly, they gave me enough freedom necessary for my work. Ilya Tsvankin, Vladimir Grechka, and Ken Larner were in everyday contact with me, always willing to discuss various details of my research and, at the same time, always putting the research into a broader context. They were extremely helpful in improving my written and oral presentations; they taught me the necessary basics of professional scientific communication. I am grateful to my committee members for this educational and constructive relationship.

I would like to devote a separate paragraph to my advisors. I consider myself very lucky to have such an advisor as Ilya Tsvankin and co-advisor Vladimir Grechka during my PhD study, as well as advisors Vlastislav Červený and Ivan Pšenčík during my MS study. I have always admired remarkable insights of these scientists into a broad range of physical problems. My advisors, true professionals, taught me a great deal of science. But they also showed me their human side on many occasions, so I understood that true science cannot be really done without a moral maturity, mutual respect, ability to help and understand each other, ability to admit a mistake, and, of course, ability to relax. Ilya Tsvankin, Vladimir Grechka, Vlastislav Červený, and Ivan Pšenčík showed me all that. They will always remain my teachers.

I thank CWP research group for financial support and for providing me with creative working environment during my PhD study. I thank my CWP friends for many helpful and interesting discussions on various not-only-research topics. I especially thank CWP staff: Jo Ann Fink, Barbara McLenon, Michelle Szobody, and Lela Webber for their ever lasting support and for making CWP a place where it was always fun to work. For the very same reason, I want to thank Sara Summers from the Department of Geophysics.

My friends have been always very important for my life and work. They are

always ready to share good or bad times. They let me relax and they help me to solve problems when I need it. I am grateful for their honest opinions. My friends often become my teachers. First, I thank my good old friends from the Czech Republic for their lasting friendship: Maťa Baslar, Mira Kašpar, Petra Šauli, and Stano Sabol. They have always been able to deliver, at the right time, various pieces of the Czech culture to remind me of my home. They have always made an effort to remind me that our friendship has deep roots. Next, I thank my good friends from my early days in Golden for their patience to talk to me, when my English was poor, and for a lot of joy we had together, when my English got better thanks to them: Katja Freitag, Gary Lampard, Summer Montgomery, Frieder Roth, Andreas Rüger, and Lisa Ryan. Finally, I would like to name my "brothers in arms" who I shared a lot of happy moments with in the last few years, who I could always count on, and whose personal presence I will truly miss after I move out of Colorado: Jared Abraham, Justin Hedley, Ed and Lucy Jenner, Albena Mateeva, Andreas Rüger, Chris, Kristen and Cameron Sneddon, and Kasper Van Wijk. I will also not forget my friends Sverre Brandsberg-Dahl, Ronny Hofmann, and Jerome Le Rousseau. I appreciate very much the help of Ed, Albena, Andreas, Kasper, Sverre, and Jerome who had many valuable suggestions related directly to my research.

My final acknowledgments belong to people personally closest to me. I thank Wendy, my closest friend, for her honest love and great support, for her independent attitude, and her thoughts that she shared with me. I am grateful to her for my home that she created for me here in Colorado and for many happy days we have there together.

My brother Libor, his wife Martina, and their children Anička and Kubíček are always in my mind. Their strong moral support has helped me significantly during my study at CSM. I thank them for standing by me at all times and for sharing their feelings with me as a member of their family and their close friend. My visits to them are always joyful occasions. I am grateful for this close bond that does not deteriorate with distance and time.

Here, I would also like to mention my grandparents, Alois and Markéta, who always cared about me and always kept their fingers crossed for me. Unfortunately, my grandfather cannot witness my achievement today with the rest of my family.

Finally, my greatest thanks go inevitably to my parents, Jaromír and Markéta. I thank them with all my heart for their unlimited support over all those years, for their love, and for their respect and trust in me. Five years ago, they understood and supported my decision to leave my home country for PhD studies at CSM. Today, I am happy to tell them that their support paid off. I devote this thesis to them.

Chapter 1

Introduction

In modern seismic exploration, acquisition and efficient utilization of high-quality three-dimensional multiazimuth, multicomponent seismic data becomes necessary to properly account for the complexity of the subsurface structure, such as heterogeneity and anisotropy. Joint analysis of P- and S-wave reflection data helps in improving seismic images and obtaining better estimates of important medium parameters. Generating S-waves in practice, however, is expensive, and in marine environments is hardly possible. A practical alternative is to use converted PS-waves, or C-waves (P-waves converted at the target horizon into S-waves), which can be acquired simultaneously with the reflected PP-waves. Moreover, high-quality PS-wave reflection data are often collected in marine surveys, using ocean bottom cable (OBC) acquisition techniques. In recent years, converted PS-waves have attracted significant interest in the broad seismic community (Stewart & Gaiser, 2000).

Amplitude variation with offset (AVO) analysis is one of the seismic techniques that may greatly benefit from use of PS-waves. The beginning of the modern era of AVO analysis can be dated back to 1982 when, in his ground-breaking presentation, Ostrander (1982) demonstrated on real data how the variation of reflected amplitudes with offset can be used for direct detection of hydrocarbons. Since then, AVO has become an important tool of seismic exploration, complementary to seismic imaging. Primarily used as a purely qualitative method for revealing amplitude anomalies, AVO indeed proved to be useful not only for detection of hydrocarbon reservoirs (Ostrander, 1982; Chiburis, 1984; Hwang & Lellis, 1988; Burnett, 1990), but also for basic reservoir characterization (Smith & Gidlow, 1987; Swan, 1993; Ursin *et al.*, 1996; Castagna *et al.*, 1998) and, more recently, for reservoir monitoring (Anderson, 1996; Lorenzen, 2000). A remarkable development of AVO techniques over the past two decades, along with the development of acquisition techniques providing high-quality data (such as OBC), resulted in an increasing capability of AVO analysis. Today, the AVO methodology is more quantitative (Demirbag *et al.*, 1993; Mallick, 1995; Cambois, 2000), and can be used to provide estimates of important reservoir characteristics such as porosity, saturation, crack density, and orientation and content of the cracks (Rüger, 1998; Bakulin *et al.*, 2000a; Ursin *et al.*, 2001).

Although the theoretical potential of quantitative AVO is promising, many practical and theoretical problems make successful implementation of AVO inversion dif-

ficult. One of the most troublesome theoretical problems is that conventional P-wave AVO inversion is poorly constrained (Jin & Beydoun, 1993; Castagna, 1993; Cambois, 2000). As a consequence, individual parameters of the reservoir cannot be found uniquely and the recovered quantities may not be sufficiently accurate. For example, in isotropic media, it is usually impossible to invert for the P- and S-wave velocities and the density of the reservoir using only P-wave AVO amplitudes (Smith & Gidlow, 1987; Downton *et al.*, 2000). The problem of constraining the AVO inversion becomes particularly critical in anisotropic media. It is known that the contribution of anisotropy to AVO amplitudes is of the first-order (Wright, 1987; Thomsen, 1993; Rüger, 1997) and should not be neglected. Moreover, proper evaluation of anisotropy also provides important information about the internal structure of the medium. An example of practical importance in oil exploration is anisotropy induced by fracturing (Rüger, 1998; Bakulin *et al.*, 2000a); accurate characterization of the fractures within a reservoir is essential for efficient reservoir management. Taking anisotropy into account, however, significantly complicates AVO analysis, and introduces further instability into the AVO inversion.

In order to make the anisotropic AVO inversion viable, more comprehensive information about the model is necessary. One possibility is to collect wide-azimuth data and analyze AVO responses for different azimuths [so-called amplitude variation with azimuth (AVAZ) analysis], as described by Lynn and Thomsen (1990), Mallick and Fraser (1991), Yardley *et al.* (1991) and Rüger (1998). As indicated above, another possibility is to use not only P- but also S-wave reflection amplitudes. A case study of AVO and AVAZ analyses of pure-mode PP- and SS-wave reflected amplitudes can be found in DeVault (1997). Although such an analysis is certainly possible, it requires expensive excitation and recording of both PP and SS reflected data. The amplitudes of converted PS-waves provide a practical substitute for those of SS-waves as suggested, for example, by Alvarez *et al.* (1999), Larsen *et al.* (1999) and Nefedkina *et al.* (1999) for isotropic media, and by Bakulin *et al.* (2000a) for anisotropic media. Even if pure-mode SS-wave amplitudes are available, the amplitudes of converted PS-waves may add important independent constraints with relatively small cost.

The objective of the research presented here is to investigate the contribution of PS-waves to AVO analysis. The main questions to answer are: 1) what additional information is contained in PS-wave reflected amplitudes and how can this information stabilize the AVO inversion, 2) what is the theoretical and practical potential of the joint PP- and PS-wave AVO inversion for isotropic and anisotropic media, and 3) how can joint AVO inversion be performed effectively. The focus of the thesis is on the PP- and PS-wave reflection coefficients rather than total AVO amplitudes. In AVO and AVAZ, the reflection coefficients at the target horizon (such as the top of a hydrocarbon reservoir) are the fundamental quantities to be analyzed as func-

tions of incidence angle and azimuth. It is beyond the scope of this thesis to address many other practical and theoretical issues closely related to AVO analysis, such as amplitude-preserving data processing, correction of AVO amplitudes for noise, amplitude calibration, and propagation phenomena. Many of these issues are discussed in the literature and other issues, especially those regarding converted PS-waves, are under investigation. Sophisticated methods are also being developed to attack these problems in complicated heterogeneous anisotropic media. Some pertinent references are provided in the thesis.

Reflection and transmission coefficients generally are complicated nonlinear functions of medium parameters; in anisotropic media, their closed analytical forms may not exist at all. Thus, exact expressions of the coefficients usually do not provide useful analytic insight for AVO and AVAZ. Therefore, simplified approximations for the reflection and transmission coefficients are of great importance in practical AVO and AVAZ analyses. Although approximations for the PP-wave reflection coefficients for both isotropic (Bortfeld, 1961; Aki & Richards, 1980; Shuey, 1985) and anisotropic (Banik, 1987; Thomsen, 1993; Rüger, 1997; Rüger, 1998; Vavryčuk & Pšenčík, 1998) media are well developed, corresponding approximations for PS-wave reflection coefficients were derived only for several simple cases (Aki & Richards, 1980; Nefedkina & Buzlukov, 1999; Li *et al.*, 1996; Rüger, 1996).

The most general approximations for converted PS-wave reflection coefficients in anisotropic media probably have been published by Vavryčuk (1999). Unfortunately, the results of Vavryčuk are not well suited for practical AVO analysis. In Chapter 2, I derive approximate PS-wave reflection coefficients for a horizontal interface separating two arbitrarily anisotropic media. The derivation is based on the assumption of weak contrast of the P- and S-wave velocities and density across the interface, and weak anisotropy in both halfspaces (hence, so-called weak-contrast, weak-anisotropy approximations). The resulting formulas are further analyzed for the following symmetries and their combinations: isotropic, transversely isotropic with vertical (VTI) and horizontal (HTI) symmetry axes, and orthorhombic. An arbitrary azimuth of the vertical symmetry planes is allowed for HTI and orthorhombic media. I write the coefficients as functions of Thomsen-type medium parameters (Thomsen, 1986; Tsvankin, 1997a; Tsvankin, 1997b) and incidence and azimuthal angles, and as a result, obtain relatively simple forms of small-incidence-angle reflection coefficients. The derived approximations are consistent with the existing expressions derived by Rüger (1996) for symmetry planes of HTI and orthorhombic media. Discussion of the approximations and numerical tests of their accuracy using several azimuthally anisotropic models conclude Chapter 2.

These approximations of PS-wave reflection coefficients, together with the approximate PP-wave reflection coefficients derived by Rüger (1997) and Vavryčuk & Pšenčík (1998), provide a basis for the joint linear inversion of PP- and PS-wave

reflection coefficients developed in Chapter 3. Using the approximations results in a considerable simplification of the inversion procedure. Another benefit is clear analytic insight, which allows us to identify the most stable combinations of the medium parameters that can be recovered from the AVO response. I discuss the joint linear inversion in detail for anisotropic media with orthorhombic and higher symmetry. First, I analyze the theoretical potential of such an inversion with the goal of evaluating which parameters are constrained by ideal noise-free data. The second part of Chapter 3 is devoted to synthetic tests for data contaminated by errors. The existence of errors drastically reduces the potential of the inversion, allowing recovery of only a limited set of the medium parameters.

Chapter 4 describes more sophisticated and expensive joint *nonlinear* inversion of the PP- and PS-wave reflection coefficients in anisotropic media. Because the exact reflection coefficients are used instead of their approximations, the nonlinear inversion may provide more accurate and reliable results than does the linear inversion but must be carried out carefully. The main difficulties caused by the nonlinearity of the problem are described at the beginning of Chapter 4. The inversion algorithm is then developed, with the consideration of two major requirements: problems attributable to the nonlinearity must be properly addressed, and the inversion still has to be computationally feasible. I apply the algorithm to several synthetic examples using isotropic, HTI and orthorhombic models to study the resolution and stability of the nonlinear inversion. The addition of *a priori* information, as well as utilization of the linear inversion results, prove to be important for the success of the nonlinear inversion.

Chapter 5 summarizes the results of the thesis and puts them into the broader context of AVO (AVAZ) analysis. The main practical result of the thesis is the development of an *inversion toolbox*. The individual tools from this toolbox, discussed in Chapters 2, 3 and 4, can be used either separately or together, depending on the desired type and quality of the final result. The *inversion toolbox* is meant to be used in conjunction with other sophisticated techniques being developed today to perform advanced AVO analysis.

Chapter 2

Converted *PS*-wave reflection coefficients in weakly anisotropic media

Linearized approximations of *PP*- and *PS*-wave reflection coefficients for anisotropic media represent the basic tool of the *inversion toolbox*. Linearized approximations are used in conventional AVO analysis for two main reasons. First, unlike the exact expressions, the approximations provide simple analytic insight necessary for qualitative understanding of the amplitude signatures of reflected waves. Hence, the behavior of the reflected amplitudes can be predicted and, consequently, identified in field seismic data ("bright spots," induced by the brine/gas interface in porous sands, is a typical example). Second, using the linearized approximations, a number of useful characteristics of a specific interface can be recovered from data, making the interface identification more reliable. Various hydrocarbon indicators (Castagna, 1993; Swan, 1993), for example, are used to distinguish between the "true" bright spots associated with a brine/gas boundary and "false" bright spots attributable to other lithological contrasts of less economic interest. In addition to their contribution to qualitative AVO, linearized approximations often are also sufficiently accurate in the absolute sense for a reasonable range of incidence angles. Therefore, they may provide a basis for a quantitative linear inversion for such medium parameters as velocity or density contrasts across the interface.

Several approximations for reflection and transmission coefficients for isotropic media can be found, for example, in Bortfeld (1961), Richards & Frasier (1976), Aki & Richards (1980) and Shuey (1985). The *P*-wave reflection coefficient for weakly anisotropic VTI (transversely isotropic with a vertical symmetry plane) media and small incidence angles was first obtained by Banik (1987) and later extended for larger incidence angles by Thomsen (1993). Rüger (1996; 1997; 1998) refined Thomsen's (1993) expression and derived a complete set of approximate reflection and transmission coefficients for VTI media. He further extended the derivation for symmetry planes of HTI (transversely isotropic with a horizontal symmetry axis) and orthorhombic media, provided that their vertical symmetry planes in the incidence and reflecting halfspaces are aligned. Also, he obtained the azimuthally-dependent *P*-wave reflection coefficient for an interface between two HTI media. Finally, Pšenčík & Vavryčuk (1998) and Vavryčuk & Pšenčík (1998) presented azimuthally-dependent,

weak-contrast, weak-anisotropy P-wave reflection and transmission coefficients valid for arbitrarily anisotropic media. Approximate forms for PS-wave reflection coefficients for isotropic media are described, for example, in Donati (1998), Larsen *et al.* (1999), Alvarez *et al.* (1999) and Nefedkina & Buzlukov (1999). An approximation of PS-wave reflection coefficient, derived for symmetry-plane reflection at an HTI/HTI interface, has been obtained by Li *et al.* (1996). Rüger (1996) derived the approximate PS-wave reflection coefficients for VTI media and the vertical symmetry planes of HTI media.

The goal of this chapter, which can be regarded as an extension of the Rüger's (1996) work, is to derive azimuthally-dependent, weak-contrast, weak-anisotropy PS-wave reflection coefficients for arbitrarily anisotropic media.

2.1 Analytic development

To find a linearized form of the plane PS-wave reflection coefficients for arbitrarily anisotropic media, I follow the approach by Vavryčuk & Pšenčík (1998) that they introduced for PP-wave reflection coefficients (Appendix A). Their derivation is, in principle, similar to that of Banik (1987) and Thomsen (1993). However, in their approach a different medium parameterization and more complicated methodology are necessary in order to account for arbitrary anisotropy.

2.1.1 Perturbation approach

As in the case of exact reflection and transmission coefficients, approximate forms result from evaluation of boundary conditions satisfied at the interface (i.e., the continuity of the displacement and traction vectors across the interface). Here, however, the boundary conditions are evaluated only approximately, assuming weak contrasts of elastic medium parameters across the interface, and weak anisotropy in both halfspaces.

As an auxiliary step, consider a homogeneous isotropic full-space separated by a fictitious planar interface into two halfspaces characterized by the same density ρ^0 and identical sets of density-normalized stiffness coefficients

$$a^0_{ijkl} = (\alpha^2 - 2\beta^2)\delta_{ij}\delta_{kl} + \beta^2(\delta_{ik}\delta_{jl} + \delta_{il}\delta_{jk}), \tag{2.1}$$

where α and β represent P- and S-wave velocities (for consistency, I use the same notation as Vavryčuk & Pšenčík, 1998). I shall refer to such an isotropic space as the *background* medium. The elastic medium parameters of the true halfspaces under consideration can then be expressed in terms of perturbations from the background

medium as

$$\begin{aligned} a_{ijkl}^{(I)} &= a_{ijkl}^{0} + \delta a_{ijkl}^{(I)}, \\ \rho^{(I)} &= \rho^{0} + \delta\rho^{(I)}, \end{aligned} \tag{2.2}$$

where I=1 and 2 denote the incidence and reflecting halfspaces, respectively. Assuming that the perturbations $\delta a_{ijkl}^{(I)}$ and $\delta\rho^{(I)}$ for both I=1,2 are small, i.e.,

$$|\delta a_{ijkl}^{(I)}| \ll ||a_{ijkl}^{0}||, \qquad |\delta\rho^{(I)}| \ll \rho^{0}, \tag{2.3}$$

(for example, Vavryčuk & Pšenčík, 1998, define the norm $||a_{ijkl}^{0}||$ as $||a_{ijkl}^{0}|| = max|a_{ijkl}^{0}|$), it is possible to simplify the exact boundary conditions by linearizing them in the perturbations.

Note that conditions (2.3) are equivalent to both the assumption of weak contrasts of the elastic parameters a_{ijkl} and density ρ across the interface, and the assumption of weak anisotropy in both halfspaces (since a_{ijkl}^{0} corresponds to isotropic media).

2.1.2 Slowness and polarization vectors

In order to linearize the exact boundary conditions at the interface, the slownesses and polarization vectors of the incident wave and all reflected and transmitted waves need to be determined.

Consider a horizontal plane interface [the normal $\boldsymbol{n} = (0, 0, 1)$], and an incident plane P-wave propagating in the halfspace denoted as 1 and approaching the interface in the negative z-direction; see Figure 2.1 for the basic convention. For simplicity, the incidence plane, defined by the normal $\boldsymbol{n}$ and the slowness vector of the incident P-wave, coincides with the [x, z] plane of the reference Cartesian coordinate system (later, the formulas are generalized for an arbitrary azimuth; see Appendix B). In arbitrarily anisotropic media, three reflected and three transmitted waves, here denoted as P-wave (quasi compressional), and S_1- and S_2-waves (quasi shear), are generated at the interface.

Under the assumption of weak anisotropy, the slowness vectors can be written in terms of perturbations from the slowness vectors in the background medium, i.e.,

$$\boldsymbol{p}^{(N)} \approx \boldsymbol{p}^{0(N)} + \delta\boldsymbol{p}^{(N)}, \tag{2.4}$$

where $N = 0, 1, 2, 3$ correspond to the incident P-wave and reflected S_1-, S_2- and P-waves, respectively, and $N = 4, 5, 6$ correspond to the S_1-, S_2- and P- transmitted waves, respectively. The quantities $\boldsymbol{p}^{0(N)}$ are the slowness vectors in the isotropic

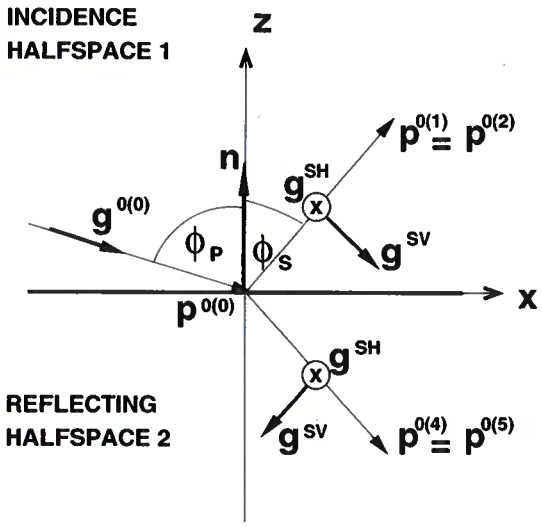

Figure 2.1. Convention for the zero-azimuth reflection and transmission (in the incidence plane [x, z]) in the background medium. The vector $\boldsymbol{n}$ is the normal to the reflector, $\boldsymbol{p}^{0(0)}$ is the background slowness vector of the incident P-wave, and $\boldsymbol{p}^{0(1)} = \boldsymbol{p}^{0(2)}$ and $\boldsymbol{p}^{0(4)} = \boldsymbol{p}^{0(5)}$ are the background slowness vectors of the reflected and transmitted S-waves, respectively. ϕ_P and ϕ_S denote the P-wave incidence and the S-wave reflection and transmission phase angles, respectively. The vector $\boldsymbol{g}^{0(0)}$ denotes the polarization vector of the incident P-wave in the background medium, and $\boldsymbol{g}^{SV}$ and $\boldsymbol{g}^{SH}$ are the reflected SV- and SH-wave's polarization vectors in the background medium ($\boldsymbol{g}^{SH}$ points away from the reader, parallel to the y-axis).

background medium which satisfy the following relations:

$$\begin{aligned} \boldsymbol{p}^{0(0)} = \boldsymbol{p}^{0(6)} &= (\sin\phi_P/\alpha, 0, \cos\phi_P/\alpha), \\ \boldsymbol{p}^{0(1)} = \boldsymbol{p}^{0(2)} &= (\sin\phi_P/\alpha, 0, -\cos\phi_S/\beta), \\ \boldsymbol{p}^{0(3)} &= (\sin\phi_P/\alpha, 0, -\cos\phi_P/\alpha), \\ \boldsymbol{p}^{0(4)} = \boldsymbol{p}^{0(5)} &= (\sin\phi_P/\alpha, 0, \cos\phi_S/\beta), \end{aligned} \tag{2.5}$$

where α and β are the isotropic background P- and S- wave velocities, as defined in equation (2.1), ϕ_P is the P-wave incidence phase angle, and ϕ_S is the S-wave reflection phase angle (Figure 2.1). The quantities $\delta\boldsymbol{p}^{(N)}$ in equation (2.4) are linear perturbations of the corresponding background slownesses due to the perturbations of the medium parameters δa_{ijkl} defined in equation (2.2). Using first-order perturbation theory (Jech & Pšenčík, 1989), Vavryčuk & Pšenčík (1998) derived analytic expressions for the perturbations $\delta\boldsymbol{p}^{(N)}$ as linear functions of the perturbations δa_{ijkl} (see Appendix A).

Similarly to the expressions for the slowness vectors (2.4), the polarization vectors can be written as

$$\boldsymbol{g}^{(N)} \approx \boldsymbol{g}^{0(N)} + \delta\boldsymbol{g}^{(N)}, \tag{2.6}$$

where N has the same meaning as that in equation (2.4), $\boldsymbol{g}^{0(N)}$ are the background slowness vectors, and $\delta\boldsymbol{g}^{(N)}$ the corresponding linear perturbations, also derived by Vavryčuk & Pšenčík (1998) (Appendix A). The P-wave background polarization vectors are simply given as

$$\begin{aligned} \boldsymbol{g}^{0(0)} = \boldsymbol{g}^{0(6)} &= (\sin\phi_P/\alpha, 0, \cos\phi_P), \\ \boldsymbol{g}^{0(3)} &= (\sin\phi_P/\alpha, 0, -\cos\phi_P). \end{aligned} \tag{2.7}$$

The S-wave polarization vectors in isotropic media usually are projected onto the incidence [x, z] plane (SV-wave polarization, here denoted as $\boldsymbol{g}^{SV}$) and the direction perpendicular to the plane (SH-wave polarization, denoted as $\boldsymbol{g}^{SH}$); see Figure 2.1. Jech & Pšenčík (1989), however, showed that such a choice is no longer acceptable if the S-wave polarization vectors in a weakly anisotropic medium are to be found by means of small (linear) perturbations from the S-wave polarization vectors in the background isotropic medium. To minimize the perturbations, the chosen polarization vectors in the background isotropic medium must be rotated in the plane perpendicular to the corresponding S-wave slowness vector by a certain *polarization angle* Φ. Jech & Pšenčík (1989) and Pšenčík (1998) derived an explicit analytic expression for the polarization angle Φ as a function of the parameter perturbations δa_{ijkl} defined in equation (2.2). Unfortunately, the angle Φ is not a linear function of δa_{ijkl}. This fact complicates the final approximations for PS-wave reflection coefficients, and their

application becomes more involved than that for PP-wave reflections, as discussed below.

For now, I assume that the polarization angle Φ is known and is taken as positive in the counter-clockwise direction from the vector $\boldsymbol{g}^{SV}$ towards the vector $\boldsymbol{g}^{SH}$. In the incidence background medium, the polarization angle Φ defines the "best" orientation (best in the sense of minimizing the perturbations) of the components S_1^0 and S_2^0 of the reflected S-wave in the plane $[\boldsymbol{g}^{SV}, \boldsymbol{g}^{SH}]$. The components S_1^0 and S_2^0 thus replace the familiar components SV and SH in the derivation below. Similar to SV and SH, the S_1^0 and S_2^0 components are mutually perpendicular; their polarization vectors are

$$\begin{aligned} \boldsymbol{g}^{0(1)} &= (-\cos\phi_S \cos\Phi, \sin\Phi, -\sin\phi_S \cos\Phi), \\ \boldsymbol{g}^{0(2)} &= (\cos\phi_S \sin\Phi, \cos\Phi, \sin\phi_S \sin\Phi). \end{aligned} \tag{2.8}$$

Clearly, if $\Phi = 0$ (as in isotropic media, see Jech & Pšenčík, 1989), S_1^0 reduces to the conventional SV-wave (polarized in the $\boldsymbol{g}^{SV}$ direction) and S_2^0 to the SH-wave (polarized in the $\boldsymbol{g}^{SH}$ direction). The background polarization vectors (2.8), together with the perturbations introduced in equation (2.6), define the reflected S_1- and S_2-waves in the weakly anisotropic medium.

Similarly, for the transmitted S-waves,

$$\begin{aligned} \boldsymbol{g}^{0(4)} &= (\cos\phi_S \cos\Psi, \sin\Psi, -\sin\phi_S \cos\Psi), \\ \boldsymbol{g}^{0(5)} &= (-\cos\phi_S \sin\Psi, \cos\Psi, \sin\phi_S \sin\Psi), \end{aligned} \tag{2.9}$$

where Ψ is the corresponding polarization angle in the reflecting halfspace.

Once the slowness and polarization vectors are specified, it is possible to linearize the boundary conditions at the interface and analytically evaluate all reflection and transmission coefficients for a given incident wave. For detailed derivation of the linearized boundary conditions, see Vavryčuk & Pšenčík (1998) and Appendix A.

2.1.3 General forms of the approximate PS-wave reflection coefficients

Appendices A and B describe how the linearized boundary conditions can be used to derive approximations for the PS-wave reflection coefficients. First, approximations are obtained for the incidence plane $[x, z]$ only (Appendix A); then they are generalized for an arbitrary azimuthal angle of the source-receiver line, denoted in the following as ψ (Appendix B). The final and most general formulas can be written as follows:

$$\begin{aligned} R_{PS_1} &= R_{PSV} \cos\Phi + R_{PSH} \sin\Phi, \\ R_{PS_2} &= -R_{PSV} \sin\Phi + R_{PSH} \cos\Phi. \end{aligned} \tag{2.10}$$

Here, R_{PS_1} and R_{PS_2} are the approximate reflection coefficients of the reflected PS_1- and PS_2-waves, respectively, and the angle Φ is the polarization angle defined in equations (2.8). R_{PSV} and R_{PSH} depend on the incidence angle ϕ_P, the reflection angle ϕ_S, and the azimuthal angle ψ, and are linear functions of the contrasts

$$\Delta A_{ij} = A_{ij}^{(2)} - A_{ij}^{(1)}, \tag{2.11}$$

where $A_{ij}^{(1)}$ and $A_{ij}^{(2)}$ represent the density normalized elastic medium parameters a_{klmn} of the incidence and reflecting halfspaces, respectively, written in the well-known Voigt notation (Tsvankin, 2001). Explicit expressions for R_{PSV} and R_{PSH} are listed in Appendix B [equations (B.3)-(B.5)] and will be discussed in detail later.

It should be emphasized that, in the weak-anisotropy approximation, coefficients (2.10) determine the amplitudes of the PS_1- and PS_2- reflected waves polarized in the vicinity of the $\boldsymbol{g}^{0(1)}$ and $\boldsymbol{g}^{0(2)}$ directions, respectively [see equations (2.8)]. Thus, the true displacements of the reflected PS_1- and PS_2-waves can be approximated as

$$\begin{aligned} U^{(1)}\boldsymbol{g}^{(1)} &\approx \boldsymbol{g}^{0(1)} \cdot R_{PS_1} \cdot U^{(0)}, \\ U^{(2)}\boldsymbol{g}^{(2)} &\approx \boldsymbol{g}^{0(2)} \cdot R_{PS_2} \cdot U^{(0)}, \end{aligned} \tag{2.12}$$

where $U^{(1)}$ and $U^{(2)}$ are the true amplitudes of the reflected PS_1 and PS_2 waves, respectively, polarized in the directions of the corresponding polarization vectors $\boldsymbol{g}^{(1)}$ and $\boldsymbol{g}^{(2)}$, and $U^{(0)}$ is the amplitude of the incidence P-wave. The perturbations of the true polarization vectors $\delta g^{(1)}$, $\delta g^{(1)}$ [equation (2.6)] are neglected in equation (2.12) since they contribute to the nonlinear (higher-order) terms only. Relations (2.12) will be used later to account for the polarization angle Φ.

Because of the nonlinearity of the angle Φ, the coefficients (2.10) are not linear functions of the medium parameters A_{ij}. Therefore, the term *linearized reflection coefficient*, commonly used for P-wave approximations, is not strictly correct for the converted-wave approximations in equations (2.10). Also, the coefficients (2.10) contain all 21 contrast parameters ΔA_{ij} (see Appendix B), compared to only 13 parameters present in the R_{PP} approximations even in the most general, triclinic symmetry (see Vavryčuk & Pšenčík, 1998).

Another interesting (but not surprising) observation following from equations (2.10) and (B.3)-(B.5) is that even a vertically incident P-wave can generate a reflected S-wave at a horizontal interface. The quantities largely responsible for such a reflection, in the first-order approximation, are the elastic contrasts ΔA_{34} and ΔA_{35}. In isotropic media, A_{34} and A_{35} vanish, and the conversion at normal incidence does not exist. This is also true for a horizontal interface between two anisotropic halfspaces with horizontal symmetry planes. Similarly, we can identify the contrasts in medium parameters mostly responsible for the "unusual" incidence-plane P-SH reflections (i.e., the reflected S-wave has a nonzero displacement component perpen-

dicular to the incidence plane). For instance, for incidence plane coinciding with the [x,z] plane of the reference coordinate system, nonzero contrasts ΔA_{14}, ΔA_{16}, ΔA_{34}, ΔA_{36}, ΔA_{45} and ΔA_{56} would generate such a reflection. Hence, this reflection exists only if [x,z] is not a symmetry plane. Below, I show that the P-SH reflection can occur, for example, outside the vertical symmetry planes for an isotropic/HTI or VTI/HTI interface.

Finally, note that the approximate reflection coefficients in equations (2.10) are derived using a purely *isotropic* background medium (defined in Section 2.1.1). Different approximations can be derived using, for instance, elliptically anisotropic or transversely isotropic background. Such approximations may have two main advantages. First, if the true anisotropic symmetry of the medium is close to the symmetry of the background, smaller perturbations from such an anisotropic background may be necessary than those from the isotropic background, resulting in a higher numerical accuracy of the corresponding approximations. Second, if the true anisotropic symmetry of the incident halfspace is close to the symmetry of the background, the nonlinear polarization angle Φ [equations (2.10)] would vanish from the final equations and hence the PS-wave approximate reflection coefficients become purely linear (in terms of perturbations ΔA_{ij}).

On the other hand, if the true anisotropic symmetry of either the incident or reflecting halfspace differs from the anisotropic symmetry of the background (note that this inevitably happens when each halfspace has different symmetry), larger perturbations from the background may be necessary than those from the isotropic background, resulting in a *lower* numerical accuracy of the approximations in general. Also, for anisotropic symmetry of the incident halfspace different from the symmetry of the background, the approximate reflection coefficients remain generally nonlinear. Moreover, for isotropic background, approximate reflection coefficients depend on one background parameter only (the average velocity ratio $\bar{\beta}/\bar{\alpha}$, see the next section). For anisotropic background, however, more background medium characteristics have to be determined *a priori*, including anisotropy parameters, orientation of the symmetry planes of the background, and polarizations of S-waves propagating in such a background. Of course, an incorrect determination of these background characteristics may result in a background that is quite different from the true medium. Large perturbations are then necessary and, consequently, the resulting approximations may become less accurate.

I therefore conclude that the benefit of using an anisotropic rather than isotropic background is not evident. However, it is intuitively clear that although an anisotropic background may produce higher numerical accuracy of the approximations for some *special* cases (such as the case of two halfspaces with identically oriented anisotropic symmetry above and below the interface), isotropic-background approximations are more universal. Importantly, due to a simpler background parameterization, the

isotropic-background approximations (2.10) may be better suited for practical applications.

2.1.4 Coefficients R_{PS_1} and R_{PS_2} for orthorhombic media

Here, I specify the general equations (2.10) for an interface between two orthorhombic media using the Thomsen-type parameterization of Tsvankin (1997b). Assuming orthorhombic (or higher) symmetry leads to a significant simplification of the general equations (2.10).

The first step is to choose the background velocities α and β and the density ρ^0. Following Banik (1987) and others, the background values are defined as the arithmetic mean of the corresponding quantities in both halfspaces, i.e.,

$$\begin{aligned} \alpha &\equiv \bar{\alpha} \equiv \frac{1}{2}(\alpha^{(1)} + \alpha^{(2)}), \\ \beta &\equiv \bar{\beta} \equiv \frac{1}{2}(\beta^{(1)} + \beta^{(2)}), \\ \rho^0 &\equiv \bar{\rho} \equiv \frac{1}{2}(\rho^{(1)} + \rho^{(2)}). \end{aligned} \tag{2.13}$$

It is not immediately clear which velocities (i.e., in which direction) in (2.13) should be averaged for anisotropic media. It has been suggested (Pšenčík & Martins, 2000), however, that for small and moderate incidence angles, the choice of vertical velocities is appropriate. Small- and moderate-incidence-angle reflection coefficients are also most important for practical applications.

The choice of vertical velocity is still non-unique for S-waves since, in general, in anisotropic media there are two vertically propagating S-waves with two different velocities. Numerical tests I carried out for the approximate R_{PP} coefficients suggest that it is acceptable to choose the S-wave background velocity anywhere between the two vertical velocities of the S_1- and S_2-waves. The resulting formulas differ slightly in accuracy, but these differences are often negligible, especially for small and moderate incidence angles. This conclusion is also in agreement with that of Pšenčík & Martins (2000). Therefore, I define the background velocities (2.13) as the average of the following velocities of the two halfspaces:

$$\alpha^{(I)} = \sqrt{A_{33}^{(I)}}, \qquad \beta^{(I)} = \sqrt{A_{55}^{(I)}}, \qquad I = 1, 2. \tag{2.14}$$

The second necessary step in the derivation is the choice of medium parameterization. Tsvankin (1997b) introduced an efficient way of parameterizing orthorhombic media by generalizing Thomsen's notation for VTI media (Thomsen, 1986). Without

any changes I adopt the following anisotropy parameters (Tsvankin, 1997b):

$$\epsilon_I^{(1)} \equiv \frac{A_{22}^{(I)} - A_{33}^{(I)}}{2A_{33}^{(I)}}, \tag{2.15}$$

$$\epsilon_I^{(2)} \equiv \frac{A_{11}^{(I)} - A_{33}^{(I)}}{2A_{33}^{(I)}}, \tag{2.16}$$

$$\gamma_I^{(S)} \equiv \frac{A_{44}^{(I)} - A_{55}^{(I)}}{2A_{55}^{(I)}}, \tag{2.17}$$

where I=1,2 represent the incidence and reflecting halfspaces, respectively. Further, I introduce three other parameters,

$$\tilde{\delta}_I^{(1)} \equiv \frac{A_{23}^{(I)} + 2A_{44}^{(I)} - A_{33}^{(I)}}{A_{33}^{(I)}}, \tag{2.18}$$

$$\tilde{\delta}_I^{(2)} \equiv \frac{A_{13}^{(I)} + 2A_{55}^{(I)} - A_{33}^{(I)}}{A_{33}^{(I)}}, \tag{2.19}$$

$$\tilde{\delta}_I^{(3)} \equiv \frac{A_{12}^{(I)} + 2A_{66}^{(I)} - A_{11}^{(I)}}{A_{11}^{(I)}}. \tag{2.20}$$

They differ from those in Tsvankin (1997b), defined as

$$\delta_I^{(1)} \equiv \frac{(A_{23}^{(I)} + A_{44}^{(I)})^2 - (A_{33}^{(I)} - A_{44}^{(I)})^2}{2A_{33}^{(I)}(A_{33}^{(I)} - A_{44}^{(I)})}, \tag{2.21}$$

$$\delta_I^{(2)} \equiv \frac{(A_{13}^{(I)} + A_{55}^{(I)})^2 - (A_{33}^{(I)} - A_{55}^{(I)})^2}{2A_{33}^{(I)}(A_{33}^{(I)} - A_{55}^{(I)})}, \tag{2.22}$$

$$\delta_I^{(3)} \equiv \frac{(A_{12}^{(I)} + A_{66}^{(I)})^2 - (A_{11}^{(I)} - A_{66}^{(I)})^2}{2A_{11}^{(I)}(A_{11}^{(I)} - A_{66}^{(I)})}. \tag{2.23}$$

Sayers (1994) showed that the anisotropy parameters (2.18), (2.19) and (2.20) represent linearized forms of the parameters (2.21), (2.22) and (2.23), respectively, and, for weak anisotropy, the two sets of parameters are numerically close to one other. Because the parameters (2.21)-(2.23) are nonlinear functions of stiffnesses A_{ij}, they cannot be used to carry the derivation of the approximate R_{PS_1} and R_{PS_2} coefficients (that are linearized in A_{ij}). However, although parameters (2.18)-(2.20) must be used for the *derivation*, for weak anisotropy either set of parameters can be used in the final formulas without significantly changing accuracy (Pšenčík & Martins, 2000). It should be emphasized that the parameters (2.15)-(2.23) are defined in a Cartesian

coordinate system with the axes x_1, x_2 and x_3 defining three symmetry planes of the orthorhombic medium under investigation. [This local Cartesian coordinate system may thus differ from the reference Cartesian coordinate system used to derive general equations (2.10).] A generalized form of the parameterization (2.15)-(2.20) for arbitrary weakly anisotropic media has been introduced by Mensch & Rasolofosaon (1997) and Pšenčík & Gajewski (1998).

As shown below, the six anisotropy parameters (2.15)-(2.20) [together with the background parameters (2.13) and (2.14)] are sufficient for expressing the coefficients R_{PS_1} and R_{PS_2}, whereas orthorhombic media are fully described by seven anisotropy parameters (plus two vertical velocities). Tsvankin's (1997b) original notation for orthorhombic media contains the parameters (2.15), (2.16), (2.21)-(2.23) and two other parameters γ_1 and γ_2, with the splitting parameter $\gamma^{(S)}$ [definition (2.17)] then defined as an auxiliary coefficient depending on γ_1 and γ_2. The approximations for R_{PS_1}, R_{PS_2}, however, are more sensitive to the difference $\gamma_1 - \gamma_2$ rather than to the individual parameters γ_1 and γ_2. Thus, the number of parameters can be reduced from seven to six. Tsvankin (1997b) shows that the parameter $\gamma^{(S)}$ reduces to the difference $\gamma_1 - \gamma_2$ in the weak-anisotropy approximation.

In the following, I assume that one of the symmetry planes of both orthorhombic halfspaces is horizontal. The x-axis of the reference coordinate system introduced in Figure 2.1 lies within one of the vertical symmetry planes of the incidence orthorhombic halfspace (the $[x_1, x_3]$ symmetry plane of the local coordinate system used in the definitions of the anisotropy parameters above). The vertical symmetry planes of the reflecting orthorhombic halfspace are rotated with respect to the vertical planes of the incidence orthorhombic halfspace by an angle denoted as κ. Then, the following elastic parameters vanish:

$$A_{14}^{(1)} = A_{15}^{(1)} = A_{16}^{(1)} = A_{24}^{(1)} = A_{25}^{(1)} = A_{26}^{(1)} = A_{34}^{(1)} =$$

$$= A_{35}^{(1)} = A_{36}^{(1)} = A_{45}^{(1)} = A_{46}^{(1)} = A_{56}^{(1)} = 0, \tag{2.24}$$

and

$$A_{14}^{(2)} = A_{15}^{(2)} = A_{24}^{(2)} = A_{25}^{(2)} = A_{34}^{(2)} = A_{35}^{(2)} = A_{46}^{(2)} =$$

$$= A_{56}^{(2)} = 0.$$

Substituting relations (2.24), along with definitions (2.13)-(2.20), into equations (B.3), (B.4) and (B.5), and further linearizing them in the anisotropy parameters

(2.15)-(2.20), yields the final formulas for the PS-wave reflection coefficients:

$$\begin{aligned} R_{PS_1} &= R_{PSV}\cos\Phi + R_{PSH}\sin\Phi, \\ R_{PS_2} &= -R_{PSV}\sin\Phi + R_{PSH}\cos\Phi. \end{aligned} \tag{2.25}$$

Equations (2.25) are formally identical to the general equations (2.10). Now, however,

$$\begin{aligned} R_{PSV} &= V_1\frac{\sin\phi_P}{\cos\phi_S} + V_2\cos\phi_P\sin\phi_P + V_3\frac{\sin^3\phi_P}{\cos\phi_S} \\ &\quad + V_4\cos\phi_P\sin^3\phi_P + V_5\frac{\sin^5\phi_P}{\cos\phi_S}, \\ R_{PSH} &= H_1\sin\phi_P + H_2\frac{\cos\phi_P\sin\phi_P}{\cos\phi_S} + H_3\sin^3\phi_P \\ &\quad + H_4\frac{\cos\phi_P\sin^3\phi_P}{\cos\phi_S}, \end{aligned} \tag{2.26}$$

and ϕ_P, ϕ_S are the incidence and reflection phase angles, respectively. Coefficients V_l and H_l are functions of the medium parameters [equations (2.13)-(2.20)], the azimuthal angle ψ and the angle κ. Explicit expressions for V_l and H_l are given in Appendix C [equations (C.1) and (C.2)].

Finally, the polarization angle Φ in equations (2.25) needs to be evaluated. The angle Φ can be computed analytically as long as all anisotropy parameters of the incidence medium are known. Equations for Φ are given in Appendix D. However, Φ can be also estimated directly from reflection data, which is important for practical applications.

2.1.5 Coefficients R_{PS_1} and R_{PS_2} for isotropic, VTI, and HTI halfspaces

Since isotropic, VTI and HTI media are special cases of orthorhombic media, the coefficients R_{PS_1} and R_{PS_2} derived in the previous section can be readily applied for an interface separating any of two of such halfspaces. In order to do so, the anisotropy parameters in V_l and H_l [equations (2.26)] have to be adapted for a specific model, as shown by Tsvankin (1997b). The anisotropy parameters used for VTI media are defined as

$$\begin{aligned} \epsilon &\equiv \frac{A_{11} - A_{33}}{2A_{33}}, \\ \delta &\equiv \frac{(A_{13} + A_{55})^2 - (A_{33} - A_{55})^2}{2A_{33}(A_{33} - A_{55})}, \end{aligned} \tag{2.27}$$

orthorhombic	HTI	VTI
$\epsilon^{(1)}$	0	ϵ
$\epsilon^{(2)}$	$\epsilon^{(V)}$	ϵ
$\gamma^{(S)}$	γ	0
$\tilde{\delta}^{(1)}$ or $\delta^{(1)}$	0	δ
$\tilde{\delta}^{(2)}$ or $\delta^{(2)}$	$\delta^{(V)}$	δ
$\tilde{\delta}^{(3)}$ or $\delta^{(3)}$	$\delta^{(V)} - 2\epsilon^{(V)}$	0

Table 2.1. Conversion table for the anisotropy parameters (weak-anisotropy approximation) for VTI, HTI and orthorhombic media. VTI and HTI parameters are defined by equations (2.27) and (2.28). The symmetry axis of the HTI medium points in the x-direction.

and for HTI media with the symmetry axis in the x direction,

$$\begin{aligned} \epsilon^{(V)} &\equiv \frac{A_{11} - A_{33}}{2A_{33}}, \\ \delta^{(V)} &\equiv \frac{(A_{13} + A_{55})^2 - (A_{33} - A_{55})^2}{2A_{33}(A_{33} - A_{55})}, \\ \gamma &\equiv \frac{A_{44} - A_{66}}{2A_{66}}. \end{aligned} \tag{2.28}$$

For a more detailed discussion of the anisotropy parameters for VTI and HTI media, see Tsvankin (1996; 1997a; 2001) and Thomsen (1986). For isotropic media, the anisotropy parameters vanish in V_l, and $H_l = 0$ for all $l = 1, ..., 4$; see equations (C.1) and (C.2).

Table 2.1 shows the conversions between the anisotropy parameters for different anisotropic models. For example, if the upper medium is VTI, all parameters with subscript 1 in equations (C.1) and (C.2) have to be replaced by the corresponding VTI parameters listed in the third column of Table 2.1. Also, for isotropic, VTI and HTI symmetry, the polarization angle Φ in equations (2.25) is determined from the expressions in Appendix D.

2.2 Discussion

2.2.1 Comparison of R_{PS_1} and R_{PS_2} with the results of Rüger (1996)

Although expressions (2.10) and (2.25) are more general that those obtained by Rüger (1996), the derivation described in this paper is based on the same principle of linearization of the boundary conditions. Therefore, the derived expressions should be analogous to those obtained by Rüger (1996) for the anisotropy and symmetry-axis planes of HTI media (assuming that the symmetry axes of both HTI halfspaces are aligned). Indeed, expressions (2.25) specified for an HTI/HTI interface (using Table 2.1) with the symmetry-plane rotation angle $\kappa = 0$ [equations (C.1)-(C.2)] reduce to Rüger's expressions if the azimuthal angle is set to $\psi = 0°$ or $\psi = 90°$ (see Rüger, 1996, Appendix D). (For the azimuths $\psi = 0°$ and $\psi = 90°$, the polarization angle Φ is equal to ψ, i.e., 0° and 90°, respectively.) Similar agreement has been also reported for the R_{PP} reflection coefficient by Vavryčuk & Pšenčík (1998).

Strictly, the analogy is not exact since expressions (2.25) include the linearized δ parameters (2.18)-(2.20) rather than the nonlinear parameters (2.21)-(2.23) contained in Rüger's expressions. However, in weakly anisotropic media these two sets of parameters can be formally interchanged.

2.2.2 Comparison of the coefficients R_{PS_1} and R_{PS_2} with the coefficient R_{PP}

General equations (2.10), as well as their particular forms for orthorhombic media [equations (2.25) and (2.26)], indicate that practical application of R_{PS} reflection coefficients in AVO will be more problematic than that of R_{PP} coefficients.

The first apparent complication comes from the fact that equations (2.25) include both the incidence and reflection phase angles ϕ_P and ϕ_S, which are related by Snell's law at the interface between two anisotropic media (this is not the case of the approximate R_{PP} where the S-wave reflection angle ϕ_S is eliminated during the derivation). This inconvenience, however, can be easily overcome by using the weak-contrast, weak-anisotropy assumption.

Since the factor $(\cos\phi_S)^{-1}$ in equations (2.26) is always multiplied by the contrasts in one of the medium parameters [contained in the corresponding coefficients V_1, V_3, V_5, and H_2, H_4, see equations (C.1)-(C.2)], it is possible to use purely isotropic Snell's law. The errors associated with such an approximation (i.e., neglecting anisotropy) are of the second order, and thus can be neglected in the linearized approximation. Therefore,

$$\frac{1}{\cos\phi_S} \approx \frac{1}{\sqrt{1-\frac{\bar{\beta}^2}{\bar{\alpha}^2}\sin^2\phi_P}} \approx 1 + \frac{1}{2}\frac{\bar{\beta}^2}{\bar{\alpha}^2}\sin^2\phi_P, \tag{2.29}$$

where $\bar{\alpha}$ and $\bar{\beta}$ are defined by equations (2.13) and (2.14). Equation (2.29) was simplified using the additional assumption of small $\sin^2\phi_P$. Numerical tests show that such an assumption works well for a wide range of $\bar{\alpha}/\bar{\beta}$ ratios, and for incidence angles corresponding to the offset-to-depth ratios conventionally used in AVO studies. A similar approach to that used in equation (2.29) can be also used to express the coefficients R_{PS_1} and R_{PS_2} in terms of either the reflection angle ϕ_S or horizontal slowness p_1, which may be convenient for some applications. Equation (2.29) can be directly substituted into either relations (B.3) or (2.26).

The second, more troublesome complication with R_{PS_1} and R_{PS_2} arises from the nonlinearity of the polarization angle Φ. For practical applications it is desirable to eliminate the influence of the polarization angle Φ before further analysis.

Such an elimination is straightforward if the incidence medium is either isotropic or VTI, and $\cos\Phi = 1$ and $\sin\Phi = 0$. Also, for HTI media it is possible to use relations (D.6), if the azimuth (the angle between the incidence and symmetry-axis plane) is known. In principle, this should not represent a significant complication since the azimuth of symmetry-axis plane (as well as isotropy plane) of HTI media can be estimated by using the traveltimes and polarizations of S-waves or the NMO ellipses of P- or PS-waves (Grechka & Tsvankin, 1998).

For an incidence halfspace of orthorhombic or lower symmetry, a different data-based approach has to be used to account for the angle Φ. It is convenient to formally introduce the PS-wave reflection-coefficient vector as

$$\boldsymbol{R}_{PS} = (R_{PS_1}, R_{PS_2}), \tag{2.30}$$

where R_{PS_1} and R_{PS_2} are defined by equations (2.25). From equations (2.12), the vector (2.30) is specified in the coordinate system $\boldsymbol{g}^{0(1)} - \boldsymbol{g}^{0(2)}$ and thus only approximates the exact reflection-coefficient vector $\boldsymbol{R}_{PS}^{ext} = (R_{PS_1}^{ext}, R_{PS_2}^{ext})$ specified in the coordinate system $\boldsymbol{g}^{(1)ext} - \boldsymbol{g}^{(2)ext}$ ($R_{PS_1}^{ext}$ and $R_{PS_2}^{ext}$ are the exact PS-wave reflection coefficients corresponding to the exact S-wave polarization vectors $\boldsymbol{g}^{(1)ext}$ and $\boldsymbol{g}^{(2)ext}$, respectively). It follows directly from equations (2.25) that the projection of the reflection-coefficient vector (2.30) onto the $\boldsymbol{g}^{SV}$ and $\boldsymbol{g}^{SH}$ directions, defined as for isotropic media (see Figure 2.1), gives the linear components R_{PSV} and R_{PSH}. Since $\boldsymbol{R}_{PS}^{ext} \approx \boldsymbol{R}_{PS}$, the linear components R_{PSV} and R_{PSH} can be estimated from the projection of the exact reflection coefficient vector $\boldsymbol{R}_{PS}^{ext}$ (extracted from field data) onto $\boldsymbol{g}^{SV}$ and $\boldsymbol{g}^{SH}$ directions, respectively.

Such a data projection is general and can be applied to any weakly anisotropic medium. For strong anisotropy, the projection may fail to produce satisfactory results, but equations (2.25) [as well as general equations (2.10)] are designed for weak anisotropy only. To perform the projection, a sufficiently accurate polarization analysis has to be carried out, which is, however, always necessary for proper recovery of the PS-wave amplitudes.

Finally, it should be emphasized that the approximations derived above should not be used near S-wave singular points which may exist in anisotropic media (slowness directions in which the slowness surfaces of the S_1- and S_2-waves intersect or touch each other, and both waves propagate with the same phase velocity). Due to the complicated character of the wavefield in those regions, plane PS-wave reflection coefficients fail to represent amplitude signatures close to singularities.

2.2.3 Components R_{PSV} and R_{PSH}

As soon as the components R_{PSV} and R_{PSH} are determined, they can be used in a way similar to that for reflection coefficients R_{PP} for qualitative AVO and AVAZ analyses. Moreover, the coefficients R_{PSV}, R_{PSH} and R_{PP} contain different linear combinations of the same medium parameters (see equations (2.26), (C.1) and (C.2); for R_{PP} approximation, see Vavryčuk & Pšenčík, 1998). Therefore, as discussed in Chapter 3, their joint linear inversion may provide a valuable tool for retrieving those parameters.

Equations (2.26), together with equations (C.1) and (C.2), show explicit forms for the components R_{PSV} and R_{PSH} for orthorhombic media. It follows from the equations that whereas the R_{PSV} component is a linear function of all anisotropy parameters (2.15)-(2.17) and (2.18)-(2.20) [or (2.21)-(2.23)], as well as the isotropy contrasts $\Delta\rho/\bar{\rho}$ and $\Delta\beta/\bar{\beta}$, the other component, R_{PSH}, includes the anisotropy parameters only. This is a consequence of the fact that there is only one nonzero reflection coefficient $R_{PS_1} = R_{PSV}$ in isotropic media [see equations (C.1)-(C.2), and equations (2.25) for $\Phi = 0°$]. A similar analysis shows that only one nonzero coefficient $R_{PS_1} = R_{PSV}$ exists for isotropic/VTI, VTI/isotropic and VTI/VTI interfaces (i.e., any azimuthally isotropic media). All other interfaces generate both PS_1 and PS_2 reflections, although not necessarily for all azimuths. Notice that none of the approximations for PS_1 and PS_2 contains the P-wave velocity contrast $\Delta\alpha/\bar{\alpha}$, which always appears in the P-wave reflection coefficient.

Equations (2.26), (C.1), and (C.2) also clearly show how different medium parameters control R_{PSV} and R_{PSH} components in different ranges of the incidence and azimuthal angles. For example, small- and moderate-incidence-angle reflections are controlled mostly by the parameters $\Delta\rho/\bar{\rho}$, $\Delta\beta/\bar{\beta}$, and $\delta_1^{(1)}$, $\delta_2^{(1)}$, $\delta_1^{(2)}$, $\delta_2^{(2)}$, $\gamma_1^{(S)}$ and $\gamma_2^{(S)}$ [here, as well as in the following discussion, definitions (2.21)-(2.23) are used instead of (2.18)-(2.20)]. In contrast, large-incidence-angle reflections are also substantially influenced by the parameters $\delta_1^{(3)}$, $\delta_2^{(3)}$ and $\epsilon_1^{(1)}$, $\epsilon_2^{(1)}$, $\epsilon_1^{(2)}$ and $\epsilon_2^{(2)}$. The same sets of parameters control also the R_{PP} reflection coefficients at the corresponding incidence-angle regions, as shown by Rüger (1997) (additionally, the contrast $\Delta\alpha/\bar{\alpha}$ in R_{PP} influences both the small- and large-incidence angle reflections). If the symmetry planes of the incidence and reflecting orthorhombic halfspaces have close azimuths [small angle κ in equations (C.1) and (C.2)], then only the contrasts of the

anisotropy parameters ($\Delta\delta^{(1)}$, $\Delta\delta^{(2)}$, $\Delta\delta^{(3)}$, $\Delta\gamma^{(S)}$, $\Delta\epsilon^{(1)}$ and $\Delta\epsilon^{(2)}$) determine the reflected amplitudes.

2.2.4 Approximate R_{PSV} and R_{PSH} for small incidence angles

In practical AVO analysis, one often uses reflection coefficients for relatively small incidence angles. Here, I derive simple forms of small-incidence-angle components R_{PSV} and R_{PSH} from equations (2.26).

Using the approximate reflection coefficients mainly at small incidence angles is also well justified by the fact that they lose their accuracy at large incidence angles. This might be surprising since no assumption of small incidence angles has been used in the original derivation [an exception is equation (2.29) which, however, is not an essential part of the derivation]. The loss of the accuracy of the linear approximations for large incidence angles has two main reasons. First, the terms associated with higher incidence angles contain an increasing number of nonlinear factors (i.e., higher powers of the elastic parameters) and, eventually, linear factors may vanish from such terms completely. Because the approximate reflection coefficients consist of the linear factors only, they cannot properly represent the exact reflection coefficients at large incidence angles. Second (specific to anisotropic media only), the background velocities $\bar{\alpha}$ and $\bar{\beta}$ in the approximate reflection coefficients have been selected as the vertical velocities [see the discussion of equations (2.13) and (2.14)]. Therefore, with increasing incidence angles away from the vertical, true medium velocities in anisotropic media deviate from the background velocities, causing additional loss of accuracy of the approximate reflection coefficients.

To obtain small-angle approximations of R_{PSV} and R_{PSH}, we neglect the second and higher powers of $\sin\phi_P$ in equations (2.26). Using expressions (C.1) and (C.2) and relation (2.29), we arrive at

$$
\begin{aligned}
R_{PSV} \;=\; & \left\{ -\frac{1+2g}{2}\frac{\Delta\rho}{\bar{\rho}} - 2g\frac{\Delta\beta}{\bar{\beta}} + \frac{1}{2(1+g)}\delta_2^{(2)}\cos^2(\psi-\kappa) \right. \\
& + \left[\frac{1}{2(1+g)}\delta_2^{(1)} - 2g\,\gamma_2^{(S)}\right]\sin^2(\psi-\kappa) - \frac{1}{2(1+g)}\delta_1^{(2)}\cos^2\psi \\
& \left. - \left[\frac{1}{2(1+g)}\delta_1^{(1)} - 2g\,\gamma_1^{(S)}\right]\sin^2\psi \right\}\sin\phi_P, \\
R_{PSH} \;=\; & \left\{ \left[\frac{1}{4(1+g)}(\delta_2^{(2)} - \delta_2^{(1)}) + g\,\gamma_2^{(S)}\right]\sin 2(\psi-\kappa) \right. \\
& \left. - \left[\frac{1}{4(1+g)}(\delta_1^{(2)} - \delta_1^{(1)}) + g\,\gamma_1^{(S)}\right]\sin 2\psi \right\}\sin\phi_P,
\end{aligned}
\tag{2.31}
$$

where g represents the background velocity ratio $g \equiv \bar{\beta}/\bar{\alpha}$.

Equations (2.31) work well up to incidence angles 15°-20°. To improve the accuracy for larger angles, additional terms with the factors $\sin^3\phi_P$ and $\cos\phi_P \sin^3\phi_P$ would have to be included. Unfortunately, this would lead to an increase in complexity, as follows from equations (2.26), (C.1) and (C.2).

By analogy with PP-wave reflection, equations (2.31) represent so-called PS-wave AVO gradients. Note that the PS-wave AVO gradients are associated with the term $\sin\phi_P$, whereas the PP-wave AVO gradient corresponds to $\sin^2\phi_P$: the PS-wave AVO gradients can be extracted from data by recovering the linear trends in plots $R_{PSV}(\sin\phi_P)$ and $R_{PSH}(\sin\phi_P)$. The AVO gradients can be used for fast rough estimates of the medium parameters as well as for a more sophisticated linear inversion of reflection coefficients. Joint inversion of the PP- and PS-wave AVO gradients can provide estimates of the parameters $\delta_i^{(1)}$, $\delta_i^{(2)}$ and $\gamma_i^{(S)}$, $i = 1, 2$ (assuming a nonzero angle κ). Such an inversion cannot be carried out using only approximations R_{PP} since the corresponding expressions do not allow one to separate $\delta_i^{(1)}$ from $\gamma_i^{(S)}$ (Rüger, 1997; Rüger & Tsvankin, 1997; Pšenčík & Martins, 2000).

2.3 Numerical examples

I have tested the accuracy of the approximations (2.25) and (2.26) on several anisotropic models. Most models here represent fracture-induced anisotropic media, derived from the results of Bakulin *et al.* (2000a; 2000b).

For all models, I compute both exact components R_{PSV} and R_{PSH}, their approximations and the corresponding absolute errors as functions of incidence angle and azimuth (Figures 2.2-2.4). The azimuth is measured from the x-axis of the reference coordinate system as introduced in Figure 2.1, with the orientation of the x-axis defined separately for each particular model. The "exact" components R_{PSV} and R_{PSH} are obtained by performing the projection of the exact coefficients R_{PS_1} and R_{PS_2} described above [see the discussion related to equation (2.30)]. Thus, an error associated with such a projection influences the final results. This extraction of the components R_{PSV} and R_{PSH} may simulate a processing sequence applied to field data to obtain the components R_{PSV} and R_{PSH}, which can be subsequently used in AVO analysis. Approximate components R_{PSV} and R_{PSH} are computed by using equations (2.26), (C.1), (C.2) and Table 2.1. The absolute error is determined as the difference between the exact and approximate coefficients.

Figure 2.2 shows the components R_{PSV} (left) and R_{PSH} (right) computed for VTI/HTI interface. The VTI incidence halfspace represents a typical shale layer overlaying an isotropic medium with vertical cracks that result in HTI symmetry. In this model, the cracks are gas-filled and a moderate crack density $e = 5\%$ is assumed (the crack density e is defined as [number of cracks per unit volume] $\times$ [mean cubed diameter]; for more detail, see Bakulin *et al.*, 2000a). The medium parameters for

both halfspaces can be found in the caption of Figure 2.2. The x-axis of the reference coordinate system is horizontal and coincides with the symmetry axis of the HTI medium (perpendicular to the cracks).

The component R_{PSV} in Figure 2.2 is well represented by the approximate equations. The shape of the approximate component (i.e., its variation with incidence and azimuthal angles) is close to that of the exact coefficient. The absolute error is small for the whole range of angles in the plot. However, because R_{PSV} increases with incidence angle from zero at normal incidence, any estimates of the coefficient at small incidence angles will contain large relative errors. Likely, such a small-incidence-angle reflection event will be strongly distorted by noise.

The shape of the component R_{PSH} is also approximated quite well, but the absolute errors are comparable to the magnitude of the coefficient itself. This should not be surprising since this component is small (note that the component R_{PSH} is always zero for azimuthally isotropic media or vertical symmetry planes in azimuthally anisotropic media) and thus large relative errors can be expected. Therefore, if the component R_{PSH} is detected at all in field data, equations (2.26) and (C.2) can be used primarily for qualitative rather than for quantitative analysis.

Figure 2.3 corresponds to an interface between two orthorhombic media with the vertical symmetry planes that differ by 30°. This model is represented by two perpendicular crack sets with different crack densities in each halfspace. In the incidence halfspace, the crack density of the cracks parallel to the $[x_2, x_3]$ plane of the local coordinate system (one of the symmetry planes) is $e_1 = 3\%$, and the perpendicular crack set (parallel to the other symmetry plane) has crack density $e_2 = 5\%$ (for more details, see Bakulin *et al.*, 2000b). The cracks are dry and embedded in an isotropic host rock with the P- and S-wave velocities 3.6 km/s and 2.3 km/s, respectively. In the reflecting halfspace (below the reflector), the crack sets are interchanged ($e_1 = 5\%$, $e_2 = 3\%$) and the isotropic host rock is characterized by the P- and S-wave velocities 4.17 km/s and 2.52 km/s, respectively. Additionally, the entire crack system of the reflecting halfspace is rotated with respect to the crack system of the incidence halfspace by the angle $\kappa = 30°$. The resulting medium parameters of both halfspaces are provided in the caption of Figure 2.3. The reference coordinate system is associated with the symmetry planes of the incidence orthorhombic medium, with the horizontal x-axis perpendicular to the $[x_2, x_3]$ symmetry plane. This model represents the most general configuration that can be treated by equations (2.26), (C.1) and (C.2).

Figure 2.3 (left) shows that the approximation for the component R_{PSV} is sufficiently high. The absolute error generally increases with azimuth but is small for all incidence angles plotted (especially for azimuths smaller than 60°). Small differences in the azimuthal variation of the exact and approximate R_{PSV} components are associated with a small value of the first-order term responsible for the azimuthal variation of the R_{PSV} approximation. In such a case, the contribution of higher-order terms

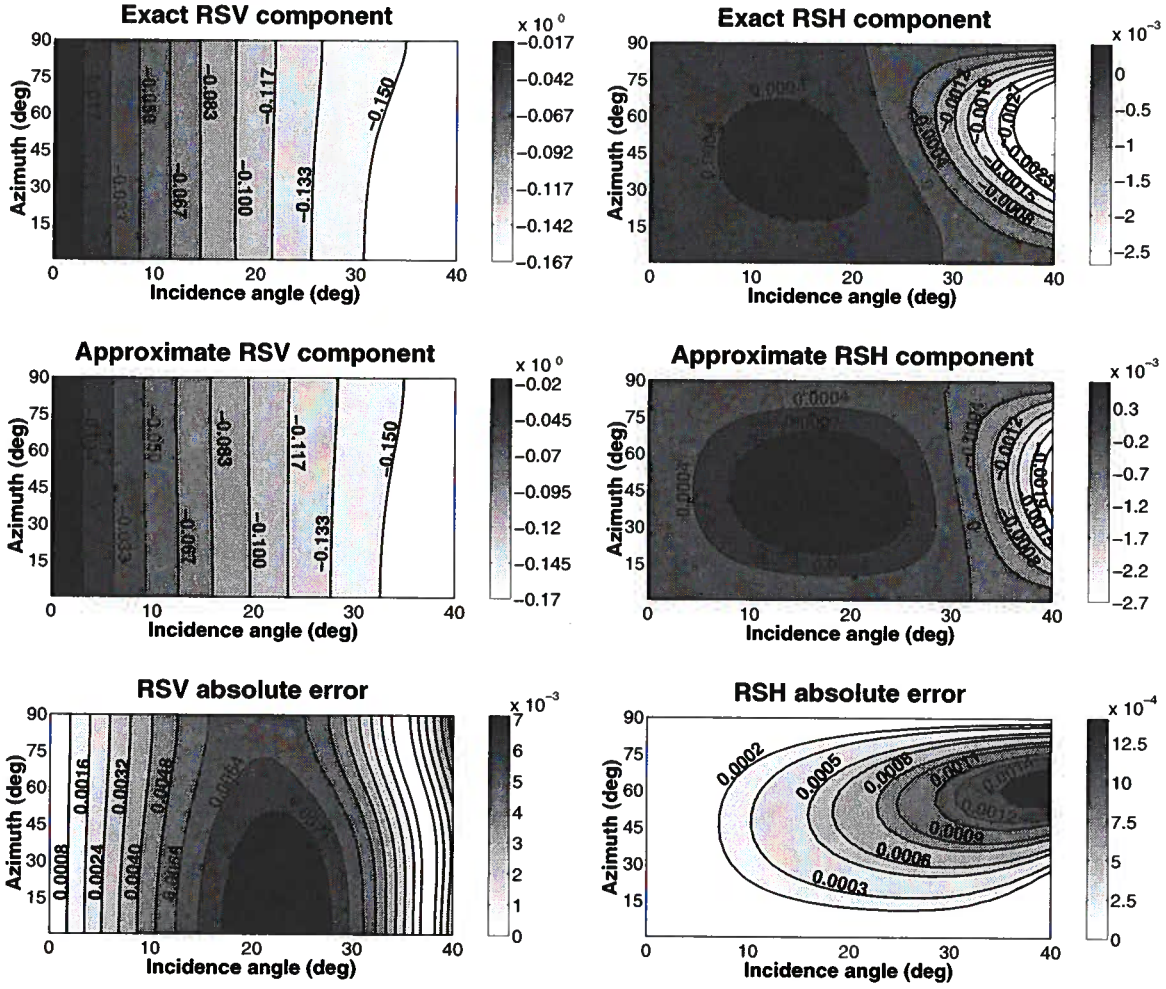

Figure 2.2. Components R_{PSV} (left) and R_{PSH} (right) of the PS-wave reflection coefficients for a VTI/HTI interface as functions of the incidence angle and azimuth: exact components (top), weak-contrast, weak-anisotropy approximations (middle) and absolute errors (bottom) defined as the difference between the exact and approximate components. Parameters of the VTI incidence halfspace: $\rho = 2.0\,\mathrm{g/cm^3}$, $V_{P0} = 2.9\,\mathrm{km/s}$, $V_{S0} = 1.5\,\mathrm{km/s}$, $\epsilon = 0.2$, $\delta = 0.1$, $\gamma = 0.1$; HTI reflecting halfspace: $\rho = 2.2\,\mathrm{g/cm^3}$, $V_{P0} = 3.3\,\mathrm{km/s}$, $V_{44} = 1.8\,\mathrm{km/s}$, $\epsilon^{(V)} = -0.13$, $\delta^{(V)} = -0.14$ and $\gamma^{(V)} = -0.053$; $V_{44} = \sqrt{A_{44}}$.

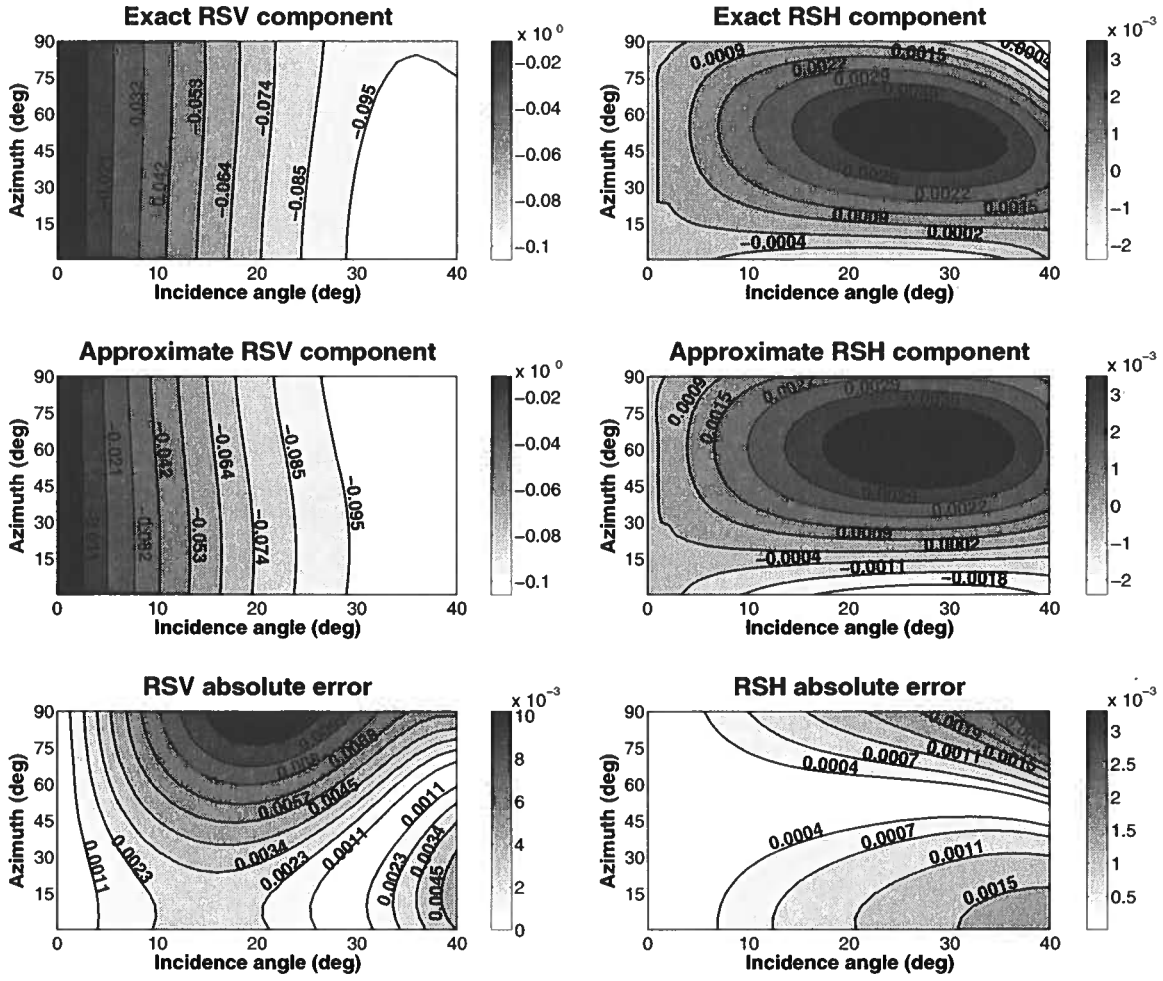

Figure 2.3. Components R_{PSV} (left) and R_{PSH} (right) of the PS-wave reflection coefficients for an orthorhombic/orthorhombic interface as functions of the incidence angle and azimuth: exact components (top), weak-contrast, weak-anisotropy approximations (middle) and absolute errors (bottom) defined as the difference between the exact and approximate components. The vertical symmetry planes of the halfspaces differ by the angle $\kappa = 30°$. Parameters of the incidence medium: $\rho = 2.1$ g/cm^3, $V_{33} = 3.57$ km/s, $V_{44} = 2.16$ km/s, $\epsilon^{(1)} = -0.14$, $\delta^{(1)} = -0.14$, $\gamma^{(1)} = -0.06$, $\epsilon^{(2)} = -0.082$, $\delta^{(2)} = -0.082$, $\gamma^{(2)} = -0.035$, $\delta^{(3)} = -0.058$; reflecting medium: $\rho = 2.3$ g/cm^3, $V_{33} = 4.17$ km/s, $V_{44} = 2.52$ km/s, $\epsilon^{(1)} = -0.082$, $\delta^{(1)} = -0.082$, $\gamma^{(1)} = -0.035$, $\epsilon^{(2)} = -0.14$, $\delta^{(2)} = -0.14$, $\gamma^{(2)} = -0.06$, $\delta^{(3)} = 0.05$; $V_{33} = \sqrt{A_{33}}$ and $V_{44} = \sqrt{A_{44}}$.

(neglected in the approximations) becomes comparable to that of the first-order term. The shape of the approximation R_{PSH} (Figure 2.3 left) is also sufficiently accurate, at least up to an incidence angle of 30°. Notice that the component R_{PSH} does not vanish for azimuths 0° and 90°, as it did in the previous example. This is caused by the misalignment of the vertical symmetry planes of the incidence and reflecting halfspaces. Figure 2.3 suggests that expressions (2.26), (C.1) and (C.2) can work reasonably well even for complicated models.

The final model (Figure 2.4) is derived from the previous one by increasing the strength of the anisotropy in both halfspaces (by increasing the crack densities to more than 10%). As expected, the accuracy of the component R_{PSV} decreased relative to that from the previous model. Moreover, the azimuthal variation of R_{PSV} is no longer approximated adequately. A similar failure is observed for the component R_{PSH}. Note that the "exact" components R_{PSV} and R_{PSH} have been obtained by the projection of the exact reflection-vector $\boldsymbol{R}_{PS}^{ext}$ onto the $\boldsymbol{g}^{SV}$ and $\boldsymbol{g}^{SH}$ directions, an operation that becomes inaccurate for a strongly anisotropic incidence medium.

Extensive numerical tests indicate that the accuracy of the approximations R_{PSV} and R_{PSH} generally decreases for lower anisotropic symmetries. However, the tests also indicate that approximations may still work acceptably for strongly anisotropic models with strong velocity and density contrasts. Also, the accuracy of the approximate R_{PSV} component is usually comparable to that of the R_{PP} approximation tested previously in the literature. The accuracy of the R_{PSH} component, however, will be significantly lower for the reasons mentioned above. In most cases, it will be impossible to extract the component R_{PSH} from field data due to a low signal-to-noise ratio.

2.4 Summary of Chapter 2

I derived first-order approximations for converted-wave reflection coefficients R_{PS_1} and R_{PS_2} at a weak-contrast horizontal interface separating two weakly anisotropic media of arbitrary symmetry. The general expressions were written explicitly for an orthorhombic/orthorhombic interface with differing vertical symmetry planes using Thomsen-type medium parameterization. Also, I obtained simple forms of the reflection-coefficient approximations for small incidence angles (i.e., PS-wave AVO gradients). The resulting expressions can be applied for any combination of isotropic, VTI, HTI and orthorhombic halfspaces.

The expressions for the coefficients R_{PS_1} and R_{PS_2} are more complicated than the corresponding ones for R_{PP}. In order to recover the R_{PS_1} and R_{PS_2} coefficients from field data, and to extract their linear components (here denoted as R_{PSV} and R_{PSH}), an accurate polarization analysis must be carried out. Moreover, the existence of S-wave singular points may complicate the recovery and reduce the applicability

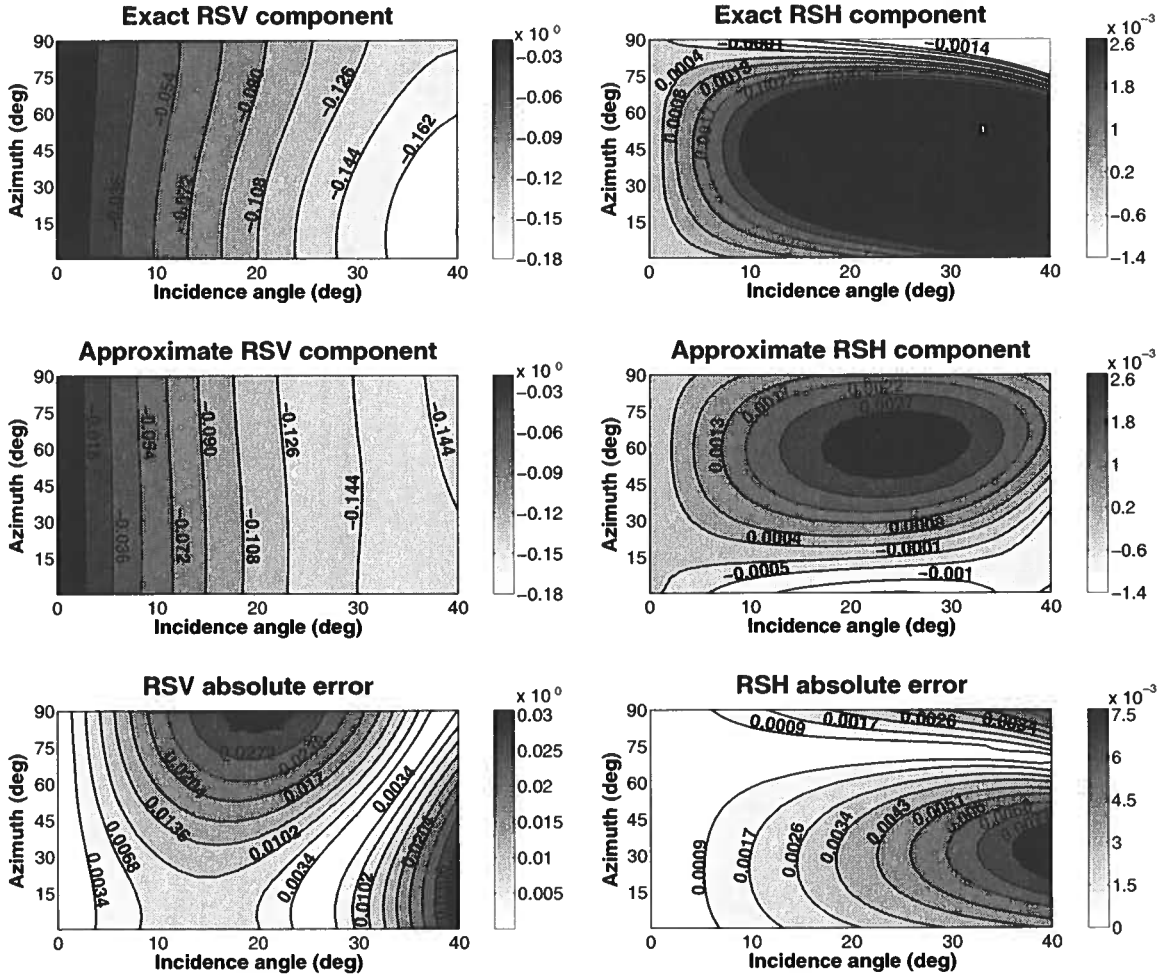

Figure 2.4. Components R_{PSV} (left) and R_{PSH} (right) of the PS-wave reflection coefficients for a strong-contrast, strong-anisotropy orthorhombic/orthorhombic interface as a function of the incidence angle and azimuth: exact components (top), weak-contrast, weak-anisotropy approximations (middle) and absolute errors (bottom) defined as the difference between the exact and approximate components. The vertical symmetry planes of the orthorhombic halfspaces differ by the angle $\kappa = 30°$. Parameters of the incidence medium: $\rho = 2.0\,\mathrm{g/cm^3}$, $V_{33} = 3.4\,\mathrm{km/s}$, $V_{44} = 1.8\,\mathrm{km/s}$, $\epsilon^{(1)} = -0.27$, $\delta^{(1)} = -0.28$, $\gamma^{(1)} = -0.1$, $\epsilon^{(2)} = -0.19$, $\delta^{(2)} = -0.20$, $\gamma^{(2)} = -0.07$, $\delta^{(3)} = -0.11$; reflecting medium: $\rho = 2.2\,\mathrm{g/cm^3}$, $V_{33} = 4.2\,\mathrm{km/s}$, $V_{44} = 2.4\,\mathrm{km/s}$, $\epsilon^{(1)} = -0.18$, $\delta^{(1)} = -0.20$, $\gamma^{(1)} = -0.08$, $\epsilon^{(2)} = -0.24$, $\delta^{(2)} = -0.25$, $\gamma^{(2)} = -0.1$, $\delta^{(3)} = 0.06$; $V_{33} = \sqrt{A_{33}}$ and $V_{44} = \sqrt{A_{44}}$.

of the coefficients.

Numerical tests show good overall agreement of the derived approximations with the corresponding exact coefficients for models with moderate velocity and density contrasts, and moderate anisotropy. The accuracy of the component R_{PSV} is usually comparable to that of R_{PP} approximations in the literature. Besides, the approximate R_{PSV} frequently work well even for relatively large incidence angles. Although the component R_{PSH} is a direct indicator of azimuthal anisotropy, it, unfortunately, is usually small and is likely to be distorted by noise. Decreasing accuracy of the approximate R_{PSV} and R_{PSH} generally is expected for lower anisotropic symmetries.

The equations derived in this paper can be further used to analyze the R_{PS_1} and R_{PS_2} coefficients for an interface separating arbitrarily anisotropic halfspaces, including TI halfspaces with arbitrarily tilted symmetry axes or orthorhombic halfspaces that have no horizontal symmetry planes.

Chapter 3

Joint linear inversion of *PP*- and *PS*-wave reflection coefficients in anisotropic media

Joint linear inversion of *PP*- and *PS*-wave reflection coefficients was suggested and performed for isotropic media, for example, by Alvarez *et al.* (1999), Larsen *et al.* (1999) and Nefedkina *et al.* (1999). The development of such an inversion for *anisotropic* media (as the second tool in the *inversion toolbox*), is the objective of this chapter. The results of Chapter 2 provide the necessary theoretical foundation for the inversion.

The main motivation for developing the linear inversion is its simplicity: it is fast and allows for a straightforward error analysis. One of the most important contributions of this tool is its capability to provide relatively simple analytical insight. Such an insight is essential to recognize (or exclude) possible types of anisotropic symmetry of the medium, to identify the combinations of the medium parameters constrained by data, and to suggest the necessary *a priori* information.

In this chapter, I discuss the joint linear inversion of *PP*- and *PS*-wave reflection coefficients for anisotropic media with orthorhombic and higher symmetry. I use the approximations of the *PS*-wave reflection coefficients derived in Chapter 2, together with the approximate *PP*-wave reflection coefficients derived by Rüger (1997) and Vavryčuk & Pšenčík (1998). First, I analyze the theoretical potential of such an inversion by applying it to ideal, noise-free data. Second, I develop an algorithm for the more realistic inversion of data contaminated by errors and test it on several synthetic examples.

3.1 Linear inversion of noise-free data

Performing an ideal inversion of data with no errors is, of course, impossible in practice. Such an analysis, however, establishes the theoretical limitations of the inversion by showing the maximum amount of information that can be extracted using *PP*- and *PS*-wave amplitudes. A model of orthorhombic symmetry is used for this investigation. The results can be immediately applied to any higher anisotropic symmetries, such as transversely isotropic media with vertical (VTI) or horizontal (HTI) symmetry axis (we assume a horizontal reflecting interface throughout), or isotropic

media. For models with lower anisotropic symmetries (monoclinic, triclinic), or tilt of symmetry, the analysis would be more complex because of the more complicated structure of the approximations R_{PP}, R_{PS_1} and R_{PS_2}. The principle, however, remains the same.

3.1.1 Variation of the reflection coefficients with incidence angle and azimuth

As in Chapter 2, I assume a horizontal interface separating two orthorhombic halfspaces. Each orthorhombic halfspace has three mutually perpendicular symmetry planes, one of which is horizontal. The $[x, z]$ plane of the reference Cartesian coordinate system coincides with one of the vertical symmetry planes of the incidence orthorhombic halfspace, and the $[x, y]$ plane is parallel to the interface (as well as to the horizontal symmetry planes of both halfspaces).

Approximate PP-wave reflection coefficient

A detailed discussion of the approximations of the PP-wave reflection coefficients in anisotropic media (denoted in the following as R_{PP}) can be found in Rüger (1997) and Vavryčuk & Pšenčík (1998). Under the convention introduced in Chapter 2, R_{PP} can be written as (Vavryčuk & Pšenčík, 1998)

$$R_{PP} = P_0 + P_1 \sin^2\phi + P_2 \sin^2\phi \tan^2\phi, \tag{3.1}$$

where ϕ is the phase incidence angle (for simplicity, the symbol ϕ is used here instead of ϕ_P used in Chapter 2), and the terms P_0, P_1 and P_2 represent the P-wave AVO intercept, gradient and large-incidence-angle terms, respectively. The intercept is given by

$$P_0 = \frac{1}{2}\frac{\Delta Z}{\bar{Z}} \approx \frac{1}{2}\frac{\Delta\rho}{\bar{\rho}} + \frac{1}{2}\frac{\Delta\alpha}{\bar{\alpha}}. \tag{3.2}$$

As in Chapter 2, α is the vertical P-wave velocity and ρ is the density, $Z = \alpha\rho$ is the vertical P-wave impedance, $\Delta X = X_2 - X_1$ denotes the contrast in quantity X across the interface (the subscripts 1 and 2 refer to the incidence and reflecting halfspaces, respectively), and $\bar{X} = \frac{1}{2}(X_1 + X_2)$ denotes the average value of X. The approximate relation (3.2) is valid for small contrasts $\Delta\rho$ and $\Delta\alpha$. The P-wave AVO gradient P_1 can be written as follows (Vavryčuk & Pšenčík, 1998):

$$P_1 = P_1^{(ABS)} + P_1^{(M)} \sin\psi\cos\psi + P_1^{(L)} \sin^2\psi, \tag{3.3}$$

where ψ is the azimuth of the incidence plane, treated as positive in the counter-

clockwise direction from the x-axis towards the y-axis of the reference coordinate system (the incidence plane is defined by the incident P-wave slowness vector and the normal to the interface). As seen in equation (3.3), the P-wave AVO gradient P_1 contains three terms: the term $P_1^{(ABS)}$ is azimuthally independent, the $P_1^{(M)}$ term is pronounced mostly at intermediate azimuths (with the maxima at $\psi = 45° \pm k90°$, where $k = 0, 1, 2, 3$), and the $P_1^{(L)}$ term dominates the azimuthal behavior for larger azimuths close to $\psi = \pm 90°$. The explicit forms of $P_1^{(ABS)}$, $P_1^{(M)}$ and $P_1^{(L)}$ are

$$P_1^{(ABS)} = \frac{1}{2}\left[-(\delta_2^{(2)} - \delta_2^{(1)} + 8\frac{\bar{\beta}^2}{\bar{\alpha}^2}\gamma_2^{(S)})\sin^2\kappa + \delta_2^{(2)} - \delta_1^{(2)} + \frac{\Delta\alpha}{\bar{\alpha}} - 4\frac{\bar{\beta}^2}{\bar{\alpha}^2}\frac{\Delta G}{\bar{G}}\right], \tag{3.4}$$

$$P_1^{(M)} = \frac{1}{2}\left[(\delta_2^{(2)} - \delta_2^{(1)} + 8\frac{\bar{\beta}^2}{\bar{\alpha}^2}\gamma_2^{(S)})\sin 2\kappa\right], \tag{3.5}$$

$$P_1^{(L)} = \frac{1}{2}\left[-(\delta_2^{(2)} - \delta_2^{(1)} + 8\frac{\bar{\beta}^2}{\bar{\alpha}^2}\gamma_2^{(S)})\cos 2\kappa + (\delta_1^{(2)} - \delta_1^{(1)} + 8\frac{\bar{\beta}^2}{\bar{\alpha}^2}\gamma_1^{(S)})\right]. \tag{3.6}$$

In these equations, $\bar{\alpha}$ is defined in equation (3.2) and $\bar{\beta}$ is the average $\frac{1}{2}(\beta_1+\beta_2)$, where β_1 and β_2 represent the vertical S-wave velocities in the two halfspaces, respectively [corresponding to the stiffness tensor elements A_{55}; see definitions (2.13)-(2.14)]. In equation (3.4), $G = \rho\beta^2$ is the vertical shear modulus. In the weak-contrast approximation,

$$\frac{\Delta G}{\bar{G}} \approx \frac{\Delta\rho}{\bar{\rho}} + 2\frac{\Delta\beta}{\bar{\beta}}\,. \tag{3.7}$$

The anisotropy parameters of the incidence orthorhombic halfspace ($\gamma_1^{(S)}$, $\delta_1^{(1)}$, $\delta_1^{(2)}$) and the reflecting orthorhombic halfspace ($\gamma_2^{(S)}$, $\delta_2^{(1)}$, $\delta_2^{(2)}$) are defined as in Tsvankin
(1997b); see equations (2.17), (2.21) and (2.22), respectively. Note that the anisotropy parameters are defined in the *local* Cartesian coordinate systems $[x_1, x_2, x_3]_1$ (incidence halfspace) and $[x_1, x_2, x_3]_2$ (reflecting halfspace). For each halfspace j, the coordinate systems are chosen such that $[x_1, x_3]_j$ and $[x_2, x_3]_j$ planes coincide with the two vertical symmetry planes of the medium. Consequently, the local coordinate system of the incidence halfspace $[x_1, x_2, x_3]_1$ also coincides with the reference coordinate system $[x, y, z]$ used in equation (3.1). Finally, the angle κ in equations (3.4)-(3.6) is the misalignment angle defined along with equations (2.24)-(2.26). Under the chosen convention, κ is also the azimuth of the $[x_1, x_3]_2$ vertical symmetry plane of the reflecting orthorhombic halfspace. If $\kappa = 0$, the vertical symmetry planes of the incidence and reflecting halfspaces are aligned.

The azimuthal variation of the large-incidence-angle term P_2 in equation (3.1) can be expressed as

$$\begin{aligned} P_2 &= P_2^{(ABS)} + P_2^{(M1)} \sin 2\psi \cos 2\psi + P_2^{(M2)} \sin\psi \cos\psi \\ &\quad + P_2^{(M3)} \sin^2\psi \cos^2\psi + P_2^{(L)} \sin^2\psi. \end{aligned} \tag{3.8}$$

Equation (3.8) shows that the azimuthal variation at large incidence angles is controlled by five terms. The $P_2^{(ABS)}$ and $P_2^{(L)}$ terms are analogous to the $P_1^{(ABS)}$ and $P_1^{(L)}$ terms, respectively, in equation (3.3). Equation (3.8), however, also contains three intermediate-azimuth terms $P_2^{(M1)}$, $P_2^{(M2)}$ and $P_2^{(M3)}$; the $P_2^{(M1)}$ term is most pronounced at azimuths close to $22.5° \pm k45°$ ($k = 0, \ldots, 7$), the $P_2^{(M2)}$ and $P_2^{(M3)}$ terms influence the behavior of the reflection coefficient R_{PP} mainly at azimuths close to $\psi = 45° \pm k90°$ ($k = 0, 1, 2, 3$) (in general, $P_2^{(M2)}$ makes a larger contribution). Explicit expressions for the components are

$$\begin{aligned} P_2^{(ABS)} &= \frac{1}{2}\left[\frac{1}{4}(\delta_2^{(3)} + \epsilon_2^{(2)} - \epsilon_2^{(1)}) \sin^2 2\kappa - (\epsilon_2^{(2)} - \epsilon_2^{(1)}) \sin^2\kappa \right. \\ &\quad \left. + \epsilon_2^{(2)} - \epsilon_1^{(2)} + \frac{\Delta\alpha}{\bar{\alpha}}\right], \end{aligned} \tag{3.9}$$

$$P_2^{(M1)} = \frac{1}{2}\left[-\frac{1}{4}(\delta_2^{(3)} + \epsilon_2^{(2)} - \epsilon_2^{(1)}) \sin 4\kappa\right], \tag{3.10}$$

$$P_2^{(M2)} = \frac{1}{2}\left[(\epsilon_2^{(2)} - \epsilon_2^{(1)}) \sin 2\kappa\right], \tag{3.11}$$

$$P_2^{(M3)} = \frac{1}{2}\left[(\delta_2^{(3)} + \epsilon_2^{(2)} - \epsilon_2^{(1)}) \cos 4\kappa - (\delta_1^{(3)} + \epsilon_1^{(2)} - \epsilon_1^{(1)})\right], \tag{3.12}$$

$$P_2^{(L)} = \frac{1}{2}\left[-(\epsilon_2^{(2)} - \epsilon_2^{(1)}) \cos 2\kappa + (\epsilon_1^{(2)} - \epsilon_1^{(1)})\right]. \tag{3.13}$$

Equations (3.9)-(3.13) contain the anisotropy parameters $\epsilon_1^{(1)}$, $\epsilon_1^{(2)}$, $\delta_1^{(3)}$ (incidence halfspace) and $\epsilon_2^{(1)}$, $\epsilon_2^{(2)}$ and $\delta_2^{(3)}$ (reflecting halfspace), which differ from those that control the AVO gradient [equations (3.4)-(3.6)]. For a detailed discussion of these parameters [equations (2.15), (2.16) and (2.23)], see Tsvankin (1997b).

Approximate PS-wave reflection coefficients

In Chapter 2, I derived the approximate PS-wave reflection coefficients valid for arbitrary anisotropic media in the form

$$\begin{aligned} R_{PS_1} &= R_{PSV} \cos\Phi + R_{PSH} \sin\Phi, \\ R_{PS_2} &= -R_{PSV} \sin\Phi + R_{PSH} \cos\Phi; \end{aligned} \tag{3.14}$$

see equations (2.10) for details. As discussed by Jech & Pšenčík (1989) and in Chapter 2 above, the *polarization angle* Φ is a nonlinear function of the anisotropy parameters of the incidence halfspace. In Section 2.2.2, (Chapter 2), I showed how the polarization angle Φ can be eliminated (using Alford-type rotation) and the components R_{PSV} and R_{PSH} (linear in the medium parameters) can be extracted from reflection data. Although the component R_{PSH} may provide useful qualitative information, it is probably too weak to be extracted from data with the accuracy required for the quantitative inversion. Therefore, only the R_{PSV} component is used in the following analysis.

For the orthorhombic model, the variation of the R_{PSV} component with incidence angle ϕ is given by:

$$\begin{aligned} R_{PSV} &= S_1 \sin\phi + S_2 \sin\phi\cos\phi + S_3 \sin^3\phi + S_4 \sin^3\phi\cos\phi \\ &\quad + S_5 \sin^5\phi + S_6 \sin^7\phi. \end{aligned} \tag{3.15}$$

This equation was obtained by substituting equation (2.29) into equation (2.26) for the component R_{PSV} (again using the notation ϕ instead of ϕ_P for simplicity). Notice that the S_i terms ($i = 1, \ldots, 6$) in equation (3.15) consist of linear combinations of the V_l terms ($l = 1, \ldots, 5$) in equation (2.26). In contrast to the R_{PP} coefficient [equation (3.1)], the R_{PSV} component has no AVO intercept (i.e, $S_0 = 0$ for this model), and it has two AVO gradients S_1 and S_2:

$$S_1 = S_1^{(ABS)} + S_1^{(M)} \sin\psi\cos\psi + S_1^{(L)} \sin^2\psi, \tag{3.16}$$

$$S_2 = S_2^{(ABS)} + S_2^{(M)} \sin\psi\cos\psi + S_2^{(L)} \sin^2\psi. \tag{3.17}$$

The gradients (3.16) and (3.17) are controlled by the same medium parameters as is the P-wave AVO gradient P_1 [see equations (3.3)-(3.6)], but in different linear combinations:

$$\begin{aligned} S_1^{(ABS)} &= \frac{-1}{2(1-\frac{\bar\beta^2}{\bar\alpha^2})}(\delta_2^{(2)} - \delta_2^{(1)}) \sin^2\kappa \\ &\quad + \frac{1}{2(1-\frac{\bar\beta^2}{\bar\alpha^2})}(\delta_2^{(2)} - \delta_1^{(2)}) - \frac{1}{2}\frac{\Delta\rho}{\bar\rho}, \end{aligned} \tag{3.18}$$

$$S_1^{(M)} = \frac{1}{2(1-\frac{\bar\beta^2}{\bar\alpha^2})}(\delta_2^{(2)} - \delta_2^{(1)}) \sin 2\kappa, \tag{3.19}$$

$$S_1^{(L)} = \frac{-1}{2(1-\frac{\bar\beta^2}{\bar\alpha^2})}(\delta_2^{(2)} - \delta_2^{(1)}) \cos 2\kappa + \frac{1}{2(1-\frac{\bar\beta^2}{\bar\alpha^2})}(\delta_1^{(2)} - \delta_1^{(1)}), \tag{3.20}$$

and

$$S_2^{(ABS)} = \left(\frac{\frac{\bar{\beta}}{\bar{\alpha}}}{2(1-\frac{\bar{\beta}^2}{\bar{\alpha}^2})}(\delta_2^{(2)} - \delta_2^{(1)}) - 2\frac{\bar{\beta}}{\bar{\alpha}}\gamma_2^{(S)} \right) \sin^2\kappa \qquad (3.21)$$
$$- \frac{\frac{\bar{\beta}}{\bar{\alpha}}}{2(1-\frac{\bar{\beta}^2}{\bar{\alpha}^2})}(\delta_2^{(2)} - \delta_1^{(2)}) - \frac{\bar{\beta}}{\bar{\alpha}}\frac{\Delta G}{\bar{G}},$$

$$S_2^{(M)} = \left(\frac{-\frac{\bar{\beta}}{\bar{\alpha}}}{2(1-\frac{\bar{\beta}^2}{\bar{\alpha}^2})}(\delta_2^{(2)} - \delta_2^{(1)}) + 2\frac{\bar{\beta}}{\bar{\alpha}}\gamma_2^{(S)} \right) \sin 2\kappa, \qquad (3.22)$$

$$S_2^{(L)} = \left(\frac{\frac{\bar{\beta}}{\bar{\alpha}}}{2(1-\frac{\bar{\beta}^2}{\bar{\alpha}^2})}(\delta_2^{(2)} - \delta_2^{(1)}) - 2\frac{\bar{\beta}}{\bar{\alpha}}\gamma_2^{(S)} \right) \cos 2\kappa \qquad (3.23)$$
$$\frac{-\frac{\bar{\beta}}{\bar{\alpha}}}{2(1-\frac{\bar{\beta}^2}{\bar{\alpha}^2})}(\delta_1^{(2)} - \delta_1^{(1)}) + 2\frac{\bar{\beta}}{\bar{\alpha}}\gamma_1^{(S)}.$$

The medium parameters in equations (3.18)-(3.23) are defined in equations (3.4)-(3.6). As pointed out in Chapter 2, the PSV-wave AVO gradients do not contain the P-wave velocity contrast $\frac{\Delta\alpha}{\bar{\alpha}}$. Notice the identical dependence on the azimuth ψ of the PSV-wave AVO gradients in equations (3.16)-(3.17) and that of the PP-wave AVO gradient from equation (3.3). Also, the dependence of the PSV-wave azimuthal components (3.18)-(3.23) on the angle κ is similar to that of the PP-wave azimuthal components from equations (3.4)-(3.6).

Finally, the R_{PSV} component (3.15) contains four large-incidence-angle terms S_3, S_4, S_5 and S_6. The dependence of each of these terms on azimuth ψ is the same as that in equation (3.8) for the PP-wave AVO large-incidence-angle term. Also, the dependence of S_3, S_4, S_5 or S_6 on the anisotropy parameters $\epsilon_1^{(1)}$, $\epsilon_1^{(2)}$, $\epsilon_2^{(1)}$, $\epsilon_2^{(2)}$, $\delta_1^{(3)}$ and $\delta_2^{(3)}$ is identical, to within a common multiplier, to that described in equations (3.9)-(3.13) for the P_2 term. As discussed below, the large-incidence-angle terms S_3, S_4, S_5 and S_6 represent redundant information and in the idealized case of the noise-free data are unnecessary. For their explicit expressions see Appendix E.

3.1.2 Inversion of small-incidence-angle terms for noise-free data

The small-incidence-angle terms P_0, P_1, S_1, and S_2 discussed above are of primary interest in the quantitative inversion. The large-incidence-angle terms are generally less accurate and may be severely contaminated by noise. Also, a trade-off between the small-incidence-angle and large-incidence-angle terms for any finite range of angles reduces the accuracy of the latter.

In the following, I assume that both the PP- and PS-wave reflections from the horizon under investigation are available for a sufficiently wide range of incidence angles and azimuths (in theory, three different incidence angles and three different azimuths are enough). Also, the reflection coefficients R_{PP} and R_{PSV} are assumed to be extracted from noise-free reflection data. Additionally, I assume that the azimuth of one of the vertical symmetry planes of the incidence orthorhombic halfspace has been identified, so the reference Cartesian coordinate system $[x, y, z]$ introduced above can be properly oriented. This assumption is quite reasonable since azimuthal move-out velocity analysis carried out for the orthorhombic overburden can be used to find the symmetry-plane orientation (Grechka & Tsvankin, 1999). Under these assumptions, the individual parameter combinations P_0, $P_1^{(ABS)}$, $P_1^{(M)}$, and $P_1^{(L)}$ [equations (3.2), (3.4)-(3.6)] together with $S_1^{(ABS)}$, $S_1^{(M)}$, $S_1^{(L)}$, $S_2^{(ABS)}$, $S_2^{(M)}$, and $S_2^{(L)}$ [equations (3.18)-(3.23)] can be extracted using corresponding equations (3.1) and (3.3), together with (3.15)-(3.17).

Let us assume in the following that $\kappa \neq 0$. Then the ten combinations P_0, $P_1^{(ABS)}$, $P_1^{(M)}$, $P_1^{(L)}$, and $S_1^{(ABS)}$, $S_1^{(M)}$, $S_1^{(L)}$, $S_2^{(ABS)}$, $S_2^{(M)}$, and $S_2^{(L)}$ give us ten independent constraints on the medium parameters. Let us initially assume that the $\frac{\bar{\beta}}{\bar{\alpha}}$ ratio is known. Using three combinations (3.5), (3.19) and (3.22), we can recover two medium parameters $(\delta_2^{(2)} - \delta_2^{(1)})$ and $\gamma_2^{(S)}$ along with the angle κ specifying the azimuth of one of the symmetry planes of the reflecting halfspace; however, since there are two perpendicular vertical symmetry planes, there is ambiguity in estimating κ. Both κ and $\kappa \pm 90°$ allow us to satisfy equations (3.5), (3.19) and (3.22), resulting in estimates of $(\delta_2^{(2)} - \delta_2^{(1)})$ and $\gamma_2^{(S)}$ with opposite signs. The transformation $[\kappa \longrightarrow \kappa \pm 90°$, $(\delta_2^{(2)} - \delta_2^{(1)}) \longrightarrow -(\delta_2^{(2)} - \delta_2^{(1)})$ and $\gamma_2^{(S)} \longrightarrow -\gamma_2^{(S)}]$ is, in the weak-anisotropy approximation, equivalent to the rotation of the reflecting orthorhombic halfspace by 90° around the z-axis of the reference coordinate system. In other words, the choice of κ or $\kappa \pm 90°$ for orthorhombic media is arbitrary; a particular choice simply defines the azimuths of the symmetry plane $[x_1, x_3]_2$ of the local Cartesian coordinate system of the reflecting halfspace. As discussed below, however, the choice of κ or $\kappa \pm 90°$ is no longer arbitrary for a reflecting halfspace with HTI symmetry.

The recovered combinations $(\delta_2^{(2)} - \delta_2^{(1)})$, $\gamma_2^{(S)}$, and the angle κ can be then substituted into equations (3.6), (3.20), and (3.23) which allow us to estimate two other medium parameters $(\delta_1^{(2)} - \delta_1^{(1)})$ and $\gamma_1^{(S)}$, and also add a constraint on the velocity ratio $\frac{\bar{\beta}}{\bar{\alpha}}$. Using the new constraint, the original $\frac{\bar{\beta}}{\bar{\alpha}}$ ratio can be updated, and the inversion can be repeated until the estimated parameters $\frac{\bar{\beta}}{\bar{\alpha}}$, κ, $(\delta_2^{(2)} - \delta_2^{(1)})$, $\gamma_2^{(S)}$, $(\delta_1^{(2)} - \delta_1^{(1)})$ and $\gamma_1^{(S)}$ satisfy equations (3.5), (3.6), (3.19), (3.20), (3.22) and (3.23).

The results can finally be substituted into the last three equations (3.4), (3.18) and (3.21). Together with the remaining equation (3.2) and relation (3.7), it is possible to recover one more anisotropy contrast $(\delta_2^{(2)} - \delta_1^{(2)})$ and three isotropic contrasts

$\frac{\Delta\alpha}{\bar{\alpha}}$, $\frac{\Delta\beta}{\bar{\beta}}$ and $\frac{\Delta\rho}{\bar{\rho}}$.

The inversion above can be summarized as follows: if noise-free amplitudes of both PP- and PS- reflected waves for a sufficient range of azimuths and incidence angles are available, it is in theory possible to invert the small-incidence-angle terms for the following combinations of the medium parameters:

$$\frac{\bar{\beta}}{\bar{\alpha}},\ \kappa, \tag{3.24}$$

$$\frac{\Delta\alpha}{\bar{\alpha}},\ \frac{\Delta\beta}{\bar{\beta}},\ \frac{\Delta\rho}{\bar{\rho}}, \tag{3.25}$$

$$(\delta_1^{(2)} - \delta_1^{(1)}),\ (\delta_2^{(2)} - \delta_2^{(1)}),\ (\delta_2^{(2)} - \delta_1^{(2)}), \tag{3.26}$$

$$\gamma_1^{(S)},\ \gamma_2^{(S)}. \tag{3.27}$$

To recover the combinations of the anisotropy parameters (3.26) and (3.27), the conditions $\kappa \neq 0°$ and $\kappa \neq 90°$ are necessary. If $\kappa \to 0°$ (or $\kappa \to 90°$), a similar analysis to that above shows that it is impossible to separate the anisotropy parameters of the incidence and reflecting halfspaces, and the only combinations of the anisotropy parameters constrained by the data are

$$(\delta_1^{(2)} - \delta_1^{(1)}) - (\delta_2^{(2)} - \delta_2^{(1)}),\ (\delta_2^{(2)} - \delta_1^{(2)}), \tag{3.28}$$

$$(\gamma_1^{(S)} - \gamma_2^{(S)}). \tag{3.29}$$

A direct indication that either $\kappa = 0°$ or $\kappa = 90°$ is that all three terms $P_1^{(M)}$, $S_1^{(M)}$ and $S_2^{(M)}$ vanish [see equations (3.5), (3.19) and (3.22)].

The parameters (3.24)-(3.29) represent the maximum information that can be obtained from the joint inversion of the PP- and PS-wave reflected amplitudes recorded at small and moderate offsets.

3.1.3 Inversion of large-incidence-angle terms for noise-free data

If the reflected PP- and PS-wave amplitudes at large incidence angles ($\phi > 35°$) are available, the recovered parameters (3.24)-(3.29) can be further used in the inversion of the large-incidence-angle terms P_2 [equation (3.8)], and S_3, S_4, S_5 and S_6 [equations (3.15) and (E.1)-(E.3)] for the parameters $\epsilon_1^{(1)}$, $\epsilon_2^{(1)}$, $\epsilon_1^{(2)}$, $\epsilon_2^{(2)}$, $\delta_1^{(3)}$ and $\delta_2^{(3)}$. The approximations R_{PP}, R_{PS_1} and R_{PS_2}, however, rarely have a sufficient accuracy at incidence angles exceeding 35°. Therefore, the linear inversion of P_2, S_3, S_4, S_5 and S_6 is questionable. It is unlikely to provide us with good estimates of the parameters $\epsilon_1^{(1)}$, $\epsilon_2^{(1)}$, $\epsilon_1^{(2)}$, $\epsilon_2^{(2)}$, $\delta_1^{(3)}$ and $\delta_2^{(3)}$, but can perhaps be used to recover *trends* of these parameters, i.e., their relative spatial changes.

From equations (3.8)-(3.13), (3.15) and (E.1)-(E.3), the azimuthal variation of

the reflection coefficients at large incidence angles is more complex and is controlled by five terms rather than three. The equations also show that both PP and PS reflections are controlled by the same linear combinations of the parameters $\epsilon_1^{(1)}$, $\epsilon_2^{(1)}$, $\epsilon_1^{(2)}$, $\epsilon_2^{(2)}$, $\delta_1^{(3)}$ and $\delta_2^{(3)}$. Therefore, for noise-free data, just one of the reflection coefficients is theoretically sufficient to recover those combinations. Redundancy in using both PP and PS reflected amplitudes, however, can be used to better constrain inversion of noise-contaminated data.

If the R_{PP} reflection coefficient has been measured for five different azimuths at large incidence angles, the terms $P_2^{(ABS)}$, $P_2^{(M1)}$, $P_2^{(M2)}$, $P_2^{(M3)}$ and $P_2^{(L)}$ [see equations (3.9)-(3.13)] can be recovered. Using the $\frac{\bar{\beta}}{\bar{\alpha}}$, κ and $\frac{\Delta\alpha}{\bar{\alpha}}$ estimates from the inversion of the small-incidence-angle terms, the joint inversion of the large-incidence-angle terms yields the following additional combinations of the medium parameters:

$$(\epsilon_1^{(2)} - \epsilon_1^{(1)}),\ (\epsilon_2^{(2)} - \epsilon_2^{(1)}),\ (\epsilon_2^{(2)} - \epsilon_1^{(2)}), \tag{3.30}$$

$$\delta_1^{(3)} \text{ and } \delta_2^{(3)}, \tag{3.31}$$

provided $\kappa \neq 0°$ and $\kappa \neq 90°$. If $\kappa \to 0°$ or $\kappa \to 90°$, the only combinations that can be constrained by the data are

$$(\epsilon_1^{(2)} - \epsilon_1^{(1)}) - (\epsilon_2^{(2)} - \epsilon_2^{(1)}),\ (\epsilon_2^{(2)} - \epsilon_1^{(2)}), \tag{3.32}$$

$$(\delta_1^{(3)} - \delta_2^{(3)}). \tag{3.33}$$

3.1.4 Inversion for isotropic, VTI and HTI media

The inversion results (3.24)-(3.33) for an orthorhombic medium can be applied without any difficulties to higher anisotropic symmetries, such as HTI, VTI or isotropic. The recovered model parameters (3.24) and (3.25) remain formally unchanged for all anisotropic models. The anisotropic combinations (3.26)-(3.33) can be converted into the corresponding expressions for VTI and HTI media using Table 3.1. For example, if the incidence halfspace is VTI and the reflecting halfspace is HTI, all combinations of the anisotropy parameters with the subscripts 1 and 2 in equations (3.26)-(3.33) have to be replaced with the corresponding VTI and HTI combinations listed in the third and second column of Table 3.1, respectively. The same method was used in Chapter 2 to convert the approximate coefficients R_{PS_1} and R_{PS_2} derived for orthorhombic media to the approximations valid for VTI and HTI symmetry (see Table 2.1). Below, I briefly discuss some special cases.

Isotropic medium. In a purely isotropic medium, all anisotropy parameters in (3.26)-(3.33) vanish, and $\kappa = 0$. Then, the $\frac{\bar{\beta}}{\bar{\alpha}}$ ratio and the isotropic contrasts (3.25) can be recovered. Notice that using both PP- and PSV-wave reflections, it is possible to invert, theoretically, for all three isotropic contrasts without additional information.

orthorhombic	HTI	VTI
$\delta^{(2)} - \delta^{(1)}$	$\delta^{(V)}$	0
$\delta^{(2)}$	$\delta^{(V)}$	δ
$\gamma^{(S)}$	γ	0
$\epsilon^{(2)} - \epsilon^{(1)}$	$\epsilon^{(V)}$	0
$\epsilon^{(2)}$	$\epsilon^{(V)}$	ϵ
$\delta^{(3)}$	$\delta^{(V)} - 2\epsilon^{(V)}$	0

Table 3.1. Conversion table for the anisotropy parameters in the weak-anisotropy approximation. The VTI and HTI parameters are defined by equations (2.27) and (2.28). The symmetry axis of the HTI medium points in the x_1-direction of the local coordinate system in each halfspace.

The PP-wave reflection coefficient alone is insufficient for this purpose, as frequently discussed in the literature (for instance, see Smith & Gidlow, 1987; Cambois, 2000).

VTI medium. If both halfspaces are VTI, the reflection coefficients are azimuthally invariant (as correctly predicted by the approximate R_{PP} and R_{PS}), i.e., the azimuthal terms (3.5), (3.6), (3.10)-(3.13), together with (3.19), (3.20), (3.22), (3.23) and the azimuthally dependent components of the large-incidence-angle terms (E.1), (E.3) vanish. Also, the angle $\kappa = 0$. If the $\frac{\bar{\beta}}{\bar{\alpha}}$ ratio is known (it can be estimated from the vertical P- and S-wave traveltimes), the three isotropic contrasts (3.25) can be theoretically recovered, along with constraints in the anisotropy parameters $(\delta_2 - \delta_1)$ and $(\epsilon_2 - \epsilon_1)$. The individual values of δ_2, δ_1, ϵ_2 and ϵ_1, however, cannot be resolved without additional information. The inversion is also possible without the knowledge of $\frac{\bar{\beta}}{\bar{\alpha}}$ by *simultaneous* inversion of small- and large-incidence-angle terms [i.e., small-incidence-angle terms alone are not sufficient to invert for $\frac{\bar{\beta}}{\bar{\alpha}}$, $\frac{\Delta\alpha}{\bar{\alpha}}$, $\frac{\Delta\beta}{\bar{\beta}}$, $\frac{\Delta\rho}{\bar{\rho}}$ and $(\delta_2 - \delta_1)$].

HTI reflecting halfspace. If one of the halfspaces possesses HTI symmetry, the reflection coefficients generally exhibit azimuthal variation. If the reflecting halfspace is HTI, the azimuth of the symmetry axis in this halfspace in general is not zero (i.e., the misalignment angle $\kappa \neq 0$). Using the conversion key from Table 3.1 and equations (3.24)-(3.27), (3.30) and (3.31), the following medium parameters can then

be theoretically estimated for HTI media:

$$
\begin{array}{rcl}
 & \frac{\bar{\beta}}{\bar{\alpha}},\ \kappa, & \\
\frac{\Delta\alpha}{\bar{\alpha}},\ \frac{\Delta\beta}{\bar{\beta}},\ \frac{\Delta\rho}{\bar{\rho}}, & & \\
(\delta_1^{(2)} - \delta_1^{(1)}) & = & \delta_1^{(V)}, \\
(\delta_2^{(2)} - \delta_2^{(1)}) & = & \delta_2^{(V)}, \\
(\delta_2^{(2)} - \delta_1^{(2)}) & = & (\delta_2^{(V)} - \delta_1^{(V)}), \\
\gamma_1^{(S)} & = & \gamma_1, \\
\gamma_2^{(S)} & = & \gamma_2, \\
(\epsilon_1^{(2)} - \epsilon_1^{(1)}) & = & \epsilon_1^{(V)}, \\
(\epsilon_2^{(2)} - \epsilon_2^{(1)}) & = & \epsilon_2^{(V)}, \\
(\epsilon_2^{(2)} - \epsilon_1^{(2)}) & = & (\epsilon_2^{(V)} - \epsilon_1^{(V)}), \\
\delta_1^{(3)} & = & (\delta_1^{(V)} - 2\epsilon_1^{(V)}), \\
\delta_2^{(3)} & = & (\delta_2^{(V)} - 2\epsilon_2^{(V)}).
\end{array}
\tag{3.34}
$$

Notice certain redundancy in equations (3.34). For instance, besides the parameters $\delta_1^{(V)}$ and $\delta_2^{(V)}$, their difference $(\delta_2^{(V)} - \delta_1^{(V)})$ can be recovered independently as well. This redundancy can help to constrain the estimates of $\delta_1^{(V)}$ and $\delta_2^{(V)}$ in field-data applications.

An important difference in the inversion for HTI media from that for orthorhombic media results from different specifications of the angle κ for these symmetries. For the orthorhombic reflecting medium, κ determines the azimuth of one of the two vertical symmetry planes, and the choice of a particular symmetry plane is arbitrary. In HTI, however, κ determines the azimuth of the *symmetry-axis plane*, which is principally different from the other (*isotropy*) plane. From detailed analysis of the equations for R_{PP} and R_{PSV}, the angle κ, and, consequently, the system of parameters (3.34), can be recovered uniquely, with two exceptions. First, if $\kappa = 0$ (i.e., the symmetry-axis planes of the HTI halfspaces above and below the interface are aligned), the data can be explained equally well with either choice of $\kappa = 0°$ or $\kappa = 90°$, the latter resulting in the erroneous recovered values of $\delta_2^{(V)} = 0$ and $\epsilon_2^{(V)} = 0$. Second, if in fact $\delta_2^{(V)} = \epsilon_2^{(V)} = 0$, two different models with κ and $\kappa = \kappa \pm 90°$ can be found with identical AVO response. Clearly, if $\delta_2^{(V)} = \epsilon_2^{(V)} = 0$, the direction of the symmetry axis plane of the reflecting medium is not distinguishable from the direction of the isotropy plane using approximate reflection coefficients R_{PP} and R_{PSV} (although the orientation of the symmetry planes in general can still be identified as long as $\gamma_2 \neq 0$).

Besides resulting in incorrect values of $\delta_2^{(V)}$ and $\epsilon_2^{(V)}$, the wrong choice of κ also results in the recovery of incorrect values of all remaining anisotropy parameters and the isotropic contrast $\Delta\beta/\bar{\beta}$. Therefore, knowledge of at least one of those parameters would eliminate the nonuniqueness, and the azimuths of the isotropy and symmetry axis planes could be correctly obtained, even for the same symmetry-axis orientation in both halfspaces (when $\kappa = 0°$). Note that if the incidence halfspace is isotropic, then $\delta_1^{(2)} = 0$, and the inversion becomes unique.

3.2 Linear inversion of noise-contaminated data

Introducing errors in the input amplitudes compromises both the stability and resolution of the inversion. In the following discussion, I focus on inversion of the small-incidence-angle terms only. Although linear inversion of the large-incidence-angle terms is possible in principle, it may not provide reliable results because of limited accuracy of the approximations R_{PP} and R_{PSV}. Moreover, extraction of the large-incidence-angle terms from data is unstable unless incidence angles exceed 40°.

Theory for linear inversion of noise-contaminated data can be found, for example, in Tarantola (1987). Appendix F provides some basic definitions used below.

3.2.1 Inversion scheme

The goal of the inversion here is to obtain a set of values for the medium parameters as close as possible to the actual set (3.24)-(3.29). The inversion takes place in two steps. First, the best least-square fit of the data representing the PP- and PS-wave reflection coefficients results in the recovery of some of the small- and large-incidence-angle terms described below. Second, the extracted small-incidence-angle terms are combined, if possible, to obtain combinations of the medium parameters, such as those in (3.24)-(3.29). Although the large-incidence-angle terms are not used in the second (parameter-estimation) step, their influence is accounted for in the first step, which improves estimates of the small-incidence-angle terms.

For the reflection coefficient R_{PP}, the system of equations used to fit the noisy data (i.e., $\mathbf{d_0^P} + \mathbf{e^P} = [d_1^P, d_2^P, ..., d_N^P]^T$, where T denotes the transpose, $\mathbf{d_0^P}$ is the data vector free of errors and $\mathbf{e^P}$ is the vector of corresponding errors contaminating $\mathbf{d_0^P}$; see Appendix F) can be written in the form of equation (F.1), with

$$\mathbf{A^P} \times \begin{bmatrix} P_0 \\ P_1^{(ABS)} \\ P_1^{(M)} \\ P_1^{(L)} \\ P_2^{(ABS)} \\ P_2^{(M1)} \\ P_2^{(M2)} \\ P_2^{(M3)} \\ P_2^{(L)} \end{bmatrix} = \begin{bmatrix} d_1^P \\ d_2^P \\ \vdots \\ d_N^P \end{bmatrix}. \tag{3.35}$$

The forward operator $\mathbf{A^P}$ is an Nx9 matrix, where N is the number of data points d_i^P measured at locations specified by (ϕ_i, ψ_i) pairs (ϕ_i is the incidence angle, ψ_i is the azimuth, i = 1, ..., N). The explicit form of $\mathbf{A}^P$ can be found in Appendix G. The components of the model vector $\mathbf{m^P} = [P_0, P_1^{(ABS)}, P_1^{(M)}, P_1^{(L)}, P_2^{(ABS)}, P_2^{(M1)}, P_2^{(M2)}, P_2^{(M3)}, P_2^{(L)}]^T$ are defined by equations (3.2), (3.4)-(3.6) and (3.9)-(3.13). In order to resolve all nine model parameters, at least three different incidence angles ϕ and five different azimuths ψ must be provided. The stability of the inversion for a particular azimuthal and incidence-angle coverage can be analyzed by evaluating the corresponding covariance matrix (see Appendix F for the definition). Such an analysis reveals, for example, that to obtain large-incidence-angle terms $P_2^{(ABS)}$, $P_2^{(M1)}$, $P_2^{(M2)}$, $P_3^{(M2)}$ and $P_2^{(L)}$ with reasonable accuracy, it is necessary to use incidence angles larger than 40°. However, unless the maximum incidence angle is smaller than 25°, the large-incidence-angle terms should be included in the system (3.35) to improve the estimates of the small-incidence-angle terms $P_1^{(ABS)}$, $P_1^{(M)}$ and $P_1^{(L)}$. The linear system in equation (3.35) can be inverted for the model vector $\mathbf{m^P}$ using well-known techniques, such as the singular-value-decomposition (SVD) (see Appendix F).

A system similar to that in equation (3.35) can be defined for the coefficient R_{PSV} using the corresponding equations (3.15)-(3.23) and (E.1)-(E.3). Analysis of the resulting covariance matrix reveals, however, that the system based on equation (3.15) is highly unstable due to the difficulty in separating the terms $\sin\phi$ and $\sin\phi\cos\phi$, as well as $\sin^3\phi$ and $\sin^3\phi\cos\phi$. The standard deviations of the small-incidence-angle terms resulting from such an inversion vary approximately within the unacceptable range $10^3 - 10^4$ (i.e., they are approximately $10^2 - 10^5$ higher than the corresponding terms), even for a full and dense azimuthal coverage and incidence angles up to 60°. A more stable form of R_{PSV} than that in equation (3.15) is necessary. For example, the approximate relation $\cos\phi \approx 1 - \frac{1}{2}\sin^2\phi$ can be used to rewrite equation (3.15)

as

$$R_{PSV} = SS_1 \sin\phi + SS_2 \sin^3\phi + SS_3 \sin^5\phi + SS_4 \sin^7\phi. \tag{3.36}$$

This approximate relation for $\cos\phi$ holds well up to incidence angle $\phi = 45°$ (with a difference of about 6%). Such an error is quite reasonable. Moreover, the approximations R_{PP} and R_{PSV} should be used for much smaller incidence angles than 45°. Equation (3.36) contains only one PSV-wave AVO gradient

$$SS_1 = SS_1^{(ABS)} + SS_1^{(M)} \sin\psi\cos\psi + SS_1^{(L)} \sin^2\psi, \tag{3.37}$$

where

$$\begin{aligned} SS_1^{(ABS)} &= \left[-\frac{1}{2(1+\frac{\bar\beta}{\bar\alpha})}(\delta_2^{(2)} - \delta_2^{(1)}) - 2\frac{\bar\beta}{\bar\alpha}\gamma_2^{(S)}\right]\sin^2\kappa \qquad (3.38)\\ &+ \frac{1}{2(1+\frac{\bar\beta}{\bar\alpha})}(\delta_2^{(2)} - \delta_1^{(2)}) - \frac{1}{2}\frac{\Delta\rho}{\bar\rho} - \frac{\bar\beta}{\bar\alpha}\frac{\Delta G}{\bar G},\\ SS_1^{(M)} &= \left[\frac{1}{2(1+\frac{\bar\beta}{\bar\alpha})}(\delta_2^{(2)} - \delta_2^{(1)}) + 2\frac{\bar\beta}{\bar\alpha}\gamma_2^{(S)}\right]\sin 2\kappa, \qquad (3.39)\\ SS_1^{(L)} &= \left[-\frac{1}{2(1+\frac{\bar\beta}{\bar\alpha})}(\delta_2^{(2)} - \delta_2^{(1)}) - 2\frac{\bar\beta}{\bar\alpha}\gamma_2^{(S)}\right]\cos 2\kappa \qquad (3.40)\\ &+\frac{1}{2(1+\frac{\bar\beta}{\bar\alpha})}(\delta_1^{(2)} - \delta_1^{(1)}) + 2\frac{\bar\beta}{\bar\alpha}\gamma_1^{(S)}. \end{aligned}$$

The large-incidence-angle terms in equation (3.36) can be formally written as

$$\begin{aligned} SS_i &= SS_i^{(ABS)} + SS_i^{(M1)} \sin 2\psi\cos 2\psi + SS_i^{(M2)} \sin\psi\cos\psi\\ &+SS_i^{(M3)} \sin^2\psi\cos^2\psi + SS_i^{(L)} \sin^2\psi, \end{aligned} \tag{3.41}$$

where $i = 2$, 3 and 4. The large-incidence-angle terms have the same structure as in the original equations (E.1), but with different multipliers (E.2). Nevertheless, their explicit forms are not needed for the inversion described below. Then, the system (F.1) takes the form

$$\mathbf{A^S} \times \begin{bmatrix} SS_1^{(ABS)} \\ SS_1^{(M)} \\ SS_1^{(L)} \\ SS_2^{(ABS)} \\ SS_2^{(M1)} \\ \vdots \\ SS_4^{(M2)} \\ SS_4^{(M3)} \\ SS_4^{(L)} \end{bmatrix} = \begin{bmatrix} d_1^S \\ d_2^S \\ \vdots \\ d_N^S \end{bmatrix}. \tag{3.42}$$

The forward operator $\mathbf{A^S}$ is an Nx18 matrix, where N is the number of data points d_i^S; the explicit form of $\mathbf{A^S}$ can be found in Appendix G. Analysis of the covariance matrix corresponding to system (3.42) shows that a sufficient coverage over incidence angles (up to 35°) and azimuths can provide us with acceptable estimates of the small-incidence-angle terms $SS_1^{(ABS)}$, $SS_1^{(M1)}$ and $SS_1^{(L)}$.

Since only one PSV-wave AVO gradient SS_1 [equation (3.37)] can be recovered from noisy data, the number of independent small-incidence-angle terms reduces from ten [equations (3.2), (3.4)-(3.6) and (3.18)-(3.23)] to seven [equations (3.2), (3.4)-(3.6) and (3.38)-(3.40)]. The loss of the three constraints implies that the medium parameters (3.24)-(3.29) cannot be resolved without additional information.

3.2.2 Synthetic examples

Here, the linear inversion is carried out for four different models: isotropic/VTI (the incidence and reflecting halfspaces are isotropic and VTI, respectively), HTI/HTI [both halfspaces are HTI, with aligned (parallel) symmetry axes above and below the interface], HTIxHTI (the same as HTI/HTI but the symmetry axes are misaligned by $\kappa = 30°$) and ORTHO/ORTHO (both halfspaces are orthorhombic with aligned vertical symmetry planes). For each model, I assume that both reflected PP- and PSV-wave amplitudes are successfully recovered. Full azimuthal coverage ψ from 0° to 360° is available with the azimuthal increment $\Delta\psi = 15°$. The PP- and PS-wave data are collected along each azimuthal line for incidence angles $\phi \leq 35°$ with the increment $\Delta\phi = 1°$. The data are generated using the exact reflection coefficients, which are contaminated by a uniformly distributed random error of 10%.

Example 1: isotropic/VTI model. The inversion algorithm is first applied on data from the model of an isotropic/VTI interface (see the caption of Figure 3.1 for the medium parameters). The upper plots in Figure 3.1 show the differences between

the exact and approximate reflection coefficients computed as functions of the incidence angle ϕ and azimuth ψ for this model. Noticeable differences can be observed for incidence angles $\phi > 20°$ for both PP and PSV reflections and are relatively large for angles exceeding 25°. Since the inversion is based on the approximate reflection coefficients R_{PP} and R_{PSV}, the inversion results, even if they are stable, may differ from the true values. In the following, I refer to such a solution as *biased.*

The lower plots in Figure 3.1 show the best-fit reflection coefficients obtained by solving the systems (3.35) and (3.42). In solving these equations, I assume that symmetry of the incidence and reflecting halfspaces is no lower than VTI. In this case, the terms $P_1^{(M)} = P_1^{(L)} = P_2^{(M1)} = P_2^{(M2)} = P_2^{(M3)} = P_2^{(L)} = 0$ in equation (3.35), and $SS_1^{(M)} = SS_1^{(L)} = SS_2^{(M1)} = SS_2^{(M2)} = SS_2^{(M3)} = SS_2^{(L)} = SS_3^{(M1)} = SS_3^{(M2)} = SS_3^{(M3)} = SS_3^{(L)} = SS_4^{(M1)} = SS_4^{(M2)} = SS_3^{(M3)} = SS_4^{(L)} = 0$ in equation (3.42); also, the reflection coefficients are azimuthally invariant [see also equations (3.2), (3.4)-(3.6), (3.9)-(3.13), (3.38)-(3.41), (E.1), (E.3) and Table 3.1]. This assumption helps to stabilize the inversion procedure. From the best-fit reflection coefficients, it is possible to recover the following combinations of the medium parameters (Table 3.2):

$$\begin{aligned} P_0 &= \frac{1}{2}\frac{\Delta\alpha}{\bar{\alpha}} + \frac{1}{2}\frac{\Delta\rho}{\bar{\rho}}, \\ P_1^{(ABS)} &= \frac{1}{2}\frac{\Delta\alpha}{\bar{\alpha}} - 2\left(\frac{\bar{\beta}}{\bar{\alpha}}\right)^2 \frac{\Delta G}{\bar{G}} + \frac{1}{2}\delta_2, \\ SS_1^{(ABS)} &= -\frac{1}{2}\frac{\Delta\rho}{\bar{\rho}} - \frac{\bar{\beta}}{\bar{\alpha}}\frac{\Delta G}{\bar{G}} + \frac{1}{2(1+\frac{\bar{\beta}}{\bar{\alpha}})}\delta_2. \end{aligned} \tag{3.43}$$

The errors in Table 3.2 are the standard deviations obtained from the corresponding diagonal elements of the covariance matrix determined as in Appendix F [see equation (F.3) for the covariance matrix $\mathbf{C}$; it is assumed that data are uncorrelated and their standard deviations, i.e., the elements of the data error matrix $\mathbf{C}_d$ in (F.3), are obtained from the misfit between the measured data and the best-fit reflection coefficient; see the lower plots in Figure 3.1]. As expected, the best constrained parameter is P_0; the parameter $SS_1^{(ABS)}$ is also recovered very well. A less stable result is obtained for the parameter $P_1^{(ABS)}$, which is generally much smaller than the other two. Although the error in $P_1^{(ABS)}$ is probably acceptable, the result is slightly biased due to the differences between the exact and approximate reflection coefficients discussed above.

Clearly, the three constraints (3.43) are not sufficient to resolve the five model parameters ($\Delta\rho/\bar{\rho}$, $\Delta\alpha/\bar{\alpha}$, $\Delta G/\bar{G}$, $\bar{\beta}/\bar{\alpha}$ and δ_2); without additional information, Table 3.2 represents the final result of the inversion. In the following, I assume that the

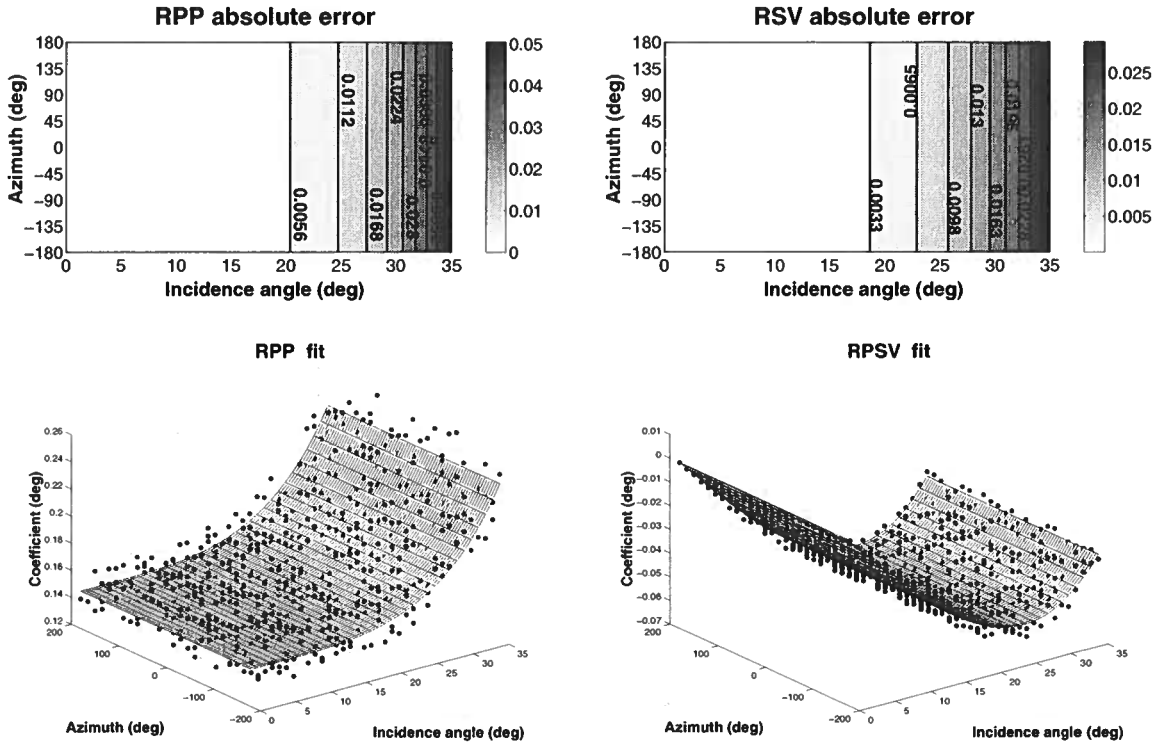

Figure 3.1. Linear inversion of the reflection coefficients R_{PP} (left) and R_{PSV} (right) for the isotropic/VTI model (Example 1). The upper plots show the differences between the exact and approximate reflection coefficients, and the surfaces in the lower plots are the best-fit reflection coefficients; error-contaminated data are marked by the dots. The medium parameters are: isotropic incidence halfspace - $\rho = 2.50\ \mathrm{g/cm^3}$, $V_{P0} = 3.00$ km/s, $V_{S0} = 1.20$ km/s; VTI reflecting halfspace - $\rho = 2.80\ \mathrm{g/cm^3}$, $V_{P0} = 3.60$ km/s, $V_{S0} = 1.44$ km/s, $\epsilon = 0.20$, $\delta = 0.15$ and $\gamma = 0.10$; V_{P0} and V_{S0} represent the vertical P- and S-wave velocities, respectively.

	P_0	$P_1^{(ABS)}$	$SS_1^{(ABS)}$
exact	0.147	0.016	-0.191
recovered	0.148 ± 0.001	0.002 ± 0.010	-0.191 ± 0.002

Table 3.2. Inverted parameters [equations (3.43)] of the R_{PP} and R_{PSV} reflection coefficients for the isotropic/VTI model (Example 1) obtained by fitting the error-contaminated data (10% uniformly distributed random error) in Figure 3.1.

	$\frac{\Delta\alpha}{\bar{\alpha}}$	$\frac{\Delta\beta}{\bar{\beta}}$	$\frac{\Delta\rho}{\bar{\rho}}$	$\frac{\Delta G}{\bar{G}}$	δ_2
exact	0.182	0.182	0.113	0.469	0.150
$\frac{\Delta\alpha}{\bar{\alpha}} = 0.182$	0.182 ± 0.000	0.151 ± 0.023	0.115 ± 0.001	0.411 ± 0.042	0.085 ± 0.046
$\frac{\Delta\beta}{\bar{\beta}} = 0.182$	0.217 ± 0.024	0.182 ± 0.000	0.080 ± 0.023	0.437 ± 0.022	0.073 ± 0.057

Table 3.3. Inverted parameters for the isotropic/VTI model (Example 1), assuming known $\frac{\bar{\beta}}{\bar{\alpha}} = 0.40$ and $\frac{\Delta\alpha}{\bar{\alpha}}$ (third row) or $\frac{\Delta\beta}{\bar{\beta}}$ (fourth row).

average ratio $\frac{\bar{\beta}}{\bar{\alpha}}$ is known, along with one of the isotropic contrasts. The $\frac{\bar{\beta}}{\bar{\alpha}}$ ratio can be estimated from the vertical P- and S-wave traveltimes. Estimating one of the isotropic contrasts is more complicated, but it can be done by using well-log or VSP data. The first three rows of Table 3.3 show what can be recovered using this *a priori* information combined with the results from Table 3.2. The estimate of the isotropic contrast $\frac{\Delta\beta}{\bar{\beta}}$ in Table 3.3 is obtained from estimates $\frac{\Delta G}{\bar{G}}$ and $\frac{\Delta\rho}{\bar{\rho}}$ [from equations (3.43)] using the nonlinear relationships between $\frac{\Delta G}{\bar{G}}$, $\frac{\Delta\rho}{\bar{\rho}}$ and $\frac{\Delta\beta}{\bar{\beta}}$ [see equation (3.7) for the linearized form]. Table 3.3 suggests that all isotropic contrasts can be recovered with a reasonable accuracy. The estimates of $\frac{\Delta\beta}{\bar{\beta}}$ and $\frac{\Delta G}{\bar{G}}$ are slightly distorted as a result of the biased estimate of $P_1^{(ABS)}$ from Table 3.2. The estimate of the anisotropic parameter δ_2, on the other hand, is the least stable and also the most biased. The δ_2 value can serve, however, as a good initial guess for more sophisticated nonlinear inversion. The δ_2 estimate from Table 3.3 also indicates that the reflecting halfspace is VTI and not isotropic. (It is impossible to draw this conclusion from the results in Table 3.2 alone: the results indicate only that the AVO response is azimuthally invariant.) Finally, the fourth row of Table 3.3 shows the inversion result assuming that the known isotropic contrast is $\frac{\Delta\beta}{\bar{\beta}}$ instead of $\frac{\Delta\alpha}{\bar{\alpha}}$. (The result for a known $\frac{\Delta\rho}{\bar{\rho}}$ is almost the same as that for a known $\frac{\Delta\alpha}{\bar{\alpha}}$.) Using $\frac{\Delta\beta}{\bar{\beta}}$ instead of $\frac{\Delta\alpha}{\bar{\alpha}}$ results in slightly less accurate estimates of $\frac{\Delta\rho}{\bar{\rho}}$ and δ_2, and a slightly better estimate of $\frac{\Delta G}{\bar{G}}$. This is a common feature observed for all tested models.

Further analysis of the inversion for the isotropic/VTI interface reveals that the estimates of $\frac{\Delta\alpha}{\bar{\alpha}}$, $\frac{\Delta\beta}{\bar{\beta}}$, $\frac{\Delta\rho}{\bar{\rho}}$, and $\frac{\Delta G}{\bar{G}}$ improve for models characterized by higher $\frac{\bar{\beta}}{\bar{\alpha}}$ ratios. The opposite is true for the estimate of the δ_2 parameter (this conclusion seems to be quite general even for models with HTI and orthorhombic symmetries). Finally, similar conclusions about the accuracy and stability were also obtained for the more complicated VTI/VTI problem. In that case, the anisotropy parameter δ_2 is replaced in the inversion by the difference $(\delta_2 - \delta_1)$.

	P_0	$P_1^{(ABS)}$	$P_1^{(L)}$	$SS_1^{(ABS)}$	$SS_1^{(L)}$
exact	0.231	−0.639	0.510	−0.754	0.407
recovered	0.230 ± 0.001	-0.727 ± 0.014	0.665 ± 0.020	-0.873 ± 0.007	0.627 ± 0.010

Table 3.8. Inversion for the parameters from equations (3.46) for the ORTHO/ORTHO model (Example 4) carried out by fitting the error-contaminated data (10% uniformly distributed random error) from Figure 3.3.

parameter γ_2 can be obtained. The accuracy of the difference $(\delta_2^{(V)} - \delta_1^{(V)})$, as well as that of the parameter $\delta_2^{(V)}$, is lower, although the estimates represent good initial guess which can be used, for example, in subsequent nonlinear inversion.

Example 4: ORTHO/ORTHO model. The last model (Figure 3.3) consists of two orthorhombic halfspaces whose vertical symmetry planes above and below the interface are aligned ($\kappa = 0°$). The small-incidence-angle terms are

$$\begin{aligned}
P_0 &= \frac{1}{2}\frac{\Delta\alpha}{\bar{\alpha}} + \frac{1}{2}\frac{\Delta\rho}{\bar{\rho}}, \\
P_1^{(ABS)} &= \frac{1}{2}\frac{\Delta\alpha}{\bar{\alpha}} - 2\left(\frac{\bar{\beta}}{\bar{\alpha}}\right)^2 \frac{\Delta G}{\bar{G}} + \frac{1}{2}(\delta_2^{(2)} - \delta_1^{(2)}), \\
P_1^{(L)} &= -\frac{1}{2}(\delta_2^{(2)} - \delta_1^{(2)}) + \frac{1}{2}(\delta_2^{(1)} - \delta_1^{(1)}) - 4\left(\frac{\bar{\beta}}{\bar{\alpha}}\right)^2 (\gamma_2^{(S)} - \gamma_1^{(S)}), \\
SS_1^{(ABS)} &= -\frac{1}{2}\frac{\Delta\rho}{\bar{\rho}} - \frac{\bar{\beta}}{\bar{\alpha}}\frac{\Delta G}{\bar{G}} + \frac{1}{2(1+\frac{\bar{\beta}}{\bar{\alpha}})}(\delta_2^{(2)} - \delta_1^{(2)}), \\
SS_1^{(L)} &= -\frac{1}{2(1+\frac{\bar{\beta}}{\bar{\alpha}})}(\delta_2^{(2)} - \delta_1^{(2)}) + \frac{1}{2(1+\frac{\bar{\beta}}{\bar{\alpha}})}(\delta_2^{(1)} - \delta_1^{(1)}) - 2\frac{\bar{\beta}}{\bar{\alpha}}(\gamma_2^{(S)} - \gamma_1^{(S)}).
\end{aligned} \tag{3.46}$$

As indicated in Figure 3.3, a strong bias in the inversion results can be expected due the large differences between the exact and approximate reflection coefficients. Indeed, except for P_0, the recovered small-incidence-angle terms (3.46) are significantly biased (Table 3.8). The estimates , however, are relatively stable.

Assuming, as before, that the ratio $\frac{\bar{\beta}}{\bar{\alpha}}$, the contrast $\frac{\Delta\alpha}{\bar{\alpha}}$, and the anisotropy parameters $\delta_1^{(1)}$, $\delta_1^{(2)}$ and $\gamma_1^{(S)}$ of the incidence halfspace are known, it is possible in principle to recover the remaining isotropic contrasts and the anisotropy parameters $\delta_2^{(1)}$, $\delta_2^{(2)}$ and $\gamma_2^{(S)}$. The third row of Table 3.9 suggests, however, that the estimates of the parameters $\delta_2^{(1)}$ and $\delta_2^{(2)}$ are unstable. The existence of the two δ-type parameters

R_{PP}	P_0	$P_1^{(ABS)}$	$P_1^{(M)}$	$P_1^{(L)}$
exact	0.147	−0.118	0.029	0.097
recovered	0.147 ± 0.001	-0.141 ± 0.010	0.030 ± 0.015	0.103 ± 0.014

R_{PSV}	$SS_1^{(ABS)}$	$SS_1^{(M)}$	$SS_1^{(L)}$
exact	−0.300	0.058	0.093
recovered	-0.332 ± 0.003	0.059 ± 0.005	0.099 ± 0.005

Table 3.6. Inverted parameters [equations (3.45)] of the reflection coefficients R_{PP} and R_{PSV} for the HTIxHTI model obtained by fitting the error-contaminated data (10% uniformly distributed random error).

	$\frac{\Delta\beta}{\bar{\beta}}$	$\frac{\Delta\rho}{\bar{\rho}}$	$\frac{\Delta G}{\bar{G}}$	κ
exact	0.182	0.113	0.469	30.0°
recovered	0.224 ± 0.043	0.113 ± 0.001	0.548 ± 0.080	$32.4° \pm 2.5°$

	γ_2	$\delta_2^{(V)} - \delta_1^{(V)}$	$\delta_2^{(V)}$
exact	0.125	−0.160	−0.060
recovered	0.121 ± 0.040	-0.161 ± 0.052	-0.061 ± 0.052

Table 3.7. Inverted isotropic contrasts, the azimuth κ of the symmetry axis of the HTI reflecting halfspace, and the anisotropy parameters γ_2, $(\delta_2^{(V)} - \delta_1^{(V)})$ and $\delta_2^{(V)}$ for the HTIxHTI model, obtained assuming known $\frac{\bar{\beta}}{\bar{\alpha}} = 0.358$, $\frac{\Delta\alpha}{\bar{\alpha}} = 0.182$, $\delta_1^{(V)} = 0.10$ and $\gamma_1 = 0.125$.

example, however, the symmetry axes of the halfspaces are misaligned by the angle $\kappa = 30°$ (the reflection coefficients for such a model differ only in details from those in Figure 3.2 and are not given here). For this model, none of the small-incidence-angle terms in equations (3.35) and (3.42) vanish:

$$\begin{aligned}
P_0 &= \frac{1}{2}\frac{\Delta\alpha}{\bar{\alpha}} + \frac{1}{2}\frac{\Delta\rho}{\bar{\rho}}, \\
P_1^{(ABS)} &= \frac{1}{2}\frac{\Delta\alpha}{\bar{\alpha}} - 2\left(\frac{\bar{\beta}}{\bar{\alpha}}\right)^2\frac{\Delta G}{\bar{G}} + \frac{1}{2}(\delta_2^{(V)} - \delta_1^{(V)}) - \frac{1}{2}\left[\delta_2^{(V)} + 8\left(\frac{\bar{\beta}}{\bar{\alpha}}\right)^2\gamma_2\right]\sin^2\kappa, \\
P_1^{(M)} &= \frac{1}{2}\left[\delta_2^{(V)} + 8\left(\frac{\bar{\beta}}{\bar{\alpha}}\right)^2\gamma_2\right]\sin 2\kappa, \\
P_1^{(L)} &= -\frac{1}{2}\left[\delta_2^{(V)} + 8\left(\frac{\bar{\beta}}{\bar{\alpha}}\right)^2\gamma_2\right]\cos 2\kappa + \frac{1}{2}\left[\delta_1^{(V)} + 8\left(\frac{\bar{\beta}}{\bar{\alpha}}\right)^2\gamma_1\right], \qquad (3.45) \\
SS_1^{(ABS)} &= -\frac{1}{2}\frac{\Delta\rho}{\bar{\rho}} - \frac{\bar{\beta}}{\bar{\alpha}}\frac{\Delta G}{\bar{G}} + \frac{1}{2(1+\frac{\bar{\beta}}{\bar{\alpha}})}(\delta_2^{(V)} - \delta_1^{(V)}) - \left[\frac{1}{2(1+\frac{\bar{\beta}}{\bar{\alpha}})}\delta_2^{(V)} + 2\frac{\bar{\beta}}{\bar{\alpha}}\gamma_2\right]\sin^2\kappa, \\
SS_1^{(M)} &= \left[\frac{1}{2(1+\frac{\bar{\beta}}{\bar{\alpha}})}\delta_2^{(V)} + 2\frac{\bar{\beta}}{\bar{\alpha}}\gamma_2\right]\sin 2\kappa, \\
SS_1^{(L)} &= -\left[\frac{1}{2(1+\frac{\bar{\beta}}{\bar{\alpha}})}\delta_2^{(V)} + 2\frac{\bar{\beta}}{\bar{\alpha}}\gamma_2\right]\cos 2\kappa + \left[\frac{1}{2(1+\frac{\bar{\beta}}{\bar{\alpha}})}\delta_1^{(V)} + 2\frac{\bar{\beta}}{\bar{\alpha}}\gamma_1\right].
\end{aligned}$$

The estimated combinations (3.45) are listed in Table 3.6, which shows that the inversion results are quite accurate. The estimate of $P_1^{(M)}$ is the least stable, with accuracy slightly lower than that for the term $P_1^{(L)}$.

Further inversion of the combinations from Table 3.6 is highly dependent on the available *a priori* information. For example, if only $\frac{\bar{\beta}}{\bar{\alpha}}$ is known, it is possible to obtain the "δ-type" combinations $(\delta_1^{(V)} - \delta_2^{(V)}\cos 2\kappa)$ and $(\delta_2^{(V)}\sin 2\kappa)$ and the "γ-type" combinations $(\gamma_1 - \gamma_2\cos 2\kappa)$ and $(\gamma_2\sin 2\kappa)$. Generally, estimates of the γ-type combinations are significantly more stable than those for the δ-type combinations (this is a general conclusion applicable to any anisotropic symmetry up to orthorhombic). In the following, I assume the "best" possible scenario: the $\frac{\bar{\beta}}{\bar{\alpha}}$ ratio, one isotropic contrast ($\frac{\Delta\alpha}{\alpha}$ in this case) and also anisotropy parameters of the incidence HTI halfspace are known. Hence, it is assumed that the parameters of the incidence halfspace have been estimated, e.g., using NMO analysis (Contreras *et al.*, 1999), so the focus of the inversion is on the reflecting halfspace.

It follows from Table 3.7 that in this case the remaining isotropic contrasts can be recovered with sufficient accuracy. Moreover, good estimates of the angle κ and

	$\frac{\Delta\beta}{\bar{\beta}}$	$\frac{\Delta\rho}{\bar{\rho}}$	$\frac{\Delta G}{\bar{G}}$	$\gamma_2-\gamma_1$	$\delta_2^{(V)}-\delta_1^{(V)}$
exact	0.182	0.113	0.469	0.000	−0.160
$\frac{\Delta\alpha}{\bar{\alpha}}=0.182$	0.217 ± 0.026	0.112 ± 0.001	0.534 ± 0.047	0.000 ± 0.034	-0.166 ± 0.035

Table 3.5. Inverted isotropic contrasts and the differences in the anisotropy parameters $(\gamma_2-\gamma_1)$ and $(\delta_2^{(V)}-\delta_1^{(V)})$ for the HTI/HTI model, assuming known $\frac{\bar{\beta}}{\bar{\alpha}}=0.358$ and $\frac{\Delta\alpha}{\bar{\alpha}}=0.182$.

and
$(\gamma_2-\gamma_1)$, as well as the isotropic contrasts $\frac{\Delta\alpha}{\bar{\alpha}}$, $\frac{\Delta\beta}{\bar{\beta}}$ and $\frac{\Delta G}{\bar{G}}$, provided $\frac{\bar{\beta}}{\bar{\alpha}}$ is known. The additional information (compared to the previous isotropic/VTI model) that makes such a recovery possible is provided by the azimuthal terms $P_1^{(L)}$ and $SS_1^{(L)}$. It turns out, however, that this inversion is highly unstable, resulting in the stable estimate of only one of the medium parameters – that of the parameter $(\gamma_2-\gamma_1)$ (with a standard deviation of ±0.035). For example, the parameter $(\delta_2^{(V)}-\delta_1^{(V)})$ can be found with an accuracy of about ±0.07 which allows for only a very rough estimate. If no other *a priori* information is available, the inversion does not allow us to estimate the other parameters.

As in the previous case, I assume in the following that estimates of $\frac{\bar{\beta}}{\bar{\alpha}}$ and $\frac{\Delta\alpha}{\bar{\alpha}}$ are available. Then, by combining the terms P_0, $P_1^{(ABS)}$ and $SS_1^{(ABS)}$ from Table 3.4, it is possible to constrain the remaining isotropic contrasts and the difference $(\delta_2^{(V)}-\delta_1^{(V)})$. Then, the terms $P_1^{(L)}$ and $SS_1^{(L)}$ can be used to obtain the parameter $(\gamma_2-\gamma_1)$ and make another estimate on the parameter $(\delta_2^{(V)}-\delta_1^{(V)})$, making the final value of this parameter quite accurate. The results are presented in Table 3.5. Bias in the estimates $\frac{\Delta\beta}{\bar{\beta}}$ and $\frac{\Delta G}{\bar{G}}$ results from biased estimates $P_1^{(ABS)}$, $SS_1^{(ABS)}$ and $SS_1^{(L)}$ in Table 3.4.

Regarding dependence of the stability of the inversion on the magnitude of the $\frac{\bar{\beta}}{\bar{\alpha}}$ ratio, the general conclusions about the isotropic contrasts for the isotropic/VTI model hold also for the HTI/HTI model; the conclusion drawn for $(\delta_2-\delta_1)$ remains valid for $(\delta_2^{(V)}-\delta_1^{(V)})$. The parameter $(\gamma_2-\gamma_1)$ is better constrained for smaller $\frac{\bar{\beta}}{\bar{\alpha}}$ ratios. Finally, the accuracy achieved for the HTI/HTI model is close to that for an isotropic/HTI model, and also to that for an VTI/HTI model if the δ_1 parameter of the VTI halfspace is known [for example from velocity analysis, see Alkhalifah *et al.* (1996)].

Example 3: HTIxHTI model. The next model is a modification of the HTI/HTI model discussed above that contains the same HTI halfspaces. In this

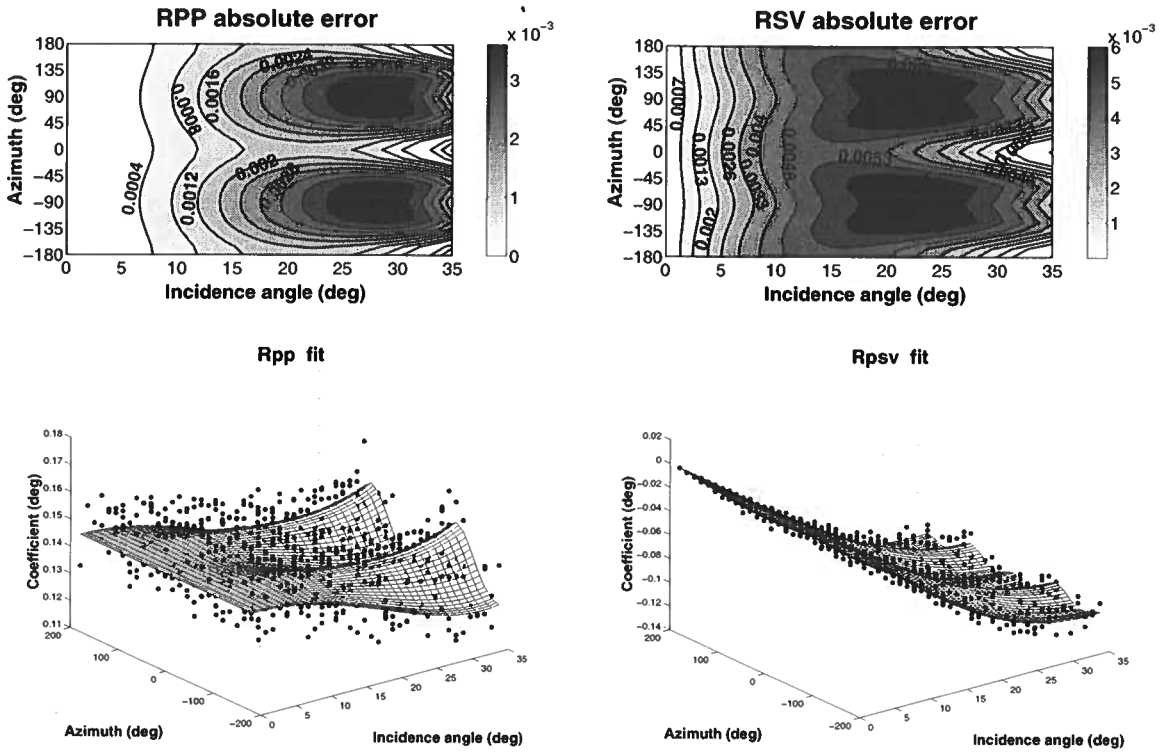

Figure 3.2. Linear inversion of the reflection coefficients R_{PP} (left) and R_{PSV} (right) for the HTI/HTI model (Example 2). The upper plots show the differences between the exact and approximate reflection coefficients, and the surfaces in the lower plots show the best-fit reflection coefficients; error-contaminated data are marked by the dots. Medium parameters are: incidence halfspace - $\rho = 2.50\,\mathrm{g/cm^3}$, $V_{33} = 3.00\,\mathrm{km/s}$, $V_{44} = 1.20\,\mathrm{km/s}$, $\epsilon^{(V)} = -0.05$, $\delta^{(V)} = 0.10$, $\gamma = 0.13$; reflecting halfspace - $\rho = 2.80\,\mathrm{g/cm^3}$, $V_{33} = 3.60\,\mathrm{km/s}$, $V_{44} = 1.44\,\mathrm{km/s}$, $\epsilon^{(V)} = -0.05$, $\delta^{(V)} = -0.06$ and $\gamma = 0.13$; $V_{33} = \sqrt{A_{33}}$ and $V_{44} = \sqrt{A_{44}}$ represent the vertical P- and S-wave velocities respectively, where A_{33} and A_{44} are the corresponding density-normalized stiffness coefficients.

	P_0	$P_1^{(ABS)}$	$P_1^{(L)}$	$SS_1^{(ABS)}$	$SS_1^{(L)}$
exact	0.147	−0.109	0.080	−0.283	0.059
recovered	0.146 ± 0.001	-0.130 ± 0.010	0.083 ± 0.014	-0.309 ± 0.003	0.061 ± 0.005

Table 3.4. Inverted parameters [equations (3.44)] of the reflection coefficients R_{PP} and R_{PSV} for the HTI/HTI model (Example 2) obtained by fitting the error-contaminated data (10% uniformly distributed random error) in Figure 3.2.

Example 2: HTI/HTI model. Figure 3.2 shows a set of plots similar to those in Figure 3.1 for the more complicated HTI/HTI model (see the caption of Figure 3.2 for the medium parameters). The symmetry axes of both halfspaces are aligned, so $\kappa = 0$ [for the definition of κ, see the discussion of equations (3.4)-(3.6)]. The upper plots of Figure 3.2 show significantly smaller differences between the exact and approximate reflection coefficients for the HTI/HTI model than those observed for the isotropic/VTI model, so the bias in the inversion is expected to be smaller. For this model, from equations (3.5), (3.10)-(3.12), (3.39), (E.1) and (E.3), the terms $P_1^{(M)} = P_2^{(M1)} = P_2^{(M2)} = P_2^{(M3)} = 0$ and $SS_1^{(M)} = SS_2^{(M1)} = SS_2^{(M2)} = SS_2^{(M3)} = SS_3^{(M1)} = SS_3^{(M2)} = SS_3^{(M3)} = SS_4^{(M1)} = SS_4^{(M2)} = SS_4^{(M3)} = 0$ in equations (3.35) and (3.42), respectively. The HTI/HTI interface, however, generates azimuthally-varying reflection coefficients (see the lower plots in Figure 3.2) with the following small-incidence-angle terms [see equations (3.2),(3.4), (3.6), (3.38), (3.40) and Table 3.1]:

$$
\begin{aligned}
P_0 &= \frac{1}{2}\frac{\Delta\alpha}{\bar{\alpha}} + \frac{1}{2}\frac{\Delta\rho}{\bar{\rho}}, \\
P_1^{(ABS)} &= \frac{1}{2}\frac{\Delta\alpha}{\bar{\alpha}} - 2\left(\frac{\bar{\beta}}{\bar{\alpha}}\right)^2 \frac{\Delta G}{\bar{G}} + \frac{1}{2}(\delta_2^{(V)} - \delta_1^{(V)}), \\
P_1^{(L)} &= -\frac{1}{2}(\delta_2^{(V)} - \delta_1^{(V)}) - 4\left(\frac{\bar{\beta}}{\bar{\alpha}}\right)^2 (\gamma_2 - \gamma_1), \\
SS_1^{(ABS)} &= -\frac{1}{2}\frac{\Delta\rho}{\bar{\rho}} - \frac{\bar{\beta}}{\bar{\alpha}}\frac{\Delta G}{\bar{G}} + \frac{1}{2(1+\frac{\bar{\beta}}{\bar{\alpha}})}(\delta_2^{(V)} - \delta_1^{(V)}), \\
SS_1^{(L)} &= -\frac{1}{2(1+\frac{\bar{\beta}}{\bar{\alpha}})}(\delta_2^{(V)} - \delta_1^{(V)}) - 2\frac{\bar{\beta}}{\bar{\alpha}}(\gamma_2 - \gamma_1).
\end{aligned}
\tag{3.44}
$$

Table 3.4 shows that all five terms are estimated with good accuracy. In theory, Table 3.4 contains enough information to estimate the model parameters $(\delta_2^{(V)} - \delta_1^{(V)})$

	$\frac{\Delta\beta}{\bar{\beta}}$	$\frac{\Delta\rho}{\bar{\rho}}$	$\gamma_2^{(S)}$	$\delta_2^{(1)}$	$\delta_2^{(2)}$
exact	0.461	0.182	−0.150	−0.100	−0.200
bias	0.753 ± 0.065	0.180 ± 0.001	-0.531 ± 0.051	-0.420 ± 0.198	0.116 ± 0.116
reduction	0.442 ± 0.065	0.180 ± 0.001	-0.116 ± 0.051	0.103 ± 0.198	-0.206 ± 0.116

Table 3.9. Inverted isotropic contrasts and the anisotropy parameters $\gamma_2^{(S)}$, $\delta_2^{(1)}$ and $\delta_2^{(2)}$ for the ORTHO/ORTHO model (Example 4), assuming known $\frac{\bar{\beta}}{\bar{\alpha}} = 0.557$, $\frac{\Delta\alpha}{\bar{\alpha}} = 0.286$, $\gamma_1^{(S)} = 0.10$, $\delta_1^{(1)} = -0.20$ and $\delta_1^{(2)} = 0.10$. The third row shows strongly biased estimates obtained by the direct inversion of the results from Table 3.8; the fourth row shows the results after applying the bias-reduction procedure (see the text for details).

instead of just one [as in VTI (δ_2) or HTI ($\delta_2^{(V)}$)] causes the loss of stability, and the data can no longer tightly constrain the parameters. Relatively stable estimates of the isotropic contrasts $\frac{\Delta\beta}{\bar{\beta}}$ and $\frac{\Delta\rho}{\bar{\rho}}$, and also the parameter $\gamma_2^{(S)}$, on the other hand, suggests that it may be feasible to recover the trends (relative spatial changes) of these parameters. The estimated values of the $\frac{\Delta\beta}{\bar{\beta}}$ and $\gamma_2^{(S)}$, nevertheless, are far from the true values due to the strong bias (Table 3.8).

The fourth row of Table 3.9 shows the results after applying a process of *bias reduction*. The bias reduction process is based on a simple idea: the exact PP- and PSV-wave reflection coefficients computed for the correct model should be sufficiently close, at least for small incidence angle reflections ($\leq 20°$), to the corresponding approximate coefficients R_{PP} and R_{PSV} computed for the recovered biased model (such as the one from the third row of Table 3.9). Knowing the biased model and the relations between the model parameters and exact and approximate reflection coefficients, it should be therefore possible in principle to recover the correct model as well. The bias reduction process can be realized in three steps. In step 1, the exact PP- and PSV-wave reflection coefficients for the orthorhombic/orthorhombic interface are constructed using the estimates from the third row of Table 3.9; the unknown medium parameters $\epsilon_1^{(1)}$, $\epsilon_1^{(2)}$, $\epsilon_2^{(1)}$, $\epsilon_2^{(2)}$, $\delta_1^{(2)}$ and $\delta_2^{(3)}$, which control the large-incidence-angle reflections, are set to zero (the coefficients are computed only for small incidence angles $\leq 20°$). In step 2, the joint linear inversion of this synthetic data is carried out (using approximate PP- and PS-wave reflection coefficients as before), resulting in new estimates of the medium parameters. Large differences between the new estimates and the corresponding estimates from Table 3.9 indicate strongly biased results. In step 3, based on the differences, the original model parameters from the third row of Table 3.9 are updated (the simple method of halving intervals is suffi-

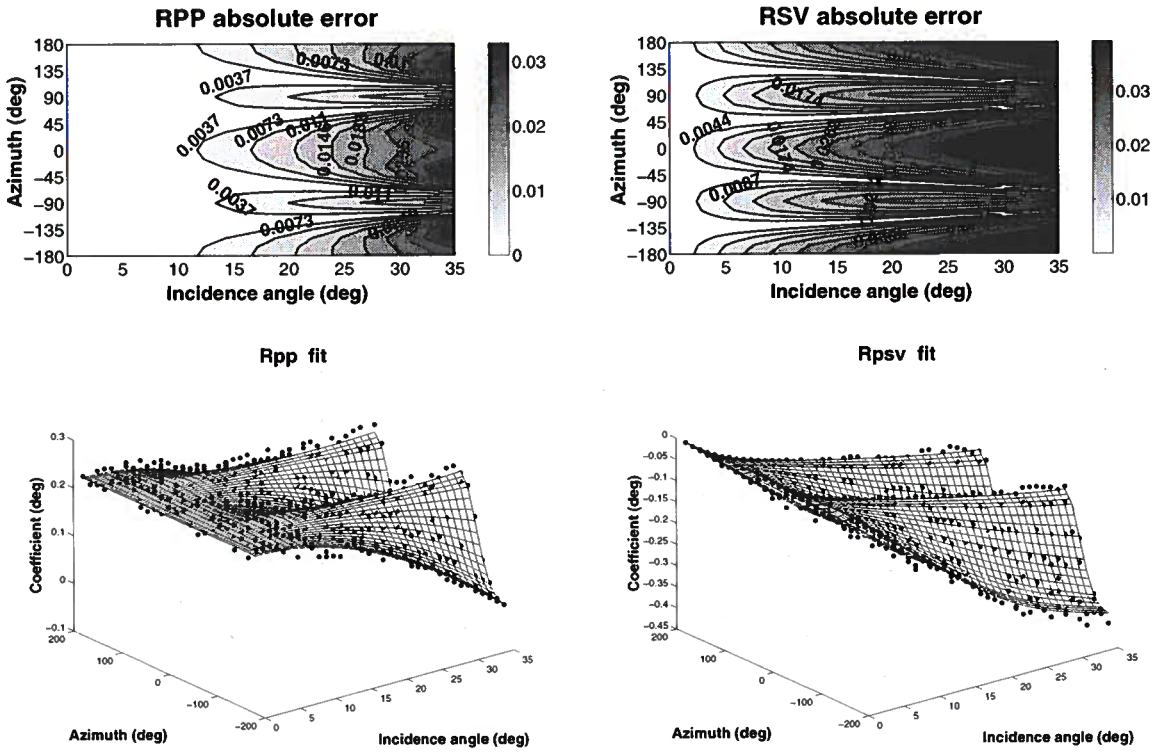

Figure 3.3. Linear inversion of the reflection coefficients R_{PP} (left) and R_{PSV} (right) for the ORTHO/ORTHO model. The upper plots show the differences between the exact and approximate reflection coefficients, and the lower plots show the best-fit reflection coefficients; error contaminated data are marked by the dots. The medium parameters are: incidence halfspace - $\rho = 2.50\,\mathrm{g/cm^3}$, $V_{33} = 3.00\,\mathrm{km/s}$, $V_{44} = 1.64\,\mathrm{km/s}$, $\epsilon^{(1)} = -0.15$, $\epsilon^{(2)} = 0.15$, $\delta^{(1)} = -0.20$, $\delta^{(2)} = 0.10$, $\delta^{(3)} = 0.15$, $\gamma^{(S)} = 0.10$; reflecting halfspace - $\rho = 3.00\,\mathrm{g/cm^3}$, $V_{33} = 4.00\,\mathrm{km/s}$, $V_{44} = 2.01\,\mathrm{km/s}$, $\epsilon^{(1)} = -0.15$, $\epsilon^{(2)} = -0.25$, $\delta^{(1)} = -0.10$, $\delta^{(2)} = -0.20$, $\delta^{(3)} = 0.10$ and $\gamma^{(S)} = -0.15$; $V_{33} = \sqrt{A_{33}}$ and $V_{44} = \sqrt{A_{44}}$ represent the vertical P- and S-wave velocities respectively, where A_{33} and A_{44} are the density-normalized stiffness coefficients.

4.3.2 Example 2: HTIxHTI model inversion using large-incidence-angle reflections

The first anisotropic model to be processed by the inversion algorithm introduced above consists of two HTI halfspaces whose symmetry axes above and below the interface are misaligned. The model is the same as the HTIxHTI model from Example 3, in Chapter 3 (see Figure 3.2 for the medium parameters). I again assume that the azimuth of the symmetry axis of the incidence HTI halfspace is known. In this tutorial example, the inversion is described in detail. In all other examples below, the analysis follows the same pattern, so only important differences are highlighted.

Using the same model parameterization as in the corresponding linear inversion (see Section 3.2.2), the model vector to be recovered can be defined as

$$\mathbf{m} = \left(\frac{\Delta\rho}{\bar{\rho}}, \frac{\Delta\alpha}{\bar{\alpha}}, \frac{\Delta\beta}{\bar{\beta}}, \frac{\bar{\beta}}{\bar{\alpha}}, \epsilon_1^{(V)}, \delta_1^{(V)}, \gamma_1, \epsilon_2^{(V)}, \delta_2^{(V)}, \gamma_2, \kappa \right), \tag{4.4}$$

where the isotropic contrasts and the $\frac{\bar{\beta}}{\bar{\alpha}}$ ratio are defined as in Example 1, the anisotropic medium parameters $\epsilon_1^{(V)}, \delta_1^{(V)}, \gamma_1$ and $\epsilon_2^{(V)}, \delta_2^{(V)}, \gamma_2$ are defined by equations (2.28) for the incidence and reflecting halfspaces, respectively, and κ is the misalignment angle between the symmetry axes [see equations (2.24)-(2.26) or (3.4)-(3.6)].

As in Example 1, PSM was generated first, using an approximate single value of the *P*-wave AVO intercept 0.15 recovered during the linear inversion [see the term P_0 in Table 3.6 and equation (3.45)]. Then the nonlinear least squares algorithm was applied in phase 2, resulting in the recovery of the final 280 models. No *a priori* information was used in this phase (also note that no *a priori* information was needed to obtain the value of the *P*-wave AVO intercept 0.15 above). The values of all isotropic contrasts were allowed to vary within the interval $(-1.5; 1.5)$, and the initial value of the $\frac{\bar{\beta}}{\bar{\alpha}}$ ratio was 0.5. All anisotropy parameters could vary within $(-1; 1)$, and the angle κ within $(0°; 90°)$. Unless defined differently, all these ranges are kept the same for all inversion examples below.

In contrast to Example 1, many local minima were identified in phase 2 of this inversion. The threshold criterion was further used to obtain the final set of models that fit the data. The threshold value was determined at $F_{obj} = 0.55$, following the approach discussed in the end of Section 4.2.

A) *Recovered models below the threshold*

Figure 4.3 shows the distribution of the recovered models with $F_{obj} \leq 0.55$ (199 models out of 280) as a function of the identified global and local minima. Clearly, the largest set of the inverted models (136 models) corresponds to the identified sharp global minimum ($F_{obj} = 0.09$; the minimum was identified with a numerical accuracy

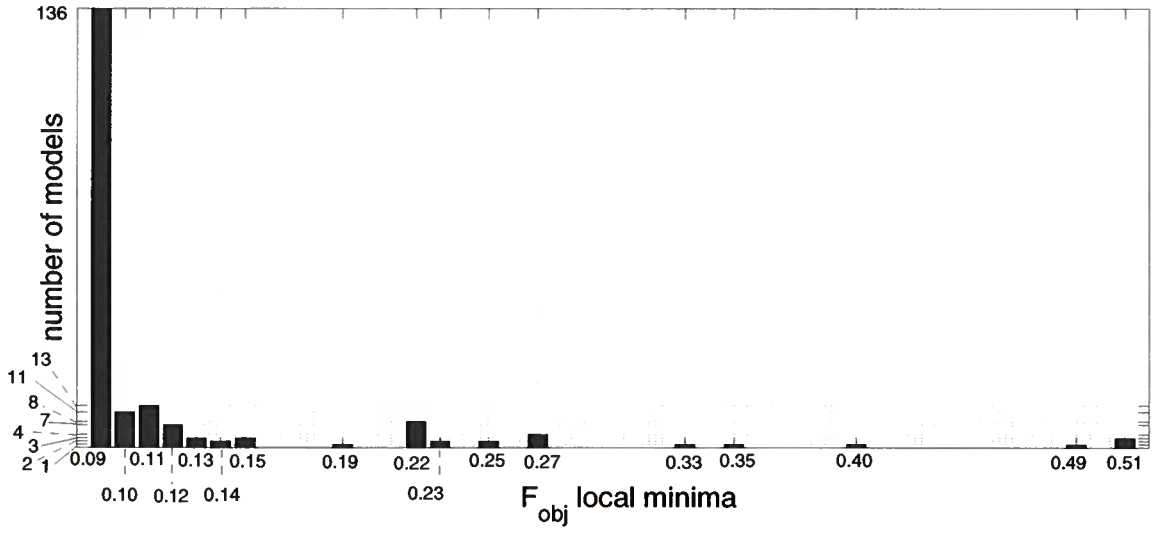

Figure 4.3. Distribution for the recovered models (Example 2); the 199 models that fit the data (with the threshold $F_{obj} = 0.55$) are localized mostly at and in the vicinity of the global minimum ($F_{obj} = 0.09$). The values of the objective function associated with the other local minima are marked on the horizontal axis.

± 0.001). However, there are still many detected local minima (19), corresponding to 63 recovered models. It should be kept in mind that since the model space was not searched completely in phase 1, there are other possible local minima not shown in Figure 4.3. The assumption here is that the algorithm detected the global minimum correctly, i.e., there is no other minimum below $F_{obj} = 0.09$.

It should be also emphasized that the term "local minimum" is used quite loosely. Strictly, to demonstrate that two models correspond to different local minima, one should show that they cannot be connected by a path that does not go uphill (such a test is time consuming, practically impossible in this inversion problem). Therefore, some of the local minima from Figure 4.3 may belong to the same "basin of attraction" (Deng, 1997) (corresponding to the same minimum). Nevertheless, this fact has no impact on the analysis that follows.

Figure 4.4 is analogous to Figure 4.2; it illustrates the character of the convergence. This figure contains all 199 models from Figure 4.3. The plot of the objective function F_{obj} (upper left corner) shows that many different descending paths were taken; for some models, the descent to either the global or a local minimum was fast (less than 10 iterations), but some models converged slowly, following more gentle slopes. A few inversions are characterized by high oscillations of the objective function. The descending paths of these inversions lie in the vicinity of walls (forbidden zones) in the model space that strongly restrict the descent along certain directions.

inversion techniques that employ the threshold criterion. In general, it is usually difficult to recognize and eliminate low-frequency noise from data, and such noise can result in significantly biased estimates.)

From numerical modeling of exact reflection coefficients (not shown here), even for interfaces between two strongly anisotropic media of lower symmetry (such as orthorhombic) and strong velocity contrasts, the reflection coefficients R_{PP}, R_{PS_1} and R_{PS_2} are smooth, low-oscillating functions in the (ϕ, ψ) domain, at least in the subcritical region. This is also predicted by the linearized approximations, which suggest that the highest rate of oscillation occurs in the azimuthal domain for large incidence angles: a maximum of three extrema can be found in any 90° interval within the range of azimuths $\psi \in (0°; 360°)$ [as can be shown using equation (3.8) or (E.1)]. The fact that the physics itself does not allow any strongly oscillating behavior of the reflection coefficients suggests that it may be reasonable to continue iterations in phase 2 regardless of the use of any threshold (i.e., keep descending to the minimum), as long as the evolution of the inverting parameters sustains a low-frequency monotonic character, as can be clearly seen, for example, for the parameter $\frac{\beta}{\alpha}$ in Figure 4.2. On the other hand, the smoothness of the reflection coefficients does not imply that the objective function (4.2) itself is simple. In fact, it still may contain many local minima. Although no a local minimum was detected in Figure 4.2, further numerical modeling of objective functions for different isotropic models indicates that there may exist models with more than one global minimum, if the contrasts of the medium parameters across the interface are sufficiently large. In that case, the threshold can play an important role in localizing the global minimum, as is used in anisotropic models (see examples below).

Many inversions done for both isotropic and anisotropic models with different error realizations (keeping the error magnitude of 10%), and also different magnitudes of errors (up to 20%, see Example 4) support the approach discussed above, as long as the noise is random. A completely different situation can occur if the data are contaminated by systematic noise (Example 8 or 9). However, as suggested later on, the inversion provides indications of the presence of such a noise, if the noise is sufficiently strong.

Example 1 suggests that the joint nonlinear inversion of PP- and PS-wave reflection coefficients can be used to recover the medium parameters of isotropic models [in the sense of equation (4.3)], if the incidence angles are as large as 45° (although only slightly worse results were obtained using incidence angles up to 35°; note that the critical angle for this weak-contrast interface is 56°). The linear inversion developed in Chapter 3 predicts this possibility theoretically (see Section 3.1.4), provided large-incidence-angle component of the approximate reflection coefficients are available. In practice, however, recovery of this component is unstable, and the linear inversion for all medium parameters is unfeasible without additional constraints.

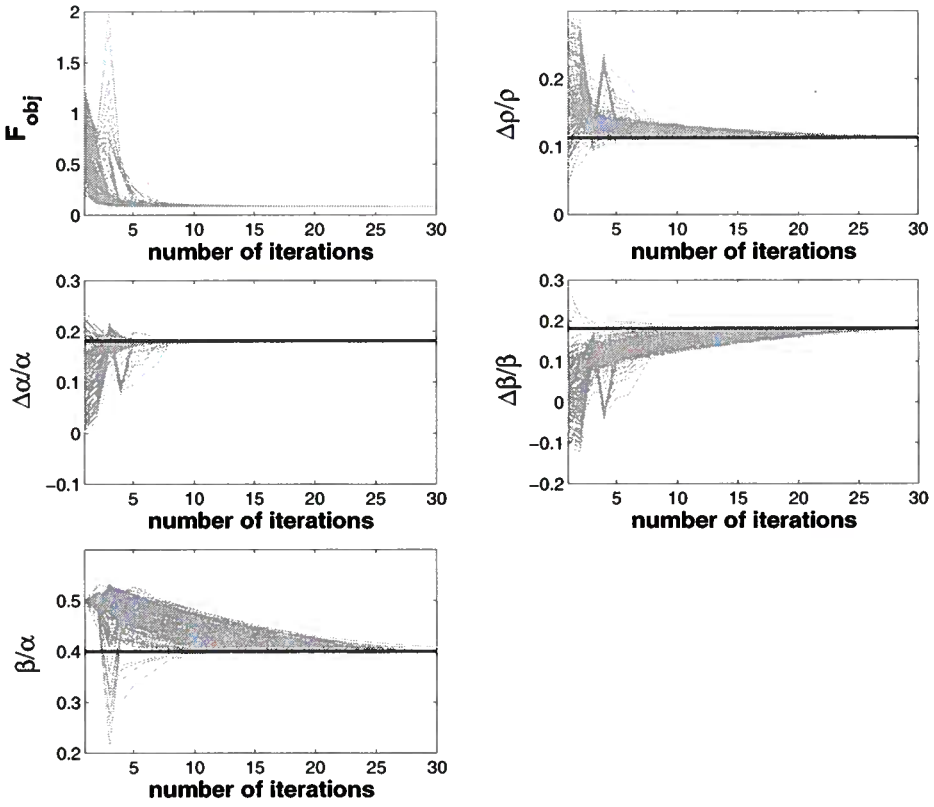

Figure 4.2. Inversion for the isotropic model (Example 1). Evolution of the objective function F_{obj} and individual medium parameters (as marked on vertical axes) with increasing number of iterations (horizontal axes). The thick horizontal line in each plot marks the true value of the corresponding medium parameter. The maximum incidence angle used is 45°.

	$\frac{\Delta\rho}{\rho}$	$\frac{\Delta\alpha}{\alpha}$	$\frac{\Delta\beta}{\beta}$	$\frac{\beta}{\alpha}$
exact	0.113	0.182	0.182	0.40
recovered	$0.112 - 0.115$	$0.181 - 0.182$	$0.177 - 0.192$	$0.39 - 0.41$

Table 4.1. Inversion results for the isotropic model (Example 1). The true values (second row) and the recovered ranges of the medium parameters (third row).

consideration as soon as possible. A similar strategy is also successfully applied for anisotropic models below, where the models from PSM satisfy an approximate value of the P-wave AVO intercept obtained from the corresponding linear inversion.

The model vector $\mathbf{m}$, which is recovered by minimizing equation (4.2), contains the following medium parameters:

$$\mathbf{m} = \left(\frac{\Delta\rho}{\bar{\rho}}, \frac{\Delta\alpha}{\bar{\alpha}}, \frac{\Delta\beta}{\bar{\beta}}, \frac{\bar{\beta}}{\bar{\alpha}} \right), \tag{4.3}$$

where the isotropic contrasts $\frac{\Delta\rho}{\bar{\rho}}$, $\frac{\Delta\alpha}{\bar{\alpha}}$, $\frac{\Delta\beta}{\bar{\beta}}$ are defined in equations (3.2)-(3.7), and the average velocities in $\frac{\bar{\beta}}{\bar{\alpha}}$ are defined by equations (2.13)-(2.14). During the inversion, the contrasts were allowed to vary within a broad range $(-1.2; 1.2)$. The starting value of the $\frac{\bar{\beta}}{\bar{\alpha}}$ ratio was chosen as 0.5 (common values of $\frac{\bar{\beta}}{\bar{\alpha}}$ vary between 0.3 and 0.7). As I concluded from the linear inversion in Chapter 3, the model vector $\mathbf{m}$ from equation (4.3) is recoverable in principle.

For this model, the inversion algorithm detected only a single minimum (with the value $F_{obj} = 0.08$) to which all 280 models converged in phase 2. Figure 4.2 shows the evolution of the objective function and all medium parameters, as the iterations proceeded. Figure 4.2 provides a useful insight into the inversion because it allows one to study not only the variance of the inverted parameters, but also the character and rate of their convergence (which reflects the topography of the objective function). Having this insight, it is possible to conclude how well or poorly constrained the individual parameters are, what parameters are most sensitive to data errors, and what kind of *a priori* information would be most valuable to support the inversion. Inversions for anisotropic models, presented below, particularly benefit from this kind of insight provided by plots analogous to those in Figure (4.2).

From Figure 4.2, the best constrained parameter with the fastest convergence (about 10 iterations) is the contrast $\frac{\Delta\alpha}{\bar{\alpha}}$, followed by $\frac{\Delta\rho}{\bar{\rho}}$ and $\frac{\Delta\beta}{\bar{\beta}}$. The least constrained parameter (with the slowest convergence), which is still well recovered, is the ratio $\frac{\bar{\beta}}{\bar{\alpha}}$. It can be also inferred from Figure 4.2 that *a priori* knowledge of either $\frac{\Delta\beta}{\bar{\beta}}$ or $\frac{\bar{\beta}}{\bar{\alpha}}$ would further aid an accurate recovery of the remaining parameters (although no *a priori* knowledge was necessary in this case). Table 4.1 summarizes the results of the inversion, and compares them to the true values. Both Figure 4.2 and Table 4.1 suggest that the estimation of all medium parameters was quite successful.

The results from Table 4.1 were obtained without using any threshold. The main reason for prescribing a reasonably conservative threshold is to avoid overfitting the data (fitting the noise results in non existing features artificially introduced in the model). In my opinion, however, there is no need for such a threshold in this particular case, as long as we assume that the noise in the data is random and of high-frequency. (This is a common and reasonable assumption, also used in most

4.3 Synthetic examples

In this section, several examples are used to analyse the joint nonlinear inversion of PP- and PS-wave reflection coefficients in anisotropic media. Four types of models are considered: isotropic, HTI/HTI (both halfspaces are HTI, with aligned symmetry axes above and below the interface), HTIxHTI (the same as HTI/HTI but the symmetry axes are misaligned by 30°), ORTHO/ORTHO (both halfspaces are orthorhombic with aligned vertical symmetry planes), and ORTHOxORTHO (as ORTHO/ORTHO but the vertical symmetry planes are misaligned by 30°). Toward the end of this section, two other examples are presented to address, albeit in a simplistic way, two practical problems: an incorrect calibration of the reflection coefficients extracted from data, and an incorrect assumption about the anisotropic symmetry (explained below).

Unless specified differently, the synthetic data are generated in the same way as for the linear inversion and contaminated by the same normally distributed random error of 10%. The azimuthal data coverage is also identical (ψ varies form 0° to 360° with the increment $\Delta\psi = 15°$). Because the accuracy of the exact reflection coefficients does not deteriorate with increasing angle, the large-incidence-angle reflection coefficients can also be used to improve the results. To analyse this possibility, the synthetic data are generated for incidence angles ϕ from 0° to 45°, with increment $\Delta\phi = 1°$.

As before, this inversion assumes high-quality data and dense data coverage. However, the algorithm does not require either a regular data grid or the recovery of all three coefficients (R_{PP}, R_{PS_1} and R_{PS_2}) at identical data points.

4.3.1 Example 1: Isotropic model

The first example tests the performance of the proposed algorithm on the most simple model of two isotropic halfspaces. The model used for the test is almost identical to the isotropic/VTI model used in Chapter 3 (Example 1). The incidence halfspace is defined by the density $\rho = 2.5\,\mathrm{g/cm^3}$, P-wave velocity $V_P = 3.0\,\mathrm{km/s}$, and S-wave velocity $V_S = 1.2\mathrm{km/s}$. The reflecting halfspace has the density $\rho = 2.8\mathrm{g/cm^3}$, P-wave velocity $V_P = 3.6\,\mathrm{km/s}$, and S-wave velocity $V_S = 1.44\,\mathrm{km/s}$.

I carried out the inversion in the two phases described above. No *a priori* information was used, except that I generated the pool of starting models (PSM) such that the P-wave AVO intercepts and gradients of all models were allowed to vary only within the intervals $(0.14; 0.16)$ and $(-0.075; -0.045)$, respectively. These values can be well recovered from the linear inversion, as documented in the previous chapter. Moreover, it is unnecessary to know these values with high accuracy (they are refined in phase 2). The main reason for restricting the ranges of the P-wave AVO intercept and gradient in building PSM is to exclude unacceptable models from

function defined by equation (4.2) (i.e., the 280 best data-fitting models) are used in the second phase (considerably more demanding on computational time). During this phase, a local-descent search method, a nonlinear least-squares algorithm (implemented in the Matlab Optimization Toolbox) is used to complete the inversion. This *large-scale* algorithm belongs to the class of *subspace trust region* algorithms, based on the *interior-reflective Newton method* (Coleman & Li, 1994; Coleman & Li, 1996). It is an sophisticated algorithm designed to solve effectively large-scale optimization problems. This iterative algorithm allows descent from a starting model to the closest minimum of the objective function, during which further refinement of the starting model is performed. If the inversion is reasonably well constrained, many from the 280 starting models should converge to the global minimum from many different "directions," thus mapping the topology of the objective function near the minimum. Then, statistical tools can be employed to evaluate the final results, such as the mean values and standard deviations of the recovered medium parameters.

The last question that needs to be addressed is the stopping criterion for the nonlinear least-squares algorithm. A reasonable commonly used criterion is based on a *threshold*, a measure of confidence in the data. This is a prescribed value of the objective function such that all the inverted models with objective function value below the threshold are classified as "models that fit the data;" the models above the threshold are rejected as "unacceptable." The iterations stop as soon as the threshold is reached. In principle, however, it is impossible to establish the threshold objectively and completely eliminate the danger of overfitting or underfitting the data. In the examples that follow, the threshold is determined under the assumption that the data are quite accurate (as in the case of the linear inversion, where the data error is 10%). Each recovered model should fit the data points within a prescribed standard deviation, whose value is determined as 10% of the value of the P-wave AVO intercept recovered from data. By accepting this approach, we believe that the P-wave AVO intercept is recovered within $\pm 10\%$ of its true value (in terms of the standard deviation), and the remaining values of the reflection coefficients are recovered with the same or better *absolute* accuracy. Since the P-wave AVO intercept is the most reliable quantity estimated from data (as shown in Chapter 3), and this value is usually quite large compared to the rest of the data, the resulting thresholds seem to be a reasonable choice.

As explained below, however, such a threshold is used only as an auxiliary information, not as the actual stopping criterion. In the examples presented here, the inversion stops when the convergence of the medium parameters being recovered no longer possess a low-frequency trend with increasing iterations. This also corresponds to small changes of the objective function ($1\% - 5\%$) between subsequent iterations.

function **P** is designed to: 1) eliminate all models that produce postcritical reflections from the considered range of angles (only subcritical reflection data are used here), 2) eliminate all visco-elastic models characterized by complex velocities (absorption is not considered, only real-valued medium parameters are allowed), and 3) eliminate all nonphysical models (strain energy must be nonnegative). The penalty function **P** produces the forbidden zones (walls) in the model space described in the previous section.

As discussed above, the main difficulty in solving multi-modal inverse problems is to identify the global minimum of the objective function (4.2) in the model space and to obtain a measure of the width of the global minimum, which tells us how accurate are the estimates of the individual medium parameters. The first problem can be solved by an extensive search over the model space using Monte Carlo-based methods [see, for example, Mosegaard and Tarantola (1995), Sen and Stoffa (1991), or Stoffa and Sen (1991)]. Such methods can become, however, prohibitively expensive, and are not usually efficient for addressing the second problem. In contrast, local-descent search methods [such as conjugate gradient methods, see Fletcher (1987)] are better suited to analyze the topography of the global minimum, but their success strongly depends on the choice of starting model, i.e., they can be easily trapped in local minima.

None of these methods alone is well suited for the inversion of the reflection coefficients in anisotropic media. For instance, for an HTI/HTI interface with misaligned symmetry axes (Example 2 below), the model space is 11-dimensional. Taking into account that a single evaluation of the objective function takes about 30 seconds (Pentium III processor) and we take only five samples (i.e., five models) in each dimension (coarse sampling, not sufficient for any reliable analysis), the time necessary for evaluation of the objective function on such a grid (5^{11} points) is approximately 475 thousand years. Soon, it would also become clear that the topology of the objective function is quite complex, and contains many local minima. Therefore, unless the starting model is sufficiently close to the true model, the local-descent search methods would also likely fail to find the true minimum.

My approach to the particular inverse problem here uses a combination of the two above methods. The inversion tests presented in this chapter are carried out in two phases. In the first phase, a Monte Carlo-based search of the model space is performed, and a pool of starting models (referred to as PSM in the following text) is generated (between 2500 to 3000 models). The model space is searched within prescribed boundaries of individual medium parameters (which are usually very broad). Although the search is partly random, the algorithm ensures that *each* dimension is covered as densely as possible, given the size of PSM, and any additional information that may be available about the model is also taken into account. After the PSM is generated, 280 models with the smallest values of the objective

Two final remarks regarding nonlinear inversion are appropriate here. First, as discussed in Snieder (1998), the results of nonlinear inversion are dependent on the *values* of the model parameters. In the context of the inversion here, it means that the stability and accuracy of the model parameters recovered for a particular anisotropic symmetry can be different for different magnitudes of the anisotropy, although the anisotropic symmetry (i.e., the forward operator) remains the same. Second, although bias due to the inaccuracy of the approximations of the reflection coefficients is removed by using the exact expressions, bias can still exist in the nonlinear inversion (as seen in some examples below). As in the case of linear inversion, bias can occur, for example, because of a nontrivial null space of the forward operator $\mathbf{G}(\mathbf{m})$ from equation (4.1) or use of an inappropriate form of the objective function [for instance, the choice of the L_2 norm in equation (4.1) can produce a large bias if the data error distribution is far from Gaussian]. Nonlinear inversion may also be subject to the bias caused by a particular discretization of the model space, finite number of iterations, or accumulated numerical errors (Deng, 1997), as well as by the choice of the starting models (see examples below).

Different inversion strategies are designed to handle some of the above difficulties, but because of the large diversity of inversion problems, there does not exist a universally optimal algorithm (Deng, 1997). A challenging part of nonlinear inversion is to find an effective strategy that works for a specific inversion problem at hand.

4.2 Inversion scheme

In the inversion for the exact reflection coefficients in anisotropic media, equation (4.1) takes the following form:

$$\begin{aligned} F_{obj}(\mathbf{m}) &= N_{PP}||\mathbf{R}_{PP}^{(\mathbf{d})} - \mathbf{R}_{PP}^{(\mathbf{f})}(\mathbf{m})||+N_{PS_1}||\mathbf{R}_{PS_1}^{(\mathbf{d})} - \mathbf{R}_{PS_1}^{(\mathbf{f})}(\mathbf{m})|| \\ &\quad +N_{PS_2}||\mathbf{R}_{PS_2}^{(\mathbf{d})} - \mathbf{R}_{PS_2}^{(\mathbf{f})}(\mathbf{m})|| + \mathbf{P}(\mathbf{R}_{PP}^{(\mathbf{f})}, \mathbf{R}_{PS_1}^{(\mathbf{f})}, \mathbf{R}_{PS_2}^{(\mathbf{f})}). \end{aligned} \tag{4.2}$$

The data vectors $\mathbf{R}_{PP}^{(\mathbf{d})}$, $\mathbf{R}_{PS_1}^{(\mathbf{d})}$ and $\mathbf{R}_{PS_2}^{(\mathbf{d})}$ are the PP-, PS_1- and PS_2-wave reflection coefficients, respectively, recovered from reflection data as functions of the incidence angle ϕ and azimuth ψ (for isotropic or VTI media, only one R_{PS} reflection coefficient exists). Similarly, the vectors $\mathbf{R}_{PP}^{(\mathbf{f})}(\mathbf{m})$, $\mathbf{R}_{PS_1}^{(\mathbf{f})}(\mathbf{m})$ and $\mathbf{R}_{PS_2}^{(\mathbf{f})}(\mathbf{m})$ represent the corresponding forward operators (i.e., the exact reflection coefficients) acting on the model vector $\mathbf{m}$ ($\mathbf{m}$ varies for different anisotropic symmetries, and is specified in each example below). In the synthetic examples below, the normalization factors N_{PP}, N_{PS_1} and N_{PS_2} ensure even weights of the PP-, PS_1- and PS_2-wave reflection coefficients in equation (4.2). These factors, however, can be also used to enhance or suppress a specific data type. For example, if PS data are more noisy than PP data, use of a higher factor $N_{PP} > N_{PS_1}$ and $N_{PP} > N_{PS_2}$ may be appropriate. Finally, the penalty

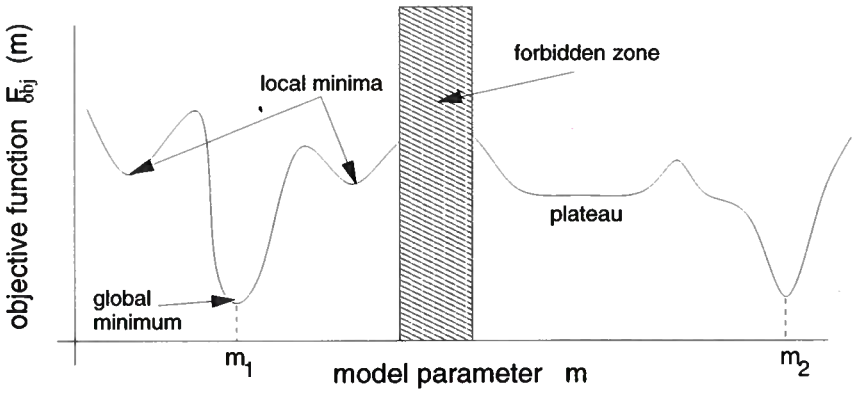

Figure 4.1. Depiction of possible shape for a nonlinear objective function F_{obj} (1-D case). Local minima, forbidden zones, and plateaus may complicate the localization and characterization of the global minimum m_1. The local minimum m_2 contributes significantly to the nonuniqueness of the inversion (see the text). Adopted from Snieder (1998).

difficult task, is to investigate how errors in the data propagate into the recovered medium parameters. The problem of resolution and error propagation [called sometimes the *appraisal problem* (Snieder, 1998)] is usually solved only approximately, using various sophisticated methods (Snieder, 1991; Mosegaard & Tarantola, 1995; Sen & Stoffa, 1991; Stoffa & Sen, 1991), in combination with *a priori* information.

Forbidden zones (Snieder, 1998), as the one shown in Figure (4.1), are regions in the model space that cannot be properly investigated because of lack of data (such as shadow zones) or regions that are disallowed by physics. For inversion of reflection coefficients, forbidden zones may exist because certain values of medium parameters are not physically possible (e.g., the condition of nonnegative strain energy is not satisfied). Such forbidden zones act as *walls* in the model space that may divert the search for the global minimum.

The features of objective functions discussed above become particularly troublesome with increasing dimension of the model space. For example, for isotropic media, the model space is four-dimensional, whereas for HTI media it is 10- or 11-dimensional (see examples below). The higher dimensionality also significantly increases computational time, especially if the forward problem has to be solved numerically, as described in the next section. A detailed discussion of the complexity of nonlinear objective functions can be found in Deng (1997) or Sambridge (1998).

4.1 Introducing nonlinearity

Although inversion of the exact reflection coefficients may provide better results, the *nonlinear* mapping of the model parameters onto the data space (using the exact reflection coefficients) is a source of significant complication. Some of the most essential problems of nonlinear inversion are highlighted below. A concise overview can be found, for example, in Snieder (1998). For more detailed discussion, see Tarantola (1987), Fletcher (1987), Törn and Žilinskas (1989), or Deng (1997).

Similarly to linear inversion, nonlinear inversion can be formulated as an optimization problem, wherein one attempts to minimize an objective (misfit) function $F_{obj}(\mathbf{m})$ with respect to the model $\mathbf{m}$:

$$F_{obj}(\mathbf{m}) = \mathbf{N}\,||\mathbf{d} - \mathbf{G}(\mathbf{m})|| + \mathbf{P}(\mathbf{m}), \tag{4.1}$$

where $\mathbf{d}$ represents the data vector, $\mathbf{G}$ is the nonlinear operator acting on the model vector $\mathbf{m}$, $\mathbf{N}$ is an arbitrary normalization factor, and $\mathbf{P}$ is a *penalty function* that helps to enhance or suppress the desired or unwanted features of the inverted models. The $||\mathbf{x}||$ represents a norm of $\mathbf{x}$, usually chosen as the L_2 (least-squares) norm. Although equation (4.1) is formally identical to the corresponding linear objective function [see the discussion of equations (F.1) and (F.2)], the analysis of the nonlinear function is significantly more complicated.

Figure 4.1 is a schematic plot of a nonlinear objective function for a single model parameter, depicting several features common for nonlinear problems. The first principal consequence of general nonlinearity is that the objective function in equation (4.1) usually has multiple minima (assuming the L_2-norm, a linear objective function has only one minimum). Any algorithm searching for the minimum of such a multimodal objective function thus can lead to a local minimum, and the correct global minimum may not be identified. The situation becomes more complicated if the values of F_{obj} at the global and certain local minima are close to each other (which often happens in practice). Without additional information, the localization of the global minimum is not guaranteed, and the model recovery becomes severely nonunique (as suggested by the two different models m_1 and m_2 in Figure (4.1) that can fit the data almost equally well). An extensive and systematic search throughout the model space, often combined with independent information, is thus necessary to obtain a reliable inversion result.

Plateaus (see Figure 4.1) represent another complication in nonlinear inversion. They exist as a consequence of medium parameters poorly constrained by the data; those parameters cannot be resolved (Snieder *et al.*, 1989). In linear inversion, the problem of resolution is well understood (Backus & Gilbert, 1967; Tarantola, 1987). In nonlinear inversion, however, it may be difficult just to detect the existence of such a plateau, and then to map its extent properly in the model space. Another, similarly

Chapter 4

Joint nonlinear inversion of PP- and PS-wave reflection coefficients in anisotropic media

The main attribute of the linear inversion discussed in the previous chapter is its simplicity and fast performance, together with a relatively straightforward error estimation. The linear inversion also provides a simple analytic insight, important for understanding the potential of inversion in general (such as the possibility to recover certain medium parameters or their combinations). Finally, linear inversion helps to identify the anisotropic symmetry of the model. In contrast, the quality of the results strongly depends on the available *a priori* information, and only the medium parameters corresponding to small- and moderate-incidence-angle reflections can be recovered (i.e., various combinations of the parameters $\frac{\Delta\alpha}{\bar{\alpha}}$, $\frac{\Delta\beta}{\bar{\beta}}$, $\frac{\Delta\rho}{\bar{\rho}}$, γ-type and δ-type coefficients). Moreover, the approximations for the reflection coefficients used in the linear inversion may break down if the weak-contrast, weak-anisotropy condition is violated.

A more sophisticated and time-consuming nonlinear inversion can be used as an alternative to attack the problems above. Clearly, inverting the *exact* reflection coefficients completely removes the bias due to the inaccuracy of the approximate reflection coefficients (although any nonlinear inversion may suffer from bias due to other reasons; see the discussion below). Also, the nonlinear inversion may produce results with better accuracy and resolution, and, possibly, with use of less *a priori* information. Several examples of nonlinear AVO inversion performed for isotropic media support these suggestions; see, for instance, Stoffa and Sen (1991), Sen and Stoffa (1991), Dahl & Ursin (1992), Mallick (1995; 1999), Lavaud *et al.* (1999) or Kabir *et al.* (2000).

This chapter is devoted to the joint nonlinear inversion of the reflection coefficients R_{PP} and R_{PS} in anisotropic media. Here, I develop the inversion algorithm (the final tool in the *inversion toolbox*) and apply it to synthetic data for isotropic, HTI and orthorhombic models. I then compare the results with those obtained from the linear inversion in the previous chapter.

inverting noise-free data can be recovered if the data are contaminated by errors. Additional *a priori* information is necessary for successful estimation of the incidence medium parameters. If good estimates of the $\frac{\bar{\beta}}{\bar{\alpha}}$ ratio, one of the isotropic contrasts, and the anisotropy coefficients of the incidence halfspace are available, acceptable estimates of the remaining isotropic contrasts can be obtained. For VTI media, also recovery of δ parameter is possible, although generally less stable. For HTI and orthorhombic media, it is feasible to determine the γ-type (shear-wave splitting) anisotropy parameter of the reflecting medium and the orientation of the vertical symmetry planes of the reflecting halfspace (angle κ). Parameter $\delta^{(V)}$ can be further estimated for HTI media. For orthorhombic media, however, the inversion for the δ-type parameters is practically impossible without additional information about the anisotropy of the reflecting orthorhombic halfspace.

Finally, large magnitudes of estimated medium parameters (> 0.2) may indicate a strong-contrast interface or strong anisotropy of the medium. Therefore, bias-reduction process should follow in such cases to evaluate and reduce bias in the estimates.

cient). Such a new "corrected" model is then used to construct again exact PP- and PS-wave reflection coefficients and step 2 is repeated. If the "corrected" model was not biased, the new inverted model parameters (obtained after the step 2 is repeated) would be sufficiently close to the corresponding parameters from the third row of Table 3.9. Several iterations (i.e., repetitions of step 2 and 3) are usually necessary to reach sufficient agreement between the newly inverted model parameters and the corresponding parameters from Table 3.9. The last "corrected" model produces AVO response similar to original data, and its linear inversion results in medium parameters close to those from Table 3.9. Therefore, this final "corrected" model should be close to the true medium, less contaminated by bias.

There are two main assumptions behind this process. First, the exact reflection coefficients at small incidence angles are mainly controlled by the linear combinations of the *recovered* medium parameters, such as those in equations (3.46). Second, changes in particular medium parameters from Table 3.9 result in similar changes of the exact and approximate reflection coefficients (i.e., the derivatives of both the exact and approximate reflection coefficients with respect to the individual parameters from Table 3.9 are close to each other). Numerical tests suggest that both assumptions hold well, except for models characterized by strong anisotropy and strong velocity and density contrasts. Note that the assumptions apply namely for small-incidence-angle reflections. The bias-reduction process generally cannot improve estimates of the medium parameters constrained by large-incidence-angle reflections (such as $\epsilon_2^{(1)}$, $\epsilon_2^{(2)}$ or $\delta_2^{(3)}$). Note also that to perform the bias-reduction process, an algorithm for computation of exact reflection coefficients must be available.

This bias-reduction process described above was successful for the recovery of $\Delta\beta/\bar{\beta}$ and $\gamma_2^{(S)}$ (fourth row of Table 3.9). The process, however, can only reduce the bias, not the variance of the inverted results. Therefore, the estimates of the poorly constrained parameters $\delta_2^{(1)}$ and $\delta_2^{(2)}$ are still unacceptable.

The analyses for HTIxHTI and ORTHO/ORTHO models illustrate the limitations of the linear inversion using small and moderate incidence angles.

3.3 Summary of Chapter 3

Using the linearized approximations of the PP- and PS-wave reflection coefficients in their joint linear inversion, I analyze results for anisotropic media of orthorhombic and higher symmetries.

The analysis of noise-free data establishes theoretical limitations of such an inversion. The approximate reflection coefficients allow us to identify the most stable combinations of the medium parameters that can be theoretically recovered using small and moderate incidence angles.

Only a limited set of the combinations of the medium parameters obtained by

	exact	$F_{obj} \leq 0.55$	$F_{obj} \leq 0.12$	$F_{obj} = 0.09$	γ_1 and $\bar{\beta}/\bar{\alpha}$ known
$\frac{\Delta\rho}{\bar{\rho}}$	0.113	0.135 ± 0.064	0.117 ± 0.019	0.111 ± 0.005	0.115 ± 0.001
$\frac{\Delta\alpha}{\bar{\alpha}}$	0.182	0.163 ± 0.064	0.180 ± 0.019	0.186 ± 0.005	0.182 ± 0.001
$\frac{\Delta\beta}{\bar{\beta}}$	0.182	0.134 ± 0.084	0.154 ± 0.031	0.165 ± 0.020	0.179 ± 0.004
$\frac{\bar{\beta}}{\bar{\alpha}}$	0.358	0.394 ± 0.027	0.387 ± 0.020	0.381 ± 0.011	0.375 ± 0.003
$\epsilon_1^{(V)}$	-0.050	-0.051 ± 0.062	-0.035 ± 0.035	-0.035 ± 0.027	-0.056 ± 0.006
$\delta_1^{(V)}$	0.100	0.086 ± 0.056	0.093 ± 0.035	0.100 ± 0.016	0.089 ± 0.004
γ_1	0.125	0.070 ± 0.074	0.076 ± 0.069	0.087 ± 0.060	0.130 ± 0.014
$\epsilon_2^{(V)}$	-0.050	-0.020 ± 0.066	-0.037 ± 0.027	-0.048 ± 0.007	-0.055 ± 0.002
$\delta_2^{(V)}$	-0.060	-0.026 ± 0.050	-0.038 ± 0.027	-0.048 ± 0.010	-0.055 ± 0.003
γ_2	0.125	0.103 ± 0.061	0.112 ± 0.026	0.111 ± 0.017	0.120 ± 0.005
κ	30°	$48.3° \pm 21.6°$	$44.8° \pm 17.5°$	$39.5° \pm 11.5°$	$30.18° \pm 2.0°$

Table 4.2. Inversion results for the HTIxHTI model (Example 2). The medium parameters (first column), their true values (second column), and their recovered values using: 1) the threshold criterion alone ($F_{obj} \leq 0.55$; third column), 2) the threshold criterion supplemented by the results of the linear inversion ($F_{obj} \leq 0.12$; fourth column), 3) no threshold criterion; only those models are selected that correspond to the global minimum ($F_{obj} = 0.09$; fifth column), and 4) the threshold criterion together with *a priori* estimates of $\gamma_1 \in (0.10; 0.15)$ and $\bar{\beta}/\bar{\alpha} \in (0.30; 0.40)$ (sixth column). The error bars represent standard deviations. The results clearly improve from left to right.

All these features indicate a complicated topology of the objective function.

Regarding the individual model parameters, Figure 4.4 and Table 4.2 (third column) clearly show that none of the parameters can be recovered with acceptable accuracy when only the threshold criterion ($F_{obj} = 0.55$) is used (the error bars in Table 4.2 represent standard deviations). Also, notice a bias in the $\frac{\bar{\beta}}{\bar{\alpha}}$ estimate in Figure 4.4. The source of this bias is, of course, different from that reported in the linear inversion (i.e., due to the low accuracy of the linearized approximations of the reflection coefficients). The bias here is apparently induced by the choice of the starting value (0.5) relatively far from the true value (0.358), probably in combination with some other factors discussed in Section 4.1.

Regarding the character of the convergence of the parameters from Figure 4.4, some parameters attain their final values already within a small number of iterations (< 10, such as the isotropic-parameters contrasts), but some parameters converge much slower (most anisotropic parameters), often in a highly oscillating way. Those parameters are more sensitive to the noise contaminating the data. In general, the

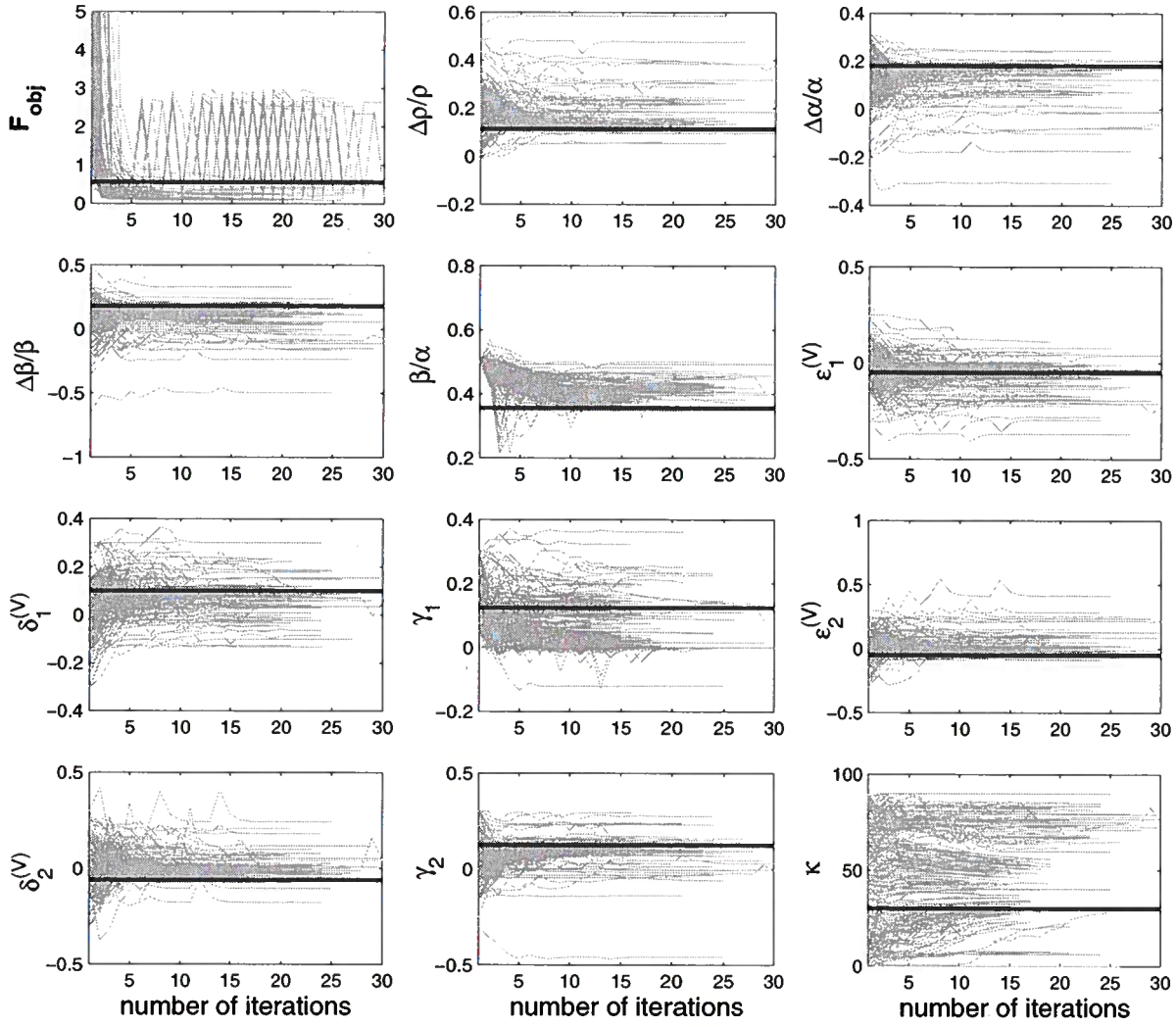

Figure 4.4. Inversion for the HTIxHTI model (Example 2). Evolution of the objective function F_{obj} and individual medium parameters (as marked on vertical axes) with increasing number of iterations (horizontal axes) for 199 models that satisfy the data ($F_{obj} \leq 0.55$). The thick horizontal line in F_{obj} plot marks the threshold 0.55. The thick horizontal line in each parameter plot marks the true value of the corresponding medium parameter.

final values of most recovered parameters do not change significantly from the corresponding starting values – a clear indication of a relatively large null-space of this inversion problem (the concept of null-space is introduced in Appendix F).

Inversion for some better constrained combinations of the medium parameters, rather than for the model vector $\mathbf{m}$ [equation (4.4)], may reduce the null-space. To find such combinations without any guidance, however, can be a tedious process. At this point, the nonlinear inversion can greatly benefit from insight provided by the corresponding linear inversion (Section 3.2.2, Example 3). Figure 4.5 depicts some combinations of the medium parameters suggested by the linear inversion as being well constrained. Among them, $\frac{\Delta G}{\bar{G}}$ is defined in equations (3.4) and (3.7), and the combinations PP, PS, PPcos, PPsin, PScos and PSsin are defined as follows:

$$\begin{aligned}
\mathrm{PP} &= \delta_2^{(V)} + 8\left(\frac{\bar{\beta}}{\bar{\alpha}}\right)^2 \gamma_2, \\
\mathrm{PS} &= \frac{1}{2(1+\frac{\bar{\beta}}{\bar{\alpha}})}\delta_2^{(V)} + 2\left(\frac{\bar{\beta}}{\bar{\alpha}}\right)\gamma_2, \\
\mathrm{PPcos} &= \mathrm{PP}\,\cos 2\kappa, \\
\mathrm{PPsin} &= \mathrm{PP}\,\sin 2\kappa, \\
\mathrm{PScos} &= \mathrm{PS}\,\cos 2\kappa, \\
\mathrm{PSsin} &= \mathrm{PS}\,\sin 2\kappa.
\end{aligned} \tag{4.5}$$

The recovered combinations in Figure 4.5 are generally more stable than the individual medium parameters. From Figure 4.5 and Table 4.3 (third column), the best-constrained parameter, as expected, is $(\frac{\Delta\rho}{\bar{\rho}} + \frac{\Delta\alpha}{\bar{\alpha}})$. Also estimates of some anisotropy parameters can be considered as reasonably accurate, such as $(\epsilon_1^{(V)} - \epsilon_2^{(V)}\cos 2\kappa)$, $(\gamma_1 - \gamma_2 \cos 2\kappa)$, $(\delta_1^{(V)} - \epsilon_1^{(V)})$, or $(\delta_2^{(V)} - \epsilon_2^{(V)})$, and estimates of $(\epsilon_2^{(V)} \sin 2\kappa)$, $(\delta_2^{(V)} \sin 2\kappa)$ and $(\gamma_2 \sin 2\kappa)$ are only slightly less accurate. Good estimates are obtained for PPsin and PSsin as well. Without additional tests, however, it is not clear why similar combinations PPcos and PScos are not recovered successfully, and how this recovery depends on κ.

B) *Recovered models in the vicinity of the global minimum*

The goal of the following analysis is to reveal whether or not a representative subset of the models in Figure 4.4 would correspond well to the true model and that could, *in theory*, be recovered. Such an analysis can be done because the true model is known. In practice, of course, this analysis is not possible; the threshold criterion itself does not allow any better recovery than that above without serious concerns about overfitting the data.

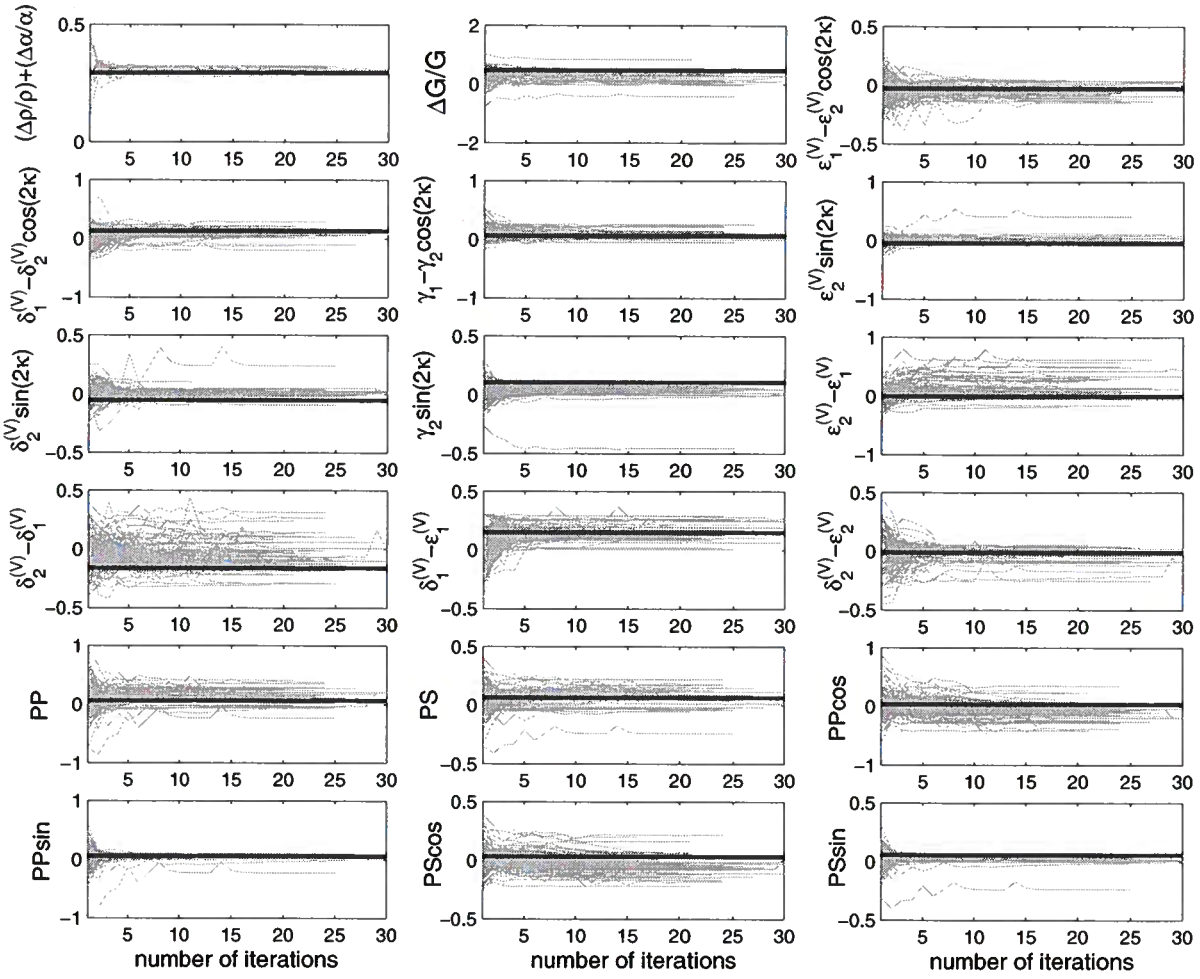

Figure 4.5. Inversion for the HTIxHTI model (Example 2). Evolution of selected combinations of the medium parameters (as suggested by the linear inversion) from Figure 4.4 with increasing number of iterations. These combinations are generally more stable than the individual medium parameters. The thick horizontal line in each plot marks the corresponding true values.

	exact	$F_{obj} \leq 0.55$	$F_{obj} \leq 0.12$	$F_{obj} = 0.09$	γ_1 and $\bar{\beta}/\bar{\alpha}$ known
$\frac{\Delta\rho}{\bar{\rho}} + \frac{\Delta\alpha}{\bar{\alpha}}$	0.295	0.298 ± 0.004	0.297 ± 0.001	0.297 ± 0.000	0.297 ± 0.001
$\frac{\Delta G}{\bar{G}}$	0.469	0.398 ± 0.115	0.419 ± 0.050	0.434 ± 0.041	0.465 ± 0.008
$\epsilon_1^{(V)} - \epsilon_2^{(V)} \cos 2\kappa$	−0.025	-0.032 ± 0.028	-0.027 ± 0.017	-0.024 ± 0.008	-0.030 ± 0.002
$\delta_1^{(V)} - \delta_2^{(V)} \cos 2\kappa$	0.130	0.100 ± 0.047	0.104 ± 0.029	0.112 ± 0.007	0.116 ± 0.001
$\gamma_1 - \gamma_2 \cos 2\kappa$	0.063	0.070 ± 0.038	0.065 ± 0.019	0.062 ± 0.015	0.071 ± 0.004
$\epsilon_2^{(V)} \sin 2\kappa$	−0.043	-0.025 ± 0.041	-0.035 ± 0.018	-0.043 ± 0.004	-0.045 ± 0.001
$\delta_2^{(V)} \sin 2\kappa$	−0.052	-0.028 ± 0.031	-0.035 ± 0.019	-0.043 ± 0.007	-0.048 ± 0.001
$\gamma_2 \sin 2\kappa$	0.108	0.078 ± 0.049	0.090 ± 0.020	0.100 ± 0.007	0.103 ± 0.001
$\epsilon_2^{(V)} - \epsilon_1^{(V)}$	0.000	0.031 ± 0.116	0.001 ± 0.050	-0.013 ± 0.021	0.004 ± 0.004
$\delta_2^{(V)} - \delta_1^{(V)}$	−0.160	-0.112 ± 0.090	-0.130 ± 0.053	-0.148 ± 0.009	-0.144 ± 0.002
$\delta_1^{(V)} - \epsilon_1^{(V)}$	0.150	0.137 ± 0.034	0.130 ± 0.017	0.135 ± 0.013	0.145 ± 0.003
$\delta_2^{(V)} - \epsilon_2^{(V)}$	−0.010	-0.006 ± 0.030	-0.001 ± 0.005	0.000 ± 0.004	-0.003 ± 0.001
PP	0.068	0.101 ± 0.075	0.095 ± 0.040	0.080 ± 0.006	0.080 ± 0.003
PS	0.067	0.071 ± 0.043	0.072 ± 0.020	0.067 ± 0.007	0.070 ± 0.003
PPcos	0.034	-0.024 ± 0.100	-0.006 ± 0.074	0.014 ± 0.032	0.039 ± 0.006
PPsin	0.059	0.066 ± 0.026	0.072 ± 0.005	0.072 ± 0.005	0.069 ± 0.001
PScos	0.034	-0.008 ± 0.061	0.002 ± 0.049	0.014 ± 0.027	0.034 ± 0.006
PSsin	0.058	0.050 ± 0.025	0.057 ± 0.007	0.060 ± 0.001	0.060 ± 0.001

Table 4.3. Inversion results for the HTIxHTI model (Example 2). Selected combinations of the medium parameters (first column), their true values (second column), and their recovered values using the threshold criterion only ($F_{obj} \leq 0.55$; third column), the threshold criterion supplemented by the results of the linear inversion ($F_{obj} \leq 0.12$; fourth column), using only the models corresponding to the global minimum ($F_{obj} = 0.09$; fifth column), and using the threshold criterion together with *a priori* estimates of $\gamma_1 \in (0.10; 0.15)$ and $\bar{\beta}/\bar{\alpha} \in (0.30; 0.40)$ (sixth column). The error bars represent standard deviations. The selected combinations (suggested by the linear inversion) are generally more stable than the individual medium parameters, see Table 4.2.

Indeed, the results above improve as models corresponding to local minima with higher values of the objective function (shown in Figure 4.3) are removed from the analysis. For example, Figure 4.6 shows only models characterized by $F_{obj} \leq 0.12$ (167 models). A significant improvement is clear for most parameters. Also, the movement of most of the parameter estimates from their initial values towards their correct values, previously obscured, is now well pronounced. Figure 4.6 indicates that some estimates of the medium parameters can be acceptable ($\frac{\Delta\rho}{\bar{\rho}}$, $\frac{\Delta\alpha}{\bar{\alpha}}$, $\epsilon_1^{(V)}$, $\epsilon_2^{(V)}$, $\delta_2^{(V)}$ or γ_2), see also Table 4.2 (fourth column). On the other hand, γ_1 and κ cannot be recovered. Also, Table 4.3 (fourth column) shows that except for $(\epsilon_2^{(V)} - \epsilon_1^{(V)})$, $(\delta_2^{(V)} - \delta_1^{(V)})$, PPcos, and PScos, all remaining combinations are well recovered. Note the exceptionally well constrained $(\delta_2^{(V)} - \epsilon_2^{(V)})$.

Figure 4.7, as a logical continuation of Figure 4.6, includes the 136 models corresponding to the global minimum only ($F_{obj} = 0.09$). Most of the parameters are now well constrained, as well as all the combinations introduced in Figure 4.5 (see the fifth columns of Table 4.2 and 4.3). The only unresolved parameters are γ_1 and κ. The existence of an elongated "valley" in the landscape of the objective function can be demonstrated, extending along the $\gamma_1 - \kappa$ dimensions. Therefore, these parameters individually are not well constrained by data, and their recovery becomes impossible in principle. As before, notice slightly biased estimate of $\frac{\bar{\beta}}{\bar{\alpha}}$, as well as estimates of $(\delta_1^{(V)} - \delta_1^{(V)} \cos 2\kappa)$, $(\delta_1^{(V)} - \delta_2^{(V)})$, $(\delta_2^{(V)} - \epsilon_2^{(V)})$, PP and PPsin.

Figure 4.7 suggests that the inversion has potential in theory to recover most of the parameters of the HTIxHTI medium. Such a recovery, however, cannot be justified in practice, unless supported by some independent constraints, in addition to the threshold criterion.

C) *Recovered models using additional constraints*

One possibility of constraining the inversion above is to use the results obtained from the linear inversion. For example, the most stable combinations recovered from the linear inversion (without any *a priori* information) are P_0, $P_1^{(ABS)}$, $P_1^{(M)}$, $P_1^{(L)}$, $SS_1^{(ABS)}$, $SS_1^{(M)}$ and $SS_1^{(L)}$ [see equations (3.45) and Table 3.6]. These combinations can be also computed for each model from Figure 4.4, and their mean values and standard deviations can be estimated. A reasonable argument can be made that the accuracy (i.e., the standard deviations) of these basic combinations obtained from the nonlinear inversion should be at least as good as the accuracy obtained from the linear inversion (see Table 3.6). If not, then the nonlinear inversion probably cannot provide any other reliable estimates either. Thus, it is possible to select only those models from Figure 4.4 that comply with this argument. Applying this criterion, only the models corresponding to $F_{obj} \leq 0.12$ qualify (this value thus depends on a particular noise level). From Figure 4.6 and Table 4.2, 4.3, quite reasonable estimates

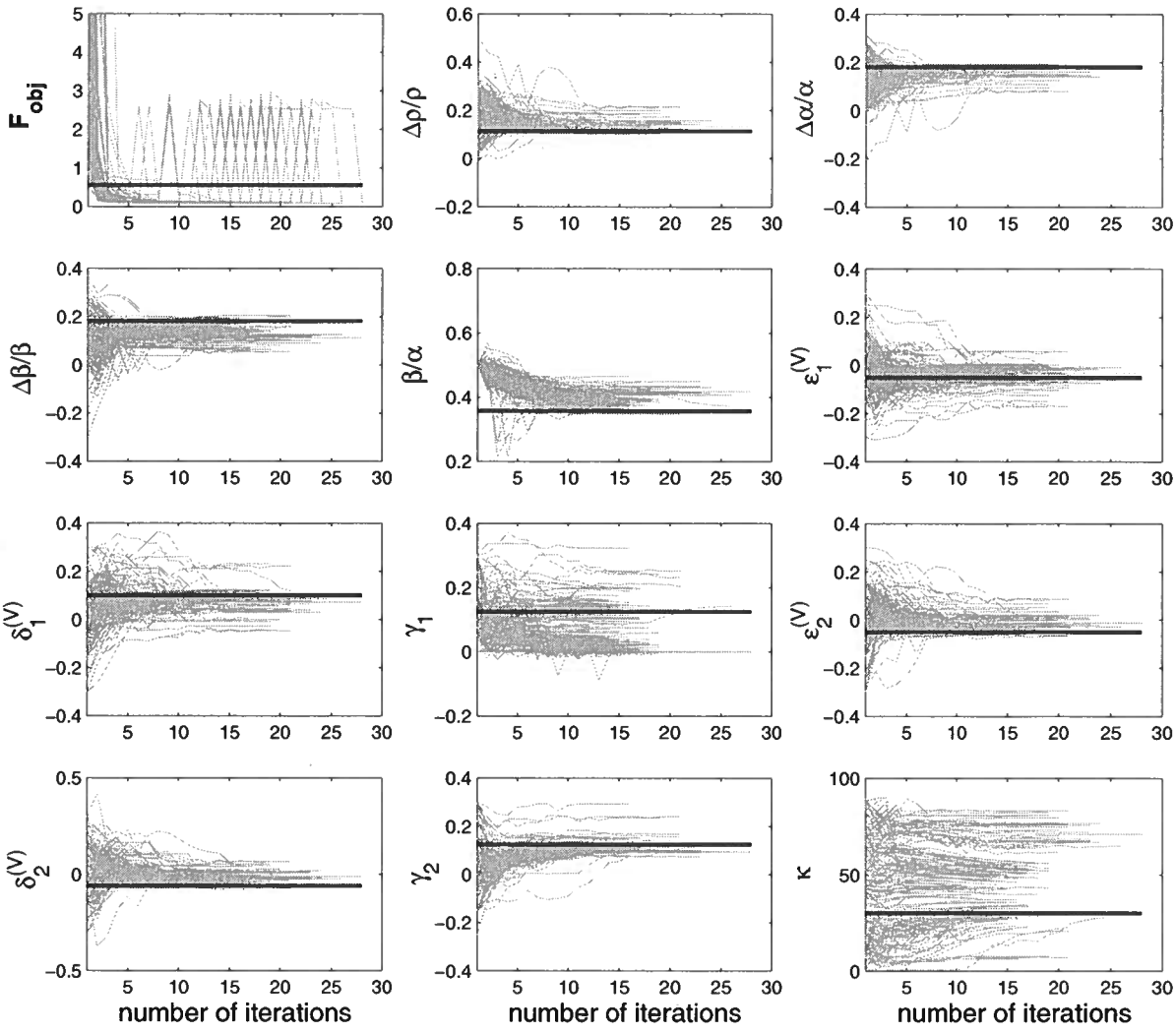

Figure 4.6. Inversion for the HTIxHTI model (Example 2). Evolution of the objective function F_{obj} and individual medium parameters with increasing number of iterations of 167 models characterized by $F_{obj} \leq 0.12$. The thick horizontal line in F_{obj} plot marks the threshold 0.55. The thick horizontal line in each parameter plot marks the true value of the corresponding parameter.

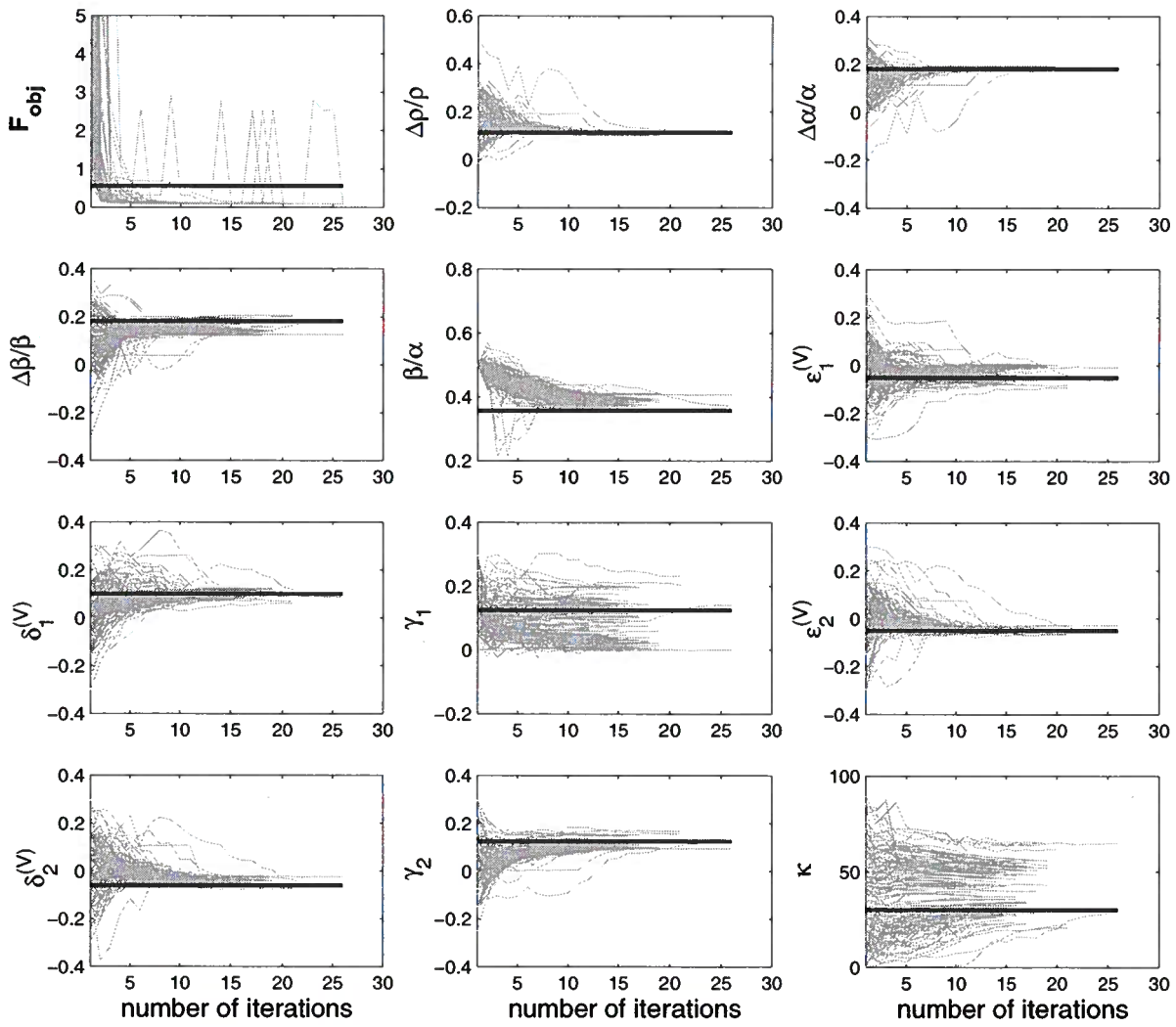

Figure 4.7. Inversion for the HTIxHTI model (Example 2). Evolution of the objective function F_{obj} and individual medium parameters with increasing number of iterations of 136 models corresponding to the global minimum $F_{obj} = 0.09$. The thick horizontal line in F_{obj} plot marks the threshold 0.55. The thick horizontal line in each parameter plot marks the true value of the corresponding parameter.

of $\frac{\Delta\rho}{\bar{\rho}}$, $\frac{\Delta\alpha}{\bar{\alpha}}$, $\epsilon_1^{(V)}$, $\epsilon_2^{(V)}$, $\delta_2^{(V)}$ and γ_2 can be obtained (together with the estimates of most of their combinations specified above). However, according to Figure 4.7, this method cannot lead to a complete recovery of all parameters of the HTIxHTI model.

An alternative way how to improve the results from Figure 4.4 is based on *a priori* information. A detailed study of the inverted models reveals that the most valuable *a priori* information is the angle κ. If κ were known within $\pm 5°$, it would lead to a complete and stable recovery of all parameters of the HTIxHTI model. Unfortunately, κ is usually one of the parameters to be recovered. However, if the reservoir thickness is sufficient, κ can be estimated from shear-wave traveltimes and polarizations, or from *P*-wave moveout analysis (Bakulin *et al.*, 2000a). A natural replacement for κ is the parameter γ_1, since this is the only parameter that can lead to a successful recovery of κ (see Figure 4.7). However, this parameter is not sufficient by itself. Another parameter that may be supplied *a priori*, in addition to γ_1, is the ratio $\frac{\bar{\beta}}{\bar{\alpha}}$. (There are some other possibilities, although less practical.) Figure 4.8 shows all 41 models recovered using the threshold criterion (i.e., models from Figure 4.4) and the following *a priori* information: $\gamma_1 \in (0.10; 0.15)$ and $\frac{\bar{\beta}}{\bar{\alpha}} \in (0.30; 0.40)$ (these parameters are thus known with $15\% - 20\%$ accuracy). Figure 4.8 and the sixth columns of Table 4.2 and Table 4.3 show that, provided these constraints of the parameters γ_1 and $\frac{\bar{\beta}}{\bar{\alpha}}$, the remaining medium parameters can be estimated with significantly improved accuracy. In practice, additional estimates obtained from the corresponding linear inversion for certain medium parameters or their combinations (using the same *a priori* information) can further support this result.

The fact that *a priori* knowledge of only one parameter (κ) is equivalent to *a priori* knowledge of two other parameters (γ_1 and $\frac{\bar{\beta}}{\bar{\alpha}}$), in terms of parameter estimation, suggests that the number of known parameters required for the inversion may depend on the magnitude of the anisotropy. For example, if the anisotropy becomes strong, the principal direction κ becomes better defined and less *a priori* information may be necessary. This is an example of how the performance of the nonlinear inversion may depend on the values of the model parameters, as discussed in Section 4.1 above.

In summary, the inversion for HTIxHTI-type models (and, possibly, all models of higher anisotropic symmetry) is feasible for good quality data and good data coverage. In order to obtain reliable estimates, however, the inversion should be supported by both the results obtained from the linear inversion and by *a priori* information about $\bar{\beta}/\bar{\alpha}$ and γ_1. If *a priori* information is not available, only certain combinations of the medium parameters can be recovered (Table 4.3). Nevertheless, when we provide necessary additional constraints, the nonlinear inversion yields significantly improved estimates to those of the linear inversion (see Table 4.2 and Table 3.7 for comparison of the results obtained from the nonlinear and linear inversions). The improvements are: 1) better resolution of the model (i.e., more model parameters can be often

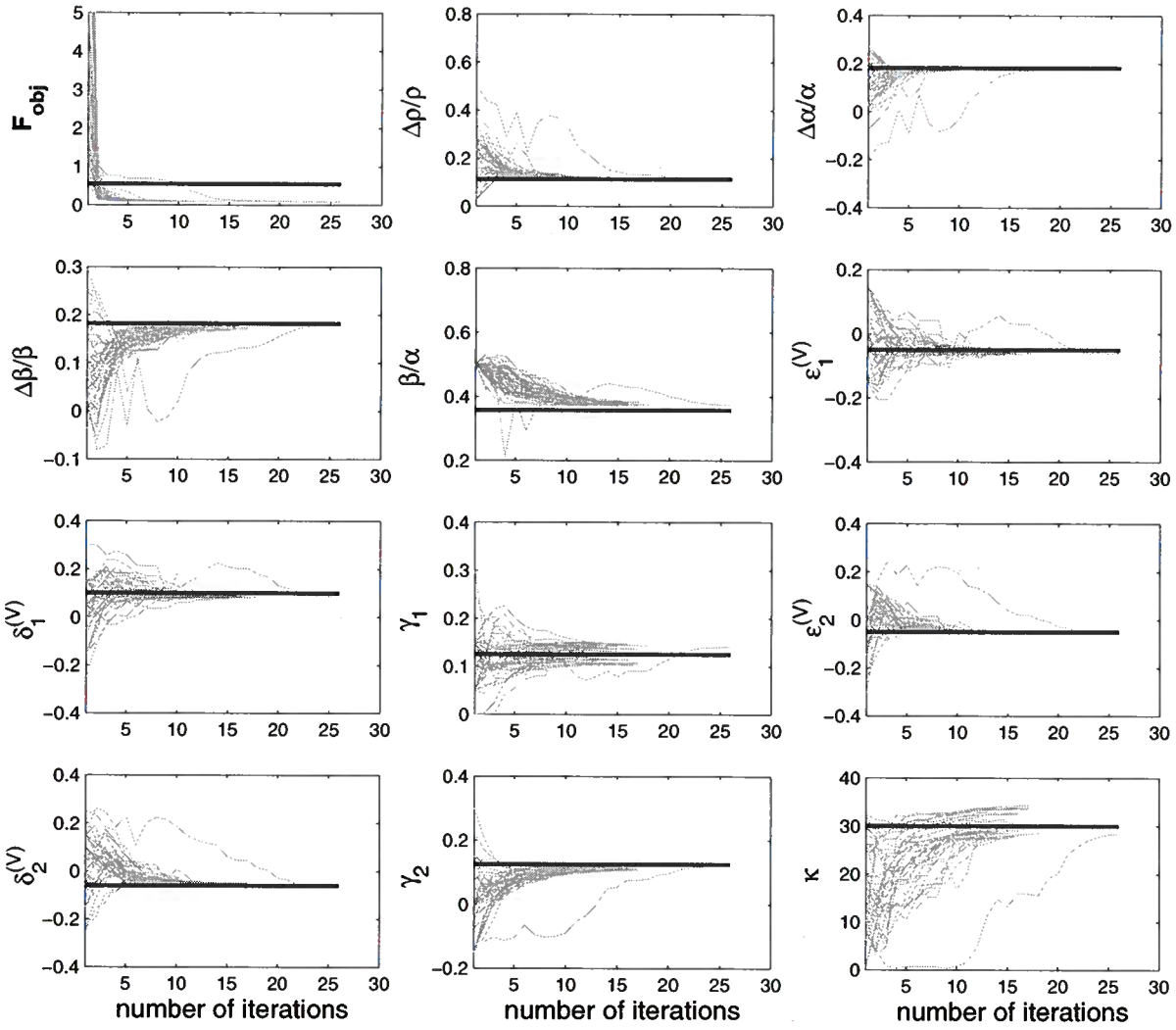

Figure 4.8. Inversion for the HTIxHTI model (Example 2). Evolution of the objective function F_{obj} and individual medium parameters with increasing number of iterations of 41 models picked from Figure 4.4, that also satisfy the following *a priori* information: $\gamma_1 \in (0.10; 0.15)$ and $\bar{\beta}/\bar{\alpha} \in (0.30; 0.40)$. The thick horizontal line in F_{obj} plot marks the threshold 0.55. The thick horizontal line in each parameter plot marks the true value of the corresponding parameter.

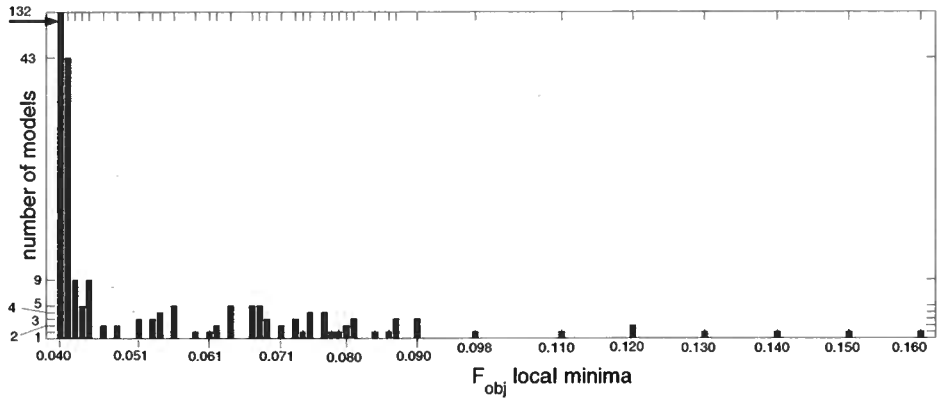

Figure 4.9. Distribution of recovered models (Example 3); the 276 models that fit the data (the threshold $F_{obj} = 0.20$) are more dispersed between the global minimum ($F_{obj} = 0.04$) and the threshold, indicating a more problematic model recovery than that in Example 2.

recover, such as $\epsilon_1^{(V)}$ and $\epsilon_2^{(V)}$), 2) higher accuracy of the inverted model parameters, and 3) less needed *a priori* information. This conclusion is quite general and also is applicable to most examples below.

4.3.3 Example 3: HTIxHTI model inversion using small- and moderate-incidence-angle reflections

In practice, large-incidence-angle reflection coefficients are often difficult to obtain, or their accuracy may be poor. Therefore it is of practical importance to understand how the loss of large incidence angles influences the results obtained in Example 2.

Here, I use the same HTIxHTI model as in Example 2, but the maximum incidence angle is reduced to 30° (from 45°). The azimuthal coverage for small and moderate incidence angles remains the same. The elimination of large incidence angles results in the loss of 375 data points.

I apply the same strategy as in Example 2 to invert this model. Figure 4.9 shows that the loss of large-incidence angle reflections results in a wider distribution of the models that fit the data than that in Figure 4.3, with more local minima (37) detected below the threshold (set at $F_{obj} = 0.20$). This clearly indicates that the inversion for this model is more problematic.

The analysis of the models corresponding to the global minimum reveals, as in the previous example, a theoretical possibility to recover the model parameters. Quite surprisingly, the models at the global minimum are recovered almost as well

	exact	$F_{obj} = 0.040$	$F_{obj} \leq 0.050$	$\beta/\bar{\alpha}$ and $\Delta\beta/\beta$ known
$\frac{\Delta\rho}{\bar{\rho}}$	0.113	0.107 ± 0.023	0.133 ± 0.056	0.102 ± 0.016
$\frac{\Delta\alpha}{\bar{\alpha}}$	0.182	0.189 ± 0.023	0.163 ± 0.056	0.194 ± 0.016
$\frac{\Delta\beta}{\bar{\beta}}$	0.182	0.180 ± 0.022	0.156 ± 0.051	0.182 ± 0.011
$\frac{\bar{\beta}}{\bar{\alpha}}$	0.358	0.377 ± 0.016	0.379 ± 0.023	0.380 ± 0.014
$\epsilon_1^{(V)}$	−0.050	-0.043 ± 0.020	-0.058 ± 0.048	-0.037 ± 0.020
$\delta_1^{(V)}$	0.100	0.085 ± 0.020	0.076 ± 0.040	0.087 ± 0.018
γ_1	0.125	0.106 ± 0.048	0.097 ± 0.050	0.098 ± 0.046
$\epsilon_2^{(V)}$	−0.050	-0.049 ± 0.018	-0.022 ± 0.052	-0.051 ± 0.013
$\delta_2^{(V)}$	−0.060	-0.057 ± 0.019	-0.036 ± 0.043	-0.056 ± 0.014
γ_2	0.125	0.119 ± 0.024	0.111 ± 0.029	0.119 ± 0.020
κ	30°	$38.5° \pm 12.4°$	$43.3° \pm 16.3°$	$39.7° \pm 12.3°$

Table 4.4. Inversion results for the HTIxHTI model (Example 3). The medium parameters (first column), their true values (second column), and their recovered values using: 1) only those models that correspond to the global minimum ($F_{obj} = 0.04$; third column), 2) the models from Figure 4.9 supplemented by the results from the linear inversion ($F_{obj} \leq 0.05$; fourth column), and 3) the models satisfying the threshold criterion ($F_{obj} \leq 0.20$) together with *a priori* estimates of $\Delta\beta/\bar{\beta} \in (0.16; 0.20)$ and $\bar{\beta}/\bar{\alpha} \in (0.30; 0.40)$ (fifth column). The error bars represent standard deviations.

as in Example 2 (compare the third column of Table 4.4 with the fifth column of Table 4.2). However, the recovered models corresponding to other local minima, even those close to the global minimum (in terms of F_{obj}), are broadly dispersed in the model space, far from the true model. Therefore, the *practical* recovery of the medium parameters is much more difficult than that in Example 2, where large-incidence-angle reflections are available.

As an example, using the estimates of $P_1^{(ABS)}$, $P_1^{(M)}$, $P_1^{(L)}$, $SS_1^{(ABS)}$, $SS_1^{(M)}$ and $SS_1^{(L)}$ obtained from the corresponding linear inversion as before, it is possible to reject all models with $F_{obj} > 0.050$. Despite this low value (i.e., the models with $F_{obj} \leq 0.050$ fit the data very well), still none of the individual medium parameters can be recovered reliably, see Figure 4.10 and Table 4.4 (fourth column). Only some of the more stable combinations introduced above can be recovered, such as $(\Delta\rho/\bar{\rho}+\Delta\alpha/\bar{\alpha})$, $(\gamma_1 - \gamma_2 \cos 2\kappa)$, $\gamma_2 \sin 2\kappa$, $(\delta_1^{(V)} - \epsilon_1^{(V)})$, $(\delta_2^{(V)} - \epsilon_2^{(V)})$, PS, PPsin and PSsin; see Figure 4.11 and Table 4.5 (third column).

It becomes clear at this point that *a priori* information is necessary for a more detailed model recovery. Even then, however, the model recovery is more complicated than that in Example 2. For instance, using the same *a priori* knowledge of $\frac{\bar{\beta}}{\bar{\alpha}}$ and

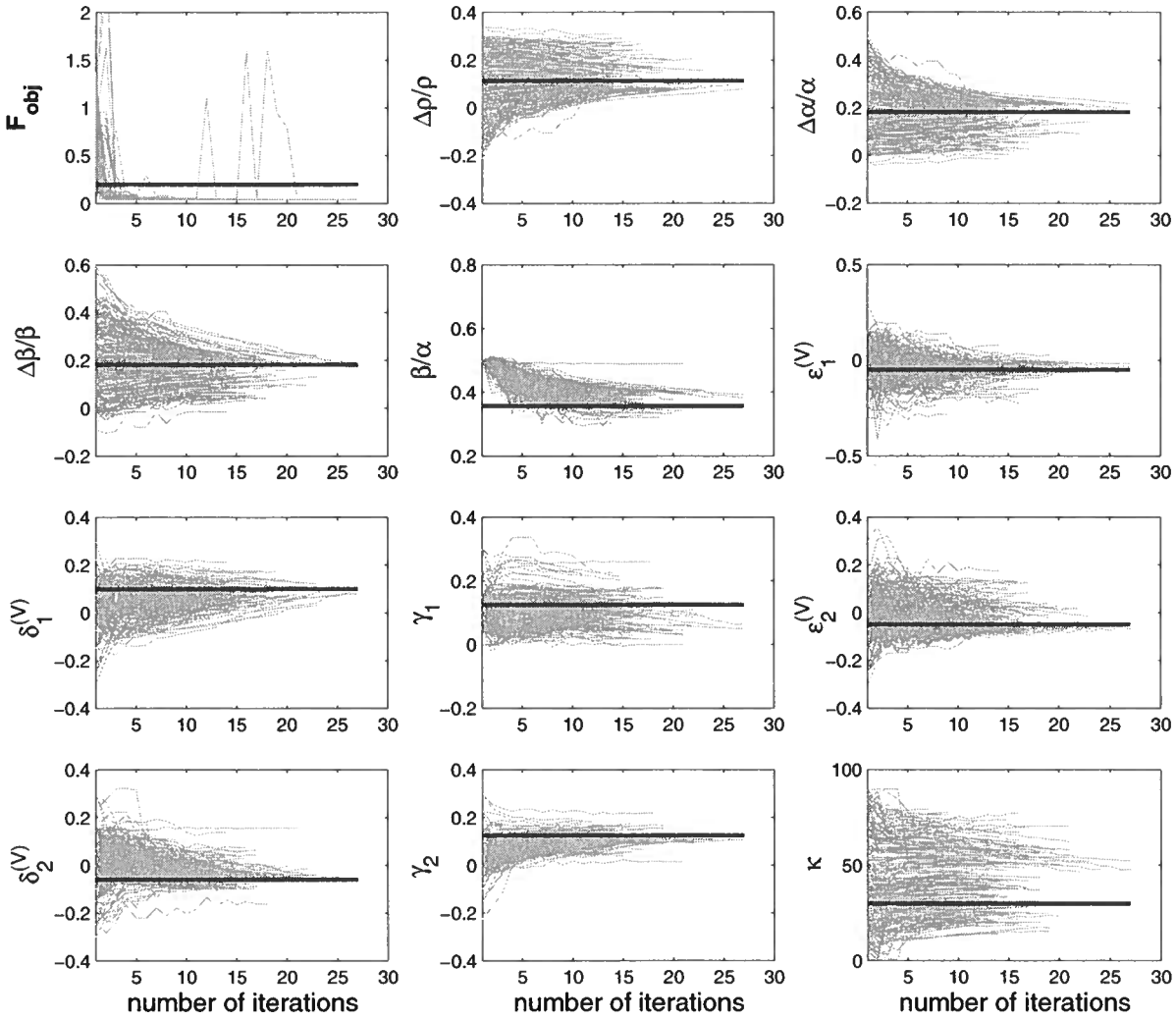

Figure 4.10. Inversion for the HTIxHTI model (Example 3). Evolution of the objective function F_{obj} and individual medium parameters with increasing number of iterations for the 202 models characterized by $F_{obj} \leq 0.050$. The thick horizontal line in F_{obj} plot marks the threshold 0.20. The thick horizontal line in each parameter plot marks the true parameter value. None of the parameters is recovered successfully.

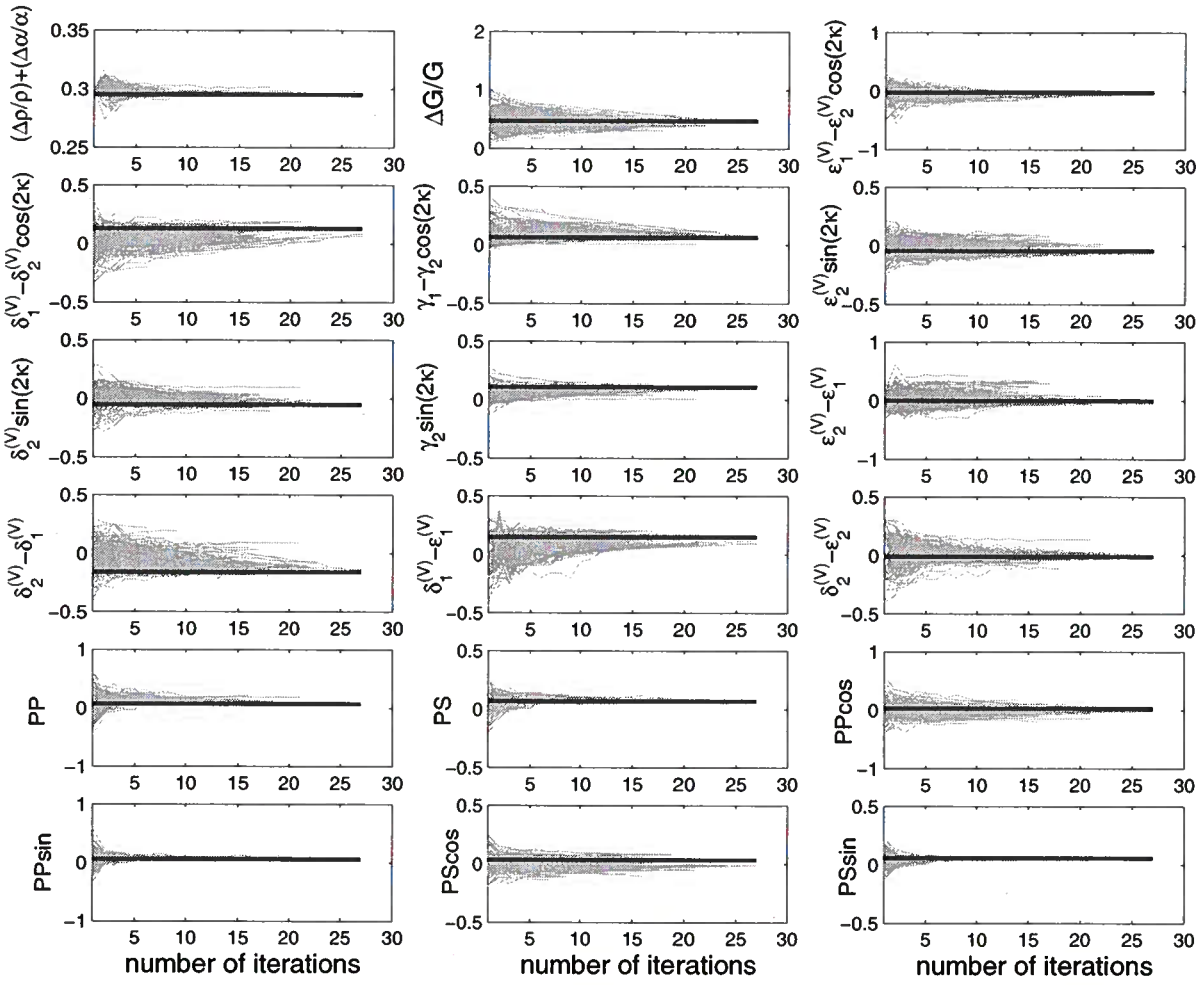

Figure 4.11. Inversion for HTIxHTI model (Example 3). Evolution of selected combinations of the medium parameters (as suggested by the linear inversion) from Figure 4.10 with increasing number of iterations. The thick horizontal lines denote the corresponding true values. Several of these combinations are recovered well.

	exact	$F_{obj} \leq 0.050$	$\Delta\beta/\beta$ and $\beta/\bar{\alpha}$ known
$\frac{\Delta\rho}{\bar{\rho}} + \frac{\Delta\alpha}{\bar{\alpha}}$	0.295	0.296 ± 0.001	0.296 ± 0.001
$\frac{\Delta G}{G}$	0.469	0.438 ± 0.049	0.458 ± 0.018
$\epsilon_1^{(V)} - \epsilon_2^{(V)} \cos 2\kappa$	−0.025	-0.049 ± 0.035	-0.030 ± 0.020
$\delta_1^{(V)} - \delta_2^{(V)} \cos 2\kappa$	0.130	0.088 ± 0.045	0.098 ± 0.036
$\gamma_1 - \gamma_2 \cos 2\kappa$	0.063	0.083 ± 0.025	0.074 ± 0.016
$\epsilon_2^{(V)} \sin 2\kappa$	−0.043	-0.023 ± 0.040	-0.046 ± 0.014
$\delta_2^{(V)} \sin 2\kappa$	−0.052	-0.034 ± 0.033	-0.050 ± 0.013
$\gamma_2 \sin 2\kappa$	0.108	0.094 ± 0.024	0.104 ± 0.011
$\epsilon_2^{(V)} - \epsilon_1^{(V)}$	0.000	0.036 ± 0.087	-0.014 ± 0.022
$\delta_2^{(V)} - \delta_1^{(V)}$	−0.160	-0.113 ± 0.065	-0.143 ± 0.022
$\delta_1^{(V)} - \epsilon_1^{(V)}$	0.150	0.134 ± 0.028	0.123 ± 0.019
$\delta_2^{(V)} - \epsilon_2^{(V)}$	−0.010	-0.014 ± 0.022	-0.006 ± 0.010
PP	0.068	0.090 ± 0.032	0.078 ± 0.009
PS	0.067	0.070 ± 0.014	0.069 ± 0.008
PPcos	0.034	-0.002 ± 0.062	0.014 ± 0.034
PPsin	0.059	0.072 ± 0.010	0.070 ± 0.006
PScos	0.034	0.004 ± 0.042	0.014 ± 0.030
PSsin	0.058	0.058 ± 0.006	0.061 ± 0.003

Table 4.5. Inversion results for the HTIxHTI model (Example 3). Selected combinations of the medium parameters (first column), their true values (second column) and their recovered values using the models from Figure 4.9 supplemented by the results of the linear inversion ($F_{obj} \leq 0.05$; third column), and using the models satisfying the threshold criterion ($F_{obj} \leq 0.20$) together with *a priori* estimates of $\Delta\beta/\bar{\beta} \in (0.16; 0.20)$ and $\bar{\beta}/\bar{\alpha} \in (0.30; 0.40)$ (fourth column). The error bars represent standard deviations.

γ_1 as in Example 2 does not lead to any significant improvement, and the results are similar to those from the previous paragraph (Table 4.4, fourth column). The essential additional information seems to be reasonable knowledge of one of the isotropic contrasts (unnecessary in Example 2). Figure 4.12 shows the results obtained with the following *a priori* information (82 models from Figure 4.9): $\bar{\beta}/\bar{\alpha} \in (0.30; 0.40)$ $[(\bar{\beta}/\bar{\alpha})_{true} = 0.356]$ and $\Delta\beta/\bar{\beta} \in (0.16; 0.20)$ $[(\Delta\beta/\bar{\beta})_{true} = 0.182]$. Figure 4.12 shows a good recovery of most of the medium parameters; see also Table 4.4 (fifth column) and Table 4.5 (fourth column). Again, the only unresolved parameters are γ_1 and κ. The poor resolution of these two parameters was indicated already in Example 2. A reasonable knowledge of γ_1 (with about 20% accuracy) removed the problem. As a consequence of the loss of large-incidence-angle reflections here, however, knowledge of γ_1 has to be almost exact (with accuracy no worse than $\pm 5\%$) to recover κ with the same accuracy as in Example 2. A more practical possibility to be considered is *a priori* knowledge of not only $\Delta\beta/\bar{\beta}$, $\bar{\beta}/\bar{\alpha}$ and γ_1, but also either $\delta_1^{(V)}$ or $\epsilon_1^{(V)}$. Then knowledge of these parameters with accuracy 15%-20% is sufficient for stable recovery of the misalignment angle κ also.

Example 3 illustrates an expected loss of resolution for a more limited angle coverage. Compared to Example 2, more *a priori* information is necessary to resolve the model; besides $\bar{\beta}/\bar{\alpha}$, the essential addition is knowledge of one of the isotropic contrasts (i.e., $\Delta\alpha/\bar{\alpha}$, $\Delta\beta/\bar{\beta}$ or $\Delta\rho/\bar{\rho}$). To recover the angle κ in practice, *a priori* knowledge of two anisotropy parameters of the incidence halfspace is also necessary (instead of just one as in Example 2).

With the loss of large-incidence-angle reflections, the output of the nonlinear inversion becomes remarkably similar to that of the linear inversion, with one exception: the nonlinear inversion provided quite good estimates of the parameters $\epsilon_1^{(V)}$ and $\epsilon_2^{(V)}$ (see Table 4.4, fifth column), whereas these parameters could not be recovered from the linear inversion. The linear inversion also predicts that these parameters are poorly constrained by data lacking large incidence angles. This difference in performance may have several explanations. First, the influence of the nonlinear terms of the reflection coefficients, which also constrains the parameters $\epsilon_1^{(V)}$ and $\epsilon_2^{(V)}$, may be nonnegligible. This, however, does not seem to be the explanation here since the nonlinear terms of the exact PP- and PS-wave reflection coefficients are small (usually much less than 10%) over the whole region of the incidence angles and azimuths used (i.e., the weak-contrast, weak-anisotropy condition is well satisfied for this model). Second, even the linearized approximations of the reflection coefficients contain "medium" and "large" incidence angle terms, associated with $\sin^3\phi$ and $\sin^2\phi\tan^2\phi$ [ϕ is the incidence angle, see equations (3.1) and (3.36)]; these terms were not used in the linear inversion in Chapter 3 but they are dependent on $\epsilon_1^{(V)}$ and $\epsilon_2^{(V)}$.

This argument seems to provide a reasonable explanation. For this model, the

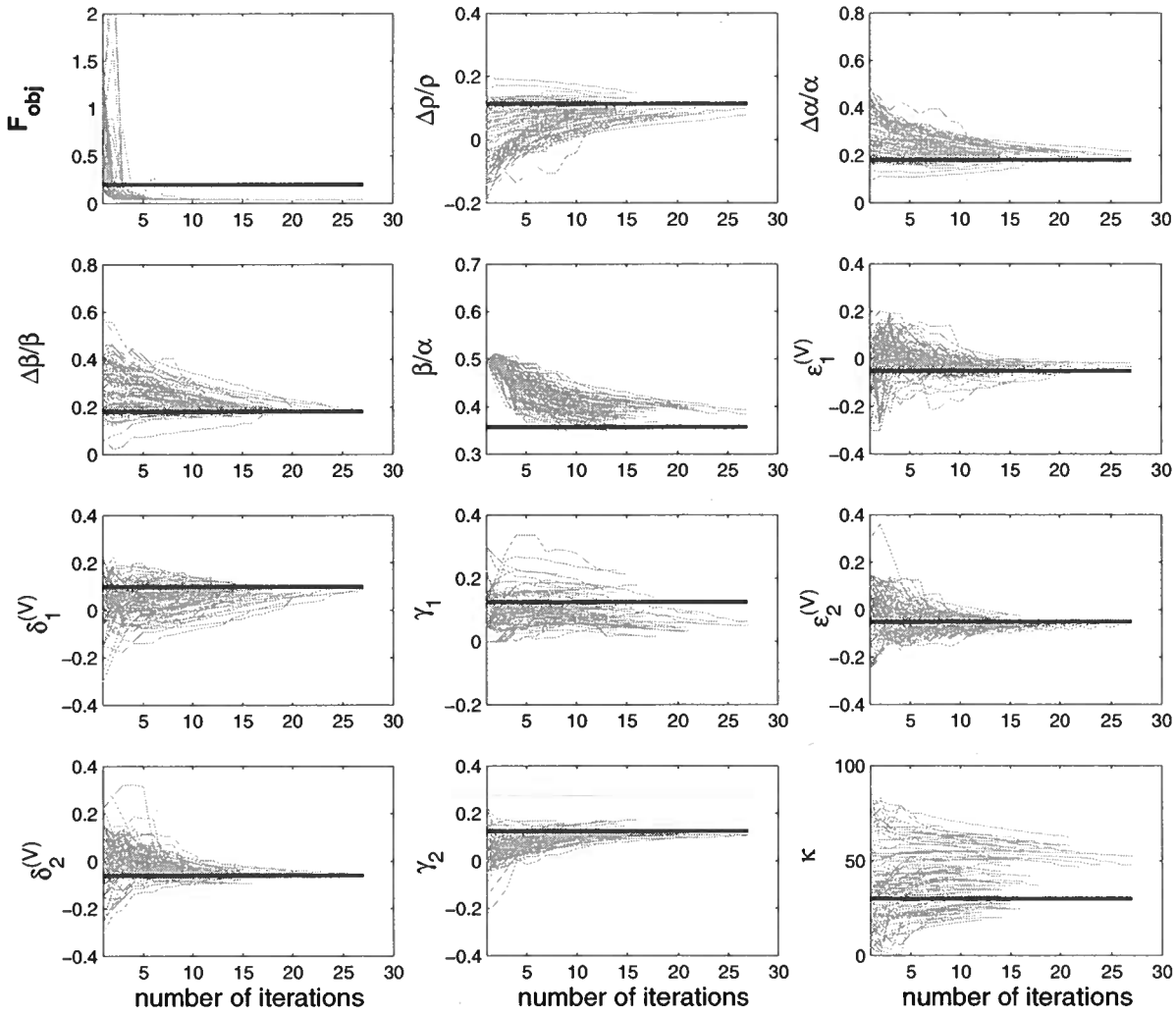

Figure 4.12. Inversion for the HTIxHTI model (Example 3). Evolution of the objective function F_{obj} and individual medium parameters with increasing number of iterations of 82 models picked from Figure 4.9, that also satisfy the following *a priori* information: $\Delta\beta/\bar{\beta} \in (0.16; 0.20)$ and $\bar{\beta}/\bar{\alpha} \in (0.30; 0.40)$. The thick horizontal line in F_{obj} plot marks the threshold 0.20. The thick horizontal line in each parameter plot marks the true parameter. The parameters γ_1 and κ remain unresolved.

medium- and large-incidence-angle terms contribute significantly to the reflection coefficients at incidence angles between 20°-30°. For instance, for certain azimuths and incidence angles close to 30°, the term associated with $\sin^2\phi\tan^2\phi$ in R_{PP} is about 1.3 times stronger than the term associated with $\sin^2\phi$ (i.e., the P-wave AVO gradient) used in the linear inversion.

Third, the nonlinear inversion uses both reflection coefficients R_{PS1} and R_{PS_2}, whereas the linear inversion uses only one projection of the reflection coefficients onto the SV direction [denoted as R_{PSV}, see equations (2.10)]. Such a projection may further reduce the amount of valuable information, especially its nonlinear component contained in the polarization vectors inside the expressions for the reflection coefficients R_{PS_1} and R_{PS2} (see the elimination of the *polarization angle* Φ in Section 2.2.2). Finally, the values of the parameters $\epsilon_1^{(V)}$ and $\epsilon_2^{(V)}$ can be also constrained largely by physics. Specifically, these parameters can attain only certain magnitudes, such that, together with the remaining medium parameters, the model is physically possible (i.e., the nonnegative strain energy condition is not violated in either the incidence or reflecting halfspace). Thus, even if only the remaining medium parameters are constrained by data, certain limitations on the values of the parameters $\epsilon_1^{(V)}$ and $\epsilon_2^{(V)}$ also exist.

In any case, good recovery of the parameters $\epsilon_1^{(V)}$ and $\epsilon_2^{(V)}$ should be understood as another example of how the *values* of the medium parameters may influence the performance of the nonlinear inversion (in this case positively). Assuming that the contribution of medium- and large-incidence-angle terms is essential for the recovery of $\epsilon_1^{(V)}$ and $\epsilon_2^{(V)}$, analysis of approximate reflection coefficients at those regions provides the following insight: in general, the recovery should become better constrained with increasing magnitude of the *difference* $(\epsilon_1^{(V)} - \epsilon_2^{(V)})$ and decreasing magnitude of the $\bar{\beta}/\bar{\alpha}$ ratio. The value of $(\epsilon_1^{(V)} - \epsilon_2^{(V)})$ should be also nonnegligible compared to the magnitudes of isotropic contrasts $\Delta\alpha/\bar{\alpha}$, $\Delta\beta/\bar{\beta}$, and $\Delta\beta/\bar{\beta}$, and also to the difference $(\delta_1^{(V)} - \delta_2^{(V)})$ (these conditions are well satisfied for the model in Example 2 and 3). More numerical testing needs to be carried out to verify this suggestion.

4.3.4 Example 4: HTIxHTI model: large data errors

Example 4 is another modification of Example 2. This time, the influence of *increasing error* in the data is investigated. The same model with the same data coverage as in Example 2 is used, except that now the data are contaminated by error that is twice as high (i.e., normally distributed random error of 20%). The inversion is accomplished by means of the same steps as before.

Without any details provided here, the results of this interesting example can be simply characterized as "in between" the results of Example 2 and Example 3. In particular, the amount of *a priori* information necessary to resolve this model

is, of course, higher than that in the case of small data errors (Example 2) but smaller than that in the case of missing large incidence angles (Example 3). For instance, reasonable knowledge (with about 20% accuracy) of one of the isotropic contrasts (such as $\Delta\beta/\bar{\beta}$), together with $\bar{\beta}/\bar{\alpha}$ and γ_1, allows for a good recovery of the remaining medium parameters, basically identical to that reported in Example 2 with *a priori* knowledge of $\bar{\beta}/\bar{\alpha}$ and γ_1 only (see the sixth row of Table 4.2). (Similar results can be also obtained even without knowledge of $\Delta\beta/\bar{\beta}$, but the inversion has to be supported by results of the linear inversion, using the estimates of P_0, $P_1^{(ABS)}$, $P_1^{(M)}$, $P_1^{(L)}$, $SS_1^{(ABS)}$, $SS_1^{(M)}$ and $SS_1^{(L)}$ in the same way as discussed in detail in Example 2.)

Example 4 suggests that the inversion may be acceptable even if the data are contaminated by relatively large random errors, as long as the data coverage is sufficient. In terms of resolution, stability and *a priori* information, the loss of data accuracy is less harmful than the loss of large-incidence-angle reflections. Therefore, it may be beneficial to include large-incidence-angle reflections in the inversion even if the corresponding error is relatively high. Of course, this conclusion holds only if the noise in data is random rather than systematic.

4.3.5 Example 5: HTI/HTI model

Example 5 is designed to study the consequences of eliminating the angle κ considering models in which the symmetry axes of the two HTI halfspaces are aligned. Thus, the misalignment angle $\kappa = 0°$ is known *a priori*. (See the corresponding linear inversion of the HTI/HTI model in Chapter 3.) The data coverage and the data error are identical to those used in Example 2. The model vector to be recovered is

$$\mathbf{m} = \left(\frac{\Delta\rho}{\bar{\rho}}, \frac{\Delta\alpha}{\bar{\alpha}}, \frac{\Delta\beta}{\bar{\beta}}, \frac{\bar{\beta}}{\bar{\alpha}}, \epsilon_1^{(V)}, \delta_1^{(V)}, \gamma_1, \epsilon_2^{(V)}, \delta_2^{(V)}, \gamma_2 \right). \tag{4.6}$$

The distribution of recovered models has basically the same character as that in Example 2 (Figure 4.3), including the values of the global minimum and threshold. Further analysis of the results shows, however, that the resolution for this model is much lower. Even if the data are of high quality, i.e., the models corresponding to the global minimum can be easily identified (such as those in Figure 4.7), only the isotropic contrasts $\Delta\rho/\bar{\rho}$, $\Delta\alpha/\bar{\alpha}$ and $\Delta\beta/\bar{\beta}$ [see equation (4.6)] can be recovered. This is not surprising, since this was already determined from the linear inversion in Chapter 3. Estimation of the *contrasts* (jumps) of the anisotropy parameters across the interface, however, should be possible.

Using the linear inversion (estimates of $P_1^{(ABS)}$, $P_1^{(M)}$, $P_1^{(L)}$, $SS_1^{(ABS)}$, $SS_1^{(M)}$ and $SS_1^{(L)}$ combinations, see Example 2), it is possible to lower the threshold to the same value as in Example 2 (i.e., $F_{obj} = 0.12$). Table 4.6 (third column) shows several

best-constrained parameters that can be recovered in this case. In Table 4.6, the parameters ΔPP and ΔPS are defined as

$$\begin{aligned} \Delta\text{PP} &= (\delta_1^{(V)} - \delta_2^{(V)}) + 8\left(\frac{\bar{\beta}}{\bar{\alpha}}\right)^2 (\gamma_1 - \gamma_2), \\ \Delta\text{PS} &= \frac{1}{2(1+\frac{\bar{\beta}}{\bar{\alpha}})}(\delta_1^{(V)} - \delta_2^{(V)}) + 2\left(\frac{\bar{\beta}}{\bar{\alpha}}\right)(\gamma_1 - \gamma_2). \end{aligned} \tag{4.7}$$

In agreement with the conclusions of Chapter 3, it is impossible to recover the anisotropy parameters individually. From Table 4.6 (third column), it is also difficult to estimate the differences $(\delta_1^{(V)} - \delta_2^{(V)})$ and $(\epsilon_1^{(V)} - \epsilon_2^{(V)})$ separately.

As in the previous examples, including *a priori* information can improve the results. Figure 4.13 shows the selected combinations from Table 4.6 recovered for 29 models using again the same *a priori* information as in Example 2 (i.e., knowledge of $\bar{\beta}/\bar{\alpha}$ and γ_1 with about 20% accuracy). This *a priori* information allows one to separate the difference $(\delta_1^{(V)} - \delta_2^{(V)})$ from $(\epsilon_1^{(V)} - \epsilon_2^{(V)})$, see the fourth column of Table 4.6. However, the resolution of the individual anisotropy parameters is still poor, and without additional constraints on either $\delta_1^{(V)}$ or $\epsilon_1^{(V)}$ their recovery is unreliable.

Example 5 provides clear evidence of decreasing resolution of the inversion for HTI models with uniform symmetry-axis orientation. Without any *a priori* information, only the isotropic contrasts and certain contrasts of the anisotropy parameters can be recovered. This is fully consistent with the prediction provided by the linear inversion in Chapter 3. More comprehensive *a priori* information can improve the model recovery; however, to resolve the model vector (4.6) completely, all $\bar{\beta}/\bar{\alpha}$, γ_1 and either $\delta_1^{(V)}$ or $\epsilon_1^{(V)}$ *a priori* estimates are necessary (again, in agreement with the linear inversion). If this information is available, however, the nonlinear inversion provides significantly improved model recovery compared to the linear inversion (see Table 4.6 in comparison with Table 3.5 showing the results of the linear inversion). Furthermore, based on the results of Example 3 above, additional loss of resolution should be expected with the loss of large-incidence-angle reflections. Then, an independent estimate of one of the isotropic contrasts may be necessary to constrain the inversion.

Finally, the typical characteristic of this inversion, a particularly large dispersion of individual anisotropy parameters coupled with well-focused estimates of their differences, may be used as an indicator of aligned symmetry axes.

4.3.6 Example 6: ORTHOxORTHO model

The next two examples demonstrate difficulties arising for lower-symmetry models with a larger number of parameters. The medium in Example 6 consists of two

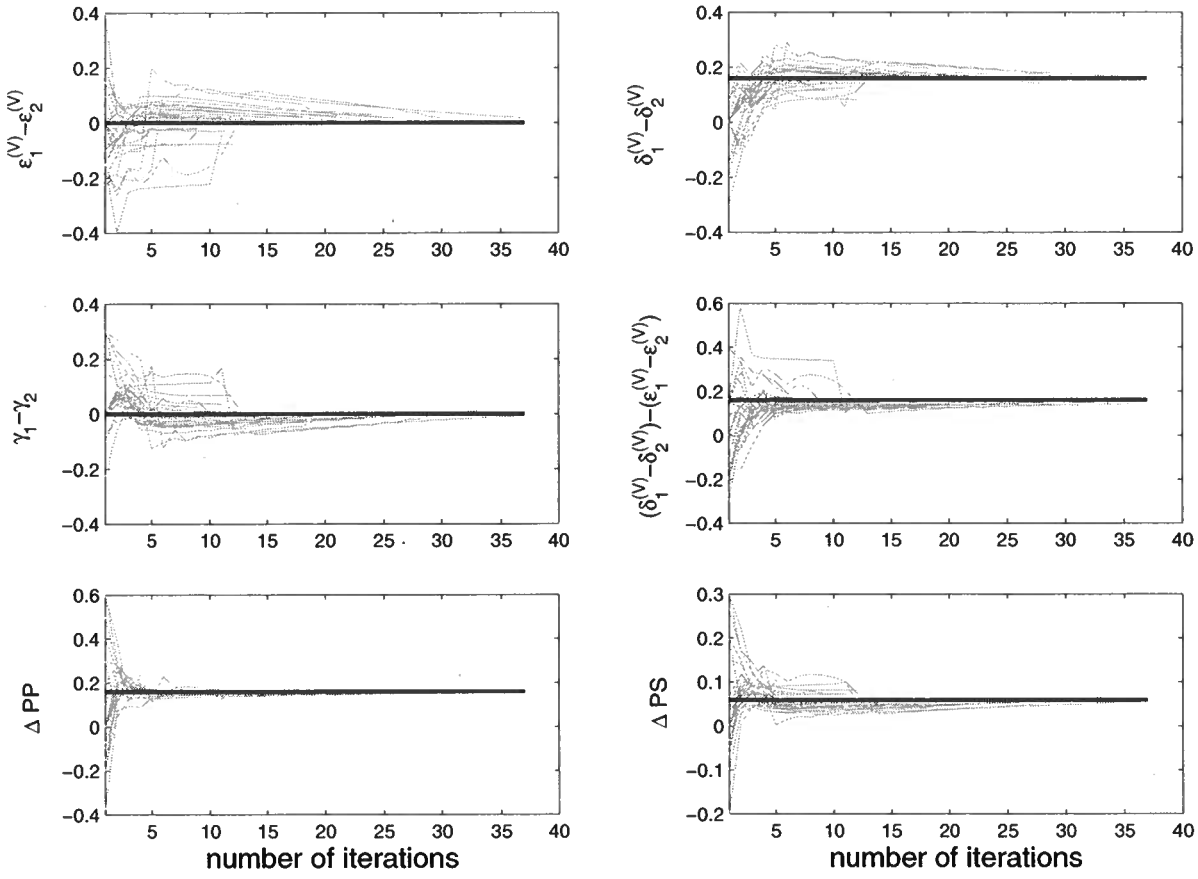

Figure 4.13. Inversion for the HTI/HTI model (Example 5). Evolution of the objective function F_{obj} and selected combinations of the medium parameters with increasing number of iterations of the 29 models with $F_{obj} \leq 0.55$ (threshold) and satisfying the following *a priori* information: $\bar{\beta}/\bar{\alpha} \in (0.30; 0.40)$ and $\gamma_1 \in (0.10; 0.15)$. The thick horizontal line in each parameter plot marks the true parameter value. See equations (4.7) for the definitions of ΔPP and ΔPS. All combinations shown on the plot are well recovered.

	exact	$F_{obj} \leq 0.12$	$F_{obj} \leq 0.55$ $\bar{\beta}/\bar{\alpha}$ and γ_1 known
$\frac{\Delta\rho}{\bar{\rho}}$	0.113	0.118 ± 0.008	0.114 ± 0.001
$\frac{\Delta\alpha}{\bar{\alpha}}$	0.182	0.180 ± 0.005	0.183 ± 0.001
$\frac{\Delta\beta}{\bar{\beta}}$	0.182	0.171 ± 0.022	0.177 ± 0.014
$\epsilon_1^{(V)} - \epsilon_2^{(V)}$	0.000	-0.035 ± 0.047	0.007 ± 0.022
$\delta_1^{(V)} - \delta_2^{(V)}$	0.160	0.137 ± 0.046	0.153 ± 0.017
$\gamma_1 - \gamma_2$	0.000	0.005 ± 0.022	0.001 ± 0.018
$(\delta_1^{(V)} - \delta_2^{(V)}) - (\epsilon_1^{(V)} - \epsilon_2^{(V)})$	0.160	0.141 ± 0.016	0.146 ± 0.006
ΔPP	0.160	0.144 ± 0.016	0.154 ± 0.004
ΔPS	0.059	0.053 ± 0.012	0.057 ± 0.007

Table 4.6. Inversion results for the HTI/HTI model (Example 5). Isotropic contrasts and selected combinations of the medium parameters (first column), their true values (second column), their recovered values using the results of the linear inversion ($F_{obj} \leq 12$, third column) and using the threshold criterion ($F_{obj} \leq 0.55$) together with *a priori* estimates of $\bar{\beta}/\bar{\alpha} \in (0.30; 0.40)$ and $\gamma_1 \in (0.10; 0.15)$. The error bars represent standard deviations.

orthorhombic halfspaces (the same as in the ORTHO/ORTHO model from Chapter 3; see Figure 3.3 for the medium parameters of the halfspaces). The vertical symmetry planes of the halfspaces are misaligned by the angle $\kappa = 30°$. The model vector now has 19 components and is defined as

$$\mathbf{m} = \left(\frac{\Delta\rho}{\bar{\rho}}, \frac{\Delta\alpha}{\bar{\alpha}}, \frac{\Delta\beta}{\bar{\beta}}, \frac{\bar{\beta}}{\bar{\alpha}}, \epsilon_1^{(1)}, \epsilon_1^{(2)}, \delta_1^{(1)}, \delta_1^{(2)}, \delta_1^{(3)}, \right. \tag{4.8}$$
$$\left. \gamma_1^{(1)}, \gamma_1^{(2)}, \epsilon_2^{(1)}, \epsilon_2^{(2)}, \delta_2^{(1)}, \delta_2^{(2)}, \delta_2^{(3)}, \gamma_2^{(1)}, \gamma_2^{(2)}, \kappa\right),$$

where the isotropic contrasts are defined by equations (3.4) and (3.7), and the anisotropy parameters $\gamma_I^{(1)}$ and $\gamma_I^{(2)}$ are

$$\gamma_I^{(1)} \equiv \frac{A_{66}^{(I)} - A_{55}^{(I)}}{2A_{55}^{(I)}}, \tag{4.9}$$

$$\gamma_I^{(2)} \equiv \frac{A_{66}^{(I)} - A_{44}^{(I)}}{2A_{44}^{(I)}}. \tag{4.10}$$

Here, the $A_{ij}^{(I)}$ are the density-normalized stiffness tensor elements [see equation (2.11)], and $I = 1, 2$ represent the incidence and reflecting halfspaces, respectively. The remaining anisotropy parameters are defined in equations (2.15), (2.16) and (2.21)-(2.23).

The results of the linear inversion in Chapter 3 indicate that the parameter estimation for orthorhombic media is quite difficult. This difficulty holds as well for the nonlinear inversion. Attempts to recover the model vector from equation (4.8) without any *a priori* information entirely failed. Also, these attempts could not help to identify *a priori* information necessary to properly constrain the inversion. Therefore, the inversion below is based on the assumptions used to invert for the parameters of the ORTHO/ORTHO model in Chapter 3 (linear inversion).

The following *a priori* information was incorporated in phases 1 and 2 of the inversion: $\bar{\beta}/\bar{\alpha} \in (0.53; 0.58)$ ($\bar{\beta}/\bar{\alpha}_{(true)} = 0.56$), $\Delta\alpha/\bar{\alpha} \in (0.27; 0.29)$ ($\Delta\alpha/\bar{\alpha}_{(true)} = 0.286$), $\delta_1^{(1)} \in (-0.21; -0.19)$ ($\delta_{1(true)}^{(1)} = -0.20$), $\delta_1^{(2)} \in (0.09; 0.11)$ ($\delta_{1(true)}^{(2)} = 0.10$), $\gamma_1^{(1)} \in (0.14; 0.16)$ ($\gamma_{1(true)}^{(1)} = 0.15$) and $\gamma_1^{(2)} \in (0.03; 0.07)$ ($\gamma_{1(true)}^{(1)} = 0.05$). Clearly, these parameters are presumed to be known with high accuracy. The remaining anisotropy parameters of the incidence halfspace are constrained more loosely: $\epsilon_1^{(1)} \in (-0.19; -0.11)$ ($\epsilon_{1(true)}^{(1)} = -0.15$), $\epsilon_1^{(2)} \in (0.11; 0.19)$ ($\epsilon_{1(true)}^{(2)} = 0.15$) and $\delta_1^{(3)} \in (0.0; 0.25)$ ($\delta_{1(true)}^{(3)} = 0.15$). No constraints are used for the other medium parameters. The focus of the inversion is on the recovery of the remaining isotropic contrasts ($\Delta\rho/\bar{\rho}$ and $\Delta\beta/\bar{\beta}$) and the anisotropy parameters of the reflecting halfspace

(i.e., a reservoir of orthorhombic symmetry).

The best results were achieved when the inversion was combined with stable estimates of $P_1^{(ABS)}$, $P_1^{(M)}$, $P_1^{(L)}$, $SS_1^{(ABS)}$, $SS_1^{(M)}$ and $SS_1^{(L)}$ provided by the linear inversion (carried out prior to the nonlinear inversion), as in the previous examples. In that case, only the following parameters were recovered acceptably (see Table 4.7, the parameters known *a priori* are not shown): $\Delta\rho/\bar{\rho}$, $\Delta\beta/\bar{\beta}$, $\epsilon_2^{(1)}$, $\epsilon_2^{(2)}$ and κ. Also the recovery of the following combinations of the medium parameters was successful: $(\Delta\rho/\bar{\rho}+\Delta\alpha/\bar{\alpha})$, $\Delta G/\bar{G}$, $(\delta_1^{(3)}+\epsilon_1^{(2)}-\epsilon_1^{(1)})$, $(\epsilon_1^{(2)}-\epsilon_2^{(2)})$, $\gamma_2^{(S)}$, $\mathrm{PP}^{(\mathrm{ortho})}$ and $\mathrm{PS}^{(\mathrm{ortho})}$, where $\gamma_2^{(S)} \approx \gamma_2^{(1)} - \gamma_2^{(2)}$ (in weak-anisotropy approximation) is defined by equation (2.17) and

$$\begin{aligned} \mathrm{PP}^{(\mathrm{ortho})} &= (\delta_2^{(2)} - \delta_1^{(2)}) + 8\left(\frac{\bar{\beta}}{\bar{\alpha}}\right)^2 \gamma_2^{(S)}, \\ \mathrm{PS}^{(\mathrm{ortho})} &= \frac{1}{2(1+\frac{\bar{\beta}}{\bar{\alpha}})}(\delta_2^{(2)} - \delta_1^{(2)}) + 2\left(\frac{\bar{\beta}}{\bar{\alpha}}\right)\gamma_2^{(S)}. \end{aligned} \tag{4.11}$$

Notice a bias in the estimates of $\epsilon_2^{(2)}$ and $(\epsilon_1^{(2)} - \epsilon_2^{(2)})$. These estimates are also the least stable ones. Neither the parameters $\delta_2^{(1)}$, $\delta_2^{(2)}$, nor their difference $(\delta_2^{(1)} - \delta_2^{(2)})$ (suggested by the linear inversion as a more stable combination) could be estimated with sufficient accuracy. As expected from the linear inversion, inversion for the parameter $\delta_2^{(3)}$ also failed.

Further improvement of the results from Table 4.7 seems to be possible only by adding *a priori* information about one of the anisotropy parameters of the *reflecting* halfspace (i.e., the reservoir). The numerical tests indicate that additional knowledge of, for example, $\delta_2^{(1)}$, $\delta_2^{(2)}$, $\gamma_2^{(1)}$, or $\gamma_2^{(2)}$, or possibly the difference $(\gamma_2^{(1)} - \gamma_2^{(2)})$, could result in the complete model recovery. This is in agreement with the results of the linear inversion. In practice, knowledge of the shear wave splitting parameter within the reservoir $\gamma_2^{(S)} \approx \gamma_2^{(1)} - \gamma_2^{(2)}$ could be sometimes available.

In any case, a complete inversion for the ORTHOxORTHO model is a difficult task. Similar difficulties can be expected for any other models with an orthorhombic reflecting halfspace (such as isotropic/ORTHO, HTIxORTHO). Of course, higher anisotropic symmetry of the incidence halfspace reduces the amount of *a priori* information necessary for the inversion, increasing the feasibility of the inversion.

4.3.7 Example 7: ORTHO/ORTHO model

In Example 7, the same ORTHO/ORTHO model from Chapter 3 was used to study the influence of eliminating the misalignment angle κ (i.e., the symmetry planes above and below the reflector are aligned), as was done in Example 5 (see Figure 3.3

	$\frac{\Delta\rho}{\bar{\rho}}$	$\frac{\Delta\beta}{\bar{\beta}}$	$\epsilon_2^{(1)}$	$\epsilon_2^{(2)}$	κ
exact	0.182	0.462	−0.150	−0.25	30°
recovered	0.190 ± 0.007	0.458 ± 0.023	-0.145 ± 0.012	-0.216 ± 0.023	$30.5° \pm 2.1°$

	$\frac{\Delta\rho}{\bar{\rho}} + \frac{\Delta\alpha}{\bar{\alpha}}$	$\Delta G/\bar{G}$	$\delta_1^{(3)} + \epsilon_1^{(2)} - \epsilon_1^{(1)}$
exact	0.468	1.018	0.450
recovered	0.468 ± 0.001	1.018 ± 0.034	0.446 ± 0.016

	$\epsilon_1^{(2)} - \epsilon_2^{(2)}$	$\gamma_2^{(S)}$	$\mathrm{PP}^{(\mathrm{ortho})}$	$\mathrm{PS}^{(\mathrm{ortho})}$
exact	0.400	−0.132	−0.427	−0.179
recovered	0.371 ± 0.021	-0.128 ± 0.020	-0.429 ± 0.012	-0.178 ± 0.008

Table 4.7. Inversion results for the ORTHOxORTHO model (Example 6). The medium parameters (first row), their true values (second row), and their recovered values (third row) obtained by using the results of the linear inversion ($F_{obj} \leq 0.26$) and hard constraints on $\Delta\alpha/\bar{\alpha}$, $\bar{\beta}/\bar{\alpha}$, $\delta_1^{(1)}$, $\delta_1^{(2)}$, $\gamma_1^{(1)}$ and $\gamma_1^{(2)}$; see the text for more details. The error bars represent standard deviations. See equations (4.11) for the definitions of $\mathrm{PP}^{(\mathrm{ortho})}$ and $\mathrm{PS}^{(\mathrm{ortho})}$.

for the medium parameters of the halfspaces). The model vector

$$\mathbf{m} = \left(\frac{\Delta\rho}{\bar{\rho}}, \frac{\Delta\alpha}{\bar{\alpha}}, \frac{\Delta\beta}{\bar{\beta}}, \frac{\bar{\beta}}{\bar{\alpha}}, \epsilon_1^{(1)}, \epsilon_1^{(2)}, \delta_1^{(1)}, \delta_1^{(2)}, \delta_1^{(3)}, \right. \\ \left. \gamma_1^{(1)}, \gamma_1^{(2)}, \epsilon_2^{(1)}, \epsilon_2^{(2)}, \delta_2^{(1)}, \delta_2^{(2)}, \delta_2^{(3)}, \gamma_2^{(1)}, \gamma_2^{(2)}\right) \tag{4.12}$$

is a reduced version of the model vector from equation (4.8), where it is known *a priori* that $\kappa = 0$. This reduction of the number of model parameters should result in a more stable inversion. On the other hand, as suggested by Example 5 and the linear inversion, the alignment of the symmetry planes results in lower resolution, since only the contrasts of the medium parameters are well constrained. However, none of these expectations is quite met. As in the previous example, the recovery of the model was not successful without using the same hard constraints on certain medium parameters of the incidence halfspace as in Example 6. With these constraints, the resolution is similar to that in Example 6, and the accuracy of the inverted parameters is only slightly higher than that in Table 4.7.

By comparing the results from Table 4.7 with the results obtained from the corresponding linear inversion in Table 3.9, one can see again that the nonlinear inversion is more accurate and yields higher resolution. For this model, however,

the nonlinear inversion requires just as much *a priori* information as does the linear inversion.

Examples 6 and 7 reveal the limitations of the joint inversion of the PP- and PS-wave reflection coefficients for orthorhombic and lower-symmetry models.

4.3.8 Example 8: Erroneous calibration of the reflection coefficients

The last two examples attempt to address, albeit in a simplistic way, two potential problems in practical applications of the inversion. Example 8 deals with the problem of erroneously calibrated reflection coefficients. Even if the reflection coefficients are correctly recovered from the reflected amplitudes in the relative sense, it is still necessary to ascertain their absolute correctness. In practice, this is done by using various wavelet extraction methods and numerical modeling, using information obtained from NMO analysis, well-log or VSP data, and using various empirical relationships based on rock physics [see, for example, Dahl & Ursin (1992), Mallick (1995; 1999) and Cambois (2000)]. A natural question to ask is what happens with the inversion if the calibration factor is determined with a significant error.

Here, I use the same HTIxHTI model as in Example 2, with the same data coverage and error contamination. However, the exact (correct) R_{PP}, R_{PS_1} and R_{PS_2} reflection coefficients computed for the HTIxHTI model are multiplied by a constant factor of two, prior to being contaminated with a 10% random error. The mean amplitude of the synthetic data is thus twice as high as the correct value (which still provides possible values of the reflection coefficients characterizing a strong-contrast interface with P-wave AVO intercept close to 0.3).

The generated data are then inverted in exactly the same way as in Example 2 to recover the model vector $\mathbf{m}$ [equation (4.4)]. The distribution of the inverted models is similar to that in Example 2 (Figure 4.3), but the absolute values of the global minimum ($F_{obj} = 0.38$), threshold ($F_{obj} = 1.80$) and all local minima are generally higher.

More interesting is Figure 4.14 (analogous to Figure 4.7), which contains 137 recovered models corresponding to the global minimum. In terms of the character of convergence, stability and resolution of the individual medium parameters, Figure 4.14 is similar to Figure 4.7 (see also Table 4.8 in comparison with Table 4.2). The principal difference is a strong bias in the contrasts $\Delta\rho/\bar{\rho}$ and $\Delta\alpha/\bar{\alpha}$. A nonnegligible but somewhat smaller bias can be seen in the $\delta_1^{(V)}$ and γ_2 estimates, and a weak bias is also detected in the estimate of $\delta_2^{(V)}$. In contrast to the strongly biased parameters $\Delta\rho/\bar{\rho}$ and $\Delta\alpha/\bar{\alpha}$, the estimates of $\Delta\beta/\bar{\beta}$, $\epsilon_1^{(V)}$ and $\epsilon_2^{(V)}$ are not biased at all. Hence, as long as the reflection coefficients are recovered with correct *relative* variations, the parameters $\Delta\beta/\bar{\beta}$, $\epsilon_1^{(V)}$, $\epsilon_2^{(V)}$ and possibly some other anisotropy parameters may not be too sensitive to the calibration factor.

	exact	$F_{obj} = 0.38$
$\frac{\Delta\rho}{\bar{\rho}}$	0.113	0.325 ± 0.003
$\frac{\Delta\alpha}{\bar{\alpha}}$	0.182	0.283 ± 0.002
$\frac{\Delta\beta}{\bar{\beta}}$	0.182	0.186 ± 0.005
$\frac{\bar{\beta}}{\bar{\alpha}}$	0.358	0.390 ± 0.004
$\epsilon_1^{(V)}$	-0.050	-0.048 ± 0.006
$\delta_1^{(V)}$	0.100	0.189 ± 0.007
γ_1	0.125	0.181 ± 0.027
$\epsilon_2^{(V)}$	-0.050	-0.049 ± 0.001
$\delta_2^{(V)}$	-0.060	-0.077 ± 0.002
γ_2	0.125	0.202 ± 0.001
κ	$30.0°$	$37.4° \pm 2.5°$

Table 4.8. Inversion results for the HTIxHTI model with erroneous calibration (Example 8). The medium parameters (first column), their true values (second column), and their recovered values from Figure 4.14. The error bars represent standard deviations.

Strong bias in the parameters $\Delta\rho/\bar{\rho}$ and $\Delta\alpha/\bar{\alpha}$ is expected since the PP-wave AVO intercept, which depends on these two parameters only [see equation (3.2)], is twice as high as the correct value. The PP- and PS-wave AVO gradients and large-incidence-angle terms are also distorted by the same factor, but they are controlled by more medium parameters. Hence, those parameters should be recovered with generally smaller bias than are the parameters $\Delta\rho/\bar{\rho}$ and $\Delta\alpha/\bar{\alpha}$.

More tests have to be performed to explain why the estimates of the parameters $\epsilon_1^{(V)}$, $\epsilon_2^{(V)}$ and $\Delta\beta/\bar{\beta}$ are not biased. However, the fact that these parameters control the reflection coefficients generally at larger incidence angles suggests that the error in calibration factor mostly influences the medium parameters that dominate the small- and moderate-incidence-angle reflections.

The key to the detection and elimination of an erroneous calibration factor degrading the inversion results seems to be, as before, *a priori* information. From Figure 4.14, mainly knowledge of the contrast $\Delta\rho/\bar{\rho}$ or $\Delta\alpha/\bar{\alpha}$, or P-wave impedance [$\approx 0.5(\Delta\rho/\bar{\rho} + \Delta\alpha/\bar{\alpha})$, see equation (3.2)] can be used to calibrate the reflection coefficients. Also *a priori* estimates (not necessarily highly accurate) of $\Delta G/\bar{G}$, $\delta_1^{(V)}$ or $(\delta_1^{(V)} - \epsilon_1^{(V)})$ are sufficient to detect an error in calibration factor. Note that the difference $(\delta_1^{(V)} - \epsilon_1^{(V)})$ is close to the parameter η (Alkhalifah & Tsvankin, 1995), which can be estimated from moveout analysis.

It may happen that it is difficult to fit the data and remain consistent with

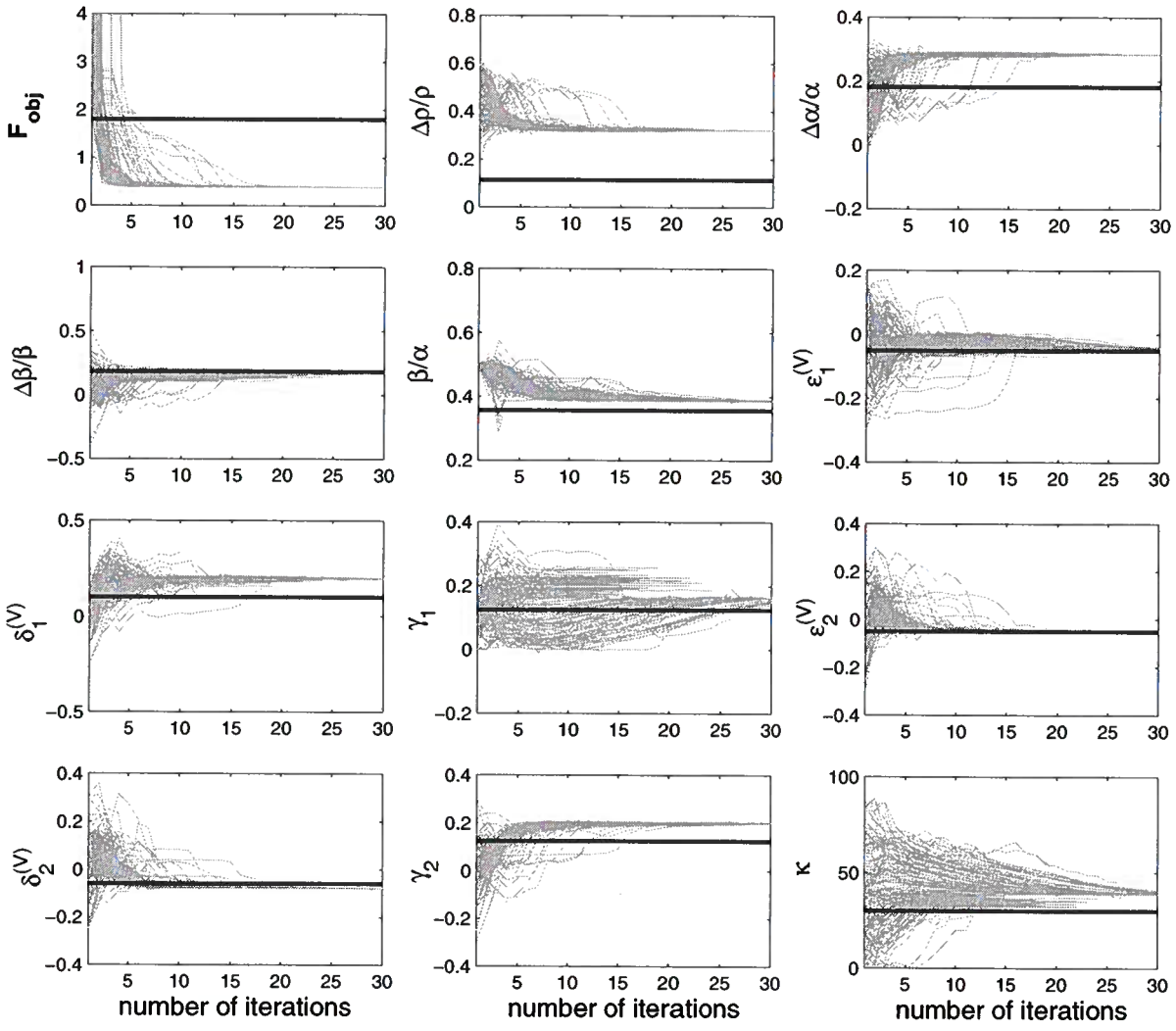

Figure 4.14. Inversion for the HTIxHTI model with erroneous calibration (Example 8). Evolution of the objective function F_{obj} and individual medium parameters with increasing number of iterations for 137 models corresponding to the vicinity of the global minimum $F_{obj} = 0.38$. The thick horizontal line in the F_{obj} plot marks the threshold 1.80. The thick horizontal line in each parameter plot marks the true parameter value. Notice the biased estimates of $\Delta\rho/\bar{\rho}$, $\Delta\alpha/\bar{\alpha}$, $\bar{\beta}/\bar{\alpha}$, $\delta_1^{(V)}$ and γ_2.

certain choice of *a priori* information. For example, if the same *a priori* information as that in Example 2 [i.e., $\bar{\beta}/\bar{\alpha} \in (0.30; 0.40)$ and $\gamma_1 \in (0.10; 0.15)$] is used, not a single model can be found that both satisfies these *a priori* constraints and fits the data (i.e., $F_{obj} \leq 1.80$). Thus, the reflection coefficients can be calibrated in an iterative fashion, as if the calibration factor was another parameter to be recovered by the inversion. Of course, this process becomes more stable with increasing data accuracy and more extensive *a priori* information. A similar conclusion was drawn by Mallick (1995), who performed a nonlinear P-wave AVO inversion for isotropic media. In his inversion, Mallick obtained the correct calibration factor for the PP-wave reflection coefficient automatically during the data-fitting procedure, without any *a priori* information.

Finally, if the calibration factor is not determined properly, and the estimates of the medium parameters are biased (or the bias is uncertain), the inversion results can still be useful in the recovery of the relative spatial parameter variations (e.g., over an oil field), which can be important in reservoir characterization. A similar approach was used in the P-wave AVO inversion for isotropic media, for example, by Smith and Gidlow (1987), Ursin *et al.* (1996) and Kelly *et al.* (2000).

4.3.9 Example 9: Misinterpreted anisotropic symmetry

The final example demonstrates implications of misinterpreted anisotropic symmetry, when a wrong physical model is used in the inversion. This is another serious potential complication in applying the inversion to field data.

A) *Inversion using a higher anisotropic symmetry*

In this example, synthetic data are generated by using the ORTHOxORTHO model from Example 6. However, they are inverted as if the model was HTIxHTI in an attempt to recover the model vector $\mathbf{m}$ from equation (4.4) (Example 2). Such a wrong *a priori* choice of the physical model could be common in practice, when a simpler model is tried first to explain the data.

First strong indications of an erroneous physical model are evident in Figure 4.15. If the physical model was truly HTIxHTI (or sufficiently close to it), a similar character in the distribution as that in Figure 4.3 should be expected. The distribution in Figure 4.15 has several noticeable differences. First, the whole distribution is shifted significantly towards larger values along the horizontal axis ($F_{obj} = 1.55$ at the global minimum). This means that the data fit is much worse than that obtained using the ORTHOxORTHO model (where $F_{obj} = 0.20$ at the global minimum, see Example 6). For example, using the same approach as in all previous examples, the threshold can be determined at $F_{obj} = 0.70$. Clearly, no single model recovered fits the data with this accuracy. If the confidence in the data quality is high, as it should be in this kind

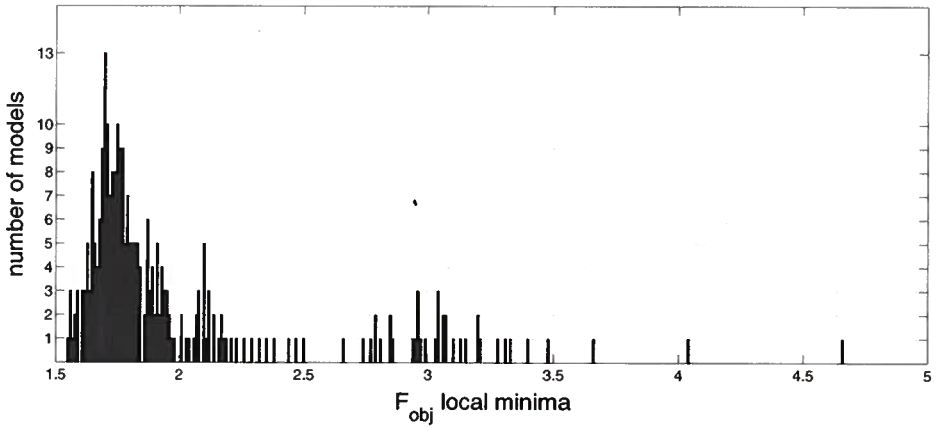

Figure 4.15. Distribution of recovered models obtained by using the erroneous anisotropy model (HTI instead of orthorhombic) (Example 9). Notice a different character of the distribution compared to that of the previous examples: the absolute values along both axes, the distribution shape, and the number of detected local minima.

of inversion, the HTIxHTI symmetry does not provide an acceptable explanation of the data and should be rejected at this point. The second difference between the distributions from Figure 4.3 and Figure 4.15 is the distribution shape; the global minimum $F_{obj} = 1.55$ of the distribution in Figure 4.15 does not correspond to the maximum number of recovered models, which is shifted to the approximate value $F_{obj} = 1.70$. Also, the minimum is not sharp (13 models in Figure 4.15 compared to 136 models in Figure 4.3); a larger number of local minima was detected.

Figure 4.16 shows the evolutions of the medium parameters for the models with $F_{obj} \leq 2.0$, i.e., the models contributing to the most significant part of the distribution from Figure 4.15 (204 models). The large dispersion of all medium parameters (namely the isotropic contrasts and $\bar{\beta}/\bar{\alpha}$) is another indication of the incorrectly chosen physical model. The parameter estimates are not accurate enough for any subset of the recovered models; i.e., the dispersion is high even for the models corresponding to a single local minimum.

The large dispersion in Figure 4.16 does not vanish with additional *a priori* information. If estimates of $\bar{\beta}/\bar{\alpha}$ and γ_1 are provided with the same accuracy as that in Example 2 (which guaranteed good results in Example 2), no significant improvement in the estimates is detected. Even $(\Delta\rho/\bar{\rho} + \Delta\alpha/\bar{\alpha})$, by all means the most stable parameter that can be recovered, exhibits large dispersion. The fact that the results cannot be improved by adding *any a priori* information is further evidence of the wrongly chosen physical model.

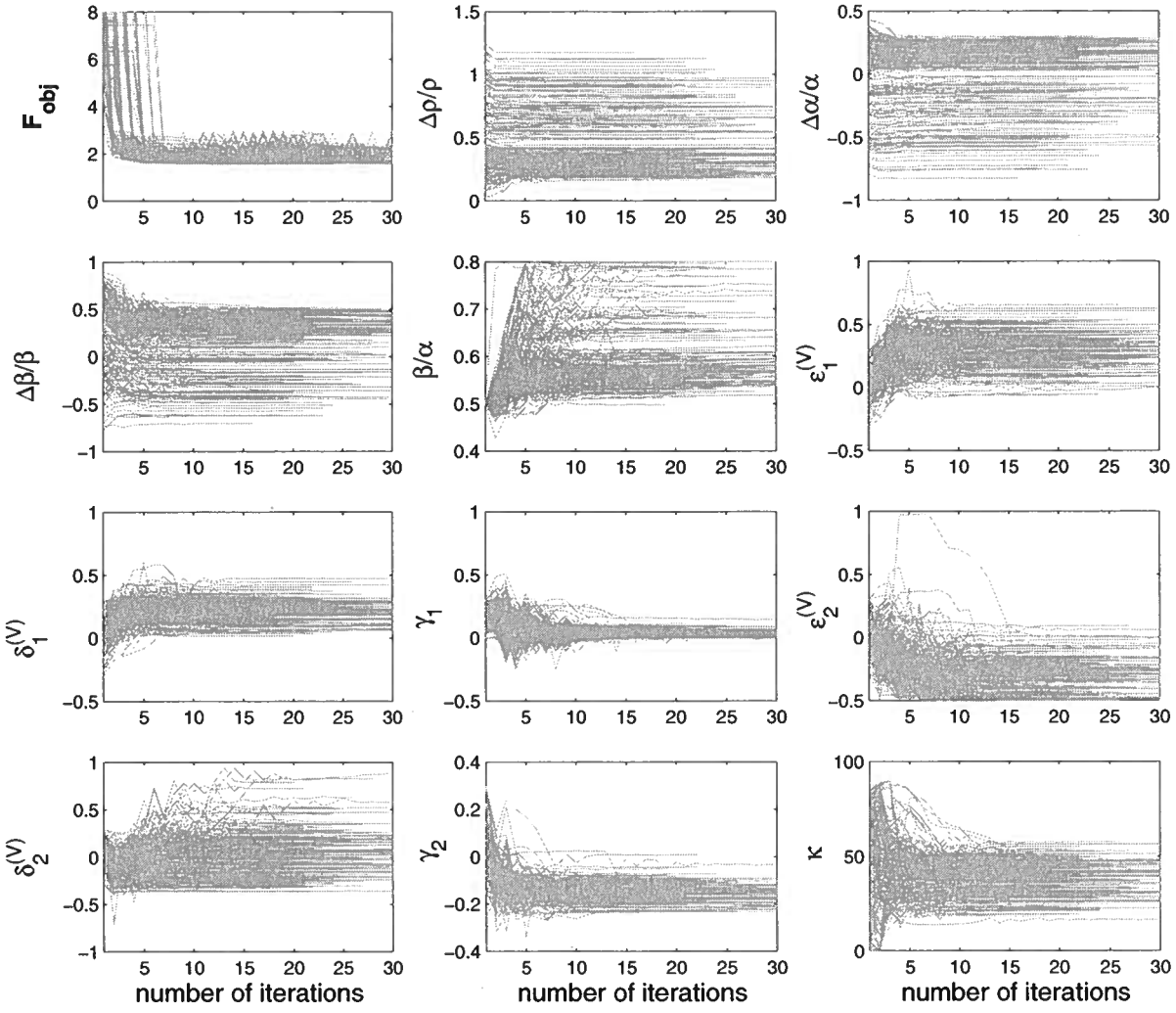

Figure 4.16. Inversion of data from the ORTHOxORTHO model using HTIxHTI symmetry (Example 9-A). Notice large dispersion of all medium parameters for the 204 recovered models. The dispersion of the estimates is not reduced by adding *a priori* information.

In summary, choosing an incorrect physical model is equivalent to adding a special type of systematic noise to the data that causes large dispersion of all estimates, and even the model parameters that are otherwise constrained well cannot be recovered. It may be also impossible to fit the data with reasonable accuracy. Using *a priori* information does not improve the model recovery. Therefore, the wrong model assumption can be often corrected.

B) *Inversion using a lower anisotropic symmetry*

Here, the situation opposite to that above is discussed. Synthetic data are generated by using the HTIxHTI model from Example 2 but they are inverted using an incorrect model of ORTHOxORTHO symmetry (as in Example 6). The choice of a lower (more general) anisotropic symmetry is justified in cases when the true symmetry is unknown. The goal of this example is to examine whether the correct symmetry can be determined.

Generally, a lower anisotropic symmetry of the model results in a less stable inversion due to the higher number of the model parameters to be recovered. As indicated in Example 6, the inversion for ORTHOxORTHO symmetry is usually possible only for certain combinations of the medium parameters. For example, unless additional *a priori* information is available, only the differences in the anisotropy parameters $(\epsilon_I^{(1)} - \epsilon_I^{(2)})$, $(\delta_I^{(1)} - \delta_I^{(2)})$ and $(\gamma_I^{(1)} - \gamma_I^{(2)})$, $I = 1, 2$, can be recovered rather than the parameters themselves. (Note from Example 6 that, although possible in principle, it may be quite difficult to recover even the differences above.) Unfortunately, to recognize HTIxHTI symmetry with confidence, it is necessary to obtain the individual anisotropy parameters of the ORTHOxORTHO model and show that $\epsilon_I^{(1)} \to 0$, $\delta_I^{(1)} \to 0$, $\gamma_I^{(1)} \to 0$ and $\delta_I^{(3)} \to (\delta_I^{(2)} - 2\epsilon_I^{(2)})$; see Table 2.1 and equation (4.9) applied on HTI symmetry. Clearly, rigorous determination of HTIxHTI symmetry from an assumed ORTHOxORTHO model is thus practically impossible.

Another alternative follows directly from Table 2.1. If the true medium has HTIxHTI symmetry, then the parameters of the inverted ORTHOxORTHO model should satisfy the following relations:

$$(\epsilon_2^{(2)} - \epsilon_2^{(1)}) - (\epsilon_1^{(2)} - \epsilon_1^{(1)}) = \epsilon_2^{(2)} - \epsilon_1^{(2)}, \tag{4.13}$$

$$(\delta_2^{(2)} - \delta_2^{(1)}) - (\delta_1^{(2)} - \delta_1^{(1)}) = \delta_2^{(2)} - \delta_1^{(2)}, \tag{4.14}$$

$$(\delta_1^{(2)} - \delta_1^{(1)}) - (\epsilon_1^{(2)} - \epsilon_1^{(1)}) = \delta_1^{(3)} + \epsilon_1^{(2)} - \epsilon_1^{(1)}, \tag{4.15}$$

$$(\delta_2^{(2)} - \delta_2^{(1)}) - (\epsilon_2^{(2)} - \epsilon_2^{(1)}) = \delta_2^{(3)} + \epsilon_2^{(2)} - \epsilon_2^{(1)}. \tag{4.16}$$

As follows from analysis of the approximate reflection coefficients for orthorhombic media [equations (3.26), (3.30) and (3.31)], combinations of the anisotropy parameters on both sides in equations (4.13)-(4.16) can be extracted from data contain-

ing large-incidence-angle reflections, even without using additional *a priori* information. Unfortunately, the relations above do not guarantee that the medium necessarily possesses HTIxHTI symmetry. For instance, if the medium parameters of the ORTHOxORTHO medium satisfy $\epsilon_1^{(1)} = \epsilon_2^{(1)}$, $\delta_1^{(1)} = \delta_2^{(1)}$, $\delta_1^{(3)} + 2(\epsilon_1^{(2)} - \epsilon_1^{(1)}) = (\delta_1^{(2)} - \delta_1^{(1)})$ and $\delta_2^{(3)} + 2(\epsilon_2^{(2)} - \epsilon_2^{(1)}) = (\delta_2^{(2)} - \delta_2^{(1)})$, then equations (4.13)-(4.16) also hold. Although this would be quite unlikely, such an ORTHOxORTHO model can certainly exist.

Next, we carry out the inversion similarly to that in Example 6. Here, however, no *a priori* information is used. First interesting observation is that the distribution of inverted models has a similar character to that in Example 2 (Figure 4.3). Most importantly, the global minimum has the same value of the objective function $F_{obj} = 0.09$, i.e., the inverted ORTHOxORTHO model fits the data *as well as* the HTIxHTI model from Example 2. Further inversion for all medium parameters of the ORTHOxORTHO model fails as expected from Example 6. However, certain combinations of the medium parameters are well recovered, as shown in Table 4.9. Unfortunately, the differences $(\epsilon_2^{(2)} - \epsilon_1^{(2)})$ and $(\delta_2^{(2)} - \delta_1^{(2)})$ are not recovered with a good accuracy, and thus equations (4.13) and (4.14) cannot be verified. Using the remaining equations (4.15) and (4.16), we obtain the following numerical comparison:

$$0.123 \pm 0.029 \approx 0.165 \pm 0.043, \tag{4.17}$$

$$-0.011 \pm 0.024 \approx -0.008 \pm 0.020. \tag{4.18}$$

Both sides of relations (4.17) and (4.18) are numerically close to each other, which, together with the same data fits of ORTHOxORTHO and HTIxHTI models reported above, is an indication that the true symmetry is HTIxHTI.

To support this suggestion, it is desirable to carry out the inversion of the same data again, this time using HTIxHTI symmetry (which is already done in Example 2). If the HTIxHTI model fits the data as well as the ORTHOxORTHO model (as in this example), one can conclude that the probability of the model having HTIxHTI symmetry is quite high.

In summary, although it may be difficult to identify the true anisotropic symmetry with absolute confidence, it is usually possible to obtain an indication of an incorrect (lower) anisotropic symmetry of the model used for the inversion. If such an indication exists [i.e., certain internal relations between inverted model parameters hold, as those in equations (4.13)-(4.16)], the inversion should be repeated using the corresponding model of higher anisotropic symmetry to obtain additional verification, i.e., comparable data misfits for the models of both symmetries. Of course, the symmetry identification becomes more reliable if more *a priori* information is available, and for simpler models under consideration.

	exact	$F_{obj} \leq 0.12$
$\frac{\Delta\rho}{\bar{\rho}} + \frac{\Delta\alpha}{\bar{\alpha}}$	0.295	0.295 ± 0.002
$\frac{\Delta G}{\bar{G}}$	0.469	0.351 ± 0.064
$\epsilon_1^{(1)} - \epsilon_1^{(2)}$	0.050	0.031 ± 0.023
$\delta_1^{(1)} - \delta_1^{(2)}$	-0.100	-0.092 ± 0.031
$\gamma_1^{(S)}$	0.125	0.082 ± 0.053
$(\delta_1^{(3)} + \epsilon_1^{(2)} - \epsilon_1^{(1)})$	0.150	0.165 ± 0.043
$\epsilon_2^{(1)} - \epsilon_2^{(2)}$	0.050	0.061 ± 0.013
$\delta_2^{(1)} - \delta_2^{(2)}$	0.060	0.073 ± 0.033
$\gamma_2^{(S)}$	0.125	0.113 ± 0.015
$(\delta_2^{(3)} + \epsilon_2^{(2)} - \epsilon_2^{(1)})$	-0.100	-0.008 ± 0.020
$\epsilon_2^{(2)} - \epsilon_1^{(2)}$	0.000	0.114 ± 0.088
$\delta_2^{(2)} - \delta_1^{(2)}$	-0.160	-0.046 ± 0.075

Table 4.9. Inversion results for HTIxHTI model using ORTHOxORTHO symmetry (Example 9-B). Selected combinations of the orthorhombic medium parameters (first column), their true values (second column) obtained by converting the corresponding medium parameters of the HTI medium using Table 2.1 (see HTIxHTI model from Example 2 for model parameters), and their recovered values using the results of the linear inversion ($F_{obj} \leq 0.12$, third column). The error bars represent standard deviations.

4.4 Summary of Chapter 4

I invert the exact *PP*- and *PS*-wave reflection coefficients in the joint nonlinear inversion for parameters of anisotropic media. This inversion requires high-quality data and good data coverage. Tests on several synthetic examples led to the following conclusions:

1. The parameters of isotropic media were fully recovered without the need for any *a priori* information (assuming that sufficiently large incidence angles exceeding 35° are available).

2. The parameters of HTIxHTI media (misaligned symmetry axes of the HTI halfspaces above and below the interface) were successfully recovered using *a priori* knowledge of the $\bar{\beta}/\bar{\alpha}$ ratio and anisotropy parameter γ_1 of the incidence halfspace (both parameters known with 20% accuracy), provided that large-incidence-angle reflections are available (maximum incidence angle used was 45°).

3. If large incidence angles are not available, the inversion for the HTIxHTI model has to be constrained by the additional estimate of one isotropic contrast ($\Delta\rho/\bar{\rho}$, $\Delta\alpha/\bar{\alpha}$ or $\Delta\beta/\bar{\beta}$). Knowledge of another anisotropy parameter of the *incidence* halfspace (such as $\delta_1^{(V)}$ or $\epsilon_1^{(V)}$) further stabilizes this inversion.

4. Using large-incidence-angle reflections, parameters of the HTIxHTI model were recovered well even with data contaminated by large errors. The inversion required *a priori* knowledge of $\bar{\beta}/\bar{\alpha}$, γ_1 and one isotropic contrast, or $\bar{\beta}/\bar{\alpha}$, γ_1 and estimates of the *PP*-wave AVO intercept and *PP*- and *PS*-wave AVO gradients (obtained from the linear inversion). Lower data accuracy is less detrimental than the loss of the large-incidence-angle reflections.

5. Inversion for the HTI/HTI model with aligned symmetry axes of the HTI halfspaces above and below the interface was successful under the same conditions as those for inversion for the HTIxHTI models above, except that only the *contrasts* of the anisotropy parameters across the interface could be recovered reliably. To recover the anisotropy parameters separately, at least some of them has to be known *a priori*.

6. The inversion for the parameters of orthorhombic media was partially successful, when *a priori* information about the anisotropy of the incidence halfspace was available. Even then, only the isotropic contrasts and the anisotropy parameters $\epsilon_2^{(1)}$, $\epsilon_2^{(2)}$ and $\gamma_2^{(S)}$ were recovered, together with a few other combinations of the medium parameters. It was impossible to invert for the parameters $\delta_2^{(1)}$,

$\delta_2^{(2)}$ and $\delta_2^{(3)}$ without more information about the anisotropy of the reflecting orthorhombic medium.

7. Inversion usually provides sufficient indications of both an erroneous calibration of the reflection coefficients and an incorrect *a priori* choice of the anisotropic symmetry of the model.

If the *a priori* information listed above is not available, only certain combinations of the medium parameters can be recovered. The combinations can be determined from the corresponding linear inversion.

The results of the linear inversion can be used as additional constraints for the nonlinear inversion. With such guidance, the nonlinear inversion generally provides higher resolution and accuracy of the inverted model parameters than does linear inversion, and often less *a priori* information is necessary.

Chapter 5

Conclusions and future work

In this thesis, I investigated the contribution of converted *PS*-waves to AVO analysis in anisotropic media. I conclude that although using converted waves cannot guarantee success of AVO analysis, *PS*-wave amplitudes, as additional source of information, can substantially help to stabilize AVO inversion. Joint inversion of *PP*- and *PS*-wave reflection coefficients often enable us to extract medium parameters (or their combinations) with good accuracy. This thesis provides the foundation for such an inversion. Emphasis on limitations of the inversion is an important part of this research.

The main product of this thesis is the *inversion toolbox* that contains three tools: 1) approximate *PP*- and *PS*-wave reflection coefficients, 2) algorithm for joint linear inversion of *PP*- and *PS*-wave reflection coefficients, and 3) algorithm for joint nonlinear inversion of *PP*- and *PS*-wave reflection coefficients.

Approximate PP- and PS-wave reflection coefficients are important for understanding amplitude signatures as they relate AVO response to the corresponding individual medium parameters in a simple fashion. Approximate *PS*-wave reflection coefficients, here derived for arbitrarily anisotropic media, can be used to reduce the ambiguity of conventional *P*-wave AVO analysis; they contain the same medium parameters as approximate reflection coefficients of *PP*-waves, but in different linear combinations. Analytic insight provided by the approximations for anisotropic media is particularly useful. The first-order contribution of anisotropy to reflected *PP*- and *PS*-wave amplitudes in different ranges of incidence angles and azimuths can be conveniently evaluated for various anisotropic symmetries. Understanding the role of anisotropy is especially important for predicting AVO responses from fractured reservoirs, where anisotropy parameters are related to such fundamental reservoir characteristics as the orientation of fractures, fracture density and fracture content. Finally, although the approximate reflection coefficients provide useful qualitative description of prestack amplitudes, they lose their numerical accuracy with increasing velocity and density contrasts across the interface, and increasing strength of the anisotropy. Also, the approximate reflection coefficients lose their accuracy with increasing incidence angle.

Algorithm for joint linear inversion of PP- and PS-wave reflection coefficients is designed to invert the approximate reflection coefficients at small and moderate

incidence angles, where they usually are sufficiently accurate. The linear inversion has several notable advantages. It is fast and provides good initial estimates of well-constrained medium parameters or their combinations. Also, error analysis is relatively simple. Most importantly, the linear inversion provides useful analytic insight, such as how to parameterize the model, what parameters can be recovered for particular anisotropic symmetries and particular data coverage, and what *a priori* information is valuable for the inversion. It also helps to identify the type of anisotropic symmetry of the model. Hence, the linear inversion provides important guidance for the more sophisticated nonlinear inversion.

As an auxiliary tool, I also developed the bias-reduction algorithm. This algorithm allows one to identify and reduce bias (caused by inaccuracy of approximate reflection coefficients) in estimates of the medium parameters obtained from the linear inversion. The bias-reduction method cannot, however, increase stability (i.e., reduce variance) of inverted medium parameters.

Algorithm for joint nonlinear inversion of PP- and PS-wave reflection coefficients is a more sophisticated tool that is significantly more expensive than the linear inversion algorithm. It is designed to invert exact reflection coefficients, which are complicated nonlinear functions of medium parameters (hence the inversion becomes nonlinear). I fully agree with Rüger (1996) who suggests that "there is evidently little hope to carry out blind (meant nonlinear) inversion of the AVO response." However, if supported by the linear inversion, the nonlinear inversion allows one to recover medium parameters with generally higher accuracy and resolution than does the linear inversion. Also, it usually requires less *a priori* information, which makes practical application of the inversion more feasible. The main reason for the higher efficiency of the nonlinear inversion is a more complete exploitation of reflection data at moderate and large incidence angles.

The three tools from the *inversion toolbox* can be used depending on the desired type and quality of the final result. The approximate reflection coefficients can be used in qualitative AVO analysis, as discussed above. If good-quality reflection data are available, linear or nonlinear inversion algorithms can be used to obtain quantitative estimates of medium parameters. Success of both the linear and nonlinear inversions depends also on quality of *a priori* information at hand.

The linear inversion should always be carried out prior to nonlinear inversion. It is capable of providing estimates of velocity and density contrasts across the interface as well as shear-wave splitting γ-type parameter. Recovery of the δ-type anisotropic parameter is also possible, but the estimate is generally less reliable.

Large magnitudes of recovered medium parameters indicate a strong-contrast interface or strong anisotropy of the medium. In such cases, however, the estimates are likely biased, and the bias-reduction process should follow the linear inversion. In general, I recommend applying the bias-reduction process always when the recovered

magnitudes of velocity or density contrast (i.e., $\Delta\alpha/\bar{\alpha}$, $\Delta\beta/\bar{\beta}$ or $\Delta\rho/\bar{\rho}$) exceeds the value 0.2, or anisotropy parameters are recovered with magnitudes higher than 0.15. Note that in order to carry out the bias-reduction process, a tool for computation of exact reflection coefficients must be available.

The bias-reduction process, however, is not a substitute for the nonlinear inversion. Nonlinear inversion carried out after the linear inversion (and bias-reduction process, if necessary) can significantly improve the parameter estimates. In addition, the nonlinear inversion enables one to recover ϵ-type anisotropy parameter. I suggest that nonlinear inversion should be used always when possible, as the final step in obtaining quantitative estimates of medium parameters.

Using appropriate medium theories, the inverted medium parameters (i.e., the parameters constrained by seismic data) can then be related to important rock properties, such as porosity (Krief *et al.*, 1990), saturation (Gassmann, 1951; Brown & Korringa, 1975), lithology (Greenberg & Castagna, 1992; Castagna *et al.*, 1985) or fracture characteristics (Hudson, 1981; Schoenberg, 1983; Hudson *et al.*, 1996; Bakulin *et al.*, 2000a; Bakulin *et al.*, 2000b). This is the ultimate goal of AVO analysis.

Application of the *inversion toolbox* on field data is the next step, the subject of future work. In order to do so, the *PP*- and *PS*-wave reflection coefficients have to be accurately recovered from data. Without doubt, this is a challenging task that requires continuing research. Careful amplitude-preserving data processing is needed. First, data-acquisition problems (variation in the source strength, geophone coupling, changes in acquisition geometry) and data-quality problems (cultural or acquisition random noise, multiples and other interfering wave modes) must be properly evaluated to exclude data not suitable for AVO analysis. Then, problems related to true amplitude recovery must be addressed: source-receiver directivity, polarization analysis, NMO correction, thin-bed tunning and wavelet extraction (accounting for offset-dependent wavelet stretching). Finally, reflection coefficients have to be extracted from prestack amplitudes as functions of the incidence angle and azimuth. In principle, the extraction of reflection coefficients requires knowledge of the medium above the interface (overburden). Clearly, this is one of the most challenging parts of AVO data processing. Prestack amplitudes should be properly corrected for geometrical spreading, transmission losses, influence of the free surface and other structural interfaces close to the sources and receivers, and attenuation. They should be also transformed from offset to the incidence-angle/azimuth domain.

The processing described above has to be carried out for both *PP*- and *PS*-waves; in anisotropic media, two different *PS*-waves with different velocities and polarizations are generated at the reflector. Both these waves should be present in the data. (Using the tools developed in this thesis, it is relatively simple to investigate the reduced inversion capability if only *PP*- or *PS*-wave data are available.) Moreover, accurate polarization analysis have to be applied to correctly recover amplitudes of

the reflected waves. Serious practical difficulties are also associated with a proper correlation of PP- and PS-wave data volumes (Zaengle & Frasier, 1993).

If possible, extracted PP- and PS-wave reflection coefficients should be properly calibrated. Without calibration, they cannot provide the correct absolute values of the inverted medium parameters. However, they can still be used to recover relative spatial variations of the parameters over a reservoir.

True-amplitude processing of 3D multicomponent, multiazimuth seismic data is certainly not a standard approach in AVO analysis today, but I believe it will become possible in future. Various amplitude-preserving processing algorithms are documented in the literature (Castagna, 1993; Resnick, 1993). Some elements of those algorithms can be modified relatively easily and used for the purpose of the AVO inversion discussed here. Continuous development of new techniques is also promising. For example, such troublesome problems of true-amplitude extraction as imperfect NMO correction and offset-dependent wavelet stretching were recently successfully treated in a 3D field data example by Jenner (2001). Correction for one of the most serious propagation phenomena, geometrical spreading, has been suggested for layered isotropic (Ursin, 1990) and VTI (Ursin & Hokstad, 2001) media. Significant practical advantage of these corrections is that they utilize standard reflection moveout data, and knowledge of medium parameters of the overburden is not necessary. Several possibilities for calibration of reflection coefficients are also documented in the literature (Demirbag *et al.*, 1993; Mallick, 1995; Larsen *et al.*, 1999; Poth *et al.*, 2001). Nevertheless, development of new techniques is still needed, especially those addressing corrections of PS-waves for overburden propagation phenomena. Geometrical spreading of S-waves, for example, is significantly influenced by anisotropy (Tsvankin, 1995) and appropriate correction has to be developed. Also, while transmission losses of PP-waves may be sometimes negligible (Jílek, 1998) and often are ignored, they have to be accounted for in the case of PS-waves.

The main argument against the reliability of quantitative AVO analysis is that corrections for propagation phenomena are usually based on simplified assumptions (such as horizontally layered media with no lateral velocity variation). For a more complex heterogeneous, anisotropic overburden, these corrections will likely fail. Their accuracy in correcting AVO amplitudes at the larger incidence angles, which can be used to improve significantly the inversion results, is also questionable. Clearly, without proper corrections, propagation phenomena can damage the valuable AVO signal. In my opinion, quantitative AVO analysis in such cases should benefit from true-amplitude prestack migration techniques. For example, a migration algorithm recently developed by Brandsberg-Dahl *et al.* (2001) allows, besides obtaining an image of the subsurface, extraction of reflection coefficients in the presence of more complex overburden (such as VTI heterogeneous layers producing multipathing). The reflection coefficients are directly obtained as functions of the incidence angle and az-

imuth. The complexity of the overburden is accounted for in an amplitude-preserving iterative process, during which the overburden parameters are updated to improve the quality of seismic images. Further development of this algorithm for the purpose of multicomponent AVO analysis is, of course, necessary. I believe, however, that the future of the work documented in this thesis is in cooperation with such sophisticated amplitude-preserving prestack migration methods that will help to extract the reflection coefficients from data.

The success of AVO analysis resides in the combined effort of geophysics, geology and reservoir engineering. I hope that this thesis makes a small contribution that among many others helps to pave the road to improved AVO. Many important questions, however, are outside the scope of this research and remain unanswered. Still, I close my thesis with an optimistic remark: as I have learned over the last few years, the roads leading to successful solutions of todays scientific problems are seldom straightforward, but we always have a chance to find them, as long as we keep wandering, with our minds open.

References

Aki, K., & Richards, P. G. 1980. *Quantitative seismology: theory and methods.* W. N. Freeman & Co., San Francisco.

Alkhalifah, T., & Tsvankin, I. 1995. Velocity analysis for transversely isotropic media. *Geophysics*, **60**, 1550–1566.

Alkhalifah, T., Tsvankin, I., Larner, K., & Toldi, J. 1996. Velocity analysis and imaging in transversely isotropic media: Methodology and a case study. *The Leading Edge*, May, 371–378.

Alvarez, K., Donati, M., & Aldana, M. 1999. AVO analysis for converted waves. *Pages 876–879 of: 69th Annual Internat. Mtg., Soc. Expl. Geophys., Expanded Abstracts.*

Anderson, R. N. 1996. *4D seismic monitoring of hydrocarbon drainage and geopressure prediction in the offshore Louisiana gulf of Mexico basin.* Ph.D. thesis, Columbia University.

Backus, G. E., & Gilbert, J. F. 1967. Numerical applications of a formalism for geophysical inverse problems. *J. R. Astron. Soc.*, **13**, 247–276.

Bakulin, A., Grechka, V., & Tsvankin, I. 2000a. Estimation of fracture parameters from reflection seismic data, Part I: HTI model due to a single fracture set. *Geophysics*, **65**, 1788–1802.

Bakulin, A., Grechka, V., & Tsvankin, I. 2000b. Estimation of fracture parameters from reflection seismic data, Part II: Fractured models with orthorhombic symmetry. *Geophysics*, **65**, 1803–1817.

Banik, N. C. 1987. An effective anisotropy parameter in transversely isotropic media. *Geophysics*, **52**, 1654–1664.

Bortfeld, R. 1961. Approximation to the reflection coefficients of plane longitudinal and transverse waves. *Geophys. Prospecting*, **9**, 485–502.

Brandsberg-Dahl, S., Hoop, M. V. De, & Ursin, B. 2001. Focusing in dip and AVA compensation on scattering-angle/azimuth gathers. *Revised version submitted to Geophysics.*

Brown, R., & Korringa, J. 1975. On the dependence of the elastic properties of a porous rock on the compressibility of the pore fluid. *Geophysics*, **40**, 608–616.

Burnett, R. C. 1990. Seismic amplitude anomalies and AVO analysis at Mestena Grande field. *Geophysics*, **55**, 1015–1025.

Cambois, G. 2000. Can *P*-wave AVO be quantitative? *The Leading Edge*, **19**, 1246–1251.

Castagna, J. P. 1993. AVO analysis - Tutorial and review. *Pages 3–36 of: Offset-dependent reflectivity - theory and practice of AVO analysis.* (Castagna and Backus, Eds.), SEG, Tulsa.

Castagna, J. P., Batzle, M. L., & Eastwood, R. L. 1985. Relationships between compressional-wave and shear-wave velocities in clastic silicate rocks. *Geophysics*, **50**, 571–581.

Castagna, J. P., Swan, H. W., & Foster, D. J. 1998. Framework for AVO gradient and intercept interpretation. *Geophysics*, **63**, 948–956.

Chiburis, E. F. 1984. Analysis of amplitude versus offset to detect gas-oil contacts in the Arabia Gulf. *Pages 669–670 of: 54th Annual Internat. Mtg., Soc. Expl. Geophys., Expanded Abstracts.*

Coleman, T. F., & Li, Y. 1994. On the convergence of reflective Newton methods for large-scale nonlinear minimization subject to bounds. *Mathematical Programming*, **67**, 189–224.

Coleman, T. F., & Li, Y. 1996. An Interior, trust region approach for nonlinear minimization subject to bounds. *SIAM Journal on Optimization*, **6**, 418–445.

Contreras, P., Grechka, V., & Tsvankin, I. 1999. Moveout inversion of *P*-wave data for horizontal transverse isotropy. *Geophysics*, **64**, 1219–1229.

Dahl, T., & Ursin, B. 1992. Non-linear AVO inversion for a stack of anelastic layers. *Geophys. Prospecting*, **40**, 243–265.

Demirbag, E., Çoruh, C., & Costain, J. K. 1993. Inversion of *P*-wave AVO. *Pages 287–302 of: Offset-dependent reflectivity - theory and practice of AVO analysis.* (Castagna and Backus, Eds.), SEG, Tulsa.

Deng, H. L. 1997. *A complexity analysis of generic optimization problems: Characterization of high-dimensional functions.* Ph.D. thesis, Colorado School of Mines, Golden, Colorado, USA.

DeVault, B. 1997. *3-D seismic prestack multicomponent amplitude analysis, Vacuum field, Lea county, New Mexico.* Ph.D. thesis, Colorado School of Mines, Golden, Colorado, USA.

Donati, S. M. 1998. Making AVO analysis for converted waves a practical issue. *Pages 2060–2063 of: 68th Annual Internat. Mtg., Soc. Expl. Geophys., Expanded Abstracts.*

Downton, J., Lines, L., Goodway, B., Xu, Y., & Li, Y. 2000. Predicting the statistical properties of the fluid stack. *Pages 224–227 of: 70th Annual Internat. Mtg., Soc. Expl. Geophys., Expanded Abstracts.*

Fletcher, R. 1987. *Practical methods of optimization.* John Wiley & Sons.

Gassmann, F. 1951. Über die Elastizität poröser Medien. *Vier. der Natur. Gesellshaft in Zürich*, **96**, 1–23.

Grechka, V., & Tsvankin, I. 1998. 3-D description of normal moveout velocity for anisotropic inhomogeneous media. *Geophysics*, **63**, 1079–1092.

Grechka, V., & Tsvankin, I. 1999. 3-D moveout velocity analysis and parameter estimation for orthorhombic media. *Geophysics*, **64**, 820–837.

Greenberg, M. L., & Castagna, J. P. 1992. Shear-wave velocity estimation in porous rocks: Theoretical formulation, preliminary verification and applications. *Geophys. Prospecting*, **40**, 195–209.

Hudson, J. A. 1981. Wave speeds and attenuation of elastic waves in material containing cracks. *Geophys. J. Roy. Astr. Soc.*, **64**, 133–150.

Hudson, J. A., Liu, E., & Crampin, S. 1996. The mechanical properties of materials with interconnected cracks and pores. *Geophys. J. Int.*, **124**, 105–112.

Hwang, L. F., & Lellis, P. J. 1988. Bright spots related to high GOR oil reservoir in Green Canyon. *Pages 761–763 of: 58th Annual Internat. Mtg., Soc. Expl. Geophys., Expanded Abstracts.*

Jech, J., & Pšenčík, I. 1989. First-order perturbation method for anisotropic media. *Geophys. J. Int.*, **99**, 369–376.

Jenner, E. 2001. *Azimuthal anisotropy of 3-D compressional wave seismic data, Weyburn field, Saskatchewan, Canada.* Ph.D. thesis, Colorado School of Mines, Golden, Colorado, USA.

Jílek, P. 1998. Propagation phenomena in AVO for transversely isotropic media: a modeling study. *Center for Wave Phenomena, CWP-289.*

Jin, S., & Beydoun, W. 1993. A stable elastic inversion for marine data. *Pages 665–668 of: 63th Annual Internat. Mtg., Soc. Expl. Geophys., Expanded Abstracts.*

Kabir, N., Lavaud, B., & Chavent, G. 2000. Estimation of the density contrast by AVO inversion beyond the linearized approximation: an indicator of gas saturation. *Pages 243–246 of: 70th Annual Internat. Mtg., Soc. Expl. Geophys., Expanded Abstracts.*

Keener, J. P. 1997. *Principles of applied mathematics: transformation and approximation.* Addison-Wesley Publishing Company.

Kelly, M. C., Skidmore, C. M., & Cotton, R. 2000. $P-P$ and $P-S$ angle stack inversion. *Pages 222–223 of: 70th Annual Internat. Mtg., Soc. Expl. Geophys., Expanded Abstracts.*

Krief, M., Garrat, J., Stellingwerff, J., & Ventre, J. 1990. A petrophysical interpretation using the velocities of P and S waves (full-waveform sonic. *The Log Analyst*, **31**, 355–369.

Larsen, A. J., Margrave, F. G., & Lu, H-X. 1999. AVO analysis by simultaneous $P-P$ and $P-S$ weighted stacking applied to 3C-3D seismic data. *Pages 721–724 of: 69th Annual Internat. Mtg., Soc. Expl. Geophys., Expanded Abstracts.*

Lavaud, B., Kabir, N., & Chavent, G. 1999. Pushing AVO inversion beyond linearized approximation. *Journal of Seismic Exploration*, **8**, 279–302.

Li, X-Y., Kühnel, T., & MacBeth, C. 1996. Mixed mode AVO response in fractured media. *Pages 1822–1825 of: 66th Annual Internat. Mtg., Soc. Expl. Geophys., Expanded Abstracts.*

Lorenzen, R. J. L. 2000. *Inversion of multicomponent time-lapse seismic data for reservoir characterization of Vacuum Field, New Mexico.* Ph.D. thesis, Colorado School of Mines, Golden, Colorado, USA.

Lynn, H. B., & Thomsen, L. A. 1990. Reflection shear-wave data collected near the principal axes of azimuthal anisotropy. *Geophysics*, **55**, 147–156.

Mallick, S. 1995. Model-based inversion of amplitude-variations-with-offset data using a genetic algorithm. *Geophysics*, **60**, 939–954.

Mallick, S. 1999. Some practical aspects of prestack wavefront inversion using a genetic algorithm: An example from the east Texas Woodbine gas sand. *Geophysics*, **64**, 326–336.

Mallick, S., & Fraser, L. N. 1991. Reflection/transmission coefficients and azimuthal anisotropy in marine studies. *Geophys. J. Int.*, **105**, 241–252.

Mensh, T., & Rasolofosaon, P. 1997. Elastic-wave velocities in anisotropic media of arbitrary symmetry - generalization of Thomsen's parameters ϵ, δ and γ. *Geophys. J. Int.*, **128**, 43–64.

Mosegaard, K., & Tarantola, A. 1995. Monte Carlo sampling of solutions to inverse problems. *J. Geophys. Res.*, **100**(B7), 12431–12447.

Nefedkina, T., & Buzlukov, V. 1999. Seismic dynamic inversion using multiwave AVO data. *Pages 888–891 of: 69th Annual Internat. Mtg., Soc. Expl. Geophys., Expanded Abstracts.*

Ostrander, W. J. 1982. Plane wave reflection coefficients for gas sands at nonnormal angles of incidence. *Pages 216–218 of: 52nd Annual Internat. Mtg., Soc. Expl. Geophys., Expanded Abstracts.*

Pšenčík, I. 1998. Green's functions for inhomogeneous weakly anisotropic media. *Geophys. J. Int.*, **135**, 279–288.

Pšenčík, I., & Gajewski, D. 1998. Polarization, phase velocity and NMO velocity of qP waves in arbitrary weakly anisotropic media. *Geophysics*, **63**, 1754–1766.

Pšenčík, I., & Martins, J. L. 2000. Properties of weak contrast PP reflection/transmission coefficients for weakly anisotropic elastic media. *To appear in Studia Geophysica et Geodaetica.*

Pšenčík, I., & Vavryčuk, V. 1998. Weak contrast PP wave displacement R/T coefficients in weakly anisotropic elastic media. *Pure Appl. Geophys.*, **151**, 699–718.

Poth, L., Castagna, J. P., & Sinha, S. 2001. AVO amplitude calibration without well control. *Pages 223–226 of: 71st Annual Internat. Mtg., Soc. Expl. Geophys., Expanded Abstracts.*

Resnick, J. R. 1993. Seismic data processing for AVO and AVA analysis. *Pages 176–189 of: Offset-dependent reflectivity - theory and practice of AVO analysis.* (Castagna and Backus, Eds.), SEG, Tulsa.

Richards, P. G., & Frasier, C. W. 1976. Scattering of elastic waves from depth-dependent inhomogeneities. *Geophysics*, **41**, 441–458.

Rüger, A. 1996. *Reflection coefficients and azimuthal AVO analysis in anisotropic media.* Ph.D. thesis, Colorado School of Mines, Dept. of Geophysics, Golden, Colorado, USA.

Rüger, A. 1997. *P*-wave reflection coefficients for transversely isotropic models with vertical and horizontal axis of symmetry. *Geophysics*, **62**, 713–722.

Rüger, A. 1998. Variation of *P*-wave reflectivity with offset and azimuth in anisotropic media. *Geophysics*, **63**, 935–947.

Rüger, A., & Tsvankin, I. 1997. Using AVO for fracture detection: analytic basis and practical solutions. *The Leading Edge*, **16**, 1429–1438.

Sambridge, M. 1998. Exploring multidimensional landscapes without a map. *Inverse Problems*, **14**, 427–440.

Sayers, C. M. 1994. *P*-wave propagation in weakly anisotropic media. *Geophys. J. Int.*, **116**, 799–805.

Schoenberg, M. 1983. Reflection of elastic waves from periodically stratified media with interfacial slip. *Geophys. Prospecting*, **31**, 265–292.

Sen, M. K., & Stoffa, P. L. 1991. Nonlinear one-dimensional seismic wavefront inversion using simulated annealing. *Geophysics*, **56**, 1624–1638.

Shuey, R. T. 1985. A simplification of Zeoppritz-equations. *Geophysics*, **50**, 609–614.

Smith, G. C., & Gidlow, P. M. 1987. Weighted stacking for rock property estimation and detection of gas. *Geophys. Prospecting*, **35**, 993–1014.

Snieder, R. 1991. An extension of Backus-Gilbert theory to nonlinear inverse problems. *Inverse Problems*, **7**, 409–433.

Snieder, R. 1998. The role of nonlinearity in inverse problems. *Inverse Problems*, **14**, 387–404.

Snieder, R., Xie, M. Y., Pica, A, & Tarantola, A. 1989. Retrieving both the impedance contrast and background velocity: A global strategy for the seismic reflection problem. *Geophysics*, **54**, 991–1000.

Stewart, R. R., & Gaiser, J. E. 2000. *Application and interpretation of converted waves.* SEG Continuing Education Short Course.

Stoffa, P. L., & Sen, M. K. 1991. Nonlinear multiparameter optimization using genetic algorithms: Inversion of plane-wave seismograms. *Geophysics*, **56**, 1794–1810.

Swan, H. W. 1993. Properties of direct AVO hydrocarbon indicators. *Pages 78–92 of: Offset-dependent reflectivity - theory and practice of AVO analysis.* (Castagna and Backus, Eds.), SEG, Tulsa.

Tarantola, A. 1987. *Inverse problem theory.* Elsevier.

Thomsen, L. 1986. Weak elastic anisotropy. *Geophysics*, **51**, 1954–1966.

Thomsen, L. 1993. Weak anisotropy reflections. *Pages 103–111 of: Offset dependent reflectivity.* (Castagna and Backus, Eds.), SEG, Tulsa.

Törn, A. A., & Žilinskas, A. 1989. *Global optimization.* Berlin, Germany: Springer-Verlag.

Tsvankin, I. 1996. *P*-wave signatures and notation for transversely isotropic media: An overview. *Geophysics*, **61**, 467–483.

Tsvankin, I. 1997a. Reflection moveout and parameter estimation for horizontal transverse isotropy. *Geophysics*, **62**, 614–629.

Tsvankin, I. 1997b. Anisotropic parameters and *P*-wave velocity in orthorhombic media. *Geophysics*, **62**, 1292–1309.

Tsvankin, I. 2001. *Seismic signatures and analysis of reflection data in anisotropic media.* Elsevier Science.

Tsvankin, I. D. 1995. Body-wave radiation patterns and AVO in transversely isotropic media. *Geophysics*, **60**, 1409–1425.

Ursin, B. 1990. Offset-dependent geometrical spreading in a layered medium. *Geophysics*, **55**, 492–496.

Ursin, B., & Hokstad, K. 2001. Geometrical spreading in a layered transversely isotropic medium with vertical symmetry axis. *To be submitted to Geophysics.*

Ursin, B., Ekren, O., & Tjåland, E. 1996. Linearized elastic parameter sections. *Geophys. Prospecting*, **44**, 427–455.

Ursin, B., Bauer, C., Zhao, H., & Fichler, C. 2001. Joint seismic inversion and gravity modeling of a shallow anomaly in the southern Barents Sea. *Submitted to Geophysics.*

Vavryčuk, V. 1999. Weak-contrast reflection/transmission coefficients in weakly anisotropic elastic media. *Geophys. J. Int.*, **138**, 553–562.

Vavryčuk, V., & Pšenčík, I. 1998. *PP*-wave reflection coefficients in weakly anisotropic elastic media. *Geophysics*, **63**, 2129–2141.

Wright, J. 1987. The effects of transverse isotropy on reflection amplitude versus offset. *Geophysics*, **52**, 564–567.

Yardley, G. S., Graham, G., & Crampin, S. 1991. Viability of shear-wave amplitude versus offset studies in anisotropic media. *Geophys. J. Int.*, **107**, 493–503.

Zaengle, J. F., & Frasier, C. W. 1993. Correlation and Interpretation of P-P and P-SV data Zamora gas field, Yolo county, California. *Pages 333–345 of: Offset-dependent reflectivity - theory and practice of AVO analysis.* (Castagna and Backus, Eds.), SEG, Tulsa.

Appendix A

Linearized boundary conditions and approximate PS-wave reflection coefficients within the incidence plane (azimuth $\phi = 0$)

Here, I follow the derivation by Vavryčuk & Pšenčík (1998) for PP-wave reflection coefficients, applying it to PS-wave reflections. For consistency, I use the same notation as that of these authors.

Exact solution of the reflection/transmission problem

Consider a planar interface with the normal $\boldsymbol{n}$, separating two homogeneous arbitrarily anisotropic halfspaces with the densities $\rho^{(1)}$, $\rho^{(2)}$ and the density-normalized stiffness tensor elements $a^{(1)}_{ijkl}$ and $a^{(2)}_{ijkl}$. A harmonic plane wave incident from the halfspace denoted as 1 generates three reflected and three transmitted waves P, S_1 and S_2. The displacement vector of each wave can be written as

$$\boldsymbol{u}^{(N)}(\boldsymbol{x},t) = U^{(N)}\boldsymbol{g}^{(N)}\exp[-i\omega(t-\boldsymbol{p}^{(N)}\cdot\boldsymbol{x})], \tag{A.1}$$

where $N = 0$ corresponds to the incident wave, $N = 1,2,3$ correspond to the reflected S_1, S_2 and P waves and $N = 4,5,6$ correspond to the transmitted S_1, S_2 and P waves, respectively. $U^{(N)}$ denotes the scalar amplitude (generally a complex number), $\boldsymbol{g}^{(N)}$ represents the unit polarization vector of the wave N, $\boldsymbol{p}^{(N)}$ is the corresponding slowness vector, and ω is the circular frequency. The traction vectors associated with the displacement vectors (A.1) are

$$\boldsymbol{T}^{(N)}(\boldsymbol{x},t) = i\omega\, U^{(N)}\boldsymbol{X}^{(N)}, \tag{A.2}$$

where $\boldsymbol{X}^{(N)}$ is so-called *amplitude normalized* traction vector,

$$\begin{aligned} X_i^{(N)} &= \rho^{(1)}a^{(1)}_{ijkl}n_j g_k^{(N)}p_l^{(N)}, \quad N = 0,1,2,3, \\ X_i^{(N)} &= \rho^{(2)}a^{(2)}_{ijkl}n_j g_k^{(N)}p_l^{(N)}, \quad N = 4,5,6. \end{aligned} \tag{A.3}$$

In equation (A.3), Einstein summation convention over repeated indices applies.

For a welded contact between the halfspaces, displacement and traction vector fields must be continuous across the interface. These boundary conditions can be written in a compact matrix form as follows:

$$\hat{\mathbf{C}} \cdot \boldsymbol{U} = \boldsymbol{B}. \tag{A.4}$$

The vector

$$\boldsymbol{B} = -(g_1^{(0)}, g_2^{(0)}, g_3^{(0)}, X_1^{(0)}, X_2^{(0)}, X_3^{(0)})^T \tag{A.5}$$

corresponds to the incident wave of amplitude $U^{(0)} = 1$ (the superscript T denotes the transpose). Also, the 6x6 matrix

$$\hat{\mathbf{C}} = \begin{bmatrix} g_1^{(1)} & g_1^{(2)} & g_1^{(3)} & -g_1^{(4)} & -g_1^{(5)} & -g_1^{(6)} \\ g_2^{(1)} & g_2^{(2)} & g_2^{(3)} & -g_2^{(4)} & -g_2^{(5)} & -g_2^{(6)} \\ g_3^{(1)} & g_3^{(2)} & g_3^{(3)} & -g_3^{(4)} & -g_3^{(5)} & -g_3^{(6)} \\ X_1^{(1)} & X_1^{(2)} & X_1^{(3)} & -X_1^{(4)} & -X_1^{(5)} & -X_1^{(6)} \\ X_2^{(1)} & X_2^{(2)} & X_2^{(3)} & -X_2^{(4)} & -X_2^{(5)} & -X_2^{(6)} \\ X_3^{(1)} & X_3^{(2)} & X_3^{(3)} & -X_3^{(4)} & -X_3^{(5)} & -X_3^{(6)} \end{bmatrix} \tag{A.6}$$

contains quantities related to the incident wave. The polarization vectors $\boldsymbol{g}^{(N)}$ and slowness vectors $\boldsymbol{p}^{(N)}$, which are needed for evaluation of the amplitude-normalized traction vectors $X_i^{(N)}$ [equation (A.3)] and the matrix $\hat{\mathbf{C}}$, must be determined by solving the Christoffel equation,

$$(a_{ijkl} p_i^{(N)} p_l^{(N)} - \delta_{jk}) g_j^{(N)} = 0. \tag{A.7}$$

In general, system (A.7) has to be solved numerically. Finally, the vector

$$\boldsymbol{U} = (R_{S_1}, R_{S_2}, R_P, T_{S_1}, T_{S_2}, T_P)^T \tag{A.8}$$

contains the reflection and transmission coefficients to be found. This vector has to be determined by solving the matrix equation (A.4), together with the Christoffel equation (A.7).

First-order perturbation of the exact solution

Using perturbations of the slowness and polarization vectors $\delta\boldsymbol{p}^{(N)}$ and $\delta\boldsymbol{g}^{(N)}$ introduced in equations (2.4) and (2.6), one can linearize the traction vectors $X^{(N)}$ defined by equations (A.3) and, consequently, vectors $\boldsymbol{B}$, $\boldsymbol{U}$ and matrix $\hat{\mathbf{C}}$ [see equa-

tions (A.5), (A.8) and (A.6)] as

$$\begin{aligned} \boldsymbol{X}^{(N)} &= \boldsymbol{X}^{0(N)} + \delta\boldsymbol{X}^{(N)}, \\ \hat{\mathbf{C}} &= \hat{\mathbf{C}}^0 + \delta\hat{\mathbf{C}}, \\ \boldsymbol{B} &= \boldsymbol{B}^0 + \delta\boldsymbol{B}, \\ \boldsymbol{U} &= \boldsymbol{U}^0 + \delta\boldsymbol{U}. \end{aligned} \tag{A.9}$$

Substituting equations (A.9) into (A.4) and keeping only linear terms, we arrive at the final matrix equation for the perturbed vector of the reflection and transmission coefficients:

$$\delta\boldsymbol{U} = (\hat{\mathbf{C}}^0)^{-1}(\delta\boldsymbol{B} - \delta\hat{\mathbf{C}} \cdot \boldsymbol{U}^0). \tag{A.10}$$

The background vector $\boldsymbol{B}^0$ does not appear in equation (A.10) because $\hat{\mathbf{C}}^0 \cdot \boldsymbol{U}^0 = \boldsymbol{B}^0$. Since the background medium is a uniform full space, a fictitious interface in such a medium generates only one transmitted wave of the same type as the incidence wave. Thus, the perturbed vector $\delta\boldsymbol{U}$ contains all desired reflection (and transmission) coefficients as perturbations of the vanishing reflection coefficients in the background medium. Equation (A.10) can be used to obtain the first-order reflection and transmission coefficients for all possible types of incidence waves and arbitrarily anisotropic media.

Approximate PS-wave reflection coefficients within the incidence plane

A specific type of the incident wave determines all the quantities on the right-hand side of equation (A.10) needed to complete the derivation. For *P*-wave incidence, the background reflection/transmission vector $\boldsymbol{U}^0$ is given by

$$\boldsymbol{U}^0 = (0, 0, 0, 0, 0, 1)^T. \tag{A.11}$$

This fact considerably simplifies the general equation (A.10), since only the 6th column of the perturbation matrix $\delta\hat{\mathbf{C}}$ has to be evaluated. Thus, equation (A.10) takes its final form,

$$\delta\boldsymbol{U} = (\hat{\mathbf{C}}^0)^{-1} \Big(\delta g_1^{(6)} - \delta g_1^{(0)}, \delta g_2^{(6)} - \delta g_2^{(0)}, \delta g_3^{(6)} - \delta g_3^{(0)},$$

$$\delta X_1^{(6)} - \delta X_1^{(0)}, \delta X_2^{(6)} - \delta X_2^{(0)}, \delta X_3^{(6)} - \delta X_3^{(0)}\Big)^T. \tag{A.12}$$

As shown in Vavryčuk & Pšenčík (1998), the inverted matrix $(\hat{\mathbf{C}}^0)^{-1}$ is given by

$$(\hat{\mathbf{C}}^0)^{-1} = \begin{pmatrix} -\frac{\beta^2 p_1^0 Y \cos\Phi}{Z_S} & \frac{\sin\Phi}{2} & -\beta p_1^0 \cos\Phi & \frac{\cos\Phi}{2\rho^0\beta} & -\frac{\beta p_1^0 \sin\Phi}{Z_S} & \frac{\beta^2 (p_1^0)^2 \cos\Phi}{Z_S} \\ \frac{\beta^2 p_1^0 Y \sin\Phi}{Z_S} & \frac{\cos\Phi}{2} & \beta p_1^0 \sin\Phi & -\frac{\sin\Phi}{2\rho^0\beta} & -\frac{\beta p_1^0 \cos\Phi}{Z_S} & -\frac{\beta^2 (p_1^0)^2 \sin\Phi}{Z_S} \\ \frac{\beta^2 p_1^0}{\alpha} & 0 & -\frac{\beta^2 p_1^0 Y}{Z_P} & -\frac{\beta^2 (p_1^0)^2}{Z_P} & 0 & \frac{1}{2\rho^0\alpha} \\ -\frac{\beta^2 p_1^0 Y \cos\Psi}{Z_S} & -\frac{\sin\Psi}{2} & \beta p_1^0 \cos\Psi & -\frac{\cos\Psi}{2\rho^0\beta} & -\frac{\beta p_1^0 \sin\Psi}{Z_S} & \frac{\beta^2 (p_1^0)^2 \cos\Psi}{Z_S} \\ \frac{\beta^2 p_1^0 Y \sin\Psi}{Z_S} & -\frac{\cos\Psi}{2} & -\beta p_1^0 \sin\Psi & \frac{\sin\Psi}{2\rho^0\beta} & -\frac{\beta p_1^0 \cos\Psi}{Z_S} & -\frac{\beta^2 (p_1^0)^2 \sin\Psi}{Z_S} \\ -\frac{\beta^2 p_1^0}{\alpha} & 0 & -\frac{\beta^2 p_1^0 Y}{Z_P} & -\frac{\beta^2 (p_1^0)^2}{Z_P} & 0 & -\frac{1}{2\rho^0\alpha} \end{pmatrix}, \tag{A.13}$$

where Z_P, Z_S and Y are defined as

$$\begin{aligned} Z_P &\equiv 2\alpha\rho^0\beta^2 p_1^0 p_3^{0P}, \\ Z_S &\equiv 2\rho^0\beta^3 p_1^0 p_3^{0S}, \\ Y &\equiv \rho^0(1 - 2\beta^2 (p_1^0)^2). \end{aligned}$$

Based on the derivation of Jech & Pšenčík (1989) and Vavryčuk & Pšenčík (1998), the perturbations of the polarization vectors in equation (A.12) can be expressed as

$$\delta g_i^{(6)} - \delta g_i^{(0)} = (\delta c^{(6)} - \delta c^{(0)}) \left[p_i^{0(0)} - \frac{n_i}{\alpha^2 (n_k p_k^{0(0)})} \right] + (\delta G_i^{(6)} - \delta G_i^{(0)}), \tag{A.14}$$

where i represents the i-th vector component. Here, $\boldsymbol{p}^{0(0)}$ is the slowness vector of the incidence P-wave in the background medium [equation (2.5)], $\boldsymbol{n}$ is the normal to the interface and α is the P-wave background velocity. $\delta c^{(N)}$ is the deviation of the magnitude of the phase velocity of the incident (N=0) or transmitted (N=6) P-wave in the weakly anisotropic medium from the corresponding magnitude in the isotropic background. By a linear perturbation of the Christoffel equation, Jech & Pšenčík (1989) obtained

$$\begin{aligned} \delta c^{(0)} &= \frac{1}{2}\alpha \delta a_{ijkl}^{(1)} p_i^{0(0)} g_j^{0(0)} g_k^{0(0)} p_l^{0(0)}, \\ \delta c^{(6)} &= \frac{1}{2}\alpha \delta a_{ijkl}^{(2)} p_i^{0(0)} g_j^{0(0)} g_k^{0(0)} p_l^{0(0)}, \end{aligned} \tag{A.15}$$

where $g_i^{0(0)}$ is given in relations (2.7) and $a_{ijkl}^{(I)}$ by relation (2.2). It immediately follows that

$$\delta c^{(6)} - \delta c^{(0)} = \frac{1}{2}\alpha \Delta a_{ijkl} p_i^{0(0)} g_j^{0(0)} g_k^{0(0)} p_l^{0(0)}, \tag{A.16}$$

where

$$\Delta a_{ijkl} \equiv \delta a^{(2)}_{ijkl} - \delta a^{(1)}_{ijkl} = a^{(2)}_{ijkl} - a^{(1)}_{ijkl} \tag{A.17}$$

are the contrasts of the elastic parameters across the interface.

The vectors $\delta G_i^{(N)}$ in (A.14) describe the deviations of the polarization vectors in the weakly anisotropic medium from the corresponding polarization vectors in the isotropic background. Using the approach described in the previous paragraph (following Jech & Pšenčík, 1989), it is possible to write

$$\delta G^{(6)}_m - \delta G^{(0)}_m = \frac{\alpha}{\alpha^2 - \beta^2} \Delta a_{ijkl} p_i^{0(0)} g_j^{0(0)} g_k^{0(0)} (\delta_{lm} - g_l^{0(0)} g_m^{0(0)}), \tag{A.18}$$

where δ_{lm} is Kronecker's delta. Notice that equation (A.14) describes the perturbations of the polarization vectors from the background due to both the contrasts in the stiffnesses across the interface and the anisotropy.

Finally, using equations (A.3) and taking into account that $\boldsymbol{n} = (0, 0, 1)$, the difference of the first-order perturbations of the amplitude-normalized traction vectors needed in equation (A.12) can be obtained as

$$\begin{aligned} \delta X^{(6)}_i - \delta X^{(0)}_i = {} & \Delta\rho a^0_{i3kl} g_k^{0(0)} p_l^{0(0)} + \rho^0 \Delta a_{i3kl} g_k^{0(0)} p_l^{0(0)} + \\ & \rho^0 a^0_{i3kl} (\delta g^{(6)}_k - \delta g^{(0)}_k) p_l^{0(0)} + \rho^0 a^0_{i3kl} g_k^{0(0)} (\delta p^{(6)}_l - \delta p^{(0)}_l). \end{aligned} \tag{A.19}$$

The quantities a^0_{i3kl} and ρ^0 are defined in equations (2.2), and Δa_{i3kl} is given by (A.17). Similarly, $\Delta\rho \equiv \rho^{(2)} - \rho^{(1)}$ is the density contrast across the interface. The difference $\delta g^{(6)}_k - \delta g^{(0)}_k$ is specified by relation (A.14). The term $\delta p^{(6)}_l - \delta p^{(0)}_l$ has a physical meaning analogous to that of $\delta g^{(6)}_l - \delta g^{(0)}_l$; however, it is now applied to the slowness vector. Using expressions in Jech & Pšenčík (1989) and Vavryčuk & Pšenčík (1998) yields the relation

$$\delta p^{(6)}_i - \delta p^{(0)}_i = -\frac{\delta c^{(6)} - \delta c^{(0)}}{\alpha^3 p_3^{0(0)}}. \tag{A.20}$$

By substituting equations (A.13), (A.14) and (A.16)-(A.20) into equation (A.12), we can find the approximate P-wave reflection and transmission coefficients. As follows from the convention above, the approximation for the R_{PS_1} reflection coefficient is obtained by using the first row of the matrix $(\hat{\mathbf{C}}^0)^{-1}$ in equation (A.12). The result

can be formally written as

$$\begin{aligned} R_{PS_1} = f\,(&\alpha, \beta, \rho^0, i, j, \Phi, \Delta A_{11}, \Delta A_{13}, \Delta A_{14}, \\ &\Delta A_{15}, \Delta A_{16}, \Delta A_{33}, \Delta A_{34}, \Delta A_{35}, \\ &\Delta A_{36}, \Delta A_{45}, \Delta A_{55}, \Delta A_{56})\,, \end{aligned} \tag{A.21}$$

where $\Delta A_{ij} = A_{ij}^{(2)} - A_{ij}^{(1)}$ are the contrasts in the density-normalized medium parameters a_{klmn} written using Voigt convention. The second coefficient, R_{PS_2}, can be derived using the second row of the matrix $(\hat{\mathbf{C}}^0)^{-1}$; however, it can be also easily obtained from the coefficient R_{PS_1} by the substitution $\cos\Phi \rightarrow -\sin\Phi$ and $\sin\Phi \rightarrow \cos\Phi$, since this is the only difference between rows 1 and 2 of the matrix $(\hat{\mathbf{C}}^0)^{-1}$.

Appendix B

General explicit expressions for the reflection coefficients R_{PS_1} and R_{PS_2}

To generalize the reflection coefficient R_{PS_1} (A.21) for an arbitrary azimuth ψ of the incidence plane, the medium parameters ΔA_{ij} must be expressed in terms of $\Delta A'_{ij}$ defined in the reference coordinate system. The tensor rotation is defined by the following matrix of directional cosines:

$$\hat{\mathbf{R}} = \begin{pmatrix} \cos\psi & -\sin\psi & 0 \\ \sin\psi & \cos\psi & 0 \\ 0 & 0 & 1 \end{pmatrix}. \tag{B.1}$$

Applying matrix (B.1) to the elements $\Delta A'_{ij}$ yields

$$\begin{aligned}
\Delta A_{11} &= \Delta A'_{11}\cos^4\psi + 2\Delta A'_{12}\cos^2\psi\sin^2\psi + 4\Delta A'_{16}\cos^3\psi\sin\psi + \\
&\quad \Delta A'_{22}\sin^4\psi + 4\Delta A'_{26}\cos\psi\sin^3\psi + 4\Delta A'_{66}\cos^2\psi\sin^2\psi, \\
\Delta A_{13} &= \Delta A'_{13}\cos^2\psi + \Delta A'_{23}\sin^2\psi + 2\Delta A'_{36}\cos\psi\sin\psi, \\
\Delta A_{14} &= \Delta A'_{14}\cos^3 - \Delta A'_{15}\cos^2\psi\sin\psi + \Delta A'_{24}\cos\psi\sin^2\psi - \Delta A'_{25}\sin^3\psi + \\
&\quad 2\Delta A'_{46}\cos^2\psi\sin\psi - 2\Delta A'_{56}\cos\psi\sin^2\psi, \\
\Delta A_{15} &= \Delta A'_{14}\cos^2\psi\sin\psi + \Delta A'_{15}\cos^3\psi + \Delta A'_{24}\sin^3\psi + \Delta A'_{25}\cos\psi\sin^2\psi + \\
&\quad 2\Delta A'_{46}\cos\psi\sin^2\psi + 2\Delta A'_{56}\cos^2\psi\sin\psi, \\
\Delta A_{16} &= -\Delta A'_{11}\cos^3\psi\sin\psi + \Delta A'_{12}(\cos^3\psi\sin\psi - \cos\psi\sin^3\psi) + \\
&\quad \Delta A'_{16}(\cos^4\psi - 3\cos^2\psi\sin^2\psi) + \Delta A'_{26}(3\cos^2\psi\sin^2\psi - \sin^4\psi) + \\
&\quad \Delta A'_{66}(2\cos^3\psi\sin\psi - 2\cos\psi\sin^3\psi), \\
\Delta A_{33} &= \Delta A'_{33}, \\
\Delta A_{34} &= \Delta A'_{34}\cos\psi - \Delta A'_{35}\sin\psi, \\
\Delta A_{35} &= \Delta A'_{34}\sin\psi + \Delta A'_{35}\cos\psi, \\
\Delta A_{36} &= -\Delta A'_{13}\cos\psi\sin\psi + \Delta A'_{23}\cos\psi\sin\psi + \Delta A'_{36}(\cos^2\psi - \sin^2\psi),
\end{aligned} \tag{B.2}$$

$$
\begin{aligned}
\Delta A_{45} &= \Delta A'_{44}\cos\psi\sin\psi + \Delta A'_{45}(\cos^2\psi - \sin^2\psi) - \Delta A'_{55}\cos\psi\sin\psi,\\
\Delta A_{55} &= \Delta A'_{44}\sin^2\psi\sin\psi + 2\Delta A'_{45}\cos\psi\sin\psi + \Delta A'_{55}\cos^2\psi,\\
\Delta A_{56} &= -\Delta A'_{14}\cos\psi\sin^2\psi - \Delta A'_{15}\cos^2\psi\sin\psi + \Delta A'_{24}\cos\psi\sin^2\psi + \Delta A'_{25}\cos^2\psi\sin\psi +\\
&\quad \Delta A'_{46}(\cos^2\psi\sin\psi - \sin^3\psi) + \Delta A'_{56}(\cos^3\psi - \cos\psi\sin^2\psi).
\end{aligned}
$$

Relations (B.2) and (A.21) can be used to derive the approximations (2.10) for the azimuthally dependent reflection coefficients R_{PS_1} and R_{PS_2} valid for arbitrarily anisotropic halfspaces. The coefficients contain the components R_{PSV} and R_{PSH} given by

$$
\begin{aligned}
R_{PSV} &= v_1 + v_2\frac{\cos\phi_P}{\cos\phi_S} + v_3\frac{\sin\phi_P}{\cos\phi_S} + v_4\cos\phi_P\sin\phi_P + v_5\sin^2\phi_P + v_6\frac{\cos\phi_P\sin^2\phi_P}{\cos\phi_S} +\\
&\quad v_7\frac{\sin^3\phi_P}{\cos\phi_S} + v_8\cos\phi_P\sin^3\phi_P + v_9\sin^4\phi_P + v_{10}\frac{\cos\phi_P\sin^4\phi_P}{\cos\phi_S} + v_{11}\frac{\sin^5\phi_P}{\cos j},\\
R_{PSH} &= h_1\frac{1}{\cos\phi_S} + h_2\cos\phi_P + h_3\sin\phi_P + h_4\frac{\cos\phi_P\sin\phi_P}{\cos\phi_S} + h_5\frac{\sin^2\phi_P}{\cos\phi_S} +\\
&\quad h_6\cos\phi_P\sin^2\phi_P + h_7\sin^3\phi_P + h_8\frac{\cos\phi_P\sin^3\phi_P}{\cos\phi_S} + h_9\frac{\sin^4\phi_P}{\cos\phi_S},
\end{aligned}
\tag{B.3}
$$

where the coefficients v_i and h_i are as follows:

$$
\begin{aligned}
v_1 &= \frac{\alpha}{2\beta(\alpha^2-\beta^2)}[\Delta A_{35}\cos\psi + \Delta A_{34}\sin\psi],\\
v_2 &= \frac{1}{2(\beta^2-\alpha^2)}[\Delta A_{35}\cos\psi + \Delta A_{34}\sin\psi],\\
v_3 &= -\frac{1}{2}\frac{\Delta\rho}{\rho^0} + \frac{1}{2(\alpha^2-\beta^2)}[-\Delta A_{33} + (\Delta A_{13} + 2\Delta A_{55})\cos^2\psi +\\
&\quad (\Delta A_{23} + 2\Delta A_{44})\sin^2\psi + (\Delta A_{36} + 2\Delta A_{45})\sin 2\psi],\\
v_4 &= -\frac{\beta}{\alpha}\frac{\Delta\rho}{\rho^0} - \frac{1}{2\alpha\beta(\alpha^2-\beta^2)}[-\beta^2\Delta A_{33} + (\beta^2\Delta A_{13} + 2\alpha^2\Delta A_{55})\cos^2\psi +\\
&\quad (\beta^2\Delta A_{23} + 2\alpha^2\Delta A_{44})\sin^2\psi + (\beta^2\Delta A_{36} + 2\alpha^2\Delta A_{45})\sin 2\psi],\\
v_5 &= \frac{1}{2\alpha\beta(\alpha^2-\beta^2)}[-(\alpha^2+4\beta^2)(\Delta A_{35}\cos\psi + \Delta A_{34}\sin\psi) +\\
&\quad (\alpha^2+2\beta^2)(\Delta A_{15}\cos^3\psi + (\Delta A_{14} + 2\Delta A_{56})\cos^2\psi\sin\psi +\\
&\quad (\Delta A_{25} + 2\Delta A_{46})\cos\psi\sin^2\psi + \Delta A_{24}\sin^3\psi)],
\end{aligned}
\tag{B.4}
$$

$$
\begin{aligned}
v_6 &= \frac{1}{2\alpha^2(\alpha^2-\beta^2)}[(2\beta^2+3\alpha^2)\Delta A_{35}\cos\psi+(2\beta^2+3\alpha^2)\Delta A_{34}\sin\psi- \\
&\quad 3\alpha^2(\Delta A_{15}\cos^3\psi+(\Delta A_{14}+2\Delta A_{56})\cos^2\psi\sin\psi+ \\
&\quad (\Delta A_{25}+2\Delta A_{46})\cos\psi\sin^2\psi+\Delta A_{24}\sin^3\psi)], \\
v_7 &= \frac{\beta^2}{\alpha^2}\frac{\Delta\rho}{\rho^0}+\frac{1}{2\alpha^2(\alpha^2-\beta^2)}[(\beta^2+\alpha^2)\Delta A_{33}- \\
&\quad (\beta^2(\Delta A_{13}+4\Delta A_{55})+2\alpha^2(\Delta A_{13}+\Delta A_{55}))\cos^2\psi- \\
&\quad (\beta^2(\Delta A_{23}+4\Delta A_{44})+2\alpha^2(\Delta A_{23}+\Delta A_{44}))\sin^2\psi- \\
&\quad (\beta^2(\Delta A_{36}+4\Delta A_{45})+2\alpha^2(\Delta A_{36}+\Delta A_{45}))\sin 2\psi+ \\
&\quad \alpha^2\Delta A_{11}\cos^4\psi++\alpha^2\Delta A_{22}\sin^4\psi+4\alpha^2\Delta A_{16}\cos^3\psi\sin\psi+ \\
&\quad 4\alpha^2\Delta A_{26}\cos\psi\sin^3\psi+2\alpha^2(\Delta A_{12}+2\Delta A_{66})\sin^2\psi\cos^2\psi], \\
v_8 &= \frac{-\beta}{2\alpha(\alpha^2-\beta^2)}[\Delta A_{33}-2(\Delta A_{13}+2\Delta A_{55})\cos^2\psi- \\
&\quad 2(\Delta A_{23}+2\Delta A_{44})\sin^2\psi-2(\Delta A_{36}+2\Delta A_{45})\sin 2\psi+ \\
&\quad \Delta A_{11}\cos^4\psi+\Delta A_{22}\sin^4\psi+4\Delta A_{16}\cos^3\psi\sin\psi+4\Delta A_{26}\cos\psi\sin^3\psi+ \\
&\quad 2(\Delta A_{12}+2\Delta A_{66})\sin^2\psi\cos^2\psi], \\
v_9 &= \frac{2\beta}{\alpha(\alpha^2-\beta^2)}[\Delta A_{35}\cos\psi+\Delta A_{34}\sin\psi-\Delta A_{15}\cos^3\psi-\Delta A_{24}\sin^3\psi- \\
&\quad (\Delta A_{14}+2\Delta A_{56})\cos^2\psi\sin\psi-(\Delta A_{25}+2\Delta A_{46})\cos\psi\sin^2\psi], \\
v_{10} &= \frac{2\beta^2}{\alpha^2(\alpha^2-\beta^2)}[-\Delta A_{35}\cos\psi-\Delta A_{34}\sin\psi+\Delta A_{15}\cos^3\psi+\Delta A_{24}\sin^3\psi+ \\
&\quad (\Delta A_{14}+2\Delta A_{56})\cos^2\psi\sin\psi+(\Delta A_{25}+2\Delta A_{46})\cos\psi\sin^2\psi], \\
v_{11} &= \frac{\beta^2}{2\alpha^2(\alpha^2-\beta^2)}[\Delta A_{33}-2(\Delta A_{13}+2\Delta A_{55})\cos^2\psi-2(\Delta A_{23}+2\Delta A_{44})\sin^2\psi- \\
&\quad 2(\Delta A_{36}+2\Delta A_{45})\sin 2\psi+\Delta A_{11}\cos^4\psi+\Delta A_{22}\sin^4\psi+4\Delta A_{16}\cos^3\psi\sin\psi+ \\
&\quad 4\Delta A_{26}\cos\psi\sin^3\psi+2(\Delta A_{12}+2\Delta A_{66})\sin^2\psi\cos^2\psi],
\end{aligned}
$$

and

$$
\begin{aligned}
h_1 &= \frac{\alpha}{2\beta(\beta^2-\alpha^2)}[\Delta A_{34}\cos\psi-\Delta A_{35}\sin\psi], \\
h_2 &= \frac{1}{2(\alpha^2-\beta^2)}[\Delta A_{34}\cos\psi-\Delta A_{35}\sin\psi], \\
h_3 &= \frac{1}{4(\alpha^2-\beta^2)}[-2(\Delta A_{36}+2\Delta A_{45})\cos 2\psi+ \\
&\quad (\Delta A_{13}-\Delta A_{23}-2\Delta A_{44}+2\Delta A_{55})\sin 2\psi],
\end{aligned}
\tag{B.5}
$$

$$
\begin{aligned}
h_4 &= \frac{1}{4\alpha\beta(\alpha^2-\beta^2)}[2(\beta^2\Delta A_{36}+2\alpha^2\Delta A_{45})\cos 2\psi + \\
&\quad (\beta^2(-\Delta A_{13}+\Delta A_{23})+2\alpha^2(\Delta A_{44}-\Delta A_{55}))\sin 2\psi], \\
h_5 &= \frac{1}{2\alpha\beta(\alpha^2-\beta^2)}[(\alpha^2+\beta^2)\Delta A_{34}\cos\psi-(\alpha^2+\beta^2)\Delta A_{35}\sin\psi- \\
&\quad (\alpha^2\Delta A_{14}+2\beta^2\Delta A_{56})\cos^3\psi+(\alpha^2\Delta A_{25}+2\beta^2\Delta A_{46})\sin^3\psi+(\alpha^2(\Delta A_{15}-2\Delta A_{46})+ \\
&\quad 2\beta^2(\Delta A_{15}-\Delta A_{25}-\Delta A_{46}))\cos^2\psi\sin\psi+(2\beta^2\Delta A_{14}-\alpha^2\Delta A_{24}-2\beta^2\Delta A_{24}+ \\
&\quad 2\alpha^2\Delta A_{56}+2\beta^2\Delta A_{56})\cos\psi\sin^2\psi], \\
h_6 &= \frac{1}{8(\alpha^2-\beta^2)}[(\Delta A_{14}+3\Delta A_{24}-4\Delta A_{34}+2\Delta A_{56})\cos\psi+ \\
&\quad 2(-3\Delta A_{15}+\Delta A_{25}+2\Delta A_{35}+2\Delta A_{46})\sin\psi- \\
&\quad (3\Delta A_{15}-3\Delta A_{25}-6\Delta A_{46})\cos 2\psi\sin\psi+3(\Delta A_{14}-\Delta A_{24}+2\Delta A_{56})\cos 3\psi], \\
h_7 &= \frac{1}{8(\alpha^2-\beta^2)}[-2(\Delta A_{16}+\Delta A_{26}-2\Delta A_{36}-4\Delta A_{45})\cos 2\psi+ \\
&\quad (\Delta A_{11}-2\Delta A_{13}-\Delta A_{22}+2\Delta A_{23}+4\Delta A_{44}-4\Delta A_{55})\sin 2\psi- \\
&\quad 2(\Delta A_{16}-\Delta A_{26})\cos 4\psi+\frac{1}{2}(\Delta A_{11}-2\Delta A_{12}+\Delta A_{22}-4\Delta A_{66})\sin 4\psi], \\
h_8 &= \frac{\beta}{8\alpha(\alpha^2-\beta^2)}[2(\Delta A_{16}+\Delta A_{26}-2\Delta A_{36}-4\Delta A_{45})\cos 2\psi \\
&\quad +(-\Delta A_{11}+2\Delta A_{13}+\Delta A_{22}-2\Delta A_{23}-4\Delta A_{44}+4\Delta A_{55})\sin 2\psi+ \\
&\quad 2(\Delta A_{16}-\Delta A_{26})\cos 4\psi-\frac{1}{2}(\Delta A_{11}-2\Delta A_{12}+\Delta A_{22}-4\Delta A_{66})\sin 4\psi], \\
h_9 &= \frac{\beta}{8\alpha(\alpha^2-\beta^2)}[(\Delta A_{14}+3\Delta A_{24}-4\Delta A_{34}+2\Delta A_{56})\cos\psi+ \\
&\quad 2(-3\Delta A_{15}+\Delta A_{25}+2\Delta A_{35}+2\Delta A_{46})\sin\psi \\
&\quad -(3\Delta A_{15}-3\Delta A_{25}-6\Delta A_{46})\cos 2\psi\sin\psi+3(\Delta A_{14}-\Delta A_{24}+2\Delta A_{56})\cos 3\psi].
\end{aligned}
$$

Here, ϕ_P and ϕ_S denote the incidence and reflection phase angles, respectively, and ψ is the azimuth of the incidence plane. The quantities A_{ij} are defined above, and α, β and ρ^0 are the background medium parameters (i.e., P- and S-wave velocities and density, respectively). Again, $\Delta x = x^{(2)} - x^{(1)}$ denotes the contrast of any parameter x across the interface.

Appendix C

Approximations R_{PS_1} and R_{PS_2} for orthorhombic media

In the text, the general approximations R_{PS_1} and R_{PS_2} [equations (2.10)] are specified for orthorhombic media. The resulting equations (2.25) contain the components R_{PSV} and R_{PSH} (2.26), composed of linear combinations of the V_j (j=1,..,5) and H_k (k=1,..,4) terms, respectively. The V_j terms are:

$$
\begin{aligned}
V_1 &= -\frac{1}{2}\frac{\Delta\rho}{\bar{\rho}} + \frac{\bar{\alpha}^2}{2(\bar{\alpha}^2-\bar{\beta}^2)}\left[\tilde{\delta}_2^{(2)}\cos^2(\psi-\kappa) + \tilde{\delta}_2^{(1)}\sin^2(\psi-\kappa) - \right. \\
&\quad \left. \tilde{\delta}_1^{(2)}\cos^2\psi - \tilde{\delta}_1^{(1)}\sin^2\psi\right], \\
V_2 &= -\frac{\bar{\beta}}{\bar{\alpha}}\frac{\Delta\rho}{\bar{\rho}} - 2\frac{\bar{\beta}}{\bar{\alpha}}\frac{\Delta\beta}{\bar{\beta}} - \frac{\bar{\alpha}\bar{\beta}}{2(\bar{\alpha}^2-\bar{\beta}^2)}\left[\tilde{\delta}_2^{(2)}\cos^2(\psi-\kappa) + \tilde{\delta}_2^{(1)}\sin^2(\psi-\kappa) - \right. \\
&\quad \left. \tilde{\delta}_1^{(2)}\cos^2\psi - \tilde{\delta}_1^{(1)}\sin^2\psi\right] - 2\frac{\bar{\beta}}{\bar{\alpha}}\left[\gamma_2^{(S)}\sin^2(\psi-\kappa) - \gamma_1^{(S)}\sin^2\psi\right], \qquad \text{(C.1)} \\
V_3 &= \frac{\bar{\beta}^2}{\bar{\alpha}^2}\frac{\Delta\rho}{\bar{\rho}} + 2\frac{\bar{\beta}^2}{\bar{\alpha}^2}\frac{\Delta\beta}{\bar{\beta}} + \frac{\bar{\beta}^2}{2(\bar{\alpha}^2-\bar{\beta}^2)}\left[-\tilde{\delta}_2^{(2)}\cos^2(\psi-\kappa) - \tilde{\delta}_2^{(1)}\sin^2(\psi-\kappa) + \right. \\
&\quad \left. \tilde{\delta}_1^{(2)}\cos^2\psi + \tilde{\delta}_1^{(1)}\sin^2\psi\right] + \frac{\bar{\alpha}^2}{\bar{\alpha}^2-\bar{\beta}^2}\left[\epsilon_2^{(2)}(\cos^4(\psi-\kappa) + 2\cos^2(\psi-\kappa)\sin^2(\psi-\kappa)) + \right. \\
&\quad \epsilon_2^{(1)}\sin^4(\psi-\kappa) - \epsilon_1^{(2)}(\cos^4\psi + 2\cos^2\psi\sin^2\psi) - \epsilon_1^{(1)}\sin^4\psi - \tilde{\delta}_2^{(1)}\sin^2(\psi-\kappa) - \\
&\quad \tilde{\delta}_2^{(2)}\cos^2(\psi-\kappa) + \tilde{\delta}_2^{(3)}\cos^2(\psi-\kappa)\sin^2(\psi-\kappa) + \tilde{\delta}_1^{(1)}\sin^2\psi + \tilde{\delta}_1^{(2)}\cos^2\psi - \\
&\quad \left. \tilde{\delta}_1^{(3)}\cos^2\psi\sin^2\psi\right] + 2\frac{\bar{\beta}^2}{\bar{\alpha}^2}\left[\gamma_2^{(S)}\sin^2(\psi-\kappa) - \gamma_1^{(S)}\sin^2\psi\right], \\
V_4 &= -\frac{\bar{\alpha}\bar{\beta}}{\bar{\alpha}^2-\bar{\beta}^2}\left[\epsilon_2^{(2)}(\cos^4(\psi-\kappa) + 2\cos^2(\psi-\kappa)\sin^2(\psi-\kappa)) + \epsilon_2^{(1)}\sin^4(\psi-\kappa) - \right. \\
&\quad \epsilon_1^{(2)}(\cos^4\psi + 2\cos^2\psi\sin^2\psi) - \epsilon_1^{(1)}\sin^4\psi - \tilde{\delta}_2^{(1)}\sin^2(\psi-\kappa) - \tilde{\delta}_2^{(2)}\cos^2(\psi-\kappa) + \\
&\quad \left. \tilde{\delta}_2^{(3)}\cos^2(\psi-\kappa)\sin^2(\psi-\kappa) + \tilde{\delta}_1^{(1)}\sin^2\psi + \tilde{\delta}_1^{(2)}\cos^2\psi - \tilde{\delta}_1^{(3)}\cos^2\psi\sin^2\psi\right],
\end{aligned}
$$

$$
\begin{aligned}
V_5 \;=\; & -\frac{\bar{\beta}^2}{\bar{\alpha}^2-\bar{\beta}^2}\Big[\epsilon_2^{(2)}(\cos^4(\psi-\kappa)+2\cos^2(\psi-\kappa)\sin^2(\psi-\kappa))+ \\
& \epsilon_2^{(1)}\sin^4(\psi-\kappa)-\epsilon_1^{(2)}(\cos^4\psi+2\cos^2\psi\sin^2\psi)-\epsilon_1^{(1)}\sin^4\psi-\tilde{\delta}_2^{(1)}\sin^2(\psi-\kappa)- \\
& \tilde{\delta}_2^{(2)}\cos^2(\psi-\kappa)+\tilde{\delta}_2^{(3)}\cos^2(\psi-\kappa)\sin^2(\psi-\kappa)+\tilde{\delta}_1^{(1)}\sin^2\psi+\tilde{\delta}_1^{(2)}\cos^2\psi- \\
& \tilde{\delta}_1^{(3)}\cos^2\psi\sin^2\psi\Big].
\end{aligned}
$$

The H_k terms are as follows:

$$
\begin{aligned}
H_1 \;=\; & \frac{\bar{\alpha}^2}{4(\bar{\alpha}^2-\bar{\beta}^2)}\Big[(\tilde{\delta}_2^{(2)}-\tilde{\delta}_2^{(1)})\sin 2(\psi-\kappa)+(\tilde{\delta}_1^{(1)}-\tilde{\delta}_1^{(2)})\sin 2\psi\Big], \\
H_2 \;=\; & \frac{\bar{\alpha}\bar{\beta}}{4(\bar{\alpha}^2-\bar{\beta}^2)}\Big[(\tilde{\delta}_2^{(1)}-\tilde{\delta}_2^{(2)})\sin 2(\psi-\kappa)+(\tilde{\delta}_1^{(2)}-\tilde{\delta}_1^{(1)})\sin 2\psi\Big]+ \\
& \frac{\bar{\beta}}{\bar{\alpha}}\Big[\gamma_2^{(S)}\sin 2(\psi-\kappa)-\gamma_1^{(S)}\sin 2\psi\Big], \qquad \text{(C.2)} \\
H_3 \;=\; & \frac{\bar{\alpha}^2}{2(\bar{\alpha}^2-\bar{\beta}^2)}\Big[\Big[\tilde{\delta}_2^{(1)}-\tilde{\delta}_2^{(2)}-\tilde{\delta}_2^{(3)}(\cos^2(\psi-\kappa)-\sin^2(\psi-\kappa))+ \\
& 2(\epsilon_2^{(2)}-\epsilon_2^{(1)})\sin^2(\psi-\kappa)\Big]\sin(\psi-\kappa)\cos(\psi-\kappa)+\Big[-\tilde{\delta}_1^{(1)}+\tilde{\delta}_1^{(2)}+ \\
& \tilde{\delta}_1^{(3)}(\cos^2\psi-\sin^2\psi)-2(\epsilon_1^{(2)}-\epsilon_1^{(1)})\sin^2\psi\Big]\sin\psi\cos\psi\Big], \\
H_4 \;=\; & -\frac{\bar{\alpha}\bar{\beta}}{2(\bar{\alpha}^2-\bar{\beta}^2)}\Big[\Big[\tilde{\delta}_2^{(1)}-\tilde{\delta}_2^{(2)}-\tilde{\delta}_2^{(3)}(\cos^2(\psi-\kappa)-\sin^2(\psi-\kappa))+ \\
& 2(\epsilon_2^{(2)}-\epsilon_2^{(1)})\sin^2(\psi-\kappa)\Big]\sin(\psi-\kappa)\cos(\psi-\kappa)+\Big[-\tilde{\delta}_1^{(1)}+\tilde{\delta}_1^{(2)}+ \\
& \tilde{\delta}_1^{(3)}(\cos^2\psi-\sin^2\psi)-2(\epsilon_1^{(2)}-\epsilon_1^{(1)})\sin^2\psi\Big]\sin\psi\cos\psi\Big].
\end{aligned}
$$

See the main text for the definitions of the quantities involved. The reference coordinate system is defined as in Figure 2.1, with the horizontal x-axis in the $[x_1, x_3]$ symmetry plane of the incidence orthorhombic halfspace.

Appendix D

Polarization angle Φ

Here, I evaluate theoretical expressions for $\cos\Phi$ and $\sin\Phi$ required in equations (2.25) for the coefficients R_{PS_1} and R_{PS_2}.

Jech & Pšenčík (1989) and Pšenčík (1998) derived general expressions for Φ that can be specified for a particular anisotropic symmetry. Adopting the convention introduced in Figure 2.1 and equations (2.8), the polarization angle Φ for an orthorhombic incidence medium can be written as:

$$\begin{aligned} \cos\Phi &= \left[\frac{1}{2}(1+\frac{A}{D})\right]^{1/2}, \\ \sin\Phi &= \frac{B}{|B|}\left[\frac{1}{2}(1-\frac{A}{D})\right]^{1/2}, \end{aligned} \tag{D.1}$$

if $B \neq 0$, or

$$\cos\Phi = 1, \qquad \sin\Phi = 0 \qquad (B=0) \tag{D.2}$$

otherwise. In (D.1),

$$D \equiv [A^2 + 4B^2]^{1/2} \tag{D.3}$$

and

$$
\begin{aligned}
A \equiv\ & 2A_{33}^{(1)}(\epsilon_1^{(2)}\cos^2\psi - \tilde{\delta}_1^{(2)})\cos^2\psi\cos^2\phi_S\sin^2\phi_S + \\
& 2A_{33}^{(1)}(\epsilon_1^{(1)}\sin^2\psi - \tilde{\delta}_1^{(1)})\sin^2\psi\cos^2\phi_S\sin^2\phi_S + \\
& 2A_{33}^{(1)}(1+2\epsilon_1^{(2)})\tilde{\delta}_1^{(3)}\cos^2\psi\sin^2\psi(\cos^2\phi_S+1)\sin^2\phi_S + \\
& 4A_{33}^{(1)}\epsilon_1^{(2)}\cos^2\psi\sin^2\psi\cos^2\phi_S\sin^2\phi_S + \\
& 2A_{33}^{(1)}(\epsilon_1^{(2)} - \epsilon_1^{(1)})\cos^2\psi\sin^2\psi\sin^2\phi_S - \\
& 2A_{55}^{(1)}\gamma_1^{(1)}\sin^2\psi\sin^2\phi_S - \\
& 2A_{55}^{(1)}\gamma_1^{(S)}\cos^2(2\psi) - \\
& 2A_{55}^{(1)}(\gamma_1^{(1)} - \gamma_1^{(S)})\cos^2\psi\sin^2\phi_S,
\end{aligned}
\tag{D.4}
$$

$$
\begin{aligned}
B \equiv\ & A_{33}^{(1)}(1+2\epsilon_1^{(2)})\tilde{\delta}_1^{(3)}\cos\psi\sin\psi\cos 2\psi\cos\phi_S\sin^2\phi_S + \\
& 2A_{33}^{(1)}(\epsilon_1^{(1)} - \epsilon_1^{(2)})\cos\psi\sin^3\psi\cos\phi_S\sin^2\phi_S + \\
& A_{33}^{(1)}(\tilde{\delta}_1^{(2)} - \tilde{\delta}_1^{(1)})\cos\psi\sin\psi\cos\phi_S\sin^2\phi_S + \\
& 2A_{55}^{(1)}\gamma_1^{(S)}\cos\psi\sin\psi\cos\phi_S,
\end{aligned}
\tag{D.5}
$$

where $\gamma_1^{(1)} \equiv (A_{66}^{(1)} - A_{55}^{(1)})/2A_{55}^{(1)}$ (Tsvankin, 1997b), and all the other quantities are defined in the text.

The functions $\cos\Phi$ and $\sin\Phi$ are singular ($D = 0$) for the directions of the reflected-wave slowness vector corresponding to S-wave singularities, where the S_1- and S_2-wave velocities are identical. For such cases, neither equations (D.1) nor the R_{PS_1} and R_{PS_2} approximations (2.25) can be used.

We can proceed in the same way as above if the incidence halfspace is HTI. However, we can also use the fact that the polarizations of S-waves propagating in HTI media are known. One of the waves is always polarized within the plane formed by the slowness vector and the (horizontal) symmetry axis, while the other is polarized in the isotropy (vertical) plane. These geometrical relationships make it possible to derive purely "geometrical" expressions for $\cos\Phi$ and $\sin\Phi$ that do not contain any medium parameters:

$$
\begin{aligned}
\cos\Phi &= \frac{\cos\phi_S\cos\psi}{\sqrt{1-\sin^2\phi_S\cos^2\psi}}, \\
\sin\Phi &= \frac{-\sin\psi}{\sqrt{1-\sin^2\phi_S\cos^2\psi}}.
\end{aligned}
\tag{D.6}
$$

As before, ϕ_S and ψ denote the S-wave reflection phase angle and the azimuth of the

incidence plane, respectively. Equations (D.6) are more stable than (D.1), with the only singular point for $\phi_S = 90°$ and $\psi = 0°$. Obviously, the incidence angle $\phi_S = 90°$ is far beyond the area of applicability of the approximations.

For a VTI incidence halfspace, the situation is even simpler. One S-wave is polarized in the incidence plane (SV) and the other is perpendicular to the (SH). Thus, it immediately follows that

$$\cos\Phi = 1, \qquad \sin\Phi = 0. \tag{D.7}$$

From equations (D.7) and (2.25), R_{PS_1} for VTI media represents the reflection coefficient of the P-SV wave (polarized in the incidence plane) and R_{PS_2} represents the reflection coefficient of the P-SH wave (polarized horizontally). Such a P-SH conversion is generated if the reflecting halfspace has HTI, orthorhombic, or lower symmetry [see equations (C.1) and (C.2)], and the incidence plane does not coincide with a vertical symmetry plane of the reflecting medium.

Equations (D.7) also hold for a purely isotropic incidence medium. In that case, R_{PS_1} and R_{PS_2} correspond to the reflection coefficients of SV and SH components of the S-wave, respectively; both components travel with the same velocity.

Appendix E

Large-incidence-angle terms of the reflection coefficient R_{PSV}

Equation (3.15) of the main text introduces the large-incidence-angle terms S_3, S_4, S_5 and S_6. Although they are never used in the inversion described here, they may be important for inversion of error-contaminated data. In conjunction with the large-incidence-angle term P_2 [equations (3.8)-(3.13)], S_3, S_4, S_5 and S_6 provide constraints on the anisotropy parameters $\epsilon_I^{(1)}$, $\epsilon_I^{(2)}$ and $\delta_I^{(3)}$ [see equations (2.15), (2.16) and (2.23)].

For the purpose of the inversion discussed here, it is convenient to represent the large-incidence-angle terms as follows:

$$
\begin{aligned}
S_i \;=\; & f_i\Big(\frac{\bar{\beta}}{\bar{\alpha}}, \frac{\Delta\rho}{\bar{\rho}}, \frac{\Delta G}{\bar{G}}, \delta_1^{(1)}, \delta_1^{(2)}, \gamma_1^{(S)}, \delta_2^{(1)}, \delta_2^{(2)}, \gamma_1^{(S)}\Big) + \\
& K_i \times \Bigg\{ \Big[\frac{1}{4}(\delta_2^{(3)} + \epsilon_2^{(2)} - \epsilon_2^{(1)}) \sin^2 2\kappa - (\epsilon_2^{(2)} - \epsilon_2^{(1)}) \sin^2\kappa + \epsilon_2^{(2)} - \epsilon_1^{(2)}\Big] \\
& -\frac{1}{4}\Big[(\delta_2^{(3)} + \epsilon_2^{(2)} - \epsilon_2^{(1)}) \sin 4\kappa\Big] \sin 2\psi \cos 2\psi \\
& + \Big[(\epsilon_2^{(2)} - \epsilon_2^{(1)}) \sin 2\kappa\Big] \sin\psi \cos\psi \\
& + \Big[(\delta_2^{(3)} + \epsilon_2^{(2)} - \epsilon_2^{(1)}) \cos 4\kappa - (\delta_1^{(3)} + \epsilon_1^{(2)} - \epsilon_1^{(1)})\Big] \sin^2\psi \cos^2\psi \\
& - \Big[(\epsilon_2^{(2)} - \epsilon_2^{(1)}) \cos 2\kappa - (\epsilon_1^{(2)} - \epsilon_1^{(1)})\Big] \sin^2\psi \Bigg\},
\end{aligned}
\tag{E.1}
$$

where $i = 3$, 4, 5 and 6 [see equation (3.15)]. All medium parameters in equation (E.1), as well as the angles ψ and κ, are defined in the main text [see equations (3.1)-(3.13)]. The constants K_i and functions f_i differ for each large-incidence-angle

term. Using the notation $g \equiv (\bar{\beta}/\bar{\alpha})^2$, we can write

$$\begin{aligned} K_3 &\equiv \frac{1}{1-g}, \\ K_4 &\equiv -\frac{\sqrt{g}}{1-g}, \\ K_5 &\equiv -\frac{g}{2(1-g)}, \\ K_6 &\equiv -\frac{g^2}{2(1-g)}, \end{aligned} \tag{E.2}$$

and

$$\begin{aligned} f_3 \equiv & \left[\left(+\frac{4+g}{4(1-g)}(\delta_2^{(2)}-\delta_2^{(1)})+2g\gamma_2^{(S)}\right)\sin^2\kappa-\frac{4+g}{4(1-g)}(\delta_2^{(2)}-\delta_1^{(2)})-\frac{1}{4}g\frac{\Delta\rho}{\bar{\rho}}+g\frac{\Delta G}{\bar{G}}\right] \\ + & \left[\left(-\frac{4+g}{4(1-g)}(\delta_2^{(2)}-\delta_2^{(1)})-2g\gamma_2^{(S)}\right)\sin 2\kappa\right]\sin\psi\cos\psi \\ + & \left[\left(+\frac{4+g}{4(1-g)}(\delta_2^{(2)}-\delta_2^{(1)})+2g\gamma_2^{(S)}\right)\cos 2\kappa-\frac{4+g}{4(1-g)}(\delta_1^{(2)}-\delta_1^{(1)})-2g\gamma_1^{(S)}\right]\sin^2\psi, \end{aligned}$$

$$\begin{aligned} f_4 \equiv & \left[\left(-\frac{\sqrt{g}}{1-g}(\delta_2^{(2)}-\delta_2^{(1)})\right)\sin^2\kappa+\frac{\sqrt{g}}{1-g}(\delta_2^{(2)}-\delta_1^{(2)})\right] \\ + & \left[\left(+\frac{\sqrt{g}}{1-g}(\delta_2^{(2)}-\delta_2^{(1)})\right)\sin 2\kappa\right]\sin\psi\cos\psi \\ + & \left[\left(-\frac{\sqrt{g}}{1-g}(\delta_2^{(2)}-\delta_2^{(1)})\right)\cos 2\kappa+\frac{\sqrt{g}}{1-g}(\delta_1^{(2)}-\delta_1^{(1)})\right]\sin^2\psi, \end{aligned} \tag{E.3}$$

$$\begin{aligned} f_5 \equiv & \left[\left(-\frac{2g-g^2}{4(1-g)}(\delta_2^{(2)}-\delta_2^{(1)})+g^2\gamma_2^{(S)}\right)\sin^2\kappa+\frac{2g-g^2}{4(1-g)}(\delta_2^{(2)}-\delta_1^{(2)})+\frac{1}{2}g^2\frac{\Delta G}{\bar{G}}\right] \\ + & \left[\left(+\frac{2g-g^2}{4(1-g)}(\delta_2^{(2)}-\delta_2^{(1)})-g^2\gamma_2^{(S)}\right)\sin 2\kappa\right]\sin\psi\cos\psi \\ + & \left[\left(-\frac{2g-g^2}{4(1-g)}(\delta_2^{(2)}-\delta_2^{(1)})+g^2\gamma_2^{(S)}\right)\cos 2\kappa+\frac{2g-g^2}{4(1-g)}(\delta_1^{(2)}-\delta_1^{(1)})-g^2\gamma_1^{(S)}\right]\sin^2\psi, \end{aligned}$$

$$
\begin{aligned}
f_6 \equiv & \left[\left(-\frac{g^2}{2(1-g)}(\delta_2^{(2)}-\delta_2^{(1)})\right)\sin^2\kappa+\frac{g^2}{2(1-g)}(\delta_2^{(2)}-\delta_1^{(2)})\right] \\
+ & \left[\left(+\frac{g^2}{2(1-g)}(\delta_2^{(2)}-\delta_2^{(1)})\right)\sin 2\kappa\right]\sin\psi\cos\psi \\
+ & \left[\left(-\frac{g^2}{2(1-g)}(\delta_2^{(2)}-\delta_2^{(1)})\right)\cos 2\kappa+\frac{g^2}{2(1-g)}(\delta_1^{(2)}-\delta_1^{(1)})\right]\sin^2\psi.
\end{aligned}
$$

All functions f_i above consist of combinations of the medium parameters that can be obtained by inverting the small-incidence-angle terms. Therefore, all f_i can be taken as known prior to the inversion of the large-incidence-angle terms (E.1). Of course, errors in f_i estimates, obtained by inverting small-incidence-angle terms, thus propagate to the inversion of large-incidence-angle terms.

Note that equation (3.8) for the P-wave large-incidence-angle term P_2 [together with equations (3.9)-(3.13)] is a special case of equation (E.1), where the corresponding function $f_{P_2} = \frac{1}{2}\frac{\Delta\alpha}{\bar{\alpha}}$ and the constant $K_{P_2} = \frac{1}{2}$. Therefore, equations (E.1) for $i = 3$, 4, 5 and 6 do not provide any independent information not contained already in the P_2 term from equation (3.8). This redundancy is convenient, however, for stabilizing the estimates of the combinations of anisotropy parameters (3.30)-(3.33) in the presence of noise.

Appendix F

Theoretical basis of a realistic linear inversion

Performing a practical linear inversion, i.e., an inversion of data contaminated by errors, is equivalent to solving the following linear system:

$$\mathbf{Am} = \mathbf{d_0} + \mathbf{e}, \tag{F.1}$$

where $\mathbf{m}$ is the vector of the model parameters to be found, $\mathbf{d_0}$ is the theoretical data vector free of errors, $\mathbf{e}$ is the vector of errors that contaminates $\mathbf{d_0}$, and the matrix $\mathbf{A}$ characterizes the projection of the model parameters onto the data space. Due to the presence of errors $\mathbf{e}$, it is impossible to find an exact mathematical solution of the system (F.1). The system can, however, be solved approximately. An approximate solution $\mathbf{m}'$ is usually found by minimizing the misfit between the measured and predicted data, so that $\mathbf{m}'$ satisfies the condition $\min ||(\mathbf{d_0} + \mathbf{e}) - \mathbf{Am}'||$, where $||\mathbf{x}|| \equiv \sqrt{\sum_{i=1}^{N} x_i^2}$ denotes the L_2 norm of the vector $\mathbf{x} = (x_i, x_2, ..., x_N)$ (this is known as the least-squares fitting procedure). It can be shown (Keener, 1997) that satisfying the above condition is equivalent to finding the so-called *generalized (pseudo) inverse* $\mathbf{A}'$ of the matrix $\mathbf{A}$, so that

$$\mathbf{m}' = \mathbf{A}'(\mathbf{d_0} + \mathbf{e}). \tag{F.2}$$

The generalized inverse $\mathbf{A}'$, which depends on the forward operator $\mathbf{A}$, always exists. The generalized inverse $\mathbf{A}'$ can be found by several different methods. In this paper, I use the method of singular value decomposition (SVD) of the matrix $\mathbf{A}$, as described in Keener (1997).

However, knowledge of the generalized inverse $\mathbf{A}'$ itself does not guarantee a good inversion result. In practical problems, the forward matrix $\mathbf{A}$ from equation (F.1) may have a nontrivial null space, i.e., some of the model parameters m_i (components of the model vector $\mathbf{m}$) are projected by the matrix $\mathbf{A}$ onto the data space as zeroes (similarly, $\mathbf{A}$ with a nontrivial pseudo-null space projects components of $\mathbf{m}$ onto the data space as small values). The more common case of the nontrivial pseudo-null space means that a particular model parameter is poorly constrained by the data and the inversion for this parameter becomes unstable (i.e., a small error in the data results in a large error in the estimated model parameter). The inversion can be

stabilized in the so-called *regularization* process designed to recover more stable linear combinations of the model parameters m_i rather than the parameters themselves. Clearly, the regularization process increases the stability, but decreases the resolution. Although regularization is extensively used in the inversion described above, a more detailed discussion is beyond the scope of this paper. For more details, see, for example, Tarantola (1987).

An important characteristic of the system (F.1) is the model *covariance matrix* $\mathbf{C}$ that describes how the data errors propagate into the results of the inversion. By definition, the covariance matrix is given by

$$\mathbf{C} \equiv \mathbf{A}'\mathbf{C_d}\mathbf{A}'^{(T)}, \tag{F.3}$$

where $\mathbf{A}'$ is the generalized inverse of matrix $\mathbf{A}$, and the superscript T denotes the transpose; matrix $\mathbf{C}_d$ characterizes data errors. If the data d_i are uncorrelated with standard deviations σ_{d_i} (as I assume for the purpose of this research), $\mathbf{C}_d$ is a diagonal matrix with elements $C_{d_{ii}} = \sigma_{d_i}^2$ (Tarantola, 1987). Similarly, the diagonal elements σ_i^2 of the matrix $\mathbf{C}$ represent the standard deviations σ_i of the corresponding model parameters m_i'. The off-diagonal elements σ_{ij} represent the error correlations of the parameters m_i' and m_j'.

Appendix G

Forward operators for the linear inversion of the coefficients R_{PP} and R_{PSV}

In the main text, I introduced inversion algorithms using the linearized PP- and PS-wave reflection coefficients. The inversion scheme for the PP-wave reflection coefficient [equation (3.35)] contains the forward operator (matrix) $\mathbf{A^P}$ with elements A^P_{ij} defined as

$$\begin{aligned}
A^P_{i1} &= 1, \\
A^P_{i2} &= \sin^2\phi_i, \\
A^P_{i3} &= \sin\psi_i \cos\psi_i \sin^2\phi_i, \\
A^P_{i4} &= \sin^2\psi_i \sin^2\phi_i, \\
A^P_{i5} &= \sin^2\phi_i \tan^2\phi_i, \\
A^P_{i6} &= \sin 2\psi_i \cos 2\psi_i \sin^2\phi_i \tan^2\phi_i, \\
A^P_{i7} &= \sin\psi_i \cos\psi_i \sin^2\phi_i \tan^2\phi_i, \\
A^P_{i8} &= \sin^2\psi_i \cos^2\psi_i \sin^2\phi_i \tan^2\phi_i, \\
A^P_{i9} &= \sin^2\psi_i \sin^2\phi_i \tan^2\phi_i,
\end{aligned} \tag{G.1}$$

where ϕ_i are the incidence angles, ψ_i are the azimuths, and $i = 1,2,\ldots,N$, where N is the number of data points.

Similarly, the inversion scheme for the PSV-wave reflection coefficient [equation (3.42)] contains the matrix $\mathbf{A}^S$ with the following elements A^S_{ij}:

$$\begin{aligned}
A^S_{i1} &= \sin\phi_i, \\
A^S_{i2} &= \sin\psi_i \cos\psi_i \sin\phi_i, \\
A^S_{i3} &= \sin^2\psi_i \sin\phi_i, \\
A^S_{i4} &= \sin^3\phi_i,
\end{aligned} \tag{G.2}$$

$$
\begin{aligned}
A^S_{i5} &= \sin 2\psi_i \cos 2\psi_i \sin^3 \phi_i, \\
A^S_{i6} &= \sin \psi_i \cos \psi_i \sin^3 \phi_i, \\
A^S_{i7} &= \sin^2 \psi_i \cos^2 \psi_i \sin^3 \phi_i, \\
A^S_{i8} &= \sin^2 \psi_i \sin^3 \phi_i, \\
A^S_{i9} &= \sin^5 \phi_i, \\
A^S_{i10} &= \sin 2\psi_i \cos 2\psi_i \sin^5 \phi_i, \\
A^S_{i11} &= \sin \psi_i \cos \psi_i \sin^5 \phi_i, \\
A^S_{i12} &= \sin^2 \psi_i \cos^2 \psi_i \sin^5 \phi_i, \\
A^S_{i13} &= \sin^2 \psi_i \sin^5 \phi_i, \\
A^S_{i14} &= \sin^7 \phi_i, \\
A^S_{i15} &= \sin 2\psi_i \cos 2\psi_i \sin^7 \phi_i, \\
A^S_{i16} &= \sin \psi_i \cos \psi_i \sin^7 \phi_i, \\
A^S_{i17} &= \sin^2 \psi_i \cos^2 \psi_i \sin^7 \phi_i, \\
A^S_{i18} &= \sin^2 \psi_i \sin^7 \phi_i.
\end{aligned}
$$